New Fundamental Insights into the Hydrogen Evolution Reaction on Pt and Ni Based Model Electrocatalysts Using Different Hydrodynamical Electrochemical Setups – The Impinging Jet Flow Cell and the Rotating Disk Electrode

Dissertation

to obtain the academic degree

Doctor of Natural Sciences

(Dr. rer. nat.)

submitted

to the Department of Chemistry,

Institute of Physical Chemistry,

Universität Hamburg

by

Christian Schneemann

Hamburg 2025

Reviewers:

First Reviewer:	Prof. Dr. Mehtap Özaslan
Second Reviewer:	Prof. Dr. Matthias Arenz

Thesis Defense Committee:

First Examiner:	Prof. Dr. Mehtap Özaslan
Second Examiner:	Prof. Dr.-Ing. Jakob Albert
Third Examiner:	Prof. Dr. Alf Mews

Date of Disputation: 17.04.2026

Date of Print Approval: 17.04.2026

The results presented in this dissertation were obtained from August 2020 until November 2025 supervised by Prof. Dr. Mehtap Oezaslan at the Technical Electrocatalysis Laboratory, Institute of Physical Chemistry, Department of Chemistry, Universität Hamburg (until September 2024 located at the Institute of Technical Chemistry, TU Braunschweig).

I. List of Publications and Conference Contributions

Journal Articles

- Khavala V.B.[=], **Schneemann C.[=]**, Kallina V., Dosche C., Thomas T., Murty B.S., Oezaslan M., Concentration-Dependent Effects of Iron Impurities on Nickel Electrodes for Hydrogen Evolution Reaction in Alkaline Media, International Journal of Hydrogen Energy **2025**, *submitted.*
- **Schneemann C.**, Traegner J., Mindermann L., Friedrichs-Schucht M., Tang B., Dietzel A., Oezaslan M., A Universal Analytical Model for the Limiting Current Characteristics in Impinging Jet Electrodes. Journal of The Electrochemical Society **2025**;172(6):66503.
- Rager K., Tang B., **Schneemann C.**, Dworzak A., Oezaslan M., Dietzel A., Ordered Porous Electrodes Obtained Using LIFT for Electrochemical Applications. Materials (Basel) **2023**;16(2):596.
- Steimecke M., Seiffarth G., **Schneemann C.**, Oehler F., Förster S., Bron M., Higher-Valent Nickel Oxides with Improved Oxygen Evolution Activity and Stability in Alkaline Media Prepared by High-Temperature Treatment of $Ni(OH)_2$. ACS Catalysis **2020**;10(6):3595–603.

[=]equal contribution

Conference Talks

- **Schneemann C.**, Traegner J., Mindermann L., Friedrichs-Schucht M., Tang B., Dietzel A., Oezaslan M.: Theory and Experiment of the Limiting Current in Impinging Jet Electrodes, 245th Meeting of the Electrochemical Society, **2024**, San Francisco, USA.
- Khavala V.B.[=], **Schneemann C.**[=], Kallina V., Dosche C., Thomas T., Murty B.S., Oezaslan M., The Role of Iron Impurities on Nickel Cathodes for Hydrogen Evolution Reaction (HER), 245th Meeting of the Electrochemical Society, **2024**, San Francisco, USA.
- **Schneemann C.**, Traegner J., Mindermann L., Friedrichs-Schucht M., Tang B., Dietzel A., Oezaslan M.: Development of an Universal Analytical Model for the Limiting Current Characteristics in Impinging Jet Electrodes, 74th Annual Meeting of the ISE, **2023**, Lyon, France.

Conference Posters

- **Schneemann C.**, Traegner J., Tang B., Tegethoff W., Dietzel A., Oezaslan M., Universal Analytical Model for the Limiting Current Characteristics in Impinging Jet Electrodes, GDCh Electrochemistry **2024**, Braunschweig, Germany.
- **Schneemann C.**, Lasek K., Blaseio S., Friedrichs-Schucht M., Dosche C., Batzill M., Oezaslan M., Two-Dimensional (2D) Platinum Tellurides for Hydrogen Evolution Reaction (HER), GDCh Electrochemistry **2024**, Braunschweig, Germany.
- Khavala V.B.[=], **Schneemann C.**[=], Kallina V., Dosche C., Thomas T., Murty B.S., Oezaslan M., The Role of Iron Impurities on Nickel Cathodes for Hydrogen Evolution Reaction (HER), GDCh Electrochemistry **2024**, Braunschweig, Germany.
- **Schneemann C.**, Lasek K., Blaseio S., Friedrichs-Schucht M., Dosche C., Batzill M., Oezaslan M., Hydrogen Evolution Reaction (HER) Performance and Stability of (2D) Platinum Telluride Model Catalyst Materials Probed by Raman Spectroscopy, 19th Confocal Raman Imaging Symposium, **2023**, Ulm, Germany.
- **Schneemann C.**, Lasek K., Blaseio S., Friedrichs-Schucht M., Dosche C., Batzill M., Oezaslan M., Highly Active Two-Dimensional (2D) Platinum Tellurides as Model Catalysts for Hydrogen Evolution Reaction (HER), 74th Annual Meeting of the ISE, **2023**, Lyon, France.
- **Schneemann C.**[=], Traegner J.[=], Tang B., Tegethoff W., Dietzel A., Oezaslan M.: Optimization of the Mass Transport Processes in an Electrochemical Wall-Jet Flow Cell, GDCh Electrochemistry **2022**, Berlin, Germany.
- **Schneemann C.**, Kolekar S.K., Batzill M., Oezaslan M., Two-Dimensional (2D) Platinum Tellurides as Model Catalysts for Hydrogen Evolution Reaction (HER), 54. Jahrestreffen Deutscher Katalytiker, **2021**, online.

[=]equal contribution

II. Contents

III. List of Symbols

α	transfer coefficient
$\alpha_{lattice}$	unit cell parameter α
$\beta(Fe)$	mass concentration of Fe in the electrolyte
$\beta_{lattice}$	unit cell parameter β
$\gamma_{lattice}$	unit cell parameter γ
ΔE_H	hydrogen chemisorption energy
ΔE_{ZPE}	difference in zero-point energy between the adsorbed and the gas phase
ΔG_H	*Gibb's* free energy of hydrogen adsorption
$\Delta\eta$	relative change of the overpotential at $t = n\,h$
Δi_{lim}^{CFD}	relative error of the total limiting current density towards CFD data
Δi_{lim}^{exp}	relative error of the total limiting current density towards experimental data
ΔS_H	difference in entropy due to hydrogen adsorption
ε	electric field
η	overpotential
ρ	electrolyte density
ϕ	polar angle
ν	kinematic viscosity of the electrolyte solution
$\tilde{\nu}$	wave number
ω	rotation speed
A	electrode surface area
A_{geo}	geometric surface area
A_{SA}	electrochemical surface area
$A_{A_{1g}/G}$	normalized Raman peak area A_{1g}/G of Raman bands of 2D-Pt_2Te_2
$A_{E_g/G}$	normalized Raman peak area E_g/G of Raman bands of 2D-$PtTe_2$
$A_{E_g(PtTe_2)/G}$	normalized Raman peak area $E_g(PtTe_2)/G$ of Raman bands of 2D-Pt_3Te_4
$A_{Ni\ 2p_{3/2}}$	area of the Ni $2p_{3/2}$ peak in XPS

$\bar{A}_{A_{1g}/G}$	average normalized Raman peak area A_{1g}/G of Raman bands of 2D-Pt_2Te_2
$\bar{A}_{E_g/G}$	average normalized Raman peak area E_g/G of Raman bands of 2D-$PtTe_2$
$\bar{A}_{E_g(PtTe_2)/G}$	average normalized Raman peak area $E_g(PtTe_2)/G$ of Raman bands of 2D-Pt_3Te_4
a	hydrodynamic constant
a^*	dimensionless hydrodynamic constant
$a_{lattice}$	unit cell parameter a
$b_{lattice}$	unit cell parameter b
B	*Levich* constant
c	concentration of reactive species
$c_{lattice}$	unit cell parameter c
c_{supp}	bulk concentration of the supporting electrolyte
c_∞	bulk concentration of the diffusing reacting species
C_{dl}	double layer capacitance
C_{pseudo}	pseudo capacitance
d	nozzle diameter
D	diffusion coefficient of the diffusing reacting species
E	electrode potential
E_{ads}	adsorption energy of hydrogen on surface
$\lvert E_{i=-0.1\ mA\ cm_{geo}^{-2}} \rvert$	absolute potential at a current density of $i = -0.1\ mA\ cm_{geo}^{-2}$
$E_{initial}$	iR-corrected and averaged potential at $t = 0\ h$
E_n	iR-corrected and averaged potential at $t = 0\ h$
E^0	standard thermodynamic potential for HER
E_{H_2}	energy of the isolated hydrogen molecule
$E_{i=-0.25\ mAcm_{geo}^{-2}}$	overpotential at a current density of $i = -0.25\ mA\ cm_{geo}^{-2}$
$E_{iR-free}$	iR-drop corrected electrode potential
$E_{slab+hydrogen}$	total energy of the slab with hydrogen
E_{slab}	energy of the isolated slab
F	*Faraday* constant
$f\left(\frac{H}{d}\right)$	empirical function of $\frac{H}{d}$

$g(Sc)$	series expression of Sc
H	electrode to nozzle distance
H_{ads}	charge of hydrogen underpotential deposition
H_{des}	charge of hydrogen underpotential desorption
I	total current
I_C	capacitive current
I_{lim}	total limiting current
I_{lim}^{RF}	limiting current of the radial channel-flow region (RF)
I_{lim}^{WJ}	limiting current of the wall-jet region (WJ)
I_{lim}^{WT}	limiting current of the wall-tube region (WT)
$I_{lim,0}^{RF}$	established equation for the limiting current of a radial channel-flow electrode
$I_{lim,0}^{RDE}$	established equation for the limiting current of the RDE
$I_{lim,0}^{WJ}$	established equation for the limiting current of a wall-jet electrode
$I_{lim,0}^{WT}$	established equation for the limiting current of a wall-tube electrode
i	total current density
i_0	exchange current density
i_{diff}	*Nernst* diffusion limited current density
i_{kin}	kinetic current density
i_{lim}	total limiting current density
$i_{lim,loc}$	local limiting current density
$i_{lim,loc}^{RF}$	local limiting current density of the radial channel-flow region
$i_{lim,loc}^{WJ}$	local limiting current density of the wall-jet region
$i_{lim,loc}^{WT}$	local limiting current density of the wall-tube region
$i_{lim,0}^{RF}$	established equation for the limiting current density of a radial channel-flow electrode
$i_{lim,0}^{WJ}$	established equation for the limiting current density of a wall-jet electrode
$i_{lim,0}^{WT}$	established equation for the limiting current density of a wall-tube electrode
k	wall-jet constant

K_0^m	average mass transport coefficient
n	number of transferred electrons
N	number of runs
R	universal gas constant
R_A	transition radius A
R_B	transition radius B
R_C	electrode radius
R_{loc}	local radius
R_u	uncompensated resistance
R_{WT-RF}	intersection radius of local current density functions $i_{lim,loc}^{WT}$ and $i_{lim,loc}^{RF}$
R_{WT-WJ}	intersection radius of local current density functions $i_{lim,loc}^{WT}$ and $i_{lim,loc}^{WJ}$
R_{WJ-RF}	intersection radius of local current density functions $i_{lim,loc}^{WJ}$ and $i_{lim,loc}^{RF}$
rf	roughness factor
s	scan rate
Sc	Schmidt number
t	time
T	temperature
u	velocity vector
u_r	velocity in the radial direction r
u_x	velocity in the axial direction x
$\dot{V}_0$	volume flow rate
Z'	real part of the impedance
$-Z''$	imaginary part of the impedance
$\lvert Q_{NiOOH} \rvert$	charge associated with the reduction of NiOOH

IV. List of Abbreviations

µ-XRF	micro-X-ray fluorescence spectroscopy
2D	two dimensional
ALWE	alkaline liquid water electrolysis
AST	accelerated stress test
BE	binding energy
CAPEX	capital investment cost
CCD	charge-coupled device
CE	counter electrode
CFD	computational fluid dynamics
CP	chronopotentiometry
CV	cyclic voltammetry
CVT	chemical vapor transport
DFT	density functional theory
DL	detection limit
ECSA	electrochemically available surface area
EDX	energy dispersive X-ray
FKM	fluorine kautschuk material
GC	glassy carbon
GDE	gas diffusion electrode
GDL	gas diffusion layer
GEIS	galvanostatic electrochemical impedance spectroscopy
GGA	generalized gradient approximation
HBE	hydrogen binding energy
HER	hydrogen evolution reaction
HFR	high frequency resistance
HOPG	highly ordered pyrolized graphite
HOR	hydrogen oxidation reaction
HPLC	high pressure liquid chromatography
HUPD	hydrogen underpotential deposition
ICP-OES	inductively coupled plasma optical emission spectroscopy
LSV	linear sweep voltammetry
MBE	molecular beam epitaxy
MEA	membrane electrode assembly
MMO	mercury-mercury oxide reference electrode
MMS	mercury-mercury sulfate reference electrode
OCP	open circuit potential
OER	oxygen evolution reaction
ORR	oxygen reduction reaction
PAW	projector-augmented wave
PB	phosphate buffered
PEEK	poly ethylene ether ketone
PEIS	potentiostatic electrochemical impedance spectroscopy
PEM	proton exchange membrane
PEMFC	proton exchange membrane fuel cell
PEMWE	proton exchange membrane water electrolysis

poly-Ni	polycrystalline Nickel electrode
PPS	polyphenylene sulfide
PTL	porous transport layer
QL	quantification limit
RDE	rotating disk electrode
rds	rate determining step
RE	reference electrode
RF	radial channel-flow electrode
RHE	reversible hydrogen electrode
rpm	rotations per minute
SA	surface area
SEM	scanning electron microscopy
TMC	transition metal chalcogenide
TOF	turn over frequency
tw	this work
WE	working electrode
WJ	wall-jet electrode
WT	wall-tube electrode
XPS	X-ray photoelectron spectroscopy

V. Zusammenfassung

Unter den Technologien der Wasserelektrolyse zur Produktion des sogenannten „grünen Wasserstoffs“ gelten die Protonenaustauschmembran-Wasserelektrolyse (PEMWE) und die alkalische Wasserelektrolyse (ALWE) als die ausgereiftesten. Trotz jüngster technologischer Fortschritte bleiben signifikante Reduktionen bei Investitions- und Betriebskosten entscheidend. Die Erreichung dieses Ziels erfordert ein umfassendes Verständnis der Reaktionsmechanismen, Degradationswege und Massentransportbeschränkungen in Elektrolysezellen, welches durch Studien an gut kontrollierten Modellkatalysatoren gewonnen werden kann. Das Hauptziel der vorliegenden Arbeit ist es deshalb, neue Einblicke in die elektrochemische Wasserstoffentwicklungsreaktion (HER) im sauren und alkalischen Medium an Modell-Elektrokatalysatoren auf Platinum- und Nickelbasis unter Verwendung zweier verschiedener elektrochemisch-hydrodynamischer Mess-Setups zu gewinnen. Die Arbeit gliedert sich in vier Teile.

Im ersten Teil wird eine neuartige Impinging-Jet-Durchflusszelle als Drei-Elektroden-Setup für hydrodynamisch-elektrochemische Messungen an atomar dünnen Modellkatalysatoren entwickelt und vorgestellt. Da bislang eine universelle analytische Lösung für den Massentransport in diesen Setups, ähnlich der *Levich*-Gleichung, fehlte, wurde ein universelles analytisches Modell für Massentransport und den massetransportlimitierten Strom entwickelt. Dieses Modell wurde anhand numerischer Simulationen und experimenteller Daten für die Oxidation von Hexacyanidoferrat(II)-Ionen über einen breiten Parameterbereich validiert. Insgesamt wurde eine sehr gute Übereinstimmung mit relativen Fehlern unter 10 % erzielt. Dieses Modell könnte zukünftig langwierige und ressourcenintensive CFD-Simulationen ersetzen. Anschließend wurden im zweiten Teil dieser Arbeit Vergleichsmessungen und Simulationen zwischen diesem Setup und der rotierenden Scheibenelektrode (RDE) anhand der HER an Pt-Modell-Elektroden durchgeführt, um das neu entwickelte Setup zu validieren. Der Vergleich zeigte, dass beide Systeme vergleichbare Gas-Sättigungsgrade, elektrochemische Pt-Features und Massentransportbedingungen aufweisen. Die theoretische Analyse deutete darauf hin, dass die Impinging-Jet-Durchflusszelle grundsätzlich bessere Massentransportbedingungen zulässt als die RDE. Dies legt nahe, dass das Impinging-Jet-Flow-Cell Setup eine vielversprechende Alternative ist, um die HER-Aktivität unter verbesserten Massentransportbedingungen

zu untersuchen. Nach der Validierung des Impinging-Jet-Flow-Cell Setups wurden im dritten Teil dieser Dissertation neuartige, atomar dünne 2D-Platin-Chalkogenid (Pt_xTe_y) Katalysatoren für die Wasserstoffentwicklungsreaktion (HER) im Saurem mit diesem Setup charakterisiert. Die experimentelle HER-Aktivität war in der Reihenfolge 2D-$PtTe_2$ ≈ 2D-Pt_2Te_2 ≪ 2D-Pt_3Te_4. Dichtefunktionaltheorie-Berechnungen führten diese Unterschiede auf den Trend der Wasserstoff-Adsorptions Gibbs Energien (ΔG_H) an Tellur-Vakanzen V_{Te} zurück: 2D-$PtTe_2$≈2D-Pt_2Te_2≪ 2D-Pt_3Te_4. Raman-Spektroskopie ergab, dass 2D-Pt_2Te_2 während der elektrochemischen Experimente teilweise in 2D-Pt_3Te_4 umgewandelt wurde, was auf seine thermodynamische Metastabilität hinweist. 2D-$PtTe_2$ zeigte während der elektrochemischen Tests eine Degradation, vermutlich durch mechanische Delaminierung. Die XPS-Analyse bestätigte, dass keine dieser Phasen Anzeichen einer Degradation zu metallischem Pt zeigten. Diese Erkenntnisse über Struktur-Aktivitäts-Beziehungen und Stabilität werden die zukünftige Entwicklung von Pt-Chalkogenid-Katalysatoren unterstützen, um den Einsatz von Platin-Gruppenmetallen (PGM) bei der HER zu reduzieren.

Der vierte Teil dieser Arbeit untersucht den Einfluss von Eisenionen im Elektrolyten auf die HER-Aktivität auf Nickeloberflächen in alkalischem Medium. Mithilfe der RDE wurden polykristalline Nickel-Modellelektroden Elektrolyten mit Eisenkonzentrationen von 0 bis 14 ppm ausgesetzt. Erste elektrochemische Tests zeigten nur geringe Unterschiede in der HER-Aktivität zwischen den verschiedenen Elektrolyten. Langzeit-Chronopotentiometrie-Tests über 24 Stunden bei konstanter Stromdichte zeigten jedoch, dass Elektroden, die höheren Eisenkonzentrationen, insbesondere 6 und 14 ppm, ausgesetzt waren, weniger Deaktivierung erfuhren und niedrigere Überspannungen aufwiesen. Strukturelle Analysen mit SEM, µ-XRF und XPS bestätigten, dass Eisen dichte, schützende Schichten auf der Nickeloberfläche bildet, die Degradationsmechanismen hemmen können. Diese Ergebnisse deuten darauf hin, dass ein kritischer Schwellenwert an Eisenionen genutzt werden kann, um die Langlebigkeit von Nickel-Kathoden in alkalischer Wasserelektrolyse zu verbessern.

Insgesamt liefert diese Arbeit neue Einblicke in die grundlegenden Faktoren, die die Wasserstoffentwicklung im saurem und im alkalischen Medium beeinflussen. Dieses Verständnis ist für die zukünftige Entwicklung von Elektrolyseuren und die nachhaltige Wasserstoffproduktion in naher Zukunft von entscheidender Bedeutung.

VI. Abstract

To reduce global CO_2 emissions to a net zero level by 2050, hydrogen is recognized as a key energy carrier. Among the water electrolysis technologies used to produce so-called "green hydrogen," proton exchange membrane water electrolysis (PEMWE) and alkaline water electrolysis (ALWE) can be considered the most mature. Despite recent technological progress, significant reductions in capital and operational costs remain critical. Achieving this requires a comprehensive understanding of reaction mechanisms, degradation pathways, and mass transport limitations in electrolysis cells, which can be informed through studies on well-controlled model catalysts.

The main objective of the present work is to gain new insights into the electrochemical HER in acidic and alkaline media at model electrocatalysts based of platinum and nickel utilizing two different electrochemical-hydrodynamic measurement setups. This work consists of four parts.

In the first part, a novel impinging jet flow cell as a three-electrode setup for hydrodynamic electrochemical measurements on atomically thin model catalysts is developed and presented. Since a universal analytical solution for mass transport in these setups, similar to the *Levich* equation has been missing to date, a universal analytical model for mass transport and limiting current was developed. This model was validated with numerical simulations and experimental data for the oxidation of the hexacyanoferrate(II) for a wide range of parameters. Overall, a very good agreement with relative errors below 10 % was achieved. This model could therefore replace time-consuming and resource-intensive computational fluid dynamics simulations in the future.

Subsequently in the second part of this thesis, comparative measurements and simulations between this setup and the rotating disk electrode (RDE) were carried out using the HER on Pt model electrodes to validate the newly developed setup. The comparison revealed that both systems could produce comparable gas-saturation levels, electrochemical Pt features and mass-transport conditions. Theoretical analysis indicated that, in principle, the impinging jet flow cell allows for higher mass-transport conditions compared to the RDE. This suggests that the impinging jet flow cell is a promising alternative for studying HER activity under enhanced mass transport conditions.

After the validation of the impinging jet flow cell setup, novel atomically thin 2D platinum chalcogenide (Pt_xTe_y) catalysts for HER in an acidic environment were characterized in this setup in the third part of this thesis. Experimental HER activity was in the order 2D-$PtTe_2$ ≈ 2D-Pt_2Te_2 ≪ 2D-Pt_3Te_4. Density functional theory calculations related these differences to the trend of hydrogen adsorption *Gibbs* free energies (ΔG_H) at tellurium vacancies V_{Te}: 2D-$PtTe_2$≈ 2D-Pt_2Te_2 ≪ 2D-Pt_3Te_4. Raman spectroscopy revealed that 2D-Pt_2Te_2 partially transformed into 2D-Pt_3Te_4 during electrochemical experiments, indicating its thermodynamic metastability. 2D-$PtTe_2$ degraded during electrochemical testing, likely by mechanical delamination. XPS analysis confirmed that none of these phases showed signs of degradation into metallic Pt. These insights into structure-activity relationships and durability will aid future development of Pt chalcogenide catalysts to reduce PGM usage in HER.

The fourth part investigates the influence of iron impurities present in the electrolyte on HER activity on nickel surfaces in alkaline media. Using the well-established rotating disk electrode (RDE) setup, polycrystalline nickel model electrodes were immersed in electrolytes with iron concentrations ranging from 0 to 14 ppm. Initial electrochemical tests showed only marginal differences in HER activity among the different electrolyte compositions. However, extended chronopotentiometry tests over 24 hours at a constant current density revealed that electrodes exposed to higher iron concentrations, specifically 6 and 14 ppm, experienced less deactivation and maintained lower overpotentials. Structural analysis with SEM, μ-XRF, and XPS confirmed that iron formed dense, protective films on the nickel surface, which could inhibit degradation mechanisms. These findings suggest that a critical iron impurity threshold exists that can be exploited to improve the durability of nickel cathodes in alkaline water electrolysis.

Overall, this work provides new insights into the fundamental factors influencing the hydrogen evolution reaction in both acidic and alkaline media. The results help to deepen the understanding of reaction mechanisms, catalyst stability, and impurity effects, which are crucial for designing future electrolysers and advancing sustainable hydrogen production in the near future.

1 General Introduction

The United Nations Climate Change Conference in December 2015 saw representatives from 197 countries commit to limiting global temperature rise to well below 2 °C above pre-industrial levels [1]. Achieving this target necessitates reducing worldwide net carbon dioxide emissions to zero by 2050 [2]. Hydrogen is recognized as a key energy carrier to support this transition, serving both as a means to store energy generated from intermittent renewable sources like solar and wind [3,4], and as a tool for decarbonizing industrial processes such as steel and chemical production [2]. As a result, global hydrogen consumption is projected to reach approximately 110 Mt by 2030 [5]. So called “Green hydrogen”, produced via water electrolysis powered by renewable energy, offers a sustainable alternative to conventional methods relying on fossil fuels. The main types of water electrolysis are proton exchange membrane water electrolysis (PEMWE) [6–8], alkaline liquid water electrolysis (ALWE) [9,10], solid oxide electrolysis [11,12] and polymer anion exchange membrane electrolysis [3,13]. Among these, PEMWE and ALWE are the most established, holding the largest market share [14]. Advancing these water electrolysis systems to lower costs requires a detailed understanding of the activity trends and catalyst degradation mechanisms for both HER and OER catalysts. The core aim of this thesis is to provide new insights into the hydrogen evolution reaction (HER) through the investigation of model electrocatalysts based on Pt in acidic media and Ni in alkaline media. To accomplish this, the study employs two complementary three-electrode systems: the rotating disk electrode and the impinging jet electrode. The subsequent chapters will review the fundamentals and current state of the art for electrolysis and the HER in both acidic and alkaline environments. They will also discuss the advantages and limitations of these three-electrode configurations, including their theoretical principles and applications, thereby providing a foundation for the experimental work presented in this thesis.

2 Theoretical Background and State of the Art

2.1 Fundamentals of Water Electrolysis

2.1.1 Proton Exchange Membrane Water Electrolysis (PEMWE)

In PEMWE, water is split into hydrogen and oxygen through electrochemical reactions at their respective electrodes. The half-cell reactions are as follows:

Anode: $H_2O \rightarrow 4\,H^+ + 4\,e^- + \,O_2$ (OER) (1)

Cathode: $2\,e^- + 2\,H^+ \rightarrow H_2O$ (HER) (2)

Figure 1 shows a simplified schematic of a PEMWE. Water is delivered via channels in bipolar plates and passes through the porous transport layer (PTL), typically made of titanium [15], to reach the anode site. At the anode side the oxygen evolution reaction (OER) takes place. Typically, catalysts based on IrO_2 or RuO_2 are used here [16], with loadings of 1-3 mg cm^{-2} [8]. Water (due to electroosmotic drag [17]) and protons are transported via the proton exchange membrane towards the cathode site. This membrane is a sulfonated polymer (commonly Nafion®) that acts as the electrolyte [8]. The catalyst coatings and the membrane together form the membrane electrode assembly (MEA). At the cathode side the hydrogen evolution reaction (HER) takes place, with Pt based catalysts being the state of the art electrocatalysts [18,19] typically with loadings of 0.5 to 1 mg cm^{-2} [20]. The product gas H_2 and water are transported outside of the cell via a gas diffusion layer (GDL) and again gas channels in the bipolar plates.

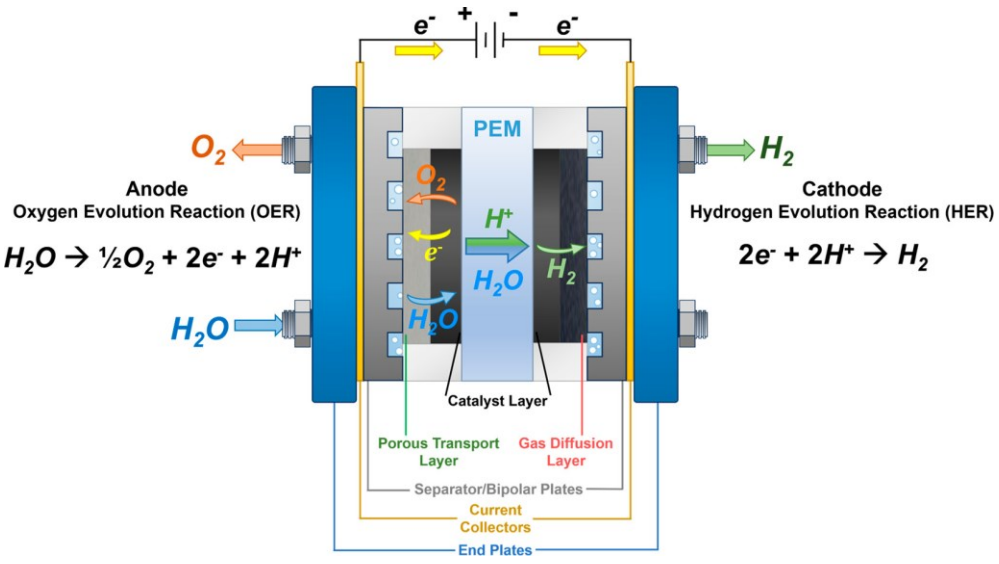

Figure 1: *Schematic illustration of proton exchange membrane water electrolysis cell. Reprinted from Wang et al. [21] under Creative Commons License (CC BY-NC-ND 4.0).*

PEMWE is typically operated at temperatures of 50-80 °C [7]. The high proton conductivity of membrane (0.1 ± 0.02 S cm^{-1}) [22] results in low ohmic losses. This allows higher current densities, with above 2 A cm^{-2}, compared to liquid alkaline water electrolysis [7]. The Nafion® membrane also typically permits low hydrogen crossover ($1.25 \cdot 10^{-4}$ cm^3 s^{-1} cm^{-2} for Nafion® 117, standard pressure, 80 °C) [23], minimizing the risk of explosive gas mixtures at low loads. This low crossover enables PEM electrolysers to operate across a wide nominal power density range (10–100%) [7] and produce very pure H_2 (> 99.99 % [24,25]), making them ideally suited for coupling with fluctuating renewable sources like wind and solar to store excess electrical energy in the form of H_2 as chemical energy carrier. Disadvantages include the high capital investment cost (CAPEX) for the stack of around 700-1400 USD kW^{-1} in the megawatt range [24], primarily due to the cost of noble metal catalysts used in the electrodes [3].

2.1.2 Alkaline Liquid Water Electrolysis (ALWE)

Among the different electrolysis technologies, alkaline liquid water electrolysis (ALWE) is considered the most mature [3]. In fact, the first large-scale ALWE plant was already in operation back in 1939 [9].

The half-cell reactions for ALWE are as follows:

Anode: $4\,OH^- \rightarrow O_2 + 2\,H_2O + 4\,e^-$ (OER) (3)

Cathode: $4\,H_2O + 4\,e^- \rightarrow 2\,H_2 + 4\,OH^-$ (HER) (4)

A schematic illustration of an ALWE is shown in **Figure 2**.

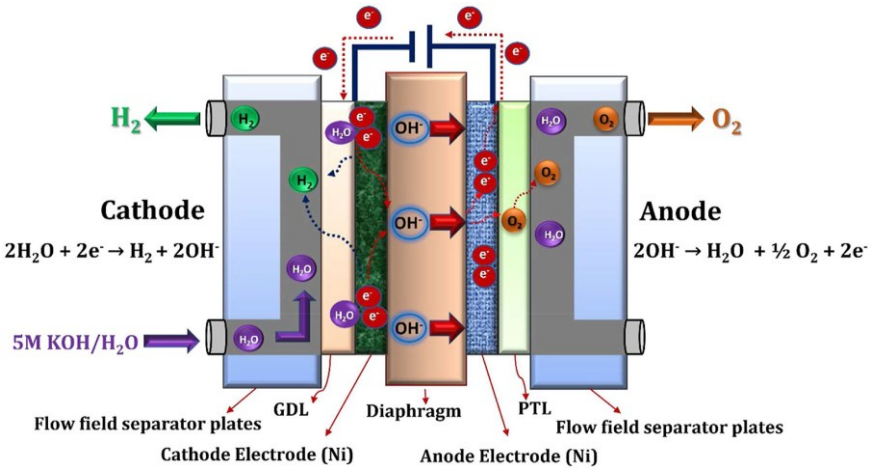

Figure 2: *Schematic illustration of alkaline liquid water electrolysis cell. Reprinted from Kumar et al. [26] under Creative Commons License (CC BY 4.0).*

Here, the cathode and anode are immersed in a concentrated liquid KOH solution (≈ 30 wt%) at operating temperatures between 70 - 90 °C [3]. Commercial Raney®Ni and stainless steel are widely used as cathode electrode materials [3,27], where the hydrogen evolution reaction (HER) takes place. For the oxygen evolution reaction (OER) on the anode, stainless steel, nickel hydroxides, cobalt oxides or nickel-iron hydroxides compounds are used [27–29]. A diaphragm separates the product gases and ensures the conduction of OH^- from the cathode to the anode side [30]. It is typically made of a porous polyphenylene sulfide polymer matrix (PPS) with ZrO_2 as a hydrophilic filler [31]. An advantage of ALWE compared to other electrolysis

technologies is the usage of non-precious metals as electrode materials. This lowers the CAPEX to around 500–1000 USD/kW in the megawatt range [24]. Also these systems possess a really good long term durability with a stack lifetime of 60,000-90,000 h [7,8]. However, due to the gas cross-over via the diaphragm alkaline water electrolysis typically cannot be operated at partial loads lower than 40 % [7] and the H_2 purity is not as high as compared to PEMWE (> 99.5 % [24,25]). Moreover, because of the liquid electrolyte and associated resistances, the maximum current density is usually limited to around 800 mA cm^{-2} [8], making ALWE systems less compact compared to PEM electrolyzers.

In summary, the two major water electrolysis technologies presented here each offer unique advantages and disadvantages. The impact of these on current research objectives will be discussed later. After exploring these two prominent electrolysis technologies, the next chapter will focus on the fundamentals of the hydrogen evolution reaction (HER).

2.2 Fundamentals of the Hydrogen Evolution Reaction

2.2.1 Reaction Mechanism

The HER generally consists of three possible reaction steps in both acidic and alkaline media, which are the *Volmer, Tafel* and *Heyrovsky* steps [32,33]:

Acidic Media:

Volmer: $* + H^+ + e^- \leftrightarrow H_{ad} - *$ (5)

Heyrovsky: $H_{ad} - * + H^+ + e^- \leftrightarrow * + H_2$ (6)

Tafel: $2\ H_{ad} - * \leftrightarrow 2\ * + H_2$ (7)

Alkaline Media:

Volmer: $* + H_2O + e^- \rightarrow H_{ad} - * + OH^-$ (8)

Heyrovsky: $H_{ad} - * + H_2O + e^- \rightarrow * + H_2 + OH^-$ (9)

Tafel: $2\ H_{ad} - * \leftrightarrow 2\ * + H_2$ (10)

In acidic media, the first step is typically the *Volmer* step, in which protons H^+ are adsorbed to active sites on the catalyst surface $*$ to form adsorbed hydrogen atoms $H_{ad} - *$. The subsequent HER pathways include the *Heyrovsky* reaction, in which an adsorbed hydrogen atom reacts with a proton and an electron to release hydrogen gas (H_2). Alternatively in the *Tafel* step, two adsorbed hydrogen atoms can combine directly to form H_2. In alkaline media, the *Volmer* step involves the electrochemical reduction of water at the catalyst surface, producing adsorbed hydrogen and hydroxide ions (OH^-). Based on these reaction steps the HER can either proceed via a *Volmer-Tafel* or *Volmer-Heyrovsky* mechanism overall, both in acidic or alkaline media. If a simplified kinetic model is assumed, one of these steps has to be slower and therefore the rate determining step (rds). However, there is a controversial discussion in literature about which step is rds, and this also depends on the material investigated [34–38].

2.2.2 Descriptors for the HER activity – The Hydrogen Binding Energy

Based on the elementary reaction steps involved in the hydrogen evolution reaction (HER), it is evident that the adsorption of hydrogen atoms on the catalyst surface plays a crucial role in influencing the overall catalytic activity. The thermodynamic descriptor ΔG_H, which represents the *Gibbs* free energy change associated with hydrogen adsorption, serves as a key indicator of catalytic HER activity. It is given by [39]:

$$\Delta G_H = \Delta E_H + \Delta E_{ZPE} - T\Delta S_H \tag{11}$$

where ΔE_H is the hydrogen chemisorption energy, ΔE_{ZPE} is the difference in zero point energy between the adsorbed and the gas phase, and ΔS_H stands for the difference in entropy due to hydrogen adsorption. The term $\Delta E_{ZPE} - T\Delta S_H$ can be estimated to be +0.24 eV at room temperature, as shown previously. [40,41] As a result, equation (11) can be simplified to:

$$\Delta G_H = \Delta E_H + 0.24\ eV \tag{12}$$

So, ΔG_H reflects the hydrogen-binding energy (ΔE_H) HBE, measuring how strongly hydrogen binds to the catalyst surface to form the $H_{ad} - *$. According to the *Sabatier* principle the optimal catalyst displays a ΔG_H close to zero, signifying a balanced interaction that facilitates both hydrogen adsorption and desorption. If ΔG_H is too negative, indicating strong hydrogen binding, the desorption of H becomes difficult, This blocks active sites on the catalyst and reduces activity. Conversely, if ΔG_H is too positive, hydrogen adsorption is too weak, leading to insufficient activation of reactants and poor catalytic performance [41].

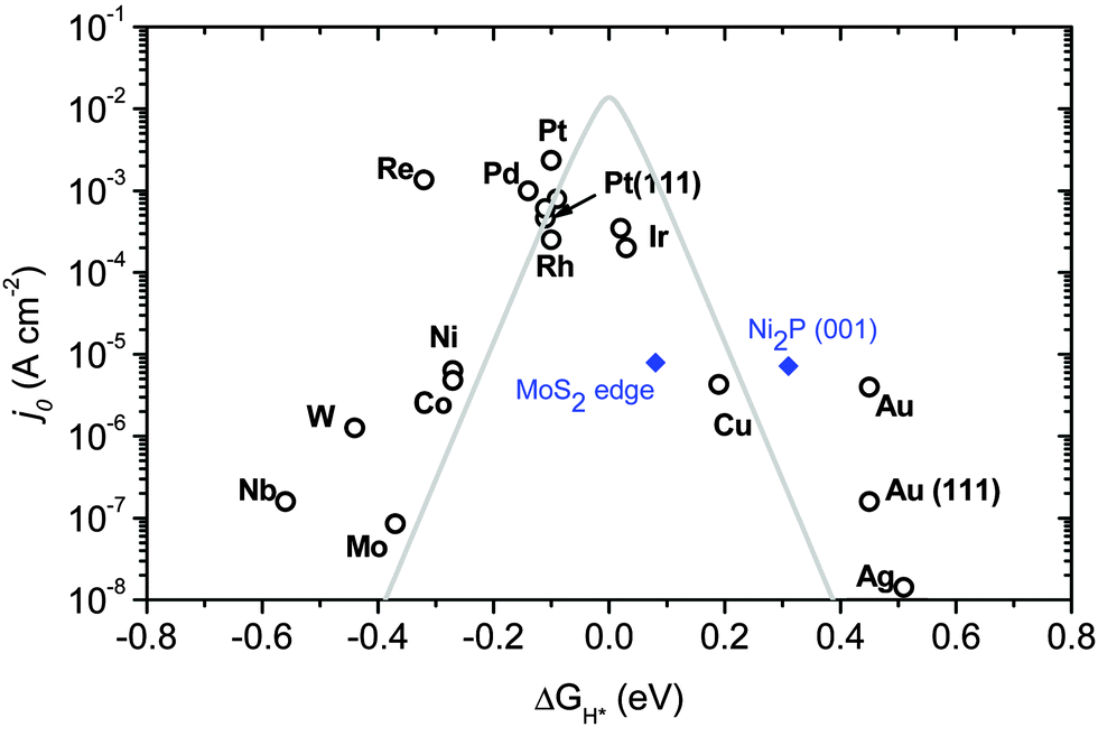

Figure 3: *Volcano plot for the HER. The exchange current density of various catalysts is plotted against the Gibbs free energy of hydrogen binding. Reprinted with permission of Royal Society of Chemistry, from Morales-Guio et al. [42]; permission conveyed through Copyright Clearance Center, Inc.*

As shown in **Figure 3** this relationship is often visualized through the volcano plot: the exchange current density i_0 is plotted against the *Gibbs* free energy of hydrogen adsorption ΔG_H, where catalysts with ΔG_H values near zero are positioned at the peak of activity. Pt ranks among the most active HER/HOR catalyst [18,43,44] due to the optimal hydrogen binding energy. As seen in **Figure 3**, even a small change of ΔG_H

lowers the exchange current density by orders of magnitude. It was shown that the trends of the HBE can be nicely explained with the d-band model, introduced by *Nørskov et al.* [45].

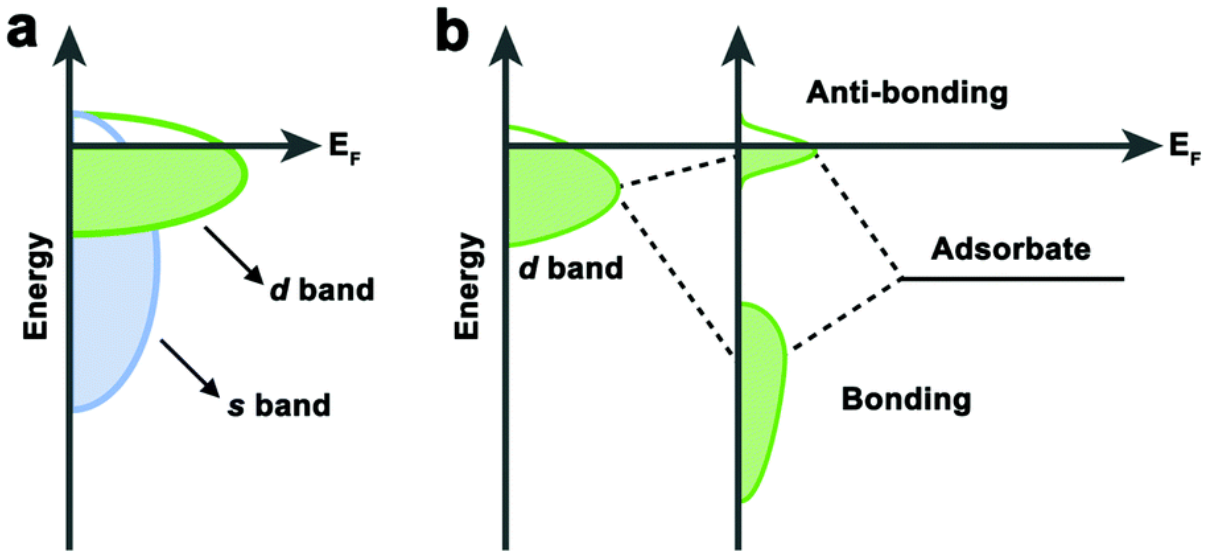

Figure 4: *Schematic Overview over the d-band model.* ***a)*** *An example of the density of states of transition metal with the s-band in blue and the d-band in green. The Fermi level is displayed as* E_F. ***b)*** *orbital splitting into a bonding and anti-bonding orbital during the adsorption and interaction of the atomic H orbitals with the metal. Reprinted with permission of Royal Society of Chemistry, from Chen et al. [46] ; permission conveyed through Copyright Clearance Center, Inc.*

In metals the atomic orbitals interact to create energy bands, specifically the s-band and d-band. As shown in **Figure 4a** the s-band for transition metals is typically very broad. For most transition metals, the properties of their s-band are fairly similar, because they're in most cases half-filled [45]. Therefore, differences in hydrogen binding energy mainly originate from variations in the Fermi level position and the characteristics of the d-band. When H_{ad} binds to a transition metal surface, its orbital interacts with the metal's d-orbital. This interaction results in the formation of a fully filled, low-energy bonding orbital and a partially filled, high-energy anti-bonding orbital, as illustrated in **Figure 4b**. The strength of the metal–hydrogen bond depends on the occupancy of the anti-bonding orbital: lower occupancy leads to stronger bonds. Since the anti-bonding states are always above the d-states, the relative position of the d-

band center to the Fermi level is a key indicator of bond strength. When the d-band center is closer to the Fermi level, the anti-bonding states are higher in energy and less occupied, which promotes stronger hydrogen adsorption. Conversely, if the Fermi level is further from the d-band center, the antibonding orbital is more occupied, resulting in weaker H_{ad} binding [45]. For example, platinum exhibits a d-band center near the Fermi level, ensuring an optimal balance of antibonding orbital filling [47]. This results in hydrogen adsorption that is neither too strong nor too weak, aligning with the *Sabatier* principle.

Importantly, the fundamental insights gained from this understanding have been extensively explored through density functional theory (DFT) simulations, which allow for the calculation of ΔG_H and other electronic structure descriptors with high accuracy. DFT studies have been instrumental in predicting and rationalizing the activity trends of various catalysts for HER and the hydrogen oxidation reaction (HOR), guiding experimental efforts for catalyst design [48–51].

The hydrogen binding energy (HBE) theory effectively links HER and HOR rate to the *Sabatier* principle. As an additional theory, *Markovic* and colleagues proposed that in alkaline media, hydroxyl (OH_{ad}^{-}) binding and surface oxophilicity also influence HER/HOR kinetics [52]. They found that on different crystal surfaces (e.g., Au, Ru, Pt, Ir), the HOR activity is influenced by the both the binding strength of hydroxide (OH_{ad}^{-}) and hydrogen (H_{ad}) species on surface, implicating a bi-functional mechanism. Ru, for example, facilitates the adsorption of OH^-, while Pt shows optimal H_{ad} binding. Their studies showed that modifying Pt with $Ni(OH)_2$ clusters or alloying with Ru can therefore improve HOR activity, indicating the importance of bifunctional catalysts [52]. However, since this thesis focuses mainly on Pt materials in acidic media and Ni materials in alkaline media, these findings are of limited relevance to describe activity trends herein.

2.3 The HER in Acidic Media

2.3.1 Pt as the Benchmark HER catalyst

Pt/C is widely regarded as the benchmark catalyst for HER in acidic media [18,53,54], due to its optimal HBE [55]. The polarization curves for the HER/HOR on Pt surfaces follow the ideal *Butler-Volmer*-Equation kinetics for a reaction with facile and reversible kinetics:

$$i_{kin} = i_0 \cdot \left[e^{\frac{\alpha F}{RT}\eta} - e^{-\left(\frac{(1-\alpha)F}{RT}\right)\eta} \right] \tag{13}$$

where i_{kin} is the kinetic current, η is the overpotential [V], α is the transfer coefficient [$0 < \alpha < 1$], F is the Faraday constant, T is the temperature [K] and R is the universal gas constant. Because of the facile kinetics, the activity factor which is mostly used to compare the HER activity is the exchange current density i_0. To accurately probe this value, setups with very high mass transport rates, such as hydrogen pump experiments [44], floating electrodes [56], or ultra-microelectrodes [57], are required. This can be understood with the *Koutecký -Levich* equation:

$$\frac{1}{i} = \frac{1}{i_{diff}} + \frac{1}{i_{kin}} \tag{14}$$

Where i is total current over the whole potential range. i_{diff} describes the current, which is obtained based on the *Nernst* diffusion overpotential expression [58]:

$$i_{diff} = i_{lim} \cdot (1 - \mathrm{e}^{-\frac{2\mathrm{F}\eta}{RT}}) \tag{15}$$

where i_{lim} is the mass-transport limiting current measured at sufficiently high overpotentials.

Inserting (13) and (14) into (15) gives for the overall *Koutecký-Levich* equation:

$$\frac{1}{i} = \frac{1}{i_0 \cdot [e^{\frac{\alpha F}{RT}\eta} - e^{-\left(\frac{(1-\alpha)F}{RT}\right)\eta}]} + \frac{1}{i_{lim} \cdot (1 - e^{-\frac{2F\eta}{RT}})} \tag{16}$$

Therefore, if the exchange current density i_0 is orders of magnitude higher than the limiting current i_{lim} equation (16) reduces to:

$$\frac{1}{i} \approx \frac{1}{i_{lim} \cdot (1 - e^{-\frac{2F\eta}{RT}})} \tag{17}$$

and the overall current i is fully described by i_{diff} alone. This results in the dilemma that measurements of the HER/HOR activity using the well-known rotating disk electrode (RDE) setup are typically erroneous and just display the "kinetics of hydrogen diffusion" with a *Tafel* slope of around 30 mV dec^{-1} and an exchange current density of around $i_0 = 1\ mA\ cm^{-2}$ [44], as shown in **Figure 5**. Here the exchange current density of Pt/C catalysts is plotted against the reciprocal temperature for different setups. It is evident that the RDE technique and channel flow electrodes consistently indicate low exchange current densities near $i_0 = 1\ mA\ cm^{-2}$, regardless of temperature. More realistic and higher values are obtained with gas diffusion electrodes, hydrogen pump methods, or ultra-microelectrodes. Using high-mass transport setups at room temperature ($T = 293\ K$) the exchange current density i_0 of Pt falls in the range around 60 – 140 mA cm^{-2} [18,44,56,59,60], which can be considered extremely high.

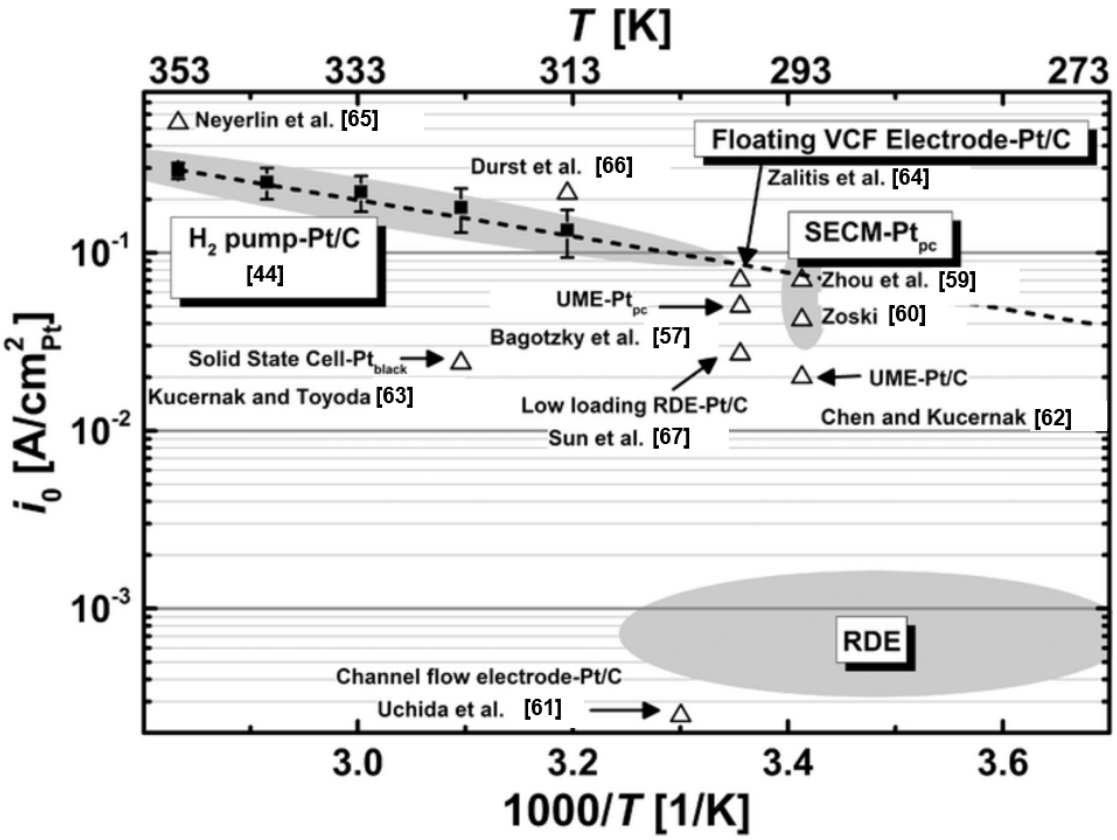

Figure 5: *Arrhenius plots HOR/HER* i_0*-values on Pt electrodes. Black square data points were determined with the* H_2 *pump setup in this work and fitted from the micropolarization equation. Open triangles mark literature* i_0*-values determined from various electrochemical setups and platinum electrodes: channel flow electrode-Pt/C (Uchida et al.) [61]; SECM-*Pt_{pc} *(Zhou et al. [59] and Zoski [60]); UME-*Pt_{pc} *(Bagotzky and Osetrova [57]); UME-Pt/C (Chen and Kucernak [62]); solid state cell-*Pt_{black} *(Kucernak and Toyoda [63]); Floating VCF Electrode-Pt/C (Zalitis et al. [64]);* H_2 *pump-Pt/C (Neyerlin et al. [65], Durst et al. [44] and Durst et al. [66]); low loading RDE-Pt/C (Sun et al. [67]). Reproduced and adapted (reference numbers changed) from Durst et al. [44] under Creative Commons License (CC BY 4.0).*

Despite platinum's impressive activity, it remains a rare metal in the earth's crust, with a concentration of about 0.599 parts per billion (ppb) (ng/g) [68]. Consequently, efforts in catalyst research are focused on reducing the platinum loading required for PEM water electrolysis [69–71], with one promising approach being the exploration of transition metal chalcogenides. The following chapters will provide an overview of current research in this area.

2.3.2 Transition Metal Chalcogenides (TMCs)

2.3.2.1 MoS_2

In attempts to reduce the Pt content in PEMWE, transition metal chalcogenides (TMCs) with the general formula MX_2, where M is a transition metal (Mo, Ti, W, Pt, Pd) and X is a chalcogen (like S, Se, Te) [72] have been studied in the past years [73–79]. Among these, MoS_2 as a noble metal free 2D layered electrocatalyst MoS_2 has been extensively investigated [73–75,80–83].

A monolayer of MoS_2 consists of one layer of Mo atoms sandwiched between two layers of chalcogen S [84]. Multiple layers of MoS_2 are then stacked on each other and held together by *van der waals* forces to form a bulk material. [75] The HER activity of bulk MoS_2 is heavily influenced by the phase [75], layer numbers [74] , edge sites [85] and doping with N [86]. The general consensus is that the metallic meta-stable 1T-MoS_2 is more active towards the HER compared to the stable semiconductor 2H-MoS_2 phase [87]. Also edge sites are known to catalyse the HER on layered MoS_2 better compared to the basal planes, due to more optimal ΔG_H adsorption free energies [88,89]. However, despite all efforts to increase the activity of MoS_2, the activities compared to state of the art Pt catalysts are still 2-3 orders of magnitude lower. [18,75,89]. This disparity is illustrated in **Figure 6** and a further supported by ΔG_H values and exchange current densities, such as those shown in **Figure 3** (blue square).

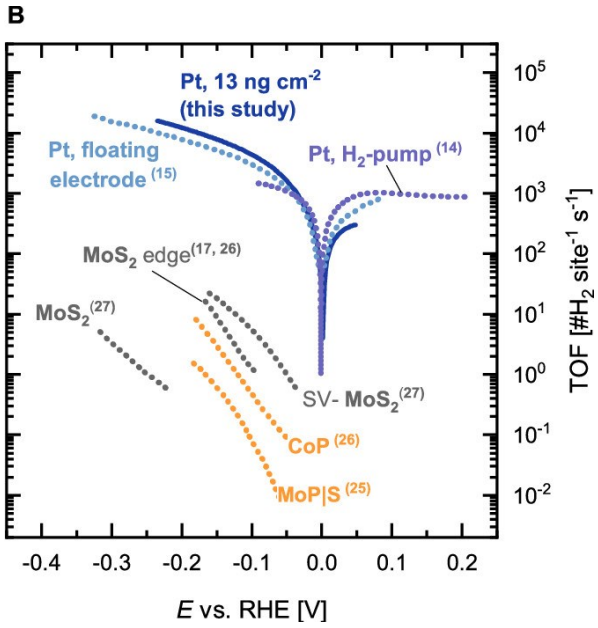

Figure 6: *(B) TOFs corresponding to the cathodic scans for the lowest-loading sample in this study (solid blue line) and other Pt/C samples using fast mass-transport techniques: floating electrode (dotted light blue line) and H_2-pump (dotted purple line) taken from refs (15) and, [14], respectively. A selection of transition metal sulfides and phosphides are added for comparison: MoP\|S, [25] CoP, [26] MoS_2 (edge), [17,26] and (MoS_2, SV-MoS_2). (27) Reprinted from Hansen et al. [18] under Creative Commons License (CC BY-NC-ND 4.0). References list: [this study]-[18];[14]-[44]; [15]-[90]; [17]-[91]; [25]-[92]; [26]-[93];*

In **Figure 6** the turnover frequency (TOF in H_2 sites^{-1} s^{-1}) is plotted against the electrode potential. The polarization curves of Pt from previously mentioned high-mass transport setups (floating electrode and H_2 pump experiments in blue colors) are compared with the activity of several MoS_2 measurements (in yellow and grey colors). It is clear that, even when accounting for the influence of edge sites, the TOF of MoS_2 remains several orders of magnitude below that of platinum. Because of the lower activity, the overpotentials for the HER are typically higher for MoS_2 compared to Pt and the *Butler-Volmer* equation in this high overpotential range (see chapter 2.3.1) simplifies to:

$$i_{kin} = i_0 \cdot \left[e^{\frac{\alpha F}{RT}\eta} - e^{-\left(\frac{(1-\alpha)F}{RT}\right)\eta} \right] \approx i_0 \cdot e^{\frac{\alpha F}{RT}\eta} \qquad (18)$$

This approximation holds because the reverse reaction (HOR) contributes negligibly at these overpotentials. Taking the logarithm yields the classical *Tafel* equation:

$$\log|i| = \frac{1}{2.303}\log|i_0| + \frac{\alpha F}{2.303\ RT}\eta \tag{19}$$

A plot of $\log\ |i|$ vs. η gives a linear behavior with the *Tafel* slope $\frac{\alpha F}{2.303\ RT}$, which serves as an indicator of reaction irreversibility. For MoS_2, the Tafel slope is often used as an activity descriptor [94–98]. Due to the significantly lower activity of MoS_2 compared to platinum, recent research efforts have increasingly shifted focus toward investigating alternative transition metal chalcogenides and related materials that hold the potential for higher HER activity and better overall performance.

2.3.2.2 Pt Chalcogenides – Structure and Raman Bands

Compared to MoS_2, the Pt chalcogenides M_xX_y (M=Pt, Pd and X=S, Se, Te) have been less studied but are regarded as promising candidates. This is because the decent activity rates of MoS_2 catalysts it is thought that replacing Mo with Pt, i.e. increasing the noble metal content should give good activity despite having reduced Pt content to metallic Pt. This thesis primarily focuses on platinum tellurides, specifically Pt_xTe_y compounds. Structure wise several phases are possible in this system, including $PtTe_2$, Pt_2Te_2, and Pt_3Te_4.

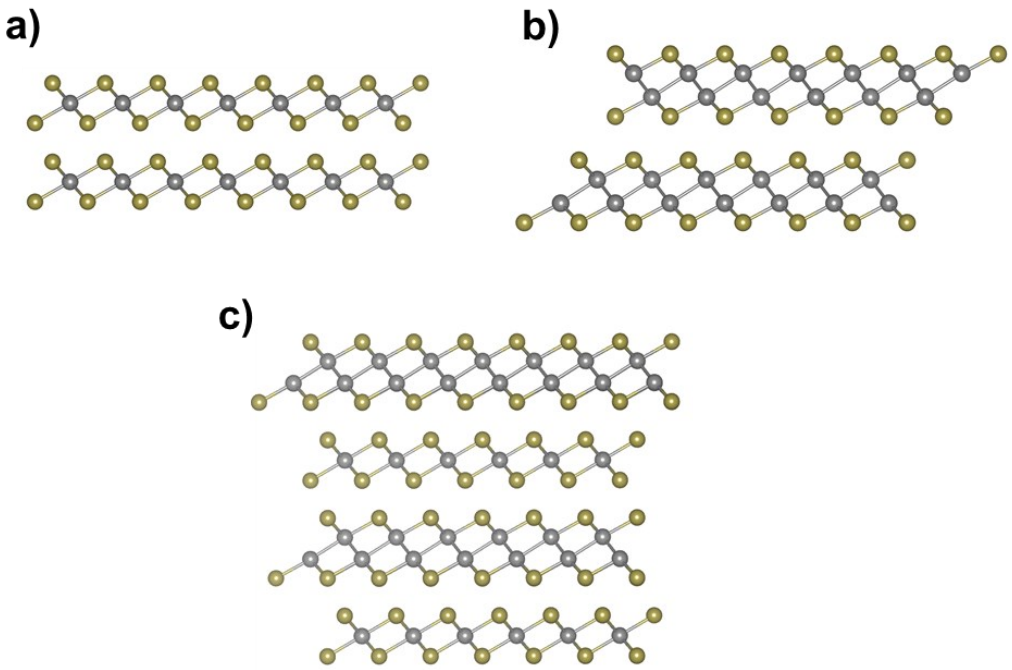

Figure 7: *Atomic structures of layered* ***a)*** *$PtTe_2$* ***b)*** *Pt_2Te_2 and* ***c)*** *Pt_3Te in a side view. Pt-grey, Te-yellow.*

Figure 7 shows the structure of these layered phases in a side-view. In $PtTe_2$ (**Figure 7a**) one row of Pt atoms (grey) are sandwiched between one row of Te on each side (yellow). Multiple layers are stacked upon in each other to form the bulk material. They're held together only by *van der waals forces* [99], similar to MoS_2 layers. In Pt_2Te_2 (**Figure 7b**) two rows of Pt are sandwiched between two rows of Te. Finally, the structure of Pt_3Te_4 (**Figure 7b**) consists of alternating Pt_2Te_2 and $PtTe_2$ layers. So in principle the surface can be terminated by both Pt_2Te_2 or $PtTe_2$ [100]. The data

from the unit cells, used to plot the layers in **Figure 7** is shown in **Table 1**. The crystal structure data of Pt is given as a reference as well.

Table 1: Lattice Parameters of the different Pt_xTe_y phases and metallic Pt.

Phase	Space Group	$\frac{a_{lattice}}{Å}$	$\frac{b_{lattice}}{Å}$	$\frac{c_{lattice}}{Å}$	$\frac{\alpha_{lattice}}{°}$	$\frac{\beta_{lattice}}{°}$	$\frac{\gamma_{lattice}}{°}$	Source
$PtTe_2$	$P\bar{3}m1$	4.02590	4.02590	5.22090	90	90	120	[101]
Pt_2Te_2	$C2/m$	6.86500	3.96200	7.04400	90	108.98	90	[102]
Pt_3Te_4	$R\bar{3}m$	3.98800	3.98800	35.3900	90	90	120	[103]
Pt	$Fm\bar{3}m$	3.94400	3.94400	3.94400	90	90	90	[104]

Each of these phases shows distinct E_g and A_{1g} lattice vibrations. The E_g and A_{1g} lattice vibrations for $PtTe_2$ and Pt_2Te_2 are displayed in **Figure 8**.

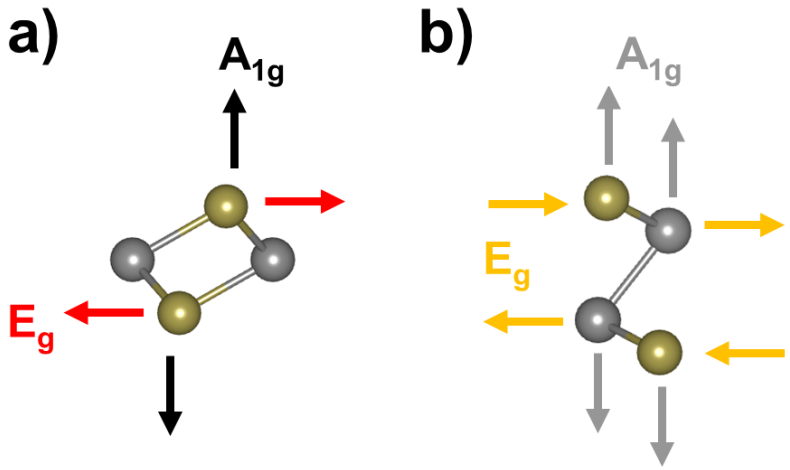

Figure 8: *Lattice vibration modes A_{1g} and E_g of a* ***a)*** *$PtTe_2$ monolayer and* ***b)*** *Pt_2Te_2 monolayer in a sideview. Color code: Pt-grey, Te-yellow.*

These lattice vibrations can be detected with Raman spectroscopy. The relevant and most prominent band positions are shown in **Table 2**. The Pt_3Te_4 phase contains the Raman bands of both $PtTe_2$ and Pt_2Te_2, because it consists of alternating layers of both.

Table 2: Raman Vibration Modes of the different Pt_xTe_y phases. [99]

Phase	Lattice Vibration	$\tilde{\nu}/cm^{-1}$
$PtTe_2$	E_g	116
	A_{1g}	158
Pt_2Te_2	E_g	92.1
	A_{1g}	118.4
Pt_3Te_4	$E_g(Pt_2Te_2)$	94
	$E_g(PtTe_2) + A_{1g}(Pt_2Te_2)$	123.3
	$A_{1g}(PtTe_2)$	158

2.3.2.3 Pt Chalcogendies – Activity for HER

Theoretical predictions suggest that certain Pt chalcogenides Pt_xX_y materials could exhibit near-ideal hydrogen adsorption free energies ΔG_H, which could significantly reduce Pt content without sacrificing HER activity [49,105,106]. Yet, few studies have practically investigated their HER activity and stability. For instance, *Chia et al.* compared the HER activity of different synthesized (via solid state synthesis method from directly from the elements) bulk PtX_2 materials – $PtTe_2$, PtS_2 and $PtSe_2$ – with each other. HER activity in 0.5 M H_2SO_4 was in the order $PtTe_2$ > $PtSe_2$ >> PtS_2 because based on electronic properties bulk PtS_2 is semiconducting, bulk $PtSe_2$ is semimetallic, and bulk $PtTe_2$ is metallic [76]. A similar activity trend in 0.5 M H_2SO_4 was later found by *Hussein et al.*, who synthesized these materials in a two-step process employing magnetron sputtering of a thin Pt film on a Ti/SiO2 substrate and subsequent annealing of the film at high temperatures with Te, Se or S [107]. *Lin et al.* [108] studied layer-dependent HER activity in $PtSe_2$ synthesized with the procedure by *Hussein et al.* [107]. They found that the HER activity in 0.5 M H_2SO_4 increases with increasing the layer thickness of the samples. Based on theoretical calculations and DFT calculations they attributed this to the increased amount of edge sites, which have more favorable ΔG_H of hydrogen adsorption. *Hu et al.*[109] investigated the layer and edge dependent properties of $PtSe_2$ crystals synthesized via chemical vapor

transport (CVT) from the elements. Measurements in a special electrolyte microdroplet cell revealed that the edge sites have a much higher HER activity in 0.5 M H_2SO_4 compared to the basal plane. They also found that the activity increases with the number of layers, because more layers expose more edge sites, and these serve as active centers for HER. *Wang et al.* [51] increased the HER activity of bulk $PtSe_2$ (produced by solid state synthesis from the elements) in 1 M KOH, by partial reduction to Pt, resulting in a so-called hetero interface. Using DFT calculations they could confirm that the Pt atoms in vicinity to Se vacancies get activated and that this is likely the origin of the increased activity. To sum up, very detailed studies regarding the HER activity of $PtSe_2$ already exist.

Less is reported for the platinum tellurides Pt_xTe_y. *Mc Manus et al.* [110] investigated the HER activity of large-area grown bulk $PtTe_2$ catalysts. For the syntehsis, they first deposited Pt via magnetron sputtering, then electrodeposited Te and afterwards annealed in a tube furnace. Their bulk material consisted of grains up to 1 µm of size. The $PtTe_2$ exhibited a much higher onset potential for the HER in 0.5 M H_2SO_4 compared to Pt. But they concluded that the material itself is stable for HER in acidic media, with only a small amount (~4 %) of Pt found in the X-Ray photoelectron spectra (XPS) after one linear sweep voltammogram. *Supriya et al.* compared the HER activity of bulk $PtTe_2$ and bulk Pt_3Te_4, synthesized via solid-state synthesis from the elements, in 0.5 M H_2SO_4 and 1 M KOH [77]. They found that the Pt_3Te_4 material was more active towards the HER in both electrolytes compared to the $PtTe_2$ material. After 100 cyclic voltammetry cycles the HER activities in 0.5 M H_2SO_4 for the bulk Pt_3Te_4 and bulk $PtTe_2$ both decreased with overpotentials for a current density of $i = -10\ mA\ cm^2$ increasing by 300 and 250 mV, respectively. Compared to the Pt/C catalyst that they tested the HER activities were much lower. *Boukhvalov et al.* [111] investigated the HER activity of bulk Pt_3Te_4, synthesized via solid-state synthesis from the elements**.** In stark contrast to the previous studies, they found remarkable HER activity with overpotentials of only 46 mV at 10 mA/cm², very close to that of pure Pt. Via DFT calculations it could be shown that the HER on pristine Pt_3Te_4 is unfavored. However,

introducing Te vacancies produces very favorable near zero free energy of H adsorption. **Figure 9** shows one example of the structure of a $PtTe_2$ terminated Pt_3Te_4 crystal with a single atom Te vancancy V_{Te}. Here a single Te atom is missing from the layer.

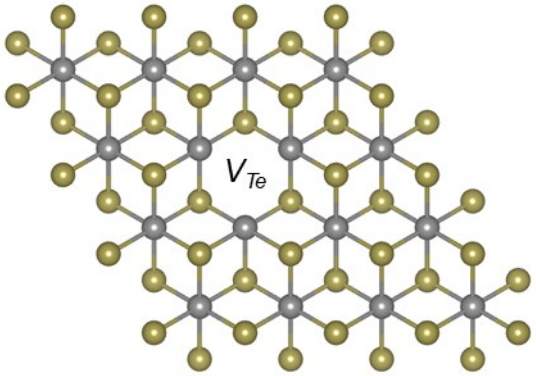

Figure 9: *Single atom Te vacancy in a $PtTe_2$ layer (3x3x1 supercell, view along the c axis). Color code: Pt-grey, Te-yellow.*

Summing up all of the previously mentioned literature, the HER activity of the Pt_xTe_y phases remains controversial. The HER kinetics can be mostly considered sluggish compared to metallic Pt. Their activity is heavily influenced by defects, vacancies, or edge sites [108,109,112,113], all of which are often abundant in bulk samples made by methods like chemical vapor transport or solid-state synthesis, as SEM images from several studies illustrate [77,107]. Investigations, which compare for example the different phases with each other, are still lacking. Also stability investigations of these phases are mostly missing so far. A comparative summary about the potentials necessary for a current density of $-0.1\ mA\ cm_{geo}^{-2}$ $|E_{i=-0.1\ mA\ cm_{geo}^{-2}}|$ and *Tafel* slopes of different Pt chalcogenides as well as some MoS_2 materials mentioned in the previous chapter (2.3.2.1) is given in **Table 3**.

Table 3: Overview about activity of different TMCs reported in literature.

Material	Electrolyte and Settings for LSV	*Tafel* Slope / mV/dec	$\lvert E_{i=-0.1\ mA\ cm_{geo}^{-2}} \rvert$ vs. RHE / mV	Source
Bulk $PtSe_2$@GC	0.5 M H_2SO_4, s = ?* mV/s, three electrode setup	47	23	[108]
Bulk Pt_3Te_4	0.5 M H_2SO_4, s = 2 mV/s, RDE	49	--**	[111]
1T-MoS_2@GC	0.5 M H_2SO_4, s = 5 mV/s, RDE	64	72	[114]
Polycrystalline bulk $PtTe_2$ films	0.5 M H_2SO_4, s = 2 mV/s, three electrode setup	85	219	[110]
2D-$PtSe_2$ (5 layer)	0.5 M H_2SO_4, s = 5 mV/s, droplet cell	89	47	[109]
Bulk $PtTe_2$	0.5 M H_2SO_4, s = 5 mV/s, RDE	95	433	[77]
Bulk $PtTe_2$	0.5 M H_2SO_4, s = 2 mV/s, RDE	110	161	[76]
2D-MoS_2@GC, 1 layer	0.5 M H_2SO4, s = 5 mV/s, RDE	140	~337	[74]
Bulk Pt_3Te_4	0.5 M H_2SO_4, s = 5 mV/s, RDE	141	280	[77]

*scan rate not reported; **baseline shifted below $i = 0\ mA\ cm^{-2}$

Because of the heavy influence of defects and such, synthesizing these materials with controlled structures is crucial for understanding their intrinsic properties. Molecular beam epitaxy (MBE) is one of the promising methods that has recently been used to synthesize TMCs with well-defined structure [115,116]. In a recent work by *Lasek et al.* they explored how different phases of 2D-Pt_xTe_y can be produced by combining

MBE with subsequent annealing at higher temperatures in vacuum [100]. First, 2D-$PtTe_2$ was grown via MBE epitaxy on MoS_2 single crystal substrates. Annealing at around 350 °C for 200 minutes, lead to the transformation of the 2D-$PtTe_2$ film to 2D-Pt_3Te_4. After raising the temperature to around 400 °C and another 300 min of annealing, the 2D-Pt_3Te_4 film is transformed into the meta stable 2D-Pt_2Te_2. MBE thus provides the possibility to synthesize 2D Pt_xTe_y materials with well-defined, phase-pure structures, something which is not feasible with conventional chemical methods. However, to the best of the authors knowledge activities for such materials have not yet been reported.

Having provided an overview of strategies aimed at reducing platinum content in electrolysis catalysts for acidic media, the subsequent chapters will focus on research related to the hydrogen evolution reaction in alkaline environments. This shift highlights the different challenges and opportunities associated with HER catalysis in alkaline conditions.

2.4 The HER in Alkaline Media

2.4.1 Noble Metals

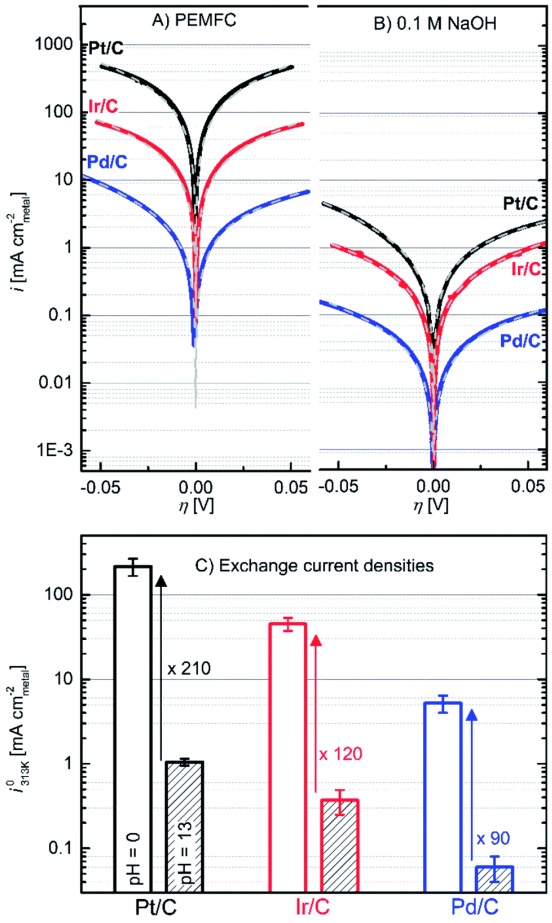

Figure 10: *Upper part: HOR/HER Tafel plots of the specific current densities on Pt/C (black lines), Ir/C (red lines) and Pd/C (blue lines) in: (A) PEMFC and (B) 0.1 M NaOH electrolyte. The Butler–Volmer fits are indicated as grey dashed lines. Lower part: HOR/HER exchange current densities (i_0 at 313 K) in PEMFC (empty columns) and 0.1 M NaOH (striped columns) averaged from Butler–Volmer and micropolarization equations. Data recorded in a H_2-saturated atmosphere at ambient pressure and 313 K. Reprinted from Durst et al. (Title: "New insights into the electrochemical hydrogen oxidation and evolution reaction mechanism.") [66] under Creative Commons License (CC BY 3.0).*

The HER rates of noble metal catalysts are orders of magnitude lower in alkaline media compared to acidic media [54,58,66]. This trend is clearly depicted in **Figure 10**. The upper part shows *Butler-Volmer* plots ($\log |i|$ vs. η) for Pt/C, Ir/C and Pd/C for btained from (A) a hydrogen pump experiment at pH = 0 and (B) rotating disk electrode (RDE) measurements in 0.1 M NaOH. All materials display much higher current

densities in acidic conditions than in alkaline environments. This difference is further reflected in the lower part of the figure, where the exchange current densities, derived from the fits in A and B, are presented as bar diagrams. The bars with an empty fill represent measurements at pH = 0, while striped bars correspond to pH = 13. For example, in the case of platinum, the exchange current density in alkaline media decreases by a factor of approximately 210, down to around $i_0 = 1\ mA\ cm^{-2}$. This lower exchange current density in the liquid electrolyte environment makes it possible to accurately determine that in an RDE setup using the *Koutecký-Levich* equation and *Butler-Volmer* equation previously mentioned (equation (14)). Due to the inherently lower activity of noble metals, non-noble metals have demonstrated sufficient catalytic performance and are widely regarded as state-of-the-art catalysts in alkaline media [3,53,117–120]. The following chapters will focus on exploring the electrochemical behavior of these non-noble metal catalysts.

2.4.2 Non-noble Metals

2.4.2.1 Nickel and its Electrochemical Features

Ni based catalysts remain one of the most investigated non-noble metal catalysts for alkaline HER [121–126] due to their excellent stability and sufficient catalytic activity. Nowadays commercial Raney®Ni and stainless steel are widely used as cathode electrode materials [3,27] for ALWE. Metallic Ni is usually found under HER conditions (< 0 V vs. RHE) [127], however other oxidation states can be found depending on the applied potential. This is illustrated in one example cyclic voltammogram (CV) in **Figure 11**.

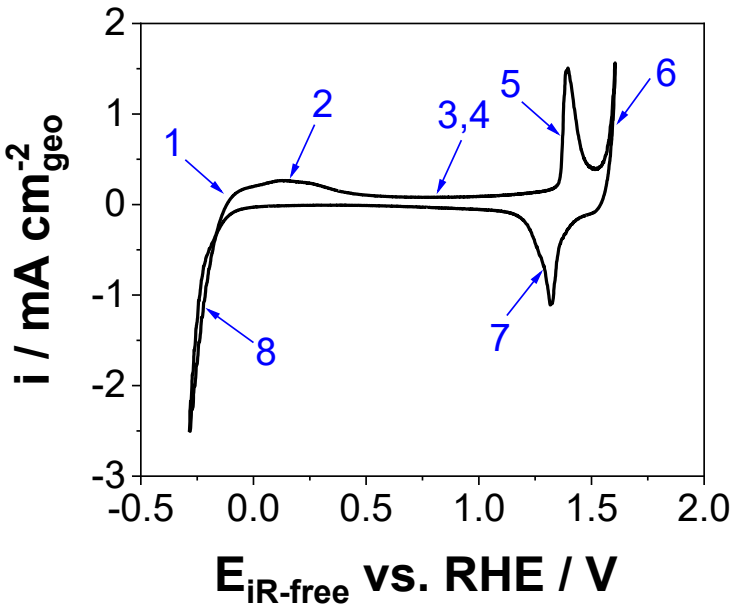

***Figure 11**: Cyclic voltammogram of a polycrystalline Ni electrode in Ar-saturated 0.1 M KOH recorded with a scan rate of* $s = 100\ mV\ s^{-1}$.

The different peaks and regions can be assigned based on the fundamental studies by *Hall et al.* [128]. In region 1 (around -0.1 V vs. RHE) NiH, which is formed during the HER, is oxidized to Ni [129]. NiH formation is a known issue during prolonged electrolysis at current densities $\geq 10\ mA\ cm_{geo}^{-2}$ and one of the main degradation mechanism of Ni electrodes [130–132]. It occurs via the following equation:

$$Ni + x\ H_2O + x\ e^- \rightleftharpoons NiH_x + x\ OH^- \ (x = 0.01 - 0.65) \qquad (20)$$

The formation of NiH influences the electronic states of the nickel d-band at the surface [130]. **Figure 12** presents the density of states for Ni (marked as M) and NiH (marked as MH). In NiH, the Fermi level intersects only the s-p band, resembling metals like Ag or Cu. This shift causes the d-band center to move away from the Fermi level, reducing the density of states at the Fermi energy. As a result, the antibonding orbitals involved in hydrogen adsorption become more occupied, weakening chemisorption. Consequently, the catalytic activity transitions from being d-band–dominated to s-p–dominated, thereby reducing nickel's electrocatalytic efficiency to that of less reactive metals.

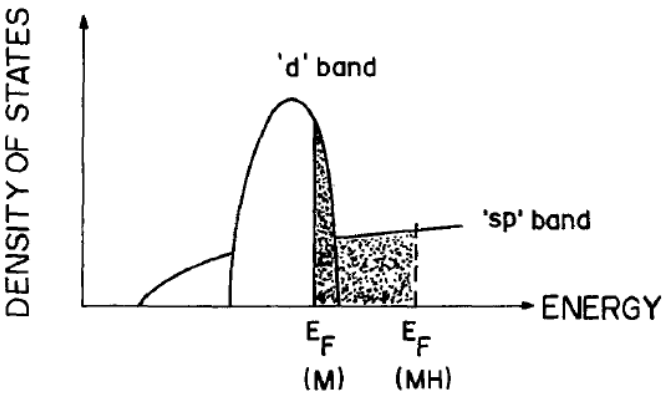

Figure 12: *Density of States for Ni (M) and NiH (MH). The Fermi levels are marked as E_F. Reprinted with permission of IOP Publishing from Soares et al. [130]; permission conveyed through Copyright Clearance Center, Inc.*

Permeation cells have been used in the past to investigate this NiH formation. Here a nickel foil separates two chambers. Hydrogen evolves on one side. Now H atoms can diffuse through the foil to the other chamber, where they are oxidized and a permeation current is measured. It was shown in such setup that the NiH forms because of atomic H uptake inside the electrode [133].

In region 2 around 0.13 V vs. RHE the NiH dissolution continues and the formation of NiO and $\alpha - Ni(OH)_2$ starts according to equations ([134], **8**-26: Electrochemical Series) :

$$Ni + 2\,OH^- \rightleftharpoons \alpha - Ni(OH)_2 + 2\,e^- \quad (21)$$

$$Ni + 2\,OH^- \rightleftharpoons NiO + H_2O + 2\,e^- \quad (22)$$

In region 3 and 4 between 0.8 and 1 V vs. RHE the processes from equations (20), (21) and (22) continue. Additionally the $\alpha - Ni(OH)_2$ transforms into $\beta - Ni(OH)_2$ via “aging”. The α-phase includes intercalated water and ions such as nitrate, carbonate, sulfate, chloride, and acetate [135–137], which result in an interlayer distance of between 7.5 and 32 Å [136,138]. The intercalated molecules and ions are mobile, resulting in a lack of fixed positions and a ‘turbostratic’ disorder where layers are randomly oriented relative to each other [139]. The β-phase has a brucite-like, trigonal crystal structure within a hexagonal lattice, space group $P - \bar{3}m1$ [140]. Its layers stack in an ABAB pattern with an interlayer spacing of about 4.6 Å [141]. These layers are

held together solely by *van der Waals* forces, with no intercalated species [142]. Via ageing the α phase therefore looses it's intercalates. At a potential of around 1.3 V vs. RHE a sharp oxidation current peak is found in the CV from **Figure 11** ((5) in **Figure 11**). α-Ni(OH)2 and β-Ni(OH)2 are oxidized to γ-NiOOH and β-NiOOH, respectively here [141,143]:

$$Ni(OH)_2 + 2\,OH^- \rightleftharpoons NiOOH + e^- + H_2O \tag{23}$$

β-NiOOH can be also 'overcharged' to γ-NiOOH at potentials above the $Ni^{2+/}Ni^{3+}$ redox potential. All these previously described phases and transformations involving $Ni(OH)_2$ and $NiOOH$ can be put summarized into a scheme, first introduced by *Bode et. al.* [141] in 1966 and also known as the Bode's phase diagram, shown in **Figure 13**.

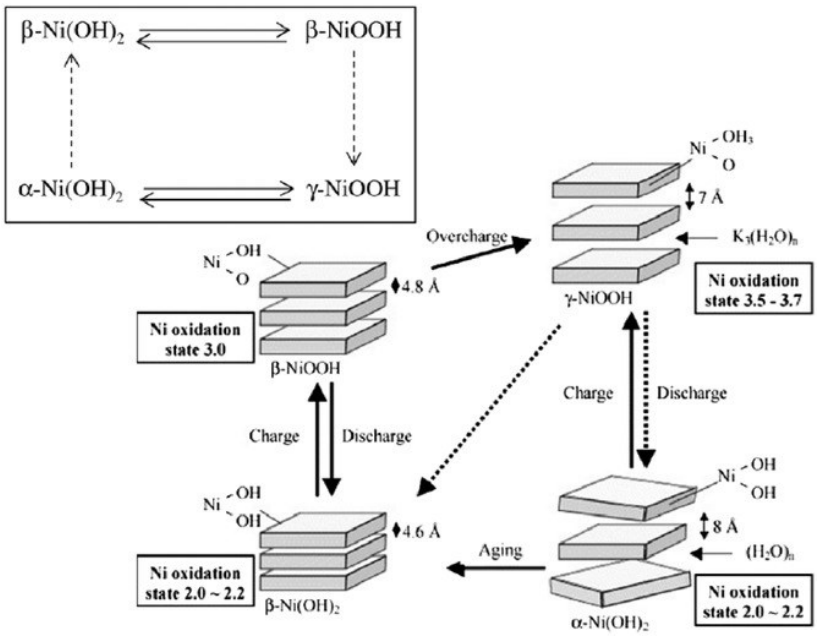

Figure 13: *Bode's phase diagram of the $Ni(OH)_2$ and $NiOOH$ phases and transitions. Reproduced with permission of Elsevier from Wehrens-Dijksma et al. [144]; permission conveyed through Copyright Clearance Center, Inc.*

At around 1.5 V vs. RHE the onset of the OER starts ((6) in **Figure 11**). In the backwards scan direction another sharp peak, a reduction current ((7) in **Figure 11**), is observed. This is attributed to the reduction of $NiOOH$:

$$NiOOH + e^- + H_2O \rightleftharpoons Ni(OH)_2 + 2\,OH^- \quad (24)$$

At potentials below 0 V vs. RHE reductive currents are observed ((8) in **Figure 11**). These are attributed to the HER as well the reduction of various Ni, NiO and $Ni(OH)_2$ species.

Because of the sluggish HER kinetics on Nickel surfaces in alkaline media, the *Tafel* slope is commonly used to compare different Ni-based catalysts with each other [53,145,146].

2.4.2.2 Iron and its Electrochemical Features

Iron is an affordable metal that sees widespread use in industrial applications [147,148]. It also demonstrates relatively high activity for the hydrogen evolution reaction, with some studies reporting low overpotentials around 260 mV at a current density of 10 mA cm^{-2} [149,150]. Additionally it is known that iron is less prone to the uptake of atomic hydrogen into the lattice and the formation of hydrides, compared to Ni [132,151]. However, general consensus is that the activity for HER of pure is lower compared to Ni [53,150,152,153]. Also iron tends to have poorer stability in alkaline environments at higher temperatures, particularly during periods when the electrolyte is not actively producing current, such as when the electrolyzer is shut down, as seen in *Pourbaix* diagrams [154].

Iron exhibits similar phase transformations during cyclic voltammetry (CV) compared to Ni, but at different potentials. **Figure 14** displays an example of an CV from an iron electrode from literature [155].

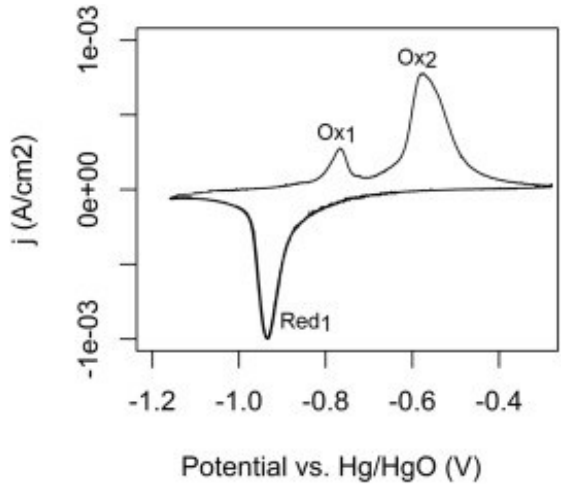

Figure 14: *Cyclic voltammetry of an iron electrode recorded with a scan rate of 500 mV s^{-1} in 5.1 M KOH. Reprinted from Posada et al. [155] under Creative Commons License (CC BY 4.0).*

The oxidation peak at around -0.76 V vs. Hg|HgO|1 M KOH (≈0.15 V vs. RHE) is assigned to the formation of iron hydroxide as follows [155,156]:

$$Fe + 2\,OH^- \rightleftharpoons Fe(OH)_2 + 2\,e^- \quad (25)$$

The other oxidation peak, at -0.57 V vs. Hg|HgO|1 M KOH (≈0.34 V vs. RHE) is assigned as follows to the oxidation of iron hydroxide to iron oxyhydroxide and ironoxide [155,156]:

$$Fe(OH)_2 + OH^- \rightleftharpoons \delta - FeOOH + H_2O + e^- \quad (26)$$

$$3\,Fe(OH)_2 + 2\,OH^- \rightleftharpoons Fe_3O_4 + 4\,H_2O + 2e^- \quad (27)$$

The reduction peak at around -0.93 V vs. Hg|HgO|1 M KOH (≈-0.02 V vs. RHE) is developed because of the reduction of all of these ironhydroxide and oxide species [155,156].

2.4.3 The Influence of Impurities on the Hydrogen Evolution Reaction (HER) in Alkaline Media

*This chapter 2.4.3 contains adapted parts from the submitted manuscript: Khavala V.B.[=], Schneemann C.[=], Kallina V., Dosche C., Thomas T., Murty B.S., Oezaslan M., Concentration-Dependent Effects of Iron Impurities on Nickel Electrodes for Hydrogen Evolution Reaction in Alkaline Media, International Journal of Hydrogen Energy **2025**, submitted. The original text has been utilized and adapted for this thesis.*

Contributions: C. Schneemann wrote the original draft of this text and adapted it for this thesis. V.B. Khavala and M. Oezaslan contributed in editing the original draft.

Impurities in the electrolyte, present in the parts per million (ppm) range, are found under industrial electrolysis conditions [131,157–159]. These impurities originate either from the KOH electrolyte itself or from the corrosion of steel compounds within the system. Commonly discussed impurities include Fe, Al, Zn, Pb and Ni [159,160]. Many studies have shown that iron impurities in the electrolyte significantly enhance the OER activity on nickel-based catalysts, even in extremely low concentrations [158,161–165].

Only few studies have examined how iron impurities influence the HER on platinum cathodes in alkaline media. *Brossard et al.* investigated the effect on platinum electrodes in a three-electrode setup with three 30 wt% KOH electrolytes: unpurified (~0.5 ppm Fe and other metals), electrolyte spiked with 14 ppm Fe^{z+} ions and purified via pre-electrolysis.[166] They observed that unpurified electrolyte caused electrode deactivation due to hydrogen lattice absorption [167]. The electrolyte with 0.5 ppm Fe^{z+} ions led to additional deactivation due to the iron and copper deposits, which are catalytically less active for HER than platinum.[53] Conversely, the electrode exposed to KOH electrolyte with 14 ppm Fe^{z+} conc. decreased overpotential for HER after 10^3 s, likely due to the formation of fine iron deposits that increase the surface roughness. *Weber et al*. studied polycrystalline platinum and Pt/C catalysts in untreated and pre-electrolyzed 0.1 M KOH in a three-electrode setup [168]. Both experienced

electrochemically active surface area reduction from impurity deposition such as Cu, Zn, Pb, decreasing HER/HOR activity. A pre-electrolysis of the electrolyte reduced this effect [168]. Thus, impurities in small concentrations have been found to be detrimental to the HER activity on Pt electrodes due to the surface poising of the highly catalytically active Pt sites as reported in several studies [166,168]. Interestingly, high concentrations of Fe^{z+} in the electrolyte seemed to have positive effects on the HER activity at Pt electrodes due to the increase of surface roughness by iron deposition [166].

Quite some effort has been put into studying the influence of impurities on nickel cathodes. Most of them are focused on three electrode setups or permeation cells. *Huot et al.* [169] demonstrated that 0.5 ppm of iron ions in 30 wt% KOH can affect the observed *Tafel* slope of nickel wires in a three-electrode setup at low overpotentials, primarily due to Fe^{3+}/Fe^{2+} redox processes. In addition, iron deposition occurs during longer exposures, which successively degrades HER performance. They further investigated the influence of 0.5 ppm of iron ion impurities on the HER activity at Ni wires by chronopotentiometry at -100 mA cm^{-2} and at -200 mA cm^{-2} in 30 wt% KOH. For both current densities, the HER overpotential increases over time with a stronger overpotential increase after 60,000 s. Post-mortem SEM-EDX and cyclic voltammetry analysis showed that iron deposits are formed on the electrode surface which are detrimental to the HER [159]. For the overpotential increase between 0 and ~ 60,000 s the deactivation was mainly attributed to the NiH formation, which is a known issue during prolonged electrolysis [130–132], as described in chapter 2.4.2.1. It was proposed in other studies that iron deposits strongly influence the NiH formation. *Armbruster et al.* showed in 1943 that the absorption of H is around 5 to 9 times higher in nickel compared to iron depending on the temperature and partial pressure [151]. In recent investigations *Mauer et al.* compared the hydrogen uptake for a nickel electrode with 40 nm of sputtered iron coating to bare nickel electrodes in a permeation cell [132]. It was shown that the hydrogen permeation currents were lower in case of

the iron coated nickel electrode in 30 wt% KOH. This displays that the diffusion of atomic hydrogen was slowed down in comparison with the bare nickel electrode. It results in reduced formation of deactivating NiH and leads to stable overpotentials over time. *Kirk et al.* noted for iron-sputtered nickel electrodes prepared with magnetron sputtering and different masks to achieve coverages of 20 – 100% , that an iron coverage of $\geq 60\,\%$ is needed for the prevention of nickel cathode deactivation [170].

Unlike, other studies discussed how the surface roughness of iron deposits influences the HER activity of nickel electrodes. A technical note by *Riley et al.* [157] compared the effects of 3 ppm vs. 0.03 ppm iron species in the 30 wt% KOH electrolyte for the HER on 1 cm^2 Ni plates at current densities of -250 mA cm^{-2} in a three-electrode setup. The behavior during the first 10,000 s remains the same with an increase of HER overpotentials over time, proposed by forming NiH. After that time period the electrode exposed to 3 ppm shows a decrease in HER overpotentials. Black structures on the electrode surface were attributed to iron deposits, which roughened the electrode. It was interpreted that this reduces the current densities due to an increase in total surface area, which in turn leads to lower overpotentials. Further studies investigated the effect of higher concentrations of iron impurities. *Brossard et al.* showed that 14 ppm of iron species in the electrolyte has positive effects on the HER activity for a Ni wire in 30 wt% KOH at -200 mA cm^{-2}. During a period of 7 h the charge transfer resistance and *Tafel* slope gradually decreased, the double capacitance increased and HER overpotentials dropped. SEM micrographs revealed iron deposits on the electrode surface and the positive effects on the HER activity ascribed to the increased surface roughness [171]. Another study by *Brossard et al.* showed similar effects on different electrode materials [153]. The HER overpotential for a Pt, Co or Ni wire decreases between 1,000 and 10,000 s in 30 wt% KOH containing 14 ppm of iron impurities during galvanostatic measurement at -100 mA cm^{-2}. All electrodes were shown to form iron deposits and eventually also a closed iron film. After 10,000 s, the HER activity of all samples was the same and all samples exhibited the

electrochemical properties of a pure iron electrode. To sum up, a high concentration of iron impurities in the electrolyte seems to have positive effects on HER activity on nickel electrodes.

In a recent study, *Flis-Kabulska et al.* evaluated how Ni–Fe alloys behave in alkaline water electrolysis using a three-electrode setup. They found that increasing iron content improves HER activity, reaching a maximum activity at around 90 wt% Fe content, but also made the alloy more prone to corrosion. When the surface was oxidized and then reduced during cathodic sweeps, reactive Fe and Ni species form, temporarily boosting the HER performance. This was linked to an increase in surface area and active sites [150]. Another study by the same authors examined iron cathodes in 25 wt% KOH at 80 °C in the previously mentioned permeation cell setup. They observed that corrosion products like $HFeO_2^-$ reduce during cathodic polarization, depositing fresh iron on the electrode surface that temporarily enhanced HER activity because of its high surface area and thereby reactivity [172]. *Demnitz et al.* compared the influence of iron impurities in 30 wt% KOH both in a three-electrode setup and in flow cell two-electrode experiments. They found a positive effect of iron addition to the electrolyte both for the HER and OER activities on Ni electrodes in both setups within the range of 10 – 800 mA cm^{-2}. [173] However, they did not investigate the mechanisms by which iron affects the electrodes activity.

Overall, summing up all of this literature, it’s still unclear whether iron improves HER by increasing surface area through deposits or by forming protective layers that prevent Ni deactivation via the formation of Ni-H as an inactive species. In addition, the effect of different iron concentrations isn’t fully understood, as most studies focus on just one or two differently parts per million concentrations in the electrolytes.

2.5 Three-Electrode Setups for HER and HOR Measurements

2.5.1 The Rotating Disk Electrode (RDE)

HER/HOR measurements require a well-defined description of the mass transport towards the working electrode in order to extract kinetic currents of electrochemical reactions with the *Koutecký-Levich* equation (see chapter 2.3.1). For decades, the rotating disk electrode (RDE) has been widely used as a hydrodynamic electrode by numerous research groups in the field of electrocatalysis for this reason.

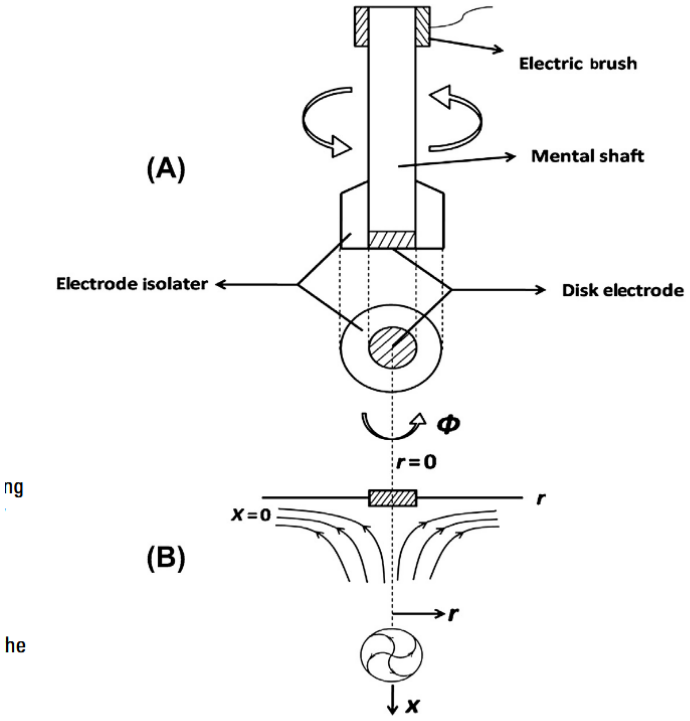

Figure 15: *(A) Schematic of the rotating disk electrode (RDE); (B) solution flow pattern near the disk electrode surface (x is the coordinate direction perpendicular to the disk electrode surface, r is the coordinate direction parallel to the disk surface, and ϕ is the coordinate direction of the electrode rotation, respectively). Reprinted with permission of Elsevier from Du et al.[174]; permission conveyed through Copyright Clearance Center, Inc.*

As depicted in **Figure 15A** the RDE consists of an electrode disk embedded into an insulating holder, commonly made of Teflon or polyethylene ether ketone (PEEK). The electrode is connected via a metal shaft that extends from the backside and is attached

to a rotator. This setup allows the electrode to be rotated at a specified angular velocity ω. The rotation of the shaft forces a convection of fluid towards the electrode disk as shown in **Figure 15B**. For the RDE, the convective-diffusion equation has been fully solved analytically for steady state. The basis of this solution of mass transport towards the RDE and that of any hydrodynamic electrode is the *Nernst-Plank* equation, which is a continuity equation, that describes the time dependent concentration $\left(\frac{\partial c}{\partial t}\right)$ of chemical species in a fluid medium:

$$\frac{\partial c}{\partial t} = \nabla\left(D\nabla c + \frac{nF}{RT}Dc\nabla\varepsilon - cu\right) \tag{28}$$

with the diffusion constant D, the concentration c of reactive species, the electric field ε, the homogenous reaction rate r, the number of transferred electrons n, the universal gas constant R, the temperature T and the velocity vector u, respectively. The right term describes the mass flux towards the electrode and consists of the diffusion term $(D\nabla c)$, the electro migration term $(\frac{nF}{RT}Dc\nabla\varepsilon)$ and the convection term (cu). Now assuming an excess concentration of a supporting electrolyte $(\frac{zF}{RT}Dc\nabla\varepsilon = 0)$ and steady state conditions $\left(\left(\frac{\partial c}{\partial t}\right) = 0\right)$ the equation (28) simplifies to:

$$\nabla(D\nabla c) = u\nabla c \tag{29}$$

also known as the “convective-diffusion” equation. This equation can be solved numerically or analytically. For its solution, a description of the velocity field u is necessary. In principle, this is described by the *Navier Stokes* equation for incompressible media $(u \cdot \nabla = 0)$, assuming a constant electrolyte density and viscosity:

$$\frac{\partial}{\partial t}(\rho u) + \nabla(\rho\, \mathrm{uu^T}) = \eta\nabla^2 u - \nabla p + \rho F \tag{30}$$

where ρ is the electrolyte density, u is the velocity vector, t is the time, η is the dynamic viscosity of the electrolyte, ∇p is the divergence of pressure and F is the external force

field vector. In case of the RDE the solution of the velocity field was obtained by *von Karman* and *Cochran* [175] in polar coordinates (r, x and ϕ as shown in **Figure 15B**) as follows:

$$u_x = -0.51\ \omega^{\frac{3}{2}} \nu^{-\frac{1}{2}} x^2 \tag{31}$$

$$u_r = 0.51\ \omega^{\frac{3}{2}} \nu^{-\frac{1}{2}} r x^2 \tag{32}$$

where u_x and u_r are the solution flow rates at r and x directions, ω is the electrode rotation rate, ν is the kinematic viscosity of the electrolyte solution, x is the distance from the electrode surface and r is the distance from the disk center at the direction parallel to the electrode surface (compare with **Figure 15B**). Since the concentration is not a function of ϕ ($\frac{\partial c}{\partial \phi} = \frac{\partial^2 c}{\partial \phi^2} = 0$) and according to equation (31) also not on the radius r ($\frac{\partial c}{\partial r} = \frac{\partial^2 r}{\partial r^2} = 0$) the convective-diffusion equation (29) simplifies towards:

$$D \frac{\partial^2 c}{\partial x^2} = u_x \left(\frac{\partial c}{\partial x}\right) \tag{33}$$

The current at the electrode surface is given by:

$$I = nFAD \left(\frac{\partial c}{\partial x}\right)_{x=0} \tag{34}$$

where A is the electrode surface area and $\left(\frac{\partial c}{\partial x}\right)_{x=0}$ is the concentration gradient at the surface. Solving equation (33) within the boundaries:

$$x = \infty \rightarrow c = c_\infty \tag{35}$$

$$x = 0 \rightarrow c = 0 \tag{36}$$

with the bulk concentration c_∞ and insertion of the solution for $\left(\frac{\partial c}{\partial x}\right)_{x=0}$ in equation (34) gives the well-known *Levich* equation [176]:

$$I_{lim,0}^{RDE} = 0.62 nFAD^{\frac{2}{3}} \omega^{\frac{1}{2}} \nu^{-\frac{1}{6}} c_\infty \tag{37}$$

The index “0” refers to established equations from the literature throughout this thesis.

The main advantage of the RDE technique lies in its well-defined mass transport, which simplifies the extraction of the kinetic current density i_{kin}, as discussed earlier. Additionally, it requires only small amounts of catalyst compared to gas diffusion electrodes (GDEs) described in subsequent sections, making it a cost-effective method for catalyst screening [177]. However, there are notable limitations. The maximum achievable mass transport is restricted by the maximum rotation speed ω and low gas solubility in the liquid electrolyte ($c_\infty \approx 1\ mmol/l$ [178,179]). That makes it impossible to accurately measure HER/HOR activities for noble metals in acidic media as mentioned earlier [43,44,54]. Furthermore, catalysts are studied in an idealized thin-film environment within a liquid electrolyte, which differs significantly from more realistic conditions involving the three-phase boundary in GDEs or membrane electrode assemblies (MEAs) [180]. Several studies have demonstrated that these differences complicate the direct transfer of catalyst activity and stability results from RDE setups to more applied systems, such as GDEs or MEAs [177,181,182].

2.5.2 Gas diffusion electrodes (GDEs)

As previously mentioned, the HER/HOR kinetics of noble metal catalysts in acidic media are too fast to be measured with the conventional RDE technique [177]. However, membrane electrode assemblies (MEAs) require much larger quantity of catalyst and more expensive equipment compared to RDEs making the effective catalyst screening of new materials more difficult [177,180]. To bridge this gap, gas diffusion electrodes have been developed [183,184]. One example of a setup like this is shown in **Figure 16**.

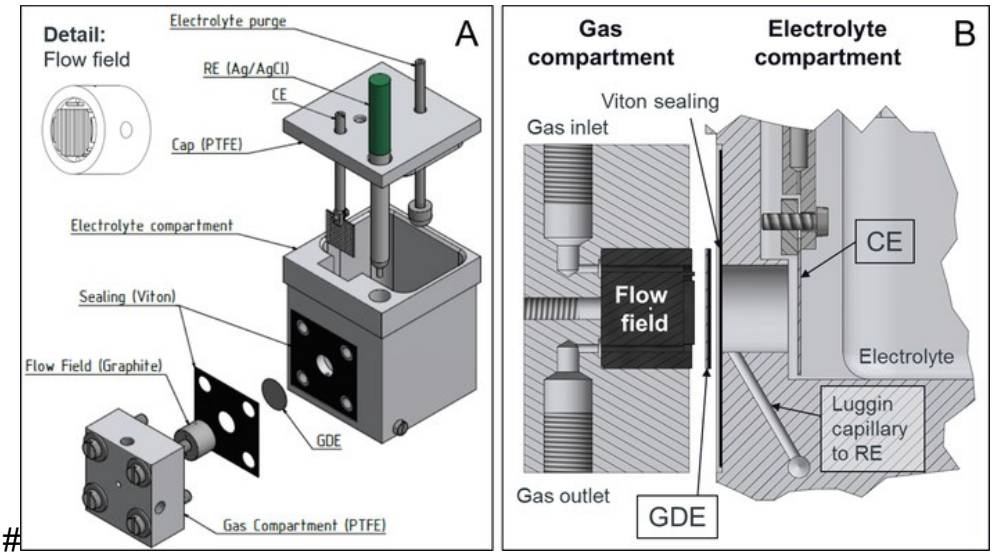

***Figure 16: A**: Scheme of the GDE half-cell setup. **B**: Detailed scheme of three-electrode assembly. Reprinted from Ehelebe et al. [184] under Creative Commons License (CC BY 4.0).*

Briefly, in this setup, the catalyst ink is coated onto a gas diffusion layer (GDL), which is positioned between the gas compartment on one side and the electrolyte compartment on the other, as shown in **Figure 16A**. The electrolyte chamber, depicted in **Figure 16B** contains a liquid electrolyte along with a reference electrode (RE) and a counter electrode (CE), similar to the RDE configuration. The catalyst layer on the GDE acts as the working electrode. Unlike the RDE, where gases dissolve directly into the electrolyte, here the gas is continuously pumped from the gas compartment through a graphite flow field onto the working electrode. This is a key advantage of the setup, as it enables much higher mass transport compared to the RDE [185], leading to higher and more realistic current densities [181], which make it possible to accurately measure exchange current densities i_0 of HER/HOR for noble metals in this setup [44]. Additionally, the presence of the three-phase boundary makes this setup more closely resemble an MEA [180,184]. However, it should be pointed out, that higher quantities of catalyst are needed compared to RDE [181]. It is also known that electrocatalysts can exhibit much higher activity in RDE compared to GDE's [186,187]. Therefore, RDE and specialized model setups remain essential for initial

screening to fully explore the catalytic potential of new model electrocatalyst materials and the next section will introduce a variety of specialized setups for these.

2.5.3 Model Electrocatalyst Setups – Droplet-Cells and Flow Cells

2.5.3.1 Droplet Cells

Often model electrocatalysts cannot be measured with the standard RDE technique or in a GDE due to their unique shape or stability requirements [88,109,188–192]. Specialized setups are therefore needed for the measurement of model electrocatalysts. One type of cell, which has been established for the measurement of single 2D TMCs flakes, are small electrolyte droplet cells also called micro reactors [88,109,190]. One example of such cell is shown in **Figure 17**.

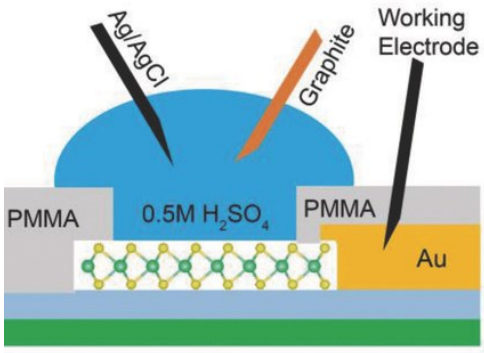

Figure 17: *Schematic cross-section view of an electrochemical micro droplet cell for the measurement of MoS_2 flakes. Reprinted with permission of John Wiley and Sons from Zhou et al. [190]; permission conveyed through Copyright Clearance Center, Inc.*

Typically, a 2D TMC is connected via a small gold wire or plate from the side as the working electrode (see **Figure 17**). The active surface area is defined by a PMMA mask, which is prepared using lithographic processes, and placed on top of the 2D TMC. The electrolyte consists of a small droplet in which both a tiny reference electrode and a counter electrode are immersed. This configuration offers the advantage of enabling highly selective measurements of both basal planes and edge sites of 2D TMCs, depending on the placement of the lithographic mask in relation to the TMC [88,109,190]. However, there are some disadvantages. Due to the small size,

the usability of standard reference electrodes is limited. Additionally, because the setup involves only a single electrolyte drop and lacks convection, mass transport is restricted. This limitation makes it challenging to accurately measure HER/HOR kinetics, as discussed in previous chapters. Therefore the other type of setup that was incorporated for measurements in this thesis are flow cells.

2.5.3.2 Flow Cells – Cell Types and Theory

This chapter 2.5.3.2 includes adapted content from the original article: Schneemann C., Traegner J., Mindermann L., Friedrichs-Schucht M., Tang B., Dietzel A., Oezaslan M., A Universal Analytical Model for the Limiting Current Characteristics in Impinging Jet Electrodes. Journal of The Electrochemical Society 2025;172(6):66503. [193]. License: Creative Commons License (CC-BY-NC-ND 4.0). Copyright: The Authors. The original text has been utilized and adapted for this thesis.

Contributions: C. Schneemann wrote the original draft of this text and further adapted it for this thesis. J. Traegner, J. Koehler, and M. Oezaslan contributed to editing the original article draft.

Flow cells have been used for a variety of tasks to couple electrochemical measurements with chemical analysis, such as liquid chromatography [194], mass spectrometry [195]. Recently, the usage for model electrocatalysts was demonstrated. One example is the work by *Temmel et al.* [196] on the investigations of square model electrodes prepared by atomic layer deposition, which otherwise cannot be realized using RDE.

Electrochemical flow cells can be generally divided into two different flow type categories. The first category involves parallel electrolyte flow over the working electrode, known as the channel electrode [178,197–199]. The mass transport for this type of electrode has been first described analytically by *Levich* [176] and later by *Blaedel et al.* [200]. In 2008, *Scherson et al.* [197] developed a *Koutecky-Levich*-like

equation for channel electrodes to separate the current into its contributions from the kinetics and mass transport.

The second category are flow cells of the confined impinging jet electrode type, where the electrolyte is pumped vertically onto the electrode surface. A schematic of a such a confined impinging jet electrode with the electrolyte flow lines is displayed in **Figure 18**. The electrolyte is pumped with a certain volume flow rate $\dot{V}_0$ through an inlet-nozzle with a diameter d. The flow is directed perpendicular towards a circular electrode with radius R_C positioned at a distance H from the inlet-nozzle. Generally, in this hydrodynamic electrode arrangement three different flow regions can be identified based on already existing hydrodynamic electrodes from literature, namely wall-tube (WT) region, wall-jet (WJ) region and radial channel-flow (RF) region.

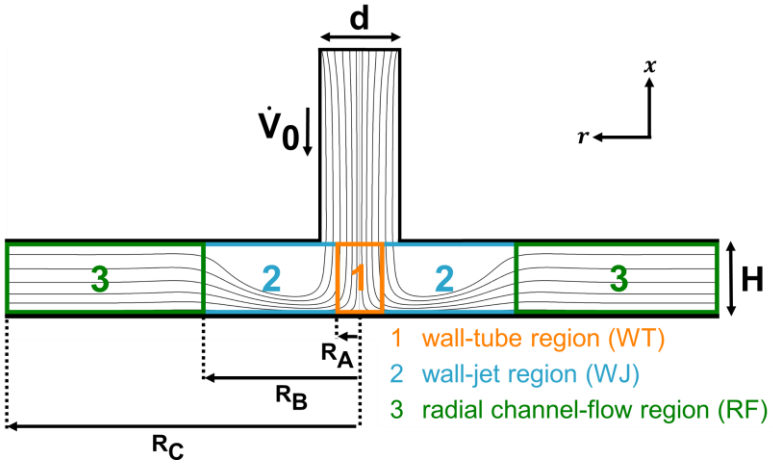

Figure 18: *Schematic two-dimensional representation of a confined impinging jet electrode with three flow regions: (1) wall-tube (WT) region, (2) wall-jet (WJ) region and (3) radial channel-flow (RF) region. Abbreviations: d – inlet diameter, H – distance between inlet-nozzle and electrode, $\dot{V}_0$ – volume flow rate, R_A, R_B – transition radii, R_C – electrode radius. Reprinted from Schneemann et al. [193] under Creative Commons License (CC BY-NC-ND 4.0).*

Near the center of the electrode, the jet deflects from the axial direction (x-axis in **Figure 18**) into a radial flow (r-axis). In this region, with electrode sizes of $0 \leq R_C \leq 0.5d$ [201], the diffusion layer thickness should be constant [202,203] and it is therefore comparable to the rotating disk electrode (RDE) arrangement. Hydrodynamic electrodes that operate within this range are commonly referred to as wall-tube

electrodes (WT, orange in **Figure 18**) [201,204–210]. The velocity field of the non-confined wall-tube configuration was initially mathematically described by *Homann* [202]:

$$u_r = ar \tag{38}$$

$$u_x = -2ax \tag{39}$$

where u_x and u_r are the solution flow rates at r and x directions and a is a hydrodynamic constant. Now applying the same boundary conditions as for the RDE (equations (35) and (36)) and inserting into the convective-diffusion equation (33) *Chin et al.* [201] obtained as a general solution for the *Sherwood* number:

$$Sh_0^{WT} = \frac{K_0^{WT} d}{D} = 0.85002\, Sc^{\frac{1}{3}} Re^{\frac{1}{2}} \sqrt{a^*}\, g(Sc) f\left(\frac{H}{d}\right) \tag{40}$$

where K_0^{WT} is the average mass transfer coefficient in the wall-tube region, D is the diffusion coefficient of the reactive species, d is the inlet-nozzle diameter, Sc is the *Schmidt* number, Re is the *Reynolds* number, $\sqrt{a^*}$ is the square-root of the hydrodynamic constant a^*, $g(Sc)$ is an asymptotic of the *Schmidt* number Sc and $f\left(\frac{H}{d}\right)$ is a function of the quotient from inlet-nozzle to electrode distance H and diameter d. Equation (40) holds for laminar flow ($Re \leq 2000$) and a uniform layer thickness, which is typically given between $0 \leq R_C \leq 0.5d$ [201]. For $\sqrt{a^*}$ and $f\left(\frac{H}{d}\right)$ different values exist in literature, determined experimentally or theoretically [201,209,211–213].

Based on Faraday's law, the limiting current for the wall-tube electrode $I_{lim,0}^{WT}$ is then given by:

$$I_{lim,0}^{WT} = n\, F\, c_\infty\, A\, Sh_0^{WT}\, \frac{D}{d} \tag{41}$$

where n is the number of transferred electrons, F is the Faraday constant, c_∞ is the bulk concentration of reactive species and A is the electrode surface area, respectively. Inserting equation (40) in (41) gives:

$$I_{lim,0}^{WT} = 0.9591\, n\, F\, c_\infty\, \pi\, R_C^2\, \sqrt{a^*}\, d^{-\frac{3}{2}}\, \dot{V}_0^{\frac{1}{2}}\, \nu^{-\frac{1}{6}}\, D^{\frac{2}{3}}\, g(Sc) f\left(\frac{H}{d}\right) \quad (42)$$

In the wall-tube setup, mass transfer to the electrode is primarily limited by the velocity at which the electrolyte is pumped onto the electrode surface. In contrast, the RDE is typically constrained by a maximum rotation speed (e.g., 10,000 rpm). To take advantage of this, microelectrode wall-tube reactors with very high mass transfer rates have been developed to investigate very fast electrochemical reactions [208,214].

Further outward from the jet center, the radial velocity decays and the boundary layer thickness increases with radial positions. Electrodes within this flow region, are described as wall-jet electrodes (WJ, light blue in **Figure 18**) [215–219]. The non-confined wall-jet was first described mathematically by *Glauert* [220].

Importantly this mathematical model assumes an infinite jet velocity at the center and infinitely thin jet diameter, thereby neglecting the existance of the wall-tube region:

$$d = 0 \quad (43)$$

$$\lim_{r \to 0} u_x = \infty \quad (44)$$

Yamada et al. [215] derived a *Levich*-like equation to determine the limiting current for a non-confined wall-jet electrode from the velocity profile descriptions developed by *Glauert* [220]:

$$I_{lim,0}^{WJ} = 1.60\, k\, n\, F\, c_\infty\, d^{-\frac{1}{2}}\, D^{\frac{2}{3}}\, \nu^{-\frac{5}{12}}\, \dot{V}_0^{\frac{3}{4}}\, R_C^{\frac{3}{4}} \quad (45)$$

with the wall-jet constant k, which they experimentally determined to be 0.86 [215], within the range of $\frac{R_c}{d} \geq 2.1$ and no confinement due to the inlet-nozzle distance H ($\frac{H}{d} \geq 2.86$) [215]. Since 1991, the non-uniformity of the current distribution on these electrodes has been emphasized as an advantage for mechanistic investigations of electrochemical reactions compared to the RDE [217,219,221,222].

In case of a small nozzle-to-electrode distance H $(0.083 \leq \frac{H}{d} \leq 0.67)$ [223], an additional flow region forms along the r-direction $\left(2 \leq \frac{R}{d} \leq 16.7\right)$ [223]. Here, the axial velocity becomes zero and the flow can be defined by a radial channel-flow [223–225]. This hydrodynamic electrode, which is often found in flow cell setups [179,189,196,226–228], is referred to as a radial channel-flow electrode (RF, green in **Figure 18**).

If a creeping flow ($Re \ll 1$) is assumed and when the boundary layer is much smaller than the distance H, the velocity in this region can be described as [223]:

$$u = \left(\frac{3\dot{V}_0}{\pi H^2}\right) \cdot \frac{x}{r} \tag{46}$$

The convective-diffusion equation for system is given by:

$$D\frac{\partial^2 c}{\partial x^2} = u\left(\frac{\partial c}{\partial r}\right) \tag{47}$$

Insertion of equation (47) into (46) and the solution, similar to *Levich's* solution for the mass-transport in laminar pipe flow [176], gives:

$$I_{lim,0}^{RF} = 3.15\, n\, F\, c_\infty\, \dot{V}_0^{\frac{1}{3}}\, H^{-\frac{2}{3}}\, D^{\frac{2}{3}}\, R_C^{\frac{4}{3}} \tag{48}$$

It was shown by *Dahlhujsen et al.* that this equation describes the limiting current also with high precision for experiments with $10 \leq Re \leq 180$ [223]. **Table 4** summarizes the general equations and restrictions for $I_{lim,0}^{m}$ of each of the above-described hydrodynamic electrode types again.

Table 4: *Common equations for the limiting current $I_{lim,0}^{m}$ of different hydrodynamic electrodes and their restrictions.*

Hydrodynamic electrode	$I_{\mathrm{lim},0}^{\mathrm{m}}$	Restrictions
wall-tube electrode[201] , *)	$I_{lim,0}^{WT} = 0.9591\, n\, F\, c_\infty\, \pi\, R_C^2\, \sqrt{a^*}\, d^{-\frac{3}{2}}\, \dot{V}_0^{\frac{1}{2}}\, \nu^{-\frac{1}{6}}\, D^{\frac{2}{3}}\, g(Sc)\, f\left(\frac{H}{d}\right)$	$Re \leq 2000$ and $0 \leq R_C \leq 0.5d$
wall-jet electrode[215] , #)	$I_{lim,0}^{WJ} = 1.60\, k\, n\, F\, c_\infty\, d^{-\frac{1}{2}}\, D^{\frac{2}{3}}\, \nu^{-\frac{5}{12}}\, \dot{V}_0^{\frac{3}{4}}\, R_C^{\frac{3}{4}}$	$\frac{R}{d} \geq 2.1$ and $\frac{H}{d} \geq 2.86$
radial channel-flow electrode[223]	$I_{lim,0}^{RF} = 3.15\, n\, F\, c_\infty\, \dot{V}_0^{\frac{1}{3}}\, H^{-\frac{2}{3}}\, D^{\frac{2}{3}}\, R_C^{\frac{4}{3}}$	$10 \leq Re \leq 180$, $2 \leq \frac{R}{d} \leq 16.7$ and $0.083 \leq \frac{H}{d} \leq 0.67$

*) $g(Sc) = \left[1 - \frac{0.084593}{Sc^{\frac{1}{3}}} - \frac{0.016368}{Sc^{\frac{2}{3}}} - \frac{0.0057398}{Sc} + \frac{0.0014288}{Sc^{\frac{4}{3}}}\right]$

#) $k = 0.86$

2.5.3.3 Advantages and Disadvantages of Flow Cell Setups

Overall, one major downside of the impinging jet flow cell setup for the measurement of HER model electrocatalysts is that there is no universal analytical approach to determine the limiting current in this flow cell. The highly complex velocity profile, with three different flow regime regions typically requires time-consuming computational fluid dynamics (CFD) simulations [179,204,205,218,227], which strongly limits the widespread use of these three-electrode setups. Analytical solutions are only obtained for special cases and geometries, like the one from *Dalhuijsen et al.* mentioned earlier [223]. Another disadvantage is that depending on the chosen construction the compression of the O-ring and thereby the surface area inside the cell are not very well defined [192]. Major advantages compared to the RDE and GDE include the possibility to measure samples with different shapes [189,192,196], which could not be measured with either of the other techniques.

3 Research Goals

The general aim of this thesis is to gain detailed insights into the HER on model based electrocatalysts based on Pt for acidic media and Ni for alkaline media using two different hydrodynamic electrochemical electrodes: the well-known RDE and an impinging jet flow cell.

The first main objective of this work is to develop an electrochemical impinging jet flow cell for the measurement of 2D squared model electrocatalyst samples in acidic media, which cannot be measured with the RDE setup. Universal analytical models to describe the mass transport in such setups in the literature have not been established yet. Thus, in first part of this thesis the goal is to develop a universal analytical model for the mass transport processes in impinging jet electrodes and to verify this model both numerically with the aid of CFD simulations and experimentally in a 3D-printed flow cell prototype utilizing the simple one-electron transfer reaction of the oxidation of ferro(II)cyanide.

After development of the 3D-printed flow cell prototype, the second objective is to compare the impinging jet flow cell with the well-known RDE setup for the HER/HOR reaction on Pt surfaces. Mass transport, electrode surface area and gas saturation for the HER/HOR are investigated with CV, linear sweep voltammetry (LSV) and electrochemical simulations based on the already established universal analytical model and compared between the RDE and the fully developed impinging jet flow cell.

In acidic media, research on the HER focuses on reducing the Pt content, as already mentioned. Pt chalcogenides seem to be promising candidates, but have not been investigated in the form of phase pure 2D model electrocatalysts yet, due to the lack of suitable measurement setups. The third objective of this thesis is to investigate the activity and stability of novel 2D Pt chalcogenides in the electrochemical flow cell developed herein in comparison with metallic Pt with a variety of techniques such as CV, LSV and chronopotentiometry. Stability and structural changes are monitored throughout the electrochemical protocol with XPS and Raman spectroscopy. These results aim to a give a clearer insight into the behavior of this catalyst group.

In alkaline media, research on the HER focuses on increasing long-term durability and impurity effects. Overall, it’s still unclear whether iron improves HER on Ni surfaces by increasing surface area through deposits or by forming protective layers that prevent

Ni deactivation via the formation of Ni-H as an inactive species. In addition, the effect of different iron concentrations isn't fully understood, as most studies focus on just one or two differently parts per million concentrations in the electrolytes. The fundamental study from the fourth part of this thesis explores how iron impurities in the electrolyte influence the HER activity of polycrystalline nickel electrodes in alkaline media. Different amounts of Fe are added to the electrolyte in the well-known RDE setup utilizing a polycrystalline Ni electrode as the model working electrode. Using techniques like XPS, SEM, μ-XRF, and electrochemical measurements differences in the electrode electrochemistry over time and the model electrode surface structure are revealed. These findings should help to improve the understanding of the electrochemical processes happening in industrial ALWE.

All in all, both the RDE and impinging jet flow cell techniques enable detailed analysis of HER activity, mass transport effects, and catalyst stability on model electrodes in acidic and alkaline media, providing essential insights for future catalyst development and optimization. This research contributes to a better understanding of how electrode structure, electrolyte impurities, and reaction conditions influence HER performance, guiding future efforts toward more efficient and durable electrocatalysts.

4 Experimental and Theoretical Methods

4.1 The Impinging Jet Flow Cell

4.1.1 Flow Cell Design and Overview

The full design of the impinging jet flow cell, including all directly connected parts, is illustrated in **Figure 19a**.

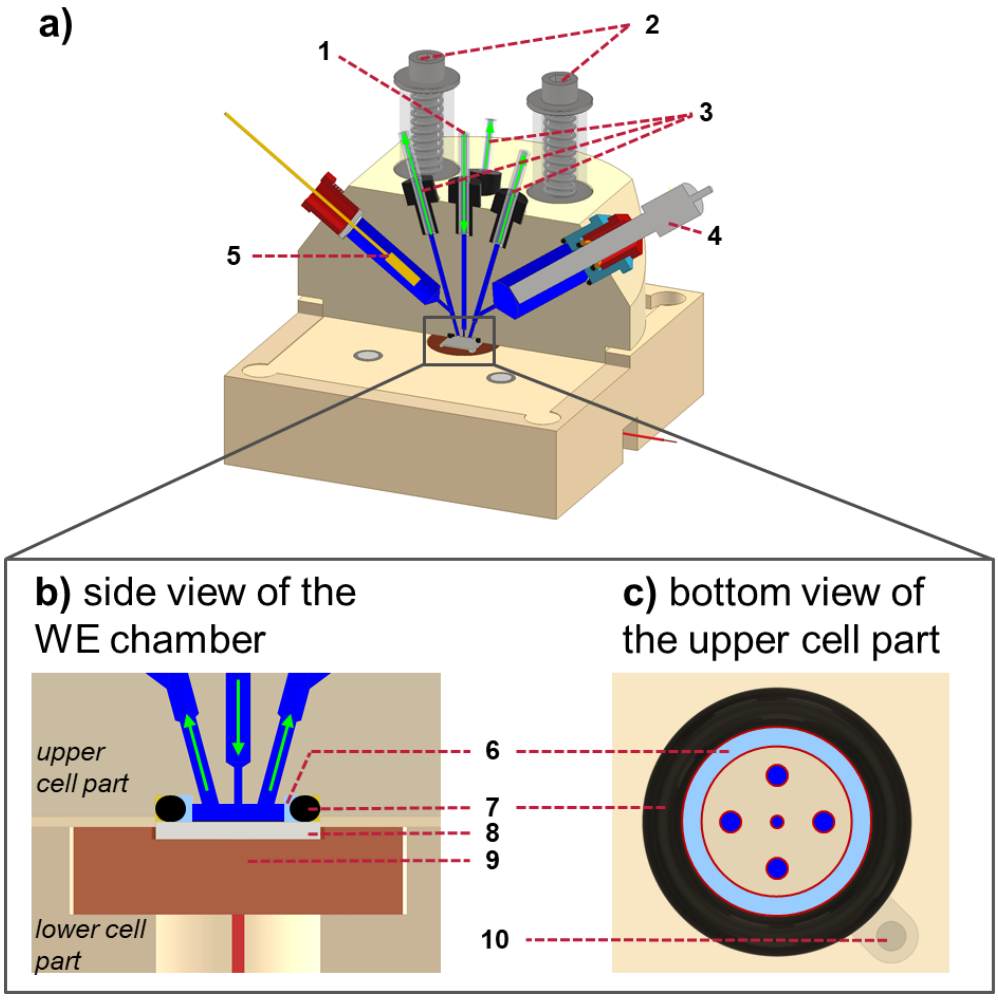

Figure 19: *Design of the electrochemical impinging jet flow cell.* ***a)*** *Full view of the cell and directly connected parts.* ***b)*** *Side view zoom-in at the working electrode chamber. The upper cell part and lower cell part are indicated.* ***c)*** *Bottom view zoom-in of the upper cell part. Legend: 1 – electrolyte inlet, 2 – spring-loaded screw system, 3 – electrolyte outlets, 4 – reference electrode, 5 – counter electrode (gold wire), 6 – dead zone* $(2.81\ mm \leq R_{loc} \leq 3.63\ mm)$ *in the O-ring groove, 7 – O-ring (FKM), 8 – working electrode in sample holder, 9 – copper sample holder and contact, 10 – contact pinhole for contacting working electrodes from the top.*

This setup, adapted from *Temmel et al.*[196], is tailored for measuring sensitive 2D MBE catalysts and features a three-electrode configuration of the impinging jet type.

4.1.2 Cell Structure

The cell comprises of two main components press-fitted against each other: the upper part contains the fluid channels, and the lower part holds the working electrode, sample holder, and electrical connections. **Figure 19b** provides a zoomed in side-view of the working electrode chamber, with the upper and lower parts indicated. **Figure 19c** offers a bottom view of the upper cell part, highlighting the fluid system and dead zones.

For the setup validation in chapter 5.1 a prototype of the upper cell part of this cell was 3D-printed in house. All HER/HOR measurements were performed in a full PEEK version of this cell, also constructed in house (chapters 5.2 and 5.3).

4.1.3 Flow System and Outlets

The design includes four symmetrically arranged outlets ((3) in **Figure 19a**) in the working electrode chamber, intended to minimize outlet effects on radial flow symmetry, as supported by *Tschupp et al.* [179] based on 3D-CFD simulation flow profiles. A dead zone near the O-ring groove (see (6) in **Figure 19b&c**) is assumed for theoretical calculations in this thesis between $2.81\ mm \leq R_{loc} \leq 3.63\ mm$ were R_{loc} is the local radius in r direction (see **Figure 18**). All flow cell models used in this thesis had an inlet diameter of $d = 0.5$ mm and a nozzle to electrode distance of $H = 0.7$ mm.

4.1.4 Peripherals

Figure 20 shows the complete system, including the just described impinging jet flow cell (2) and peripherals. A syringe pump ((1), KDS Legato 210P equipped with 60 mL polypropylene syringe) delivers electrolyte saturated with the required gas via a custom glass saturator (inside reservoir (3)), through the inlet (**Figure 19a**) onto the working electrode. The electrolyte spreads radially and exits through the four outlets in the flow cell (2), flowing toward the waste reservoir (4).

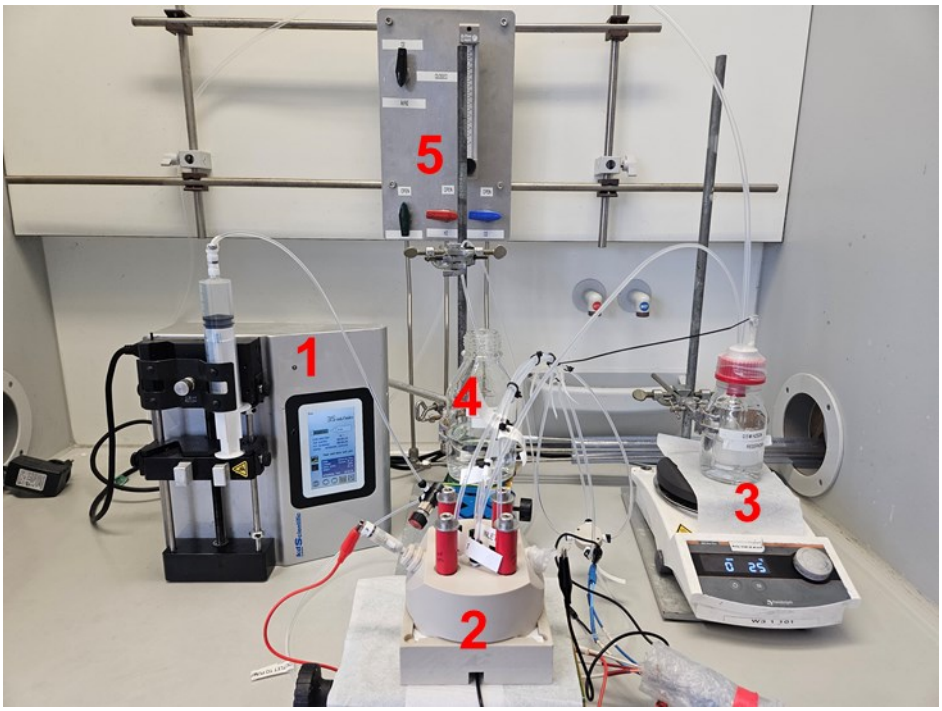

Figure 20: *Full developed impinging jet flow cell setup including complete periphery with 1) syringe pump, 2) PEEK impinging jet flow cell, 3) fresh electrolyte reservoir with gas saturation frit, 4) waste electrolyte reservoir 5) gas panel.*

4.1.5 Electrochemical Components

The working electrode ((8) in **Figure 19b**), embedded in a sample holder ((9) in **Figure 19b**), is compressed between the upper and lower flow cell parts and electrically connected via a copper contact. The sealing of the working electrode is achieved with an FKM O-ring ((6) in **Figure 19b**). To balance sealing efficiency with minimal mechanical stress, which is especially critical for delicate 2D materials, a spring-loaded screw system ((2) in in **Figure 19a**) was developed and carefully adjusted. The reference electrode ((4) in **Figure 19a**) resides in a separate compartment connected to one outlet, allowing flexibility to substitute different reference electrodes. Similarly, the counter electrode, in this study a gold mesh soldered onto a gold wire, is housed separately in its own compartment ((5) in **Figure 19a**).

4.2 Development of a Universal Analytical Model for the Limiting Current Characteristics in Impinging Jet Electrodes

This chapter 4.2 includes adapted content from the original article: Schneemann C., Traegner J., Mindermann L., Friedrichs-Schucht M., Tang B., Dietzel A., Oezaslan M., A Universal Analytical Model for the Limiting Current Characteristics in Impinging Jet Electrodes. Journal of The Electrochemical Society 2025;172(6):66503. [193]. License: Creative Commons License (CC-BY-NC-ND 4.0). Copyright: The Authors. The original text has been utilized and adapted for this thesis.

Contributions: C. Schneemann wrote the original draft of this text and further adapted it for this thesis. J. Traegner, J. Koehler, and M. Oezaslan contributed to editing the original article draft.

4.2.1 Numerical Methods – CFD Simulations

4.2.1.1 Governing Equations

The electrolyte flow profile in the impinging jet flow cell was calculated using the *Navier Stokes* equation for incompressible media (see equation (30)). The mass transport of the jet is described by the *Nernst-Planck* equation (equation (28)). The convective-diffusion equation for this system is given by equation (29). The numerical solution of equation (29) for the impinging jet gives the concentration profile over the electrode surface $\left(\frac{\partial c}{\partial x}\right)_{x=0}$. The local limiting current densities $i_{lim,loc}$ are then obtained by:

$$i_{lim,loc} = nFD\left(\frac{\partial c}{\partial x}\right)_{x=0} \tag{49}$$

The integration of $i_{lim,loc}$ over the whole electrode surface A gives the total limiting current I_{lim}.

4.2.1.2 Simulation Details

CFD simulations of the oxidation of ferrocyanide(II) to ferricyanide(III) in 0.5 M K_2SO_4 electrolyte solution were carried out using the Ansys® Fluent (Release 2023 R2) software package. A total of 350 CFD simulations within the geometry parameter range shown in **Table 5** were performed. The additional constant values for temperature T, dynamic viscosity η and electrolyte density ρ, etc. are listed in .

In this study, the parameter range was chosen based on practicability of the flow cell construction and experimental application of such parameters. As an example, inlet-nozzles with a diameter of $d \leq 0.3\,mm$ already reach resolution limits of the used 3D printing device. Additionally, a rotational symmetry was used to simulate a 2D axisymmetric space. It is noted that the outlets of the 3D-printed flow cell (see **Figure 19b)** were not modeled in detail, but a radial outlet far away of the jet center was assumed in the CFD simulations. Quad dominant meshes in the 2D axisymmetric space with inflation layers close to all solid surfaces were applied, resulting in 186,448 finite volume elements. The shear stress transport k-ω turbulence model with default parameters was used, because the *Reynold* numbers for some geometries were above 100 which is assumed to be sufficient for turbulence flow in impinging jets [229].

Table 5: *Geometry parameter range for the computational fluid dynamics (CFD) simulations.*

Parameter	minimum	maximum
d / mm	0.50	0.75
H / mm	0.70	0.70
R_C / mm	0.50	3.63
$\dot{V}_0$ / mL min^{-1}	0.05	20.00

4.2.1.3 Boundary conditions

A constant inlet velocity was applied according to the volume flow $\dot{V}_0$ and the inlet diameter d. The distance between inlet boundary and nozzle exit was sufficient to reach a fully developed steady state flow profile. The specific reactant concentrations of ferrocyanide(II) on the inlet surface are listed in **Table S1**.

A constant pressure was applied at the flow cell outlets. The reactant concentration on the electrode surface was set to zero, which is equivalent to the diffusion limited reaction rate or limiting current density i_{lim} at high overpotential. All solid boundary layers were implemented with no-slip conditions, i.e. a fluid velocity of zero on the electrode surface.

4.2.2 Experimental Methods

4.2.2.1 3D-Printed Flow Cell Setup

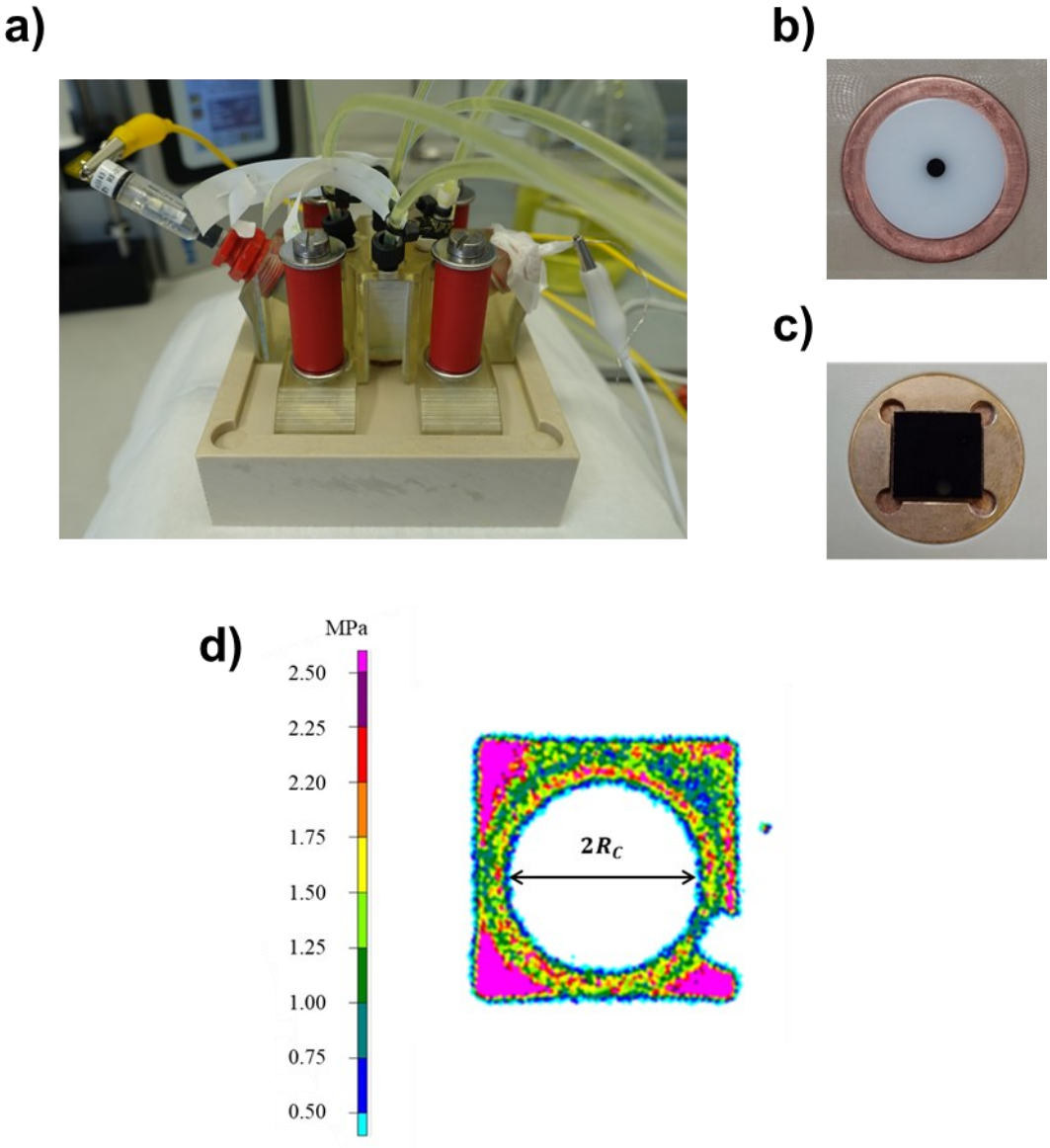

Figure 21: *Impinging jet flow cell setup for the development of the universal analytical model.* ***a)*** *Image from the 3D-printed impinging jet flow cell setup.* ***b)*** *Top-view image of the glass-carbon electrode embedded in Teflon with radius* $R_C = 1\ mm$ *inside the copper sample holder.* ***c)*** *Top-view image of the 10x10 mm glass-carbon electrode* ($R_C = 3.63\ mm$) *inside the copper sample holder.* ***d)*** *Pressure distribution profile on a 10x10x0.5 mm square glassy carbon electrode after compression with an O-ring in the flow cell setup using Fujifilm Prescale LLW pressure-sensitive film.*

Experiments were conducted with a 3D-printed (Keyence Agilista-3000 with Ar-H1 material) upper half of the electrochemical flow cell, which is shown in **Figure 21a**.

Three different working electrode radii were tested: $R_C = 0.5, 1$ and $3.63\,\mathrm{mm}$ to consider all volume flow regions (**Figure 18**) and different distances from the outlets of the flow cell. For the electrodes of $R_C = 0.5$ and $1\,\mathrm{mm}$ a glassy carbon rod (SIGRADUR® G, HTW Hochtemperatur-Werkstoffe GmbH) was embedded in-house within a Teflon cylinder (**Figure 21b**). In case of the largest electrode size ($R_C = 3.63\,\mathrm{mm}$), a 10x10x0.5 mm glassy carbon plate (SIGRADUR® G, HTW Hochtemperatur-Werkstoffe GmbH) was directly used as a working electrode (**Figure 21c**). The electrode radius ($R_C = 3.63\,\mathrm{mm}$) was defined by the O-ring (see the design by *Temmel et al.* [196]). To account for the deformation of the O-ring under sealing pressure, the actual electrode area exposed to the electrolyte was verified using pressure-sensitive foil. The pressure-sensitive film (Fujifilm Prescale, LLW, 0.5 - 2.5 MPa) was placed between the glassy carbon electrode and the O-ring that seals the working electrode compartment. After assembling and disassembling the cell, the film was scanned using the Fujifilm Pressure Distribution Mapping System (FPD-8010E), as shown in **Figure 21d**. The pressure pattern was analyzed using ImageJ (Version 1.53k), applying a scanner pixel density of 200 dpi to confirm the electrode radius of $R_C = 3.63\,mm$. To prevent the flow cell setup from electrochemical oscillation due to the very low uncompensated resistance R_u and high double layer capacitance C_{dl}, an additional resistor of 12.6 Ohm was clamped between the potentiostat and the working electrode connection only for the measurements of the largest electrode ($R_C = 3.63\,\mathrm{mm}$).

4.2.2.2 Electrochemical Parameters

For all experiments, the electrolyte was freshly prepared by dissolving 10 mM potassium hexacyanidoferrate(II) trihydrate ($K_4[Fe(CN)_6]\cdot 3\,H_2O$, VWR Chemicals, ≥99.0%) and 10 mM potassium hexacyanoferrate(III) ($K_3[Fe(CN)_6]$, VWR Chemicals, ≥99.0%) in 0.5 M potassium sulfate solution (Carl Roth, ≥99.0%). The solution was purged with argon (99.999%, Westfalen Gas) for 30 minutes prior to electrochemical experiments. The electrochemical measurements were conducted in a three-electrode configuration, using one of the glassy carbon electrodes as a working electrode, a gold mesh as a counter electrode, and a mercury/mercury sulfate (MMS) electrode as a reference electrode. Linear sweep voltammograms (LSV) were recorded at a scan rate of 1 $mV\,s^{-1}$ within the potential range of -1.0 to 0.6 V vs. $Hg|HgSO_4|K_2SO_{4,sat.}$. From

the potentiostatic electrochemical impedance spectroscopy (PEIS), the uncompensated resistance (R_u) was extracted by identifying the intersection of the impedance curve with the real axis in the Nyquist plot. For the direct measurement of the limiting currents the working electrode was chronoamperometrically held at 0.6 V vs. $Hg|HgSO_4|K_sSO_{4,sat}$ for 30 s.

4.3 Comparison of Electrochemical Behavior and Mass Transport in Impinging Jet Flow Cell and RDE Setup

4.3.1 RDE Experiments

4.3.1.1 Electrodes and Electrolyte

For all experiments, the electrolyte was freshly prepared by dissolving 14.02 mL of conc. sulphuric acid (H_2SO_4, ROTIPURAN®Ultra 95 %, Carl Roth) in 500 ml of highly purified water (18 MΩ cm at 25℃). Rotating disk electrode (RDE) experiments were performed in a self-designed electrochemical three-compartment glass cell by using a rotator (MSR Rotator, Pine Research Instrumentation) and a potentiostat (Biologic, VSP300). The electrochemical measurements were conducted in a three-electrode configuration, using polycrystalline Pt electrode ($R_C = 2.5\ mm$, Pine Research), a gold mesh as a counter electrode, and a mercury/mercury sulfate (MMS) electrode as a reference electrode.

4.3.1.2 Cleaning and HUPD Determination

The solution was purged with argon (99.999%, Westfalen Gas) for 30 minutes prior to electrochemical experiments. Initially a cleaning process with 3 cycles between 0.03 and 1.2 V with a scan rate of $s = 50\ mV\ s^{-1}$, followed by 200 cycles between 0.03 and 1.2 V with a scan rate of $s = 500\ mV\ s^{-1}$ and finally with 3 cycles between 0.03 and 1.2 V with a scan rate of $s = 50\ mV\ s^{-1}$ again was carried out. Afterwards the electrolyte was exchanged the HUPD was determined in a fresh Ar-saturated electrolyte by running 3 cycles between 0.03 V and 1 V with a scan rate of $s = 50\ mV\ s^{-1}$.

4.3.1.3 HER/HOR Polarization Curves

The solution was purged with hydrogen (99.999%, Westfalen Gas) for 30 minutes prior to electrochemical experiments. Five linear sweep voltammograms (LSV) were recorded at a scan rate of 1 $mV\ s^{-1}$ within the potential range of 0.5 to -0.05 V vs. RHE. For $iR-drop$ correction, the uncompensated resistance (R_u) was extracted from the potentiostatic electrochemical impedance spectroscopy (PEIS) by identifying the intersection of the impedance curve with the real axis in the Nyquist plot.

4.3.2 Impinging Jet Flow Cell Experiments

4.3.2.1 Electrodes and Electrolyte

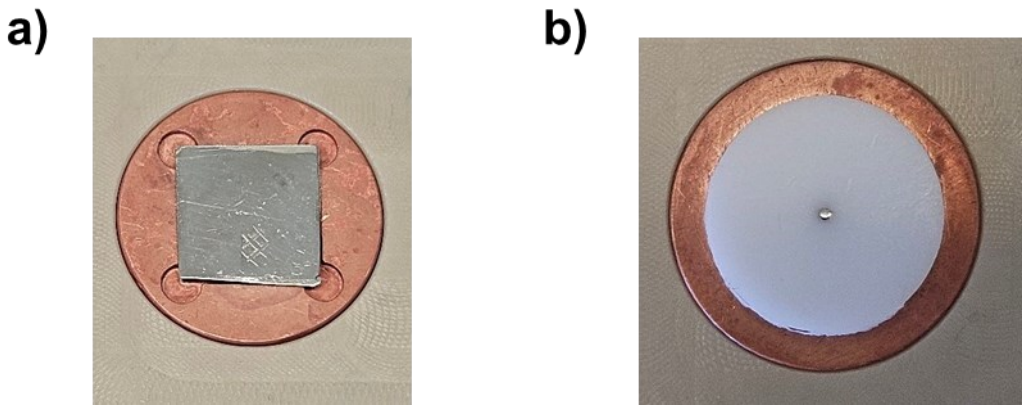

Figure 22: *Electrodes used in this study.* ***a)*** *Top-view image of the 10x10x0.5 mm Pt foil on top of a glassy carbon electrode in the copper sample holder.* ***b)*** *Top-view image of the custom designed Pt microelectrode in the copper electrode sample holder.*

For all experiments, the electrolyte was freshly prepared by dissolving 14.02 mL of conc. sulphuric acid (H_2SO_4, ROTIPURAN®Ultra 95 %, Carl Roth) in 500 ml of highly purified water (18 MΩ cm at 25℃). Inside the full PEEK version of the impinging jet flow cell (see **Figure 20**) two different working electrode radii were tested: $R_C = 0.375\ \mathrm{mm}$ and $3.63\ \mathrm{mm}$, as shown in **Figure 22**. For the electrodes of $R_C = 0.375\ \mathrm{mm}$ a Pt wire ($\geq 99.95\ \%$ trace metal basis, EVOCHEM, diameter: 0.75 mm) was embedded in-house within a Teflon disk (**Figure 22b**). In case of the larger electrode ($R_C = 3.63\ \mathrm{mm}$), a Pt foil ($\geq 99.99\ \%$ trace metals basis, Premion®, Thermo Fisher Scientific) was placed on top of the 10x10x0.5 mm glassy carbon plate (SIGRADUR® G, HTW Hochtemperatur-Werkstoffe GmbH) and used as the working electrode (**Figure 22a**). The electrode radius ($R_C = 3.63\ \mathrm{mm}$) was defined by the O-ring as previously described in chapter 4.2.2.1 in this case. To prevent the flow cell setup from

electrochemical oscillation due to the very low uncompensated resistance R_u and high double layer capacitance C_{dl}, an additional resistor of 12.6 Ohm was clamped between the potentiostat and the working electrode connection only for the measurements of the largest electrode ($R_C = 3.63\ \mathrm{mm}$).

4.3.2.2 Cleaning and HUPD Determination

The electrolyte reservoir solution (see (3) in **Figure 20**) was purged with argon (99.999%, Westfalen Gas) for 30 minutes prior to electrochemical experiments. The electrochemical measurements were conducted in a three-electrode configuration, using one of the Pt electrodes as a working electrode, a gold mesh as a counter electrode, and a mercury/mercury sulfate (MMS) electrode as a reference electrode. The cleaning process is the same as described in 4.3.1.2. Afterwards the impinging jet flow cell was flushed with fresh electrolyte and the HUPD was determined by running 3 cycles between 0.03 V and 1 V for the Pt foil ($R_C = 3.63\ mm$) and 3 cycles between 0.03 V and 1.2 V for the Pt microelectrode ($R_C = 0.375\ mm$) with a scan rate of $s = 50\ mV\ s^{-1}$.

4.3.2.3 HER/HOR Polarization Curves

The electrolyte reservoir solution (see (3) in **Figure 20**) was purged with hydrogen (99.999%, Westfalen Gas) for 30 minutes prior to electrochemical experiments. Five linear sweep voltammograms (LSV) were recorded at a scan rate of 1 $mV\ s^{-1}$ within the potential range of 0.5 to -0.05 V vs. RHE. For $iR - drop$ correction, the uncompensated resistance (R_u) was extracted from the PEIS by identifying the intersection of the impedance curve with the real axis in the Nyquist plot.

4.4 Activity and Stability of Novel 2D - Pt Chalcogenides for the HER in Acidic Media

4.4.1 Raman Spectroscopy

Raman measurements were conducted using a confocal Raman imaging microscope (alpha300 R, WITec, Germany) operated with the Control SIX Software suite (Version 6.1, WITec, Germany). Spectral detection was performed using a CCD camera. Raman maps were acquired over a 100 × 100 µm area with a spatial resolution of 1 µm. After each electrochemical step, Raman measurements were performed at identical locations utilizing the TrueOrigin portable coordinate system to ensure spatial consistency. Excitation was produced by a 532 nm laser focused through a 100× objective (Carl Zeiss, Germany, numerical aperture: 0.9), with a laser power of 1 mW to reduce thermal stress on the samples. During mapping, the integration time was set to 1 s for the 2D-$PtTe_2$@HOPG, 3 s for 2D-Pt_3Te_4@HOPG, and 5 s for 2D-Pt_2Te_2@HOPG samples, optimizing signal-to-noise ratios for each material. For single spectra aquisition, the same settings were used, but with 10 accumulations per spectrum and same integration times. The backscattered Raman signal was collected and directed to the spectrometer (600 g mm^{-1} grating; UHTS 300, WITec, Germany).

Spectral processing and data analysis were performed using the Project SIX Plus software package (Version 6.1, WITec, Germany). All mappings and spectra underwent cosmic ray removal and baseline correction.

4.4.2 Electrochemical Measurement Protocol

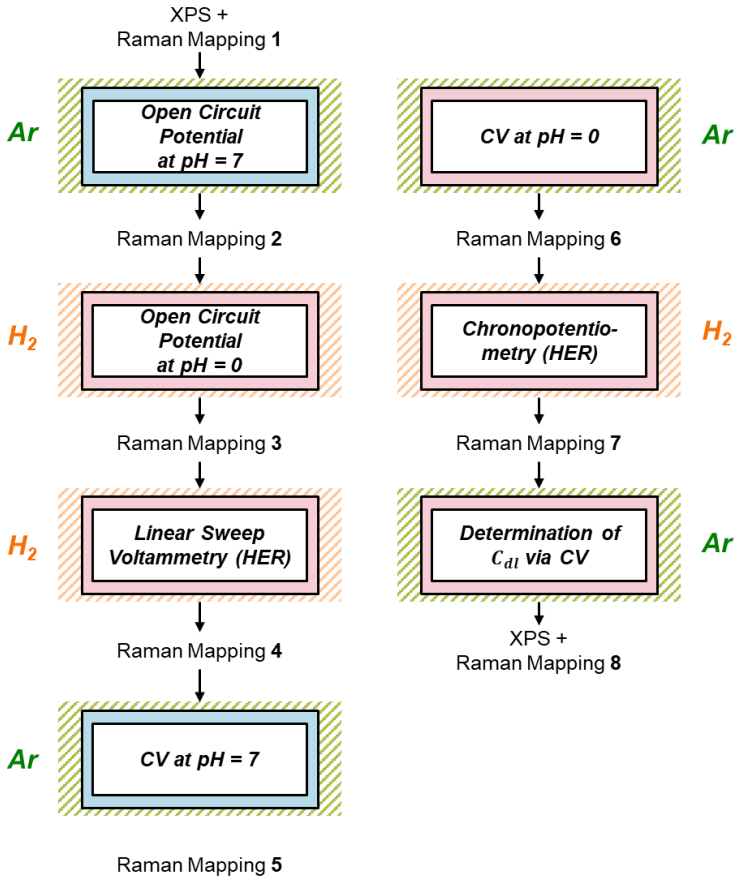

Figure 23: *Measurement protocol for 2D-Pt_xTe_y@HOPG materials. Measurements which were conducted in 0.5 M H_2SO_4 (pH = 0) are highlighted with red borders, while those in phosphate-buffered 0.1 M $NaClO_4$ (pH = 7) are indicated with blue borders around the measurement steps. Electrolyte saturations are denoted by green shading for Ar saturation and red shading for H_2 saturation Raman mapping was performed after each step, with the maps and corresponding analyses labeled from **1** to **8** in chapter 5.3.*

Three electrode experiments were conducted in the PEEK version of the electrochemical impinging jet flow cell (see (2) in **Figure 20**) connected to a potentiostat (VSP300, Biologic, France). The three-electrode arrangement consisted of the 2D-Pt_xTe_y@HOPG, HOPG or Pt foil as the working electrode, gold mesh as a counter electrode and mercury-mercury sulfate (MMS) as a reference electrode, respectively. Two different electrolytes were used: (i) Phosphate buffered (PB) 0.1 M $NaClO_4$ was prepared by dissolving 305 mg sodium dihydrogenphosphate (NaH_2PO_4, $\geq$ 99.9 %, Merck), 455 mg disodium hydrogenphosphate (Na_2HPO_4, $\geq$ 99.9 %, Merck) and 3.603 g sodium perchlorate ($NaClO_4$, $\geq$ 99.9 %, VWR Chemicals) in 250 mL highly purified water (18 MΩ cm at 25 ℃). (ii) 0.5 M sulphuric acid was prepared by dissolving 14.02 mL of conc. sulphuric acid (H_2SO_4, ROTIPURAN®Ultra 95 %, Carl Roth) in 500

ml of highly purified water (18 MΩ cm at 25 ℃). The electrolyte was saturated with argon gas (Westfalen Gas, 99.999% purity) or hydrogen gas (Westfalen Gas, 99.999% purity) for 30 minutes by bubbling through porous frit (see (3) **Figure 20c**) depending on the measurement step. The electrochemical measurement protocol for 2D-Pt_xTe_y@HOPG and HOPG, which was used for this study is shown in **Figure 23**. Before and after the electrochemical protocol, samples were investigated using Raman spectroscopy and X-ray photoelectron spectroscopy (XPS) to analyse surface changes. After each electrochemical measurement step a Raman mapping was performed *ex-situ* (labelled **(1)** to **(8)**, see **Figure 23**) with the settings described in chapter 4.4.1. The electrochemical measurement sequence begins with open circuit potential (OCP) measurements lasting 1 hour in both electrolytes (Ar-saturated), performed with the flow cell in static mode to assess chemical stability of the catalysts. Next, five cycles of linear sweep voltammetry (LSV) between 0.1 V and -0.2 V vs. RHE in H_2-saturated 0.5 M H_2SO_4 were conducted to evaluate the hydrogen evolution reaction (HER) activity (scan rate: 1 mV s^{-1}). iR-correction was performed using the high frequency resistance (HFR) of a potentiostatic impedance spectroscopy (PEIS) at the open circuit potential with a frequency from 100 kHz…1000 mHz and an amplitude of 10 mV. During the LSV and PEIS the electrolyte flow was kept at $\dot{V}_0$ = 1 mL min^{-1}. Subsequently, surface features were characterized via cyclic voltammetry (CV) in both electrolytes, with 3 cycles recorded per electrolyte (Ar-saturated), spanning from 0.03 V to 0.9 V vs. RHE. Consequently, the HER durability during a galvanostatic 45 min chronopotentiometry with $i = -0.25\ mA\ cm_{geo}^{-2}$ was tested with a flow rate of 1 mL min^{-1}. Finally, the double-layer capacitance (C_{dl}) was determined by cyclic voltammetry with different scan rates over the potential window of 0.2 to 0.4 V vs. RHE to assess electrochemical surface area.

For the Pt reference measurements a Pt foil (10x10x0.025 mm, ≥ 99.99 % trace metals basis, Premion®, Thermo Fisher Scientific) was used as the working electrode. Initially a cleaning process with 3 cycles between 0.03 and 1.2 V with a scanrate of $s = 50\ mV\ s^{-1}$, followed by 200 cycles between 0.03 and 1.2 V with a scanrate of $s = 500\ mV\ s^{-1}$ and finally with 3 cycles between 0.03 and 1.2 V with a scanrate of $s = 50\ mV\ s^{-1}$ again was carried out. Afterwards the same measurement protocol as described before (see **Figure 23**) was used.

4.5 Concentration-Dependent Effects of Iron Impurities on Nickel Electrodes for Hydrogen Evolution Reaction in Alkaline Media

*This chapter 4.5 contains adapted parts from the submitted manuscript: Khavala V.B.[=], Schneemann C.[=], Kallina V., Dosche C., Thomas T., Murty B.S., Oezaslan M., Concentration-Dependent Effects of Iron Impurities on Nickel Electrodes for Hydrogen Evolution Reaction in Alkaline Media, International Journal of Hydrogen Energy **2025**, submitted. The original text has been utilized and adapted for this thesis.*

Contributions: V.B Khavala wrote the original draft of this text. C. Schneemann adapted and added onto the original draft. M. Oezaslan contributed in editing the original draft.

4.5.1 Preparation of polycrystalline nickel disk electrode

A polycrystalline nickel (poly-Ni) cylinder ($R_C = 2.5\,mm$, HMW Hauner GmbH & Co. KG, Germany, purity trace metal basis of > 99.99 %) embedded in a PEEK changeable disk electrode assembly (Pine Research Instrumentation, AFE6MB) was used as a working electrode. The poly-Ni electrode was polished with 9, 6, 3 and 1 µm diamond suspension and 0.05 µm aluminium oxide (Buehler, Germany) onto different microcloth papers (Buehler, Germany) to obtain a mirror like Ni surface. The polished electrode was then washed in highly purified water (18 MΩ cm at 25 ℃), propan-2-ol (Fisher Chemicals, HPLC grade) and water for 5 minutes each by using an ultrasonication bath.

4.5.2 Preparation of the electrolyte including iron ion addition

Electrolyte solution (0.1 M KOH) was freshly prepared by dissolving KOH pellets (ThermoScientific, trace metal basis purity of 99.98%) in highly purified water (18 MΩ cm at 25 ℃). KOH pellets were stored under argon atmosphere and used as received without further purification. 0.1 M KOH was spiked with different amounts of iron ion stock solution to achieve concentrations of 0, 3, 6 and 14 ppm. To prepare the stock solution of 10,000 ppm iron ions, approximately 500 mg of $FeSO_4 \cdot x\ H_2O$ (Sigma-Aldrich, 99.999 %) was dissolved in 400 µL of concentrated HNO_3 (Carl Roth, ROTIPURAN® Supra 69 %) using ultrasonication bath for 5 minutes. Once $FeSO_4$ was fully dissolved, highly purified water was gradually added with intermittent

ultrasonication bath treatment until a final volume of 50 mL was reached. Since the Fe^{2+} cations are immediatly oxidized to Fe^{3+} inside the stock solution, we hereafter referred to as Fe^{z+} species. To determine the actual Fe^{z+} concentration, the stock solution was diluted and measured by inductively coupled plasma – optical emission spectrometry (ICP-OES, Agilent 5100). External calibration with standard solutions at 100, 150, 200 and 250 ppb, prepared from the Roti®Star multi-element ICP standard solution (Carl Roth; 28 elements in 5% HNO_3, 1 ppm each) was used.

4.5.3 RDE setup and electrochemical protocol

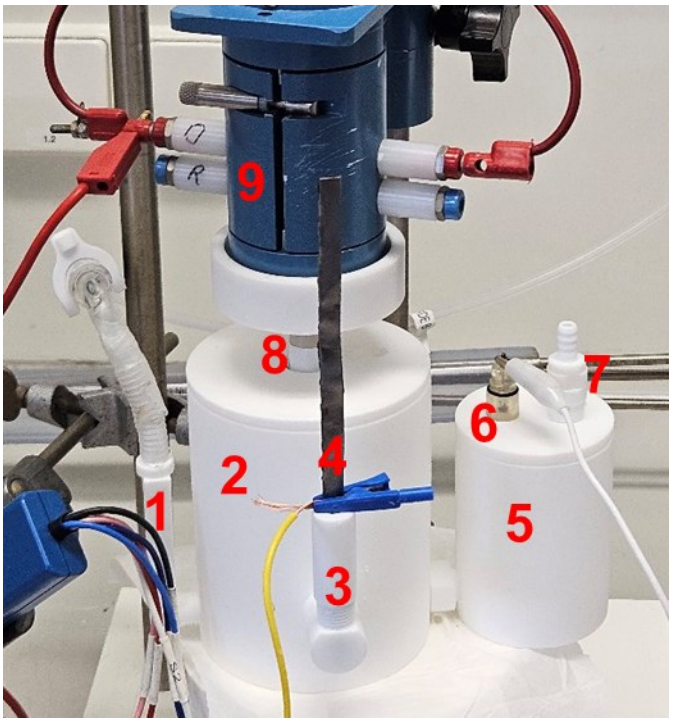

Figure 24: *Custom-made three-compartement Teflon cell with 1) gas saturator for WE chamber 2) working electrode chamber, 3) counter electrode chamber, 4) graphite counter electrode, 5) reference electrode chamber, 6) reference electrode (MMO), 7) gas saturator for RE chamber, 8) working electrode shaft, 9) MSR rotator.*

Rotating disk electrode (RDE) experiments were performed in a self-designed electrochemical Teflon cell by using a rotator (MSR Rotator, Pine Research Instrumentation, (9) in **Figure 24**) and a potentiostat (Biologic, VSP300). The Teflon cell has three compartments for each the WE, CE and RE ((2), (3) and (5) in **Figure 24**). A three-electrode arrangement consisted of a poly-Ni disk as a working electrode ((8) in **Figure 24**), graphite foil (Alfa Aesar, 99.8 %) as a counter electrode ((4) in

Figure 24) and mercury-mercury oxide (MMO) as a reference electrode ((6) in **Figure 24**), respectively. The electrolyte was saturated with argon gas (Westfalen Gas, purity of 99.999 %) for 30 minutes through the electrolyte solution using the gas saturator ((1) and (7) in **Figure 24**) . The polished poly-Ni remained in the electrolyte during the entire protocol for ca. 25 h at 2400 rpm (rotations per minute) with Ar bubbling through the electrolyte and was not removed between any step. The electrochemical protocol is illustrated in

Figure 25. First, the poly-Ni disk electrodes were electrochemically surface-stabilized with $Ni(OH)_2$ through a preconditioning step involving six cycles of cyclic voltammetry (CV) between -0.4 and 1.6 V vs. RHE at a scan rate of 100 mV s^{-1}. Five runs of linear sweep voltammograms (LSV) were then recorded to measure the initial HER polarization behavior from -0.4 to 0 V vs. RHE at 10 mV s^{-1}. Subsequently, potentiostatic electrochemical impedance spectroscopy (PEIS) was performed at -0.29 V vs. RHE using 10 mV amplitude in a frequency range of 200 kHz to 100 mHz. After determining the initial HER activity, galvanostatic accelerated stress test (AST) at a current density of $-10\ mA\ cm_{geo}^{-2}$ was carried out for 24 hours. During this 24 h period, galvanostatic electrochemical impedance spectroscopy (GEIS) was measured every hour at the same current density, using an amplitude of 100 µA and a frequency range from 50 kHz to 1.5 Hz. Afterwards, the HER activity was evaluated using the same conditions as for the initial LSV and PEIS (see above). Finally, CV measurements were employed to investigate the electrochemically active surface area of the treated poly-Ni disk electrodes. Unless stated otherwise, all potentials reported in this study were converted to the reversible hydrogen electrode (RHE) scale and corrected by the iR-drop.

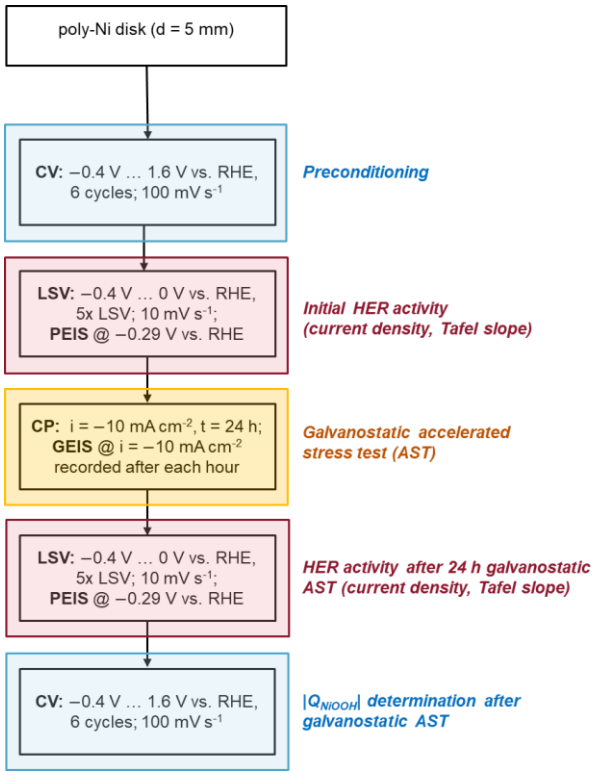

Figure 25: *Electrochemical protocol including various steps for preconditioning, establishing the initial HER activity, a galvanostatic accelerated stress test (AST) and* $|Q_{NiOOH}|$ *determination. All measurements were performed in Ar-saturated: 0.1 M KOH solution spiked with 0, 3, 6 and 14 ppm* Fe^{z+} *species.*

4.5.4 Structural Characterization

Poly-Ni disks were examined using a Helios G4 CX scanning electron microscopy (SEM) (FEI Deutschland GmbH, Germany) after 1 h and 24 h galvanostatic AST measurements. The micrographs were recorded at 100,000x magnification, with 20 kV accelerating voltage, 4 mm working distance and 0.40 nA beam current in a secondary electron contrast mode. M4 Tornado plus micro-X-ray fluorescence (µ−XRF) spectrometer (Bruker) equipped with a rhodium X-ray source operated at 50 kV and 300 µA and two silico drift detectors (SDD type: 660 PAR -LE) was employed to evaluate the thickness of Fe deposits on poly-Ni disk after 24 h galvanostatic AST. Measurements were performed with a spot size of 20 µm, pixel size of 0.01 mm^2 , acquisition time of 500 ms per pixel and <2 mbar vacuum. Analysis was performed using Bruker Software M4 TORNADO (version 1.6.621.0).

5 Results and Discussion

5.1 A Universal Analytical Model for the Limiting Current Characteristics in Impinging Jet Electrodes

This chapter is reprinted in adapted form from the original article: Schneemann C., Traegner J., Mindermann L., Friedrichs-Schucht M., Tang B., Dietzel A., Oezaslan M., A Universal Analytical Model for the Limiting Current Characteristics in Impinging Jet Electrodes. Journal of The Electrochemical Society 2025;172(6):66503. [193]. License: Creative Commons License (CC-BY-NC-ND 4.0). Copyright: The Authors.

Contributions:

- *C. Schneemann had the original project idea, led the study, carried out the literature research, developed and validated the impinging jet flow cell setup, co-developed the methodology for CFD simulations, carried out the electrochemical experiments, validated the theoretical framework of the universal analytical model numerically and experimentally, curated the data, analyzed the data, visualized the data, discussed the data within the project team, wrote and edited the original draft.*
- *J. Traegner setup and carried out the CFD simulations, analyzed CFD simulations, curated and summarized data, discussed the data within the project team and reviewed and edited the original draft. J. Traegner contributed significantly to the development of the universal analytical equation system by proposing the use of cross sections of the local current densities.*
- *Both C. Schneemann and J. Traegner developed the universal analytical equation system, building on the original conceptual idea introduced by C. Schneemann.*
- *L. Mindermann setup and performed CFD simulations and discussed data within the project team.*
- *J. Koehler reviewed and commented on the original draft.*
- *B. Tang and A. Dietzel assisted in 3D-printing the electrochemical flow cell and discussed questions about the fluidic system with C. Schneemann.*
- *M. Oezaslan supervised the work, discussed research data within the project team and reviewed and edited the original draft.*

Preface:

Computational fluid dynamics (CFD) simulations are usually required to accurately predict mass transport rates and limiting currents in impinging jet flow cells, because analytical solutions are only available for specific cases. In this chapter, a universal analytical model for the mass transport processes in impinging jet electrodes is presented, which is derived from the mathematical superimposition of three established equations from the literature. This universal model contains four logical cases depending on the input parameters of the cell geometry, volume flow rate and reaction. A direct comparison with numerical and experimental data for the oxidation of ferro(II)cyanide shows excellent agreement with average relative errors of below 10 %. Altogether, this universal analytical model is able to replace time- and resource-intensive CFD simulations to predict experimental results obtained from the impinging jet electrodes in the future.

5.1.1 Theory of the Universal Analytical Model

In order to express a universal approximation model for the limiting current for a broad variety of geometries in electrochemical impinging jet flow cells a new approach was developed. The existing equations from literature valid only within certain geometry parameter restrictions (presented in chapter 2.5.3.2) are mathematically superimposed. In a first step, the local limiting current densities $i_{lim,loc}$ of the above shown equations (**Table 4**) were calculated by deriving with respect to the electrode area A and by introducing the local radius R_{loc}, as follows:

$$i_{lim,loc}^{WT} = \frac{\mathrm{d}I_{lim,0}^{WT}}{\mathrm{d}A} = 0.9591\, n\, F\, c_\infty \sqrt{a^*}\, d^{-\frac{3}{2}}\, \dot{V}_0^{\frac{1}{2}}\, \nu^{-\frac{1}{6}}\, D^{\frac{2}{3}}\, f\left(\frac{H}{d}\right)\, g(Sc) \tag{50}$$

$$i_{lim,loc}^{WJ} = \frac{\mathrm{d}I_{lim,0}^{WJ}}{\mathrm{d}A} = 1.60\, k\, n\, F\, c_\infty\, d^{-\frac{1}{2}}\, D^{\frac{2}{3}}\, \nu^{-\frac{5}{12}}\, \dot{V}_0^{\frac{3}{4}}\, \frac{3}{8\pi}\, R_{loc}^{-\frac{5}{4}} \tag{51}$$

$$i_{lim,loc}^{RF} = \frac{\mathrm{d}I_{lim,0}^{RF}}{\mathrm{d}A} = 3.15\, n\, F\, c_\infty\, \dot{V}_0^{\frac{1}{3}}\, H^{-\frac{2}{3}}\, D^{\frac{2}{3}}\, \frac{2}{3\pi}\, R_{loc}^{-\frac{2}{3}} \tag{52}$$

Based on the local limiting current densities $i_{lim,loc}$, the three flow regions can be integrated in the form of circular annulus within the limits of R_A, R_B and R_C:

$$\begin{aligned} I_{lim}^{WT} &= \int_0^{R_A}\int_0^{2\pi} i_{lim,loc}^{WT} \cdot R_{loc}\, d\phi dR \\ &= 0.9591\, n\, F\, c_\infty\, (a^*)^{\frac{1}{2}}\, d^{-\frac{3}{2}}\, \dot{V}_0^{\frac{1}{2}}\, \nu^{-\frac{1}{6}}\, D^{\frac{2}{3}}\, f\left(\frac{H}{d}\right)\, g(\mathrm{Sc})\, \pi\, R_A^2 \end{aligned} \tag{53}$$

$$I_{lim}^{WJ} = \int_{R_A}^{R_B}\int_0^{2\pi} i_{lim,loc}^{WJ} \cdot R_{loc}\, d\phi dR = 1.60\, k\, n\, F\, c_\infty\, d^{-\frac{1}{2}}\, D^{\frac{2}{3}}\, \nu^{-\frac{5}{12}}\, \dot{V}_0^{\frac{3}{4}} \left(R_B^{\frac{3}{4}} - R_A^{\frac{3}{4}}\right) \tag{54}$$

$$I_{lim}^{RF} = \int_{R_B}^{R_C}\int_0^{2\pi} i_{lim,loc}^{RF} \cdot R_{loc}\, d\phi dR = 3.15\, n\, F\, c_\infty\, \dot{V}_0^{\frac{1}{3}}\, H^{-\frac{2}{3}}\, D^{\frac{2}{3}} \left(R_C^{\frac{4}{3}} - R_B^{\frac{4}{3}}\right) \tag{55}$$

where R_A and R_B are the transition radii between the flow regions, R_C is the electrode radius, ϕ is the polar angle, a^* is the hydrodynamic constant with an empirical value of

$(a^*)^{0.5} = 1.77642879$ [201] and $f\left(\frac{H}{d}\right)$ is an empirical term with $f\left(\frac{H}{d}\right) = \left(\frac{H}{d}\right)^{-0.054}$ [201], respectively. The sum of the current contributions of each of the flow regions results in the total limiting current I_{lim}:

$$I_{lim} = I_{lim}^{WT} + I_{lim}^{WJ} + I_{lim}^{RF} \tag{56}$$

However, knowledge of the transition radii R_A and R_B is required to determine I_{lim} and therefore a flow chart was created as a guideline in **Figure 26**.

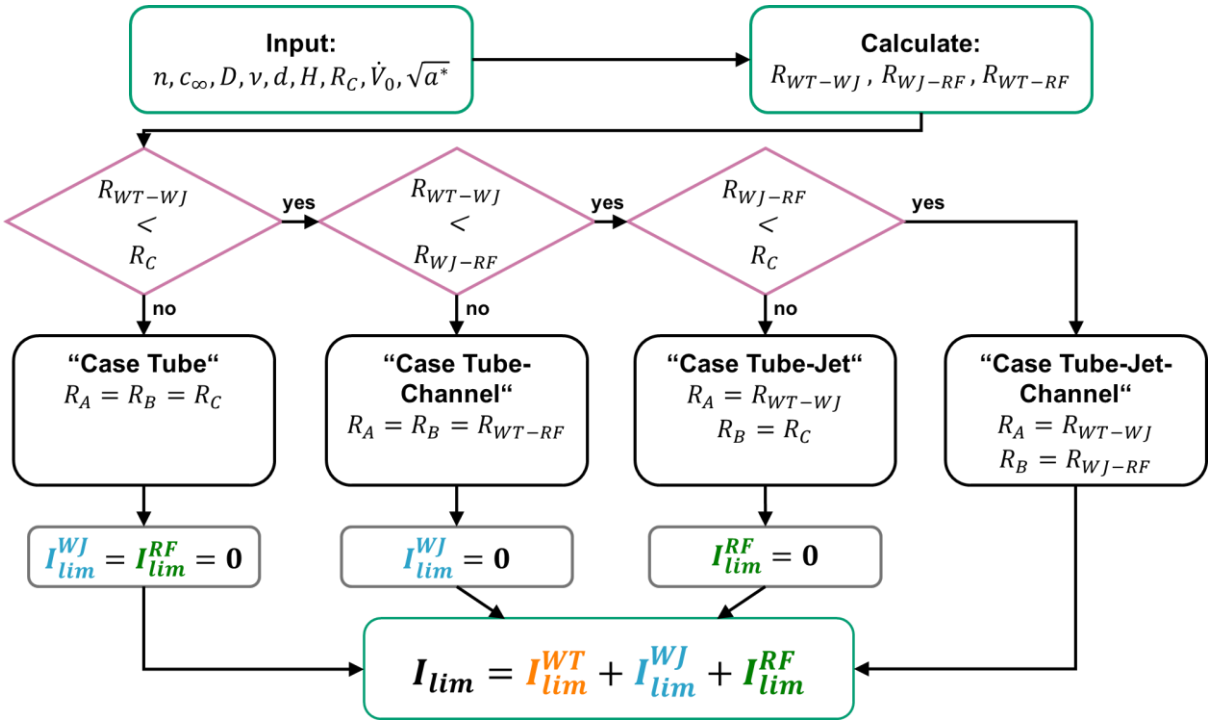

Figure 26: *Flowchart for the determination of the transition radii R_A and R_B and the resulting total limiting current I_{lim} using the equations (53) – (59). Four different cases for the transition radii can be found depending on the input parameters such as volume flow rate, electrode radius, etc.*

First, the known input parameters from the geometry and electrolyte, i.e. $n, c_\infty, D, \nu, d, H, R_C, \dot{V}_0$ and $\sqrt{a^*}$ are inserted in equations (57) to (59) to estimate the intersections of the equations (50), (51) and (52) R_{WT-WJ}, R_{WJ-RF} and R_{WT-RF}, respectively:

$$R_{WT-WJ} = \left(\frac{0.9591}{1.60} \cdot \frac{8}{3}\pi \cdot \frac{\sqrt{a^*}}{k}\right)^{-\frac{4}{5}} d^{\frac{4}{5}} \dot{V}_0^{\frac{1}{5}} \nu^{-\frac{1}{5}} g(Sc)^{-\frac{4}{5}} f \left(\frac{H}{d}\right)^{-\frac{4}{5}} \quad (57)$$

$$R_{WJ-RF} = \left(\frac{1.6\,k}{3.15} \cdot \frac{9}{16}\right)^{\frac{12}{7}} d^{-\frac{6}{7}} \dot{V}_0^{\frac{5}{7}} H^{\frac{8}{7}} \nu^{-\frac{5}{7}} \quad (58)$$

$$R_{WT-RF} = \left(\frac{0.9591}{3.15} \cdot \frac{3}{2}\pi \cdot \sqrt{a^*}\right)^{-\frac{3}{2}} d^{\frac{9}{4}} \dot{V}_0^{-\frac{1}{4}} \nu^{\frac{1}{4}} H^{-1} g(Sc)^{-\frac{3}{2}} f \left(\frac{H}{d}\right)^{-\frac{3}{2}} \quad (59)$$

The comparison of the calculated values from the equations (57), (58) and (59) gives four distinct cases (see **Figure 26**), which depend on the input parameters and will now be discussed.

The so-called “Case Tube” (with $R_{WT-WJ} > R_C$) results in $I_{lim}^{WJ} = I_{lim}^{RF} = 0$ and the equation (56) reduces to the wall-tube (WT) electrode equation[8]. This case can apply for geometries with very small electrode radius R_C in relation to the inlet diameter d. The “Case Tube-Channel” ($R_{WT-WJ} < R_C \; and \; R_{WT-WJ} > R_{WJ-RF}$) indicates the absence of the wall-jet (WJ) region with $I_{lim}^{WJ} = 0$ and is obtained at very small volume flow rates, where the jet (light blue rectangle in **Figure 18**) is not yet fully formed. For the “Case Tube-Jet” ($R_{WT-WJ} < R_C \; and \; R_{WT-WJ} < R_{WJ-RF} > R_C$) there is no radial channel-flow (RF) region, due to the small electrode radius R_c. In contrast to “Case Tube”, the electrode radius R_C is sufficiently large to encompass both the wall-tube and the wall-jet flow regions. Finally, the “Case Tube-Jet-Channel” ($R_{WT-WJ} < R_{WJ-RF} < R_C$) covers the parameter range, where all three flow regions (wall-tube, wall-jet and radial channel-flow region) coexist. To validate this universal analytical model, the calculated values are compared to numerical CFD simulations as well as experimental data including examples for each of the four “cases” in the following sections.

5.1.2 Results and Discussion

5.1.2.1 Numerical Validation of the Universal Analytical Model – Theoretical Cases and their Transition Radii R_n

The aim of this study is to provide a universal analytical model for the limiting current I_{lim} characteristics in impinging jet electrodes and validate it through both numerical and experimental approaches. The oxidation of ferrocyanide(II) to ferricyanide(III) as a simple one-electron transfer model reaction was used:

$$[Fe(CN)_6]^{4-} \rightleftharpoons [Fe(CN)_6]^{3-} + e^- \quad (60)$$

First, the universal analytical model is validated with the computational fluid dynamics (CFD) calculations using the working electrode radii of $R_C = 0.5\,,1$ and $3.63\,\mathrm{mm}$ together with the experimental parameters from **Table 5** and **Table S1**. It is noted that for the working electrode with $R_C = 3.63\,mm$, which is larger than the outlet radius of the electrolyte flow, a dead zone in the O-ring groove between $2.81\,mm \leq R_{loc} \leq 3.63\,mm$ was considered, see (6) in **Figure 19**. In this region, the local current density was presumed to be $i_{loc} = 0$ to make the theoretical conditions more comparable to the experimental. It is noted, that only a radial outlet far away from the jet center was assumed in both the analytical model and the CFD simulations. Later the effect of the four symmetrically arranged outlets in the experimental cell on the relative errors between experiment and theory will be discussed.

Figure 27 displays the dynamic changes of the different “cases” in dependence of the volume flow rate $\dot{V}_0$ using a selected flow cell geometry ($d = 0.75\,mm;\ H = 0.7\,mm;\ R_C = 2.81\,mm$). The chosen volume flow range covers three of the four “cases” discussed in **Figure 26**. Only the “Case Tube” is excluded due to the large electrode size in relation to the inlet-nozzle diameter d.

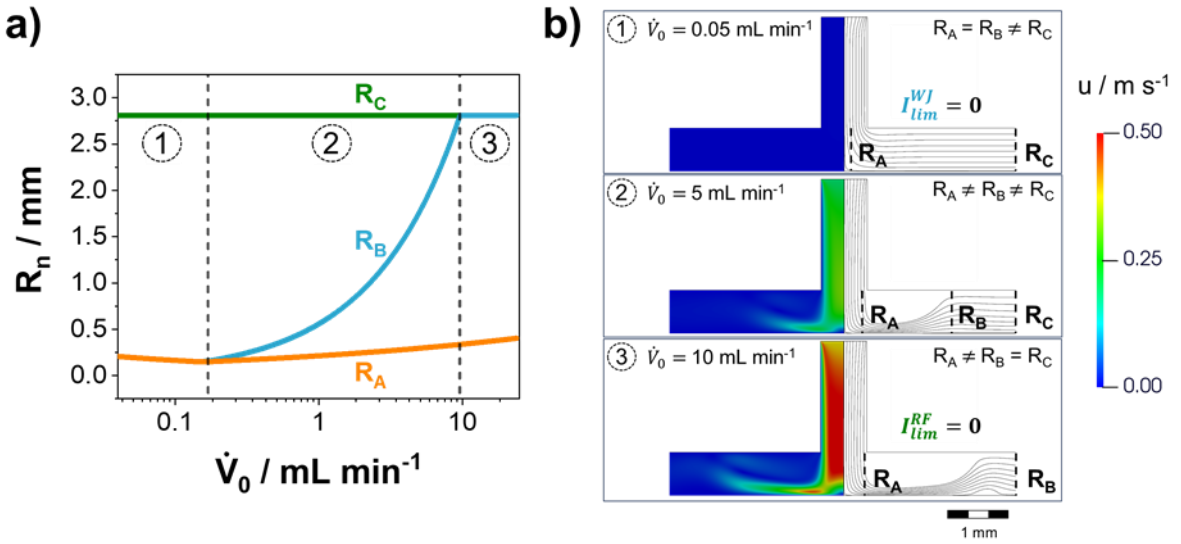

Figure 27: *Dynamic changes of the "cases" (**Figure 26**) with the volume flow rate $\dot{V}_0$ for one selected flow cell geometry ($d = 0.75\,mm$; $H = 0.7\,mm$; $R_C = 2.81\,mm$).* ***a)*** *Course of the transition radii R_A and R_B and the electrode radius R_C as a function of volume flow rate $\dot{V}_0$. The volume flow regions of the "cases" are separated by the dashed lines: (1) "Case Tube-Channel": $R_A = R_B = R_{WT-RF}$, (2) "Case Tube-Jet-Channel": $R_A = R_{WT-WJ}$ and $R_B = R_{WJ-RF}$, (3) "Case Tube-Jet": $R_A = R_{WT-WJ}$ and $R_B = R_C$.* ***b)*** *Comparison of the transition radii R_A and R_B calculated by the analytical model with velocity profiles and streamlines obtained from CFD simulations for selected "case" examples from the regions highlighted in **a)**.*

Figure 27a illustrates the course of the calculated transition radii R_A and R_B as a function of the volume flow rate $\dot{V}_0$. The volume flow rate regions of the "cases" from **Figure 26** are highlighted, namely "Case Tube-Channel" (1), "Case Tube-Jet-Channel" (2) and "Case Tube-Jet" (3). In region (1) at low volume flows ($\dot{V}_0 \leq 0.17\,mL\,min^{-1}$), the values for R_A (orange line) and R_B (light blue line) overlap. When both transition radii are equal ($R_A = R_B$) it corresponds to "Case Tube-Channel" in **Figure 26**, and the model predicts $I_{lim}^{WJ} = 0$. The volume flow rate is too slow for the formation of a wall-jet, and the electrode surface is then dominated by the radial channel-flow (RF) region. This is in agreement with the work from *Dalhuijsen et al.* proposing a mathematic solution for the radial channel-flow region in this volume flow range [223]. **Figure 27b-1** (top panel) illustrates one example of the "Case Tube-Channel" (at $\dot{V}_0 = 0.05\,mL\,min^{-1}$ in region (1), **Figure 27a**) as comparison between CFD simulations and our analytical model including the calculated radii for R_A and R_B. The streamlines and velocity profiles derived from CFD simulations clearly show the laminar radial channel-

flow region and the absence of a wall-jet, confirming the predictions of our model and from the literature [223]. The flow region transition points obtained from the CFD simulations are in very good agreement with the calculated radii R_A and R_B derived from our model.

In region (2) of **Figure 27a** ($0.17\ mL\ min^{-1} \leq \dot{V}_0 \leq 9.65\ mL\ min^{-1}$), the transition radius R_B enlarges. This is due to the expansion of the wall-jet region with higher volume flow and is a phenomenon observed in CFD simulations as well [179]. Hence, the flow cell geometry reflects "Case Tube-Jet-Channel", where all three flow regions – wall-tube, wall-jet and radial channel-flow – coexist. To underline this, an example of a CFD simulation with a volume flow $\dot{V}_0 = 5\ mL\ min^{-1}$ (**Figure 27b-2**, middle panel) corroborates the presence of all three flow regions under these conditions. In other words, from the center outwards, it commences with wall-tube region followed by wall-jet region and finally radial channel-flow region. A good match between the calculated transition radii R_A and R_B with the CFD streamlines is observed.

Another aspect of **Figure 27a** that needs to be discussed is the behaviour of the transition radius R_A (orange line), as it increases with volume flow of $\dot{V}_0 \geq 0.17\ mL\ min^{-1}$. For the construction of wall-tube electrodes the question arises how large the electrode size can be to only involve their uniform flow region. The calculated values for R_A in relation to the volume flow rate are compared with the critical maximum radii of wall-tube electrodes discussed in literature so far in **Figure S2**. According to our model's predictions, the maximum wall-tube electrode radius can apply to the range of $R_A = 0.3d$ [209] and $R_A = 0.5d$ [201] depending on the volume flow rate $\dot{V}_0$. Thus, our analytical model provides a more dynamic prediction of the maximum transition radii R_A for wall-tube electrode construction than the static values from the literature [201,209].

Finally, in the region (3) of **Figure 27a** at higher volume flows ($\dot{V}_0 \geq 9.65\ mL\ min^{-1}$), our universal analytical model predicts that R_B is equal to R_C ($R_B = R_C$) and leads to $I_{lim}^{RF} = 0$. At high volume flow, the impinging jet then covers the entire electrode and prevents the formation of the radial channel-flow (RF) region, representing "Case Tube-Jet" of the model (**Figure 26**). **Figure 27b-3** (bottom panel) shows one example from this volume flow range ($\dot{V}_0 = 10\ mL\ min^{-1}$), where the impinging jet characteristics are clearly visible and more pronounced compared to **Figure 27b-2**

(middle panel). The CFD streamlines indicate a laminar boundary layer separation and corresponding recirculation zone forming further outside on the centric electrode, which has also been reported in the literature [179,206,209,224,225]. These complex flow patterns cannot be covered by our analytical model, as it is based on the superposition of rigorously solved equations from literature and therefore represent a limitation of this model.

To summarize, the dynamic transition between the “cases” (**Figure 26**) as well as the changes of the transition radii R_A and R_B with the volume flow rate can be fully described by our so-called universal analytical model and is in very good agreement with results from the CFD simulations.

5.1.2.2 Numerical Validation of the Universal Analytical Model – Local Limiting Current Density

In the next step, the local current density functions $i_{loc} = \frac{dI_{lim}}{dA}$ derived from the universal analytical model will be compared with CFD simulations. It is noted that the resulting i_{loc} functions from both approaches need to match across the entire electrode area. This assumes that not only the total limiting current density i_{lim} is predicted well, but also the non-uniform distribution of current.
As an example, **Figure 28a** illustrates a local current density function $i_{lim,loc}$ plotted against the local radius R_{loc} for one geometry within “Case Tube-Jet-Channel” (all three flow regions exist) calculated based upon the equations from literature (equations (50) to (52)), the CFD simulations and the analytical model, respectively. First, the local current density functions from the established wall-jet and radial channel-flow equations (equations (51) and (52)), denoted as light blue and green dashed lines in **Figure 28a**, were represented. As expected, these well-known equations predict an infinite local current density characteristic near the center of the jet ($R_{loc} = 0$). This is due to the analytical assumptions in these equations, including an infinite jet velocity and an infinitesimal small jet radius at the center [215,220,223]. In addition, the local current density function of the wall-tube electrode (equation (50)), where a uniform diffusion layer thickness is assumed, is illustrated in orange dashed line, **Figure 28a**. Here the local current density remains constant with respect to the local radius R_{loc}.

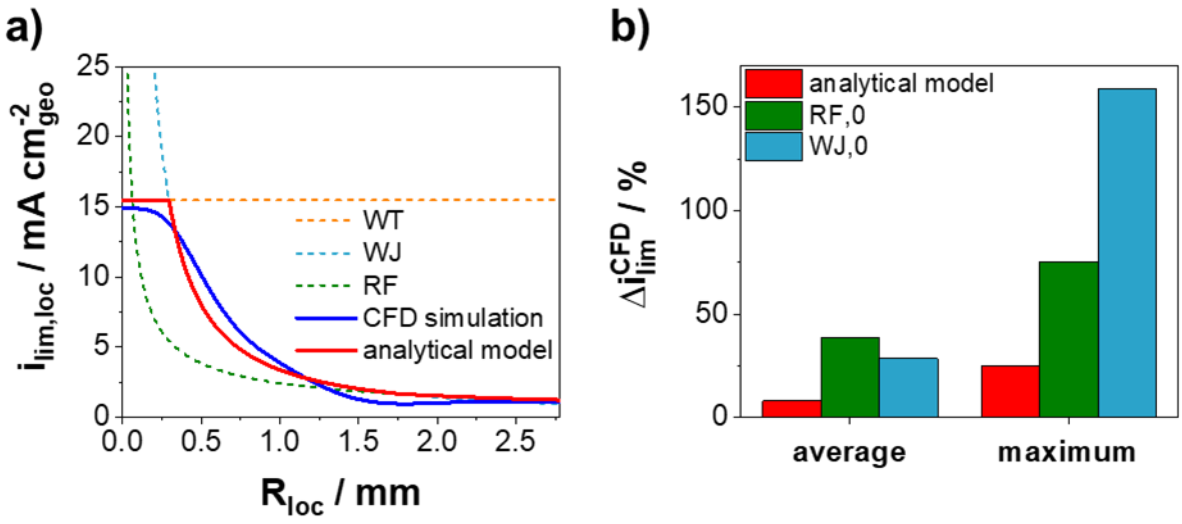

Figure 28: a) *Local limiting current density $i_{lim,loc}$ characteristics as a function of the local radius R_{loc} calculated by the equations from the literature (equations (50), (51) and (52)), CFD simulations and the analytical model for one example geometry of „Case Tube-Jet-Channel“ ($R_A = R_{WT-WJ}$ and $R_B = R_{WJ-RF}$). Parameters: $d = 0.75\ mm$; $H = 0.7\ mm$; $\dot{V}_0 = 5\ mL\ min^{-1}$; $R_C = 2.81\ mm$.* ***b)*** *Statistical comparison of the relative error of the total limiting current density from the CFD results Δi_{lim}^{CFD} for all $N = 350$ simulations. Red, light blue and green bars are denoted for the analytical model, the established equation for the wall-jet electrode (WJ,0) and the established equation for the radial channel-flow electrode (RF,0), see* ***Table 4****, respectively.*

Apart from the well-established equations from the literature, the CFD simulations were carried out for this specific geometry and volume flow rate. The resulting local current density function is denoted by blue solid line in **Figure 28a**. It is observed that a region of approximately constant local current density appears in the center of the electrode ($R_{loc} \leq 0.2\ mm$), while with increasing distance to the center ($R_{loc} > 0.2\ mm$) the local current density exponentially decreases. Obviously, this result from the CFD simulations cannot be described by a single local current density function (equations (50) to (52), see orange, light blue or green dashed lines). Only our universal analytical model (red solid line, **Figure 28a**), which is based on the superimposition of the local current density functions from the literature, is able to achieve the best agreement with the CFD simulations.

Despite the good agreement, deviations of our analytical model from the CFD simulation results are noticeable. More precisely, larger discrepancies between the universal analytical model and CFD simulations are obtained for small local radii ($0 \leq R_{loc} \leq 2.4\,mm$) compared to large radii ($R_{loc} > 2.4\,mm$). A possible explanation is based on conditions with and without jet confinement. The flow cell geometry with $H = 0.7\,mm$ imposes a distinct confinement on the jet. However, a jet confinement is not considered in the wall-tube and wall-jet equations from the literature (equations (50) and (51)) and thus also not in our universal analytical model in these flow regions. On the other hand, the radial channel-flow region is accurately predicted by the universal analytical model, as the rigorous analytical solution for this electrode type includes a confinement. Thereby, the precision of this model is higher for larger electrode radii R_C.

Further “case” examples of the local current density functions in comparison with those derived from the CFD simulations and the local current density functions from the literature are depicted in **Figure S3**. **Figure S3a** displays the local current density functions of the analytical model for the “Case Tube-Channel”. A good overlap of local current densities obtained from the analytical model and CFD simulations is observed overall, because the electrode consists mostly of the radial channel-flow region and this region has the highest precision, as described before. Only near the electrode center in the wall-tube region, both approaches differ from each other, which can be very likely explained by the jet confinement. In addition, our universal analytical model also struggles to predict complex flow patterns like the laminar boundary layer separation at high volume flows. This fact is illustrated for “Case Tube-Jet” example of the analytical model in **Figure S3b**. The laminar boundary layer separation leads to a significant deviation of the universal analytical model from the CFD simulations in the electrode area of $R_{loc} \approx 2.1\,mm$.

Overall, our universal analytical model gives a good approximation to the local current density functions obtained from the CFD simulations. The individual equations themselves reported from the literature (equations (50)-(52)) are insufficient for this purpose. In this study, two limitations of the use of our analytical model could be

identified: (i) small local radii R_{loc} or small electrode sizes R_C, likely due to the confinement of the jet, and: (ii) the prediction of complex flow patterns such as the laminar boundary layer separation, which occur at high volume flow rates $\dot{V}_0$.

5.1.2.3 Numerical Validation of the Universal Analytical Model – Total Limiting Current Densities

The next step is the determination of the total limiting current densities i_{lim} and their deviation using both approaches, CFD simulations and universal analytical model. The relative error of the total limiting current densities Δi_{lim}^{CFD} predicted by the universal analytical model and the established equations for the radial channel-flow (RF,0) and wall-jet (WJ,0) electrodes was calculated for all 350 CFD simulations (see **Table 5**) as follows:

$$\Delta i_{lim}^{CFD} = \left| \frac{i_{lim} - i_{lim}^{CFD}}{i_{lim}^{CFD}} \right| \tag{61}$$

Here, i_{lim} is the total limiting current density calculated by the analytical model (equation (56)) or by the radial channel-flow (RF,0) and wall-jet (WJ,0) equations (see **Table 4**), respectively. i_{lim}^{CFD} is the total limiting current density obtained from the CFD simulations.

Figure 28b shows the average relative error and the maximum relative error of the total limiting current density i_{lim} established by the analytical model (in red) and the individual equations for the radial channel-flow (RF,0; green) and wall-jet (WJ,0; light blue) from the literature. It is seen that the average relative error of our universal analytical model with $\Delta i_{lim}^{CFD} = 7.8\,\%$ is much lower compared to the established equations for RF and WJ electrodes. Our model exhibits a maximum relative error of 24.7%, which is significantly lower than the maximum errors of 57% and 159% associated with the radial channel-flow equation and the wall-jet equation (see **Table 4**), respectively. For our analytical model, large deviations from CFD simulations are observed at high volume flow parameter sets due to the evolution of recirculation flow patterns (see the local current density data in **Figure S3b**) and by the use of small electrode radii ($R_C \leq 1\,mm$) due to the confinement of the impinging jet in this area.

A further possible cause of the observed deviations could be the hydrodynamic constant a^*, because the wall-tube flow region (I_{lim}^{WT}) becomes a dominant term in equation (56) for small electrode sizes. In equation (53), $\sqrt{\mathrm{a}^*} = 1.77642879$ and for the empirical term $f\left(\frac{H}{d}\right) = \left(\frac{H}{d}\right)^{-0.054}$ was used, both experimentally determined by *Chin et al.* [201]. However, other values for these terms have also been reported in numerical or theoretical works [209,211,212]. Based on the comparison between our analytical model and CFD simulations, additional effort was put into determining the limiting current densities with the theoretical value for a^* [213]. **Figure S4a-c** displays the local current density functions of the analytical model with an improved approximation to the CFD simulations in the wall-tube flow region near the jet center, compared to the ones in **Figure 28a** and **Figure S3**. As the average relative error remains almost unchanged with $\Delta i_{lim}^{CFD} = 7.8\,\%$ **Figure S4d**), it is concluded that the impact of a^* on the overall statistics is minimal. In contrast, for small electrode sizes the maximum relative error of the analytical model could reduce from 24.7% to 18.4%. Based on these results, for the remainder of this thesis it was decided to further apply the hydrodynamic constant $\sqrt{\mathrm{a}^*} = 1.77642879$ determined experimentally by *Chin et al.* [201].

In summary, the universal analytical model offers a very good approximation to the numerical calculations over all $N = 350$ CFD simulations. The individual equations known from literature show larger average relative errors and larger maximum relative errors compared to our model. Despite the excellent approximation to the CFD results, it was shown that the limitations in the model are at high volume flows or very small electrode sizes ($R_c \leq 1\,mm$).

5.1.2.4 Experimental Validation of the Universal Analytical Model

To evaluate how accurately our universal analytical equation predicts or matches the experimental data, a one-electron-transfer model system was chosen, specifically the oxidation of ferrocyanide(II) in argon-saturated 0.5 M K_2SO_4. **Figure 29** shows the volume flow rate-dependent linear sweep voltammograms obtained from the glassy carbon working electrode with a radius $R_C = 3.63\,mm$ for 10 mM $[Fe(CN)_6]^{4-}$ / 10 mM $[Fe(CN)_6]^{3-}$ in 0.5 M K_2SO_4. The flow rates varied between 0.25 and 2.00 mL min^{-1}. Using our 3D-printed flow cell setup, well-defined limiting current density plateaus are clearly observed for both the reduction of ferricyanide(III) (between –0.65 and –0.50 V vs. $Hg|HgSO_4|K_2SO_{4,sat.}$) and the oxidation of ferrocyanide(II) (between 0 and 0.30 V vs. $Hg|HgSO_4|K_2SO_{4,sat.}$). Generally, the limiting current density increases with higher volume flow rate. Small changes or instability in volume flow might be noticeable in the limiting current density behavior.

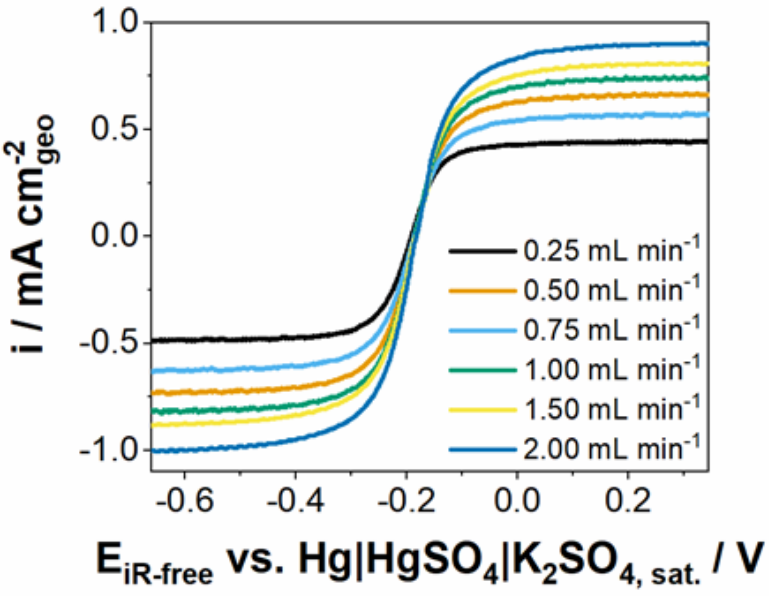

Figure 29: *Linear sweep voltammograms for 10 mM $[Fe(CN)_6]^{4-}$/ 10 mM $[Fe(CN)_6]^{3-}$ in Ar-saturated 0.5 M K_2SO_4. All measurements were recorded on a glassy carbon electrode with a scan rate of 1 mV s^{-1} at various volume flow rates. Parameters of the flow cell setup:* $d = 0.5\,mm;\ H = 0.7\,mm;\ R_C = 3.63\,mm.$

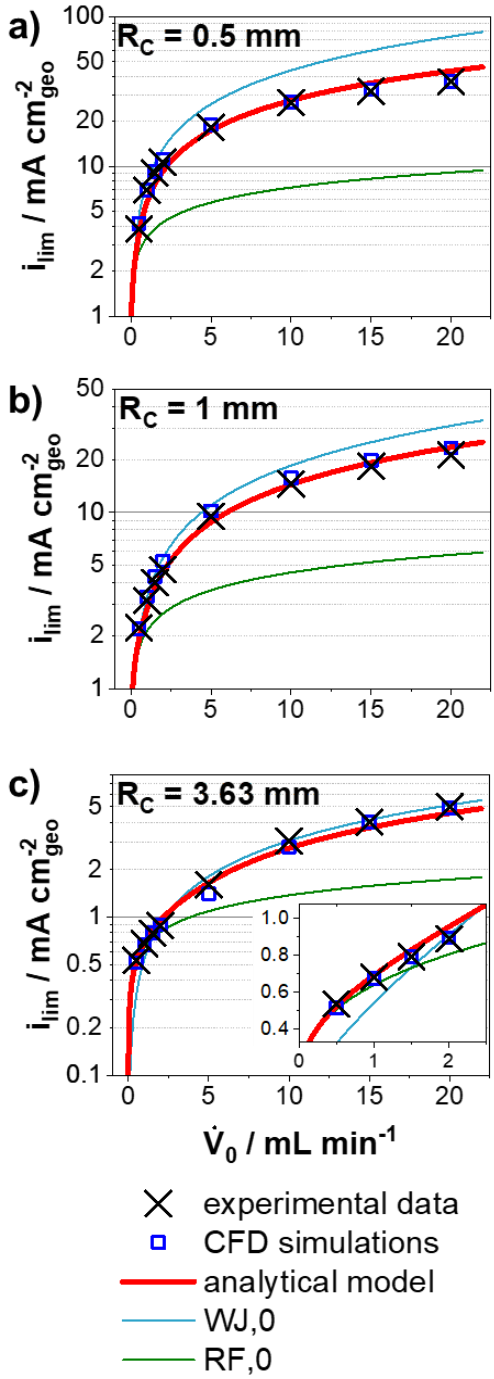

Figure 30: *Dependence of the limiting current densities i_{lim} on the volume flow rate for three electrode radii: a) R_C = 0.5 mm, b) R_C = 1 mm and c) R_C = 3.63 mm. The limiting current densities were experimentally measured for the oxidation of ferrocyanide(II) in 0.5 M K_2SO_4 and denoted as black cross symbol. The results of the limiting current densities from the CFD simulations (blue square symbol), analytical model (red solid line) and established equations for wall-jet (light blue solid line) and radial channel-flow (green solid line) electrodes are shown as direct comparison to the experimental data, respectively. The inset in c) points out the low volume flow range for R_C. Parameters of the flow cell setup: $d = 0.5\ mm, H = 0.7\ mm$.*

Furthermore, the limiting current densities for the oxidation of ferrocyanide(II) on three different glassy carbon working electrode radii (0.5, 1 and 3.63 mm) as a function of the volume flow rate were experimentally measured using chronoamperometry method. **Figure 30** displays the limiting current densities i_{lim} as a function of the volume flow rate and electrode radius R_C. Similar to **Figure 29**, we observe that the limiting current density increases with higher volume flow rate. More interesting is the direct comparison of the experimental i_{lim} data (black cross symbol) with the calculated i_{lim} obtained from the analytical model (red solid line), CFD simulations (blue square), as well as the two equations for the wall-jet (light blue solid line) and radial channel-flow (green solid line) electrodes.

First, the CFD simulations are able to predict the experimental i_{lim} data for all three electrode radii very well. The wall-jet equation (light blue solid line, **Figure 30**) typically overestimates the limiting current densities, while a tendency towards underestimation can be seen using the radial channel-flow equation (green solid line, **Figure 30**). This observation is more pronounced in a volume flow range from 5 to $20\ mL\ min^{-1}$ for the electrode radii of $R_C = 0.5\ mm$ and $R_C = 1\ mm$, as shown in **Figure 30a** and **Figure 30b**. In contrast, our universal analytical model, which combines the wall-tube, wall-jet, and radial channel-flow equations (red line in **Figure 30**), provides a much better match with both CFD and experimental data over the entire parameter range.

Another aspect to discuss is the possible practical application of confined wall-jet flow cells for measuring squared electrodes ($R_C = 3.63\ mm$) in a volume flow range between 0.5 and $2\ mL\ min^{-1}$, as demonstrated by Tschupp et al. [189]. The inset in **Figure 30c** represents such a region in the data. Evidently, a good prediction of our universal model with the CFD simulations and particularly with the experimental data for small flow rates was observed. For completion, the wall-jet equation underestimates limiting current densities at low flow rates of $0.5 \leq \dot{V}_0 \leq 1\ mL\ min^{-1}$, but agrees well at higher ($1.5 \leq \dot{V}_0 \leq 2\ mL\ min^{-1}$). The radial channel-flow equation gives the opposite trend to the experimental data, i.e. good agreement at low flow rates but poor agreement at high flow rates. Therefore, the superposition of these equations is a promising approach and results in our universal equation.

5.1.2.5 Accuracy Study of the Universal Analytical Model and CFD Simulations in Relation to the Experiments

In this section, the predictive power and accuracy of the universal analytical model and CFD simulations to the experiment is discussed in detail. Thus, the relative error of the limiting current densities Δi_{lim}^{exp} was determined and it can be expressed by:

$$\Delta i_{lim}^{exp} = \left| \frac{i_{lim} - i_{lim}^{exp}}{i_{lim}^{exp}} \right| \tag{62}$$

where i_{lim} is the limiting current density calculated by either the analytical model or CFD simulations, respectively, and i_{lim}^{exp} is the limiting current density experimentally measured.

Figure 31 shows the maximum and average relative errors calculated with the results of the i_{lim} from the universal analytical model (red bars) and CFD simulations (blue bars) related to the experimental results for three different electrode radii R_C. It is noted that for $R_C = 1\,mm$ and $R_C = 3.63\,mm$, the universal analytical model yields average relative errors of 7.5 % and 5.8 % towards the experimental data, respectively. These are comparable to the average relative errors for the CFD simulations, which refer to the experimental data. Similar trends are observed for the maximum errors with a difference of around 10 % between our model and CFD simulations. The largest average and maximum deviations of our analytical model compared to the experiment and CFD simulations are observed for the smallest electrode radius of $R_C = 0.5\,mm$ with 11.7 % and 18.2 %, see **Figure 31**.
The overall average relative error of $\Delta i_{lim}^{exp} = 8.3\,\%$ between our model and experiment for all three electrode sizes can most likely be explained by several reasons. First of all, the manufacturing tolerance of the flow cell, e.g. the position of the inlet-nozzle [207], can cause differences between the ideal theoretical and existing geometry. Additionally, experimental temperature fluctuations, which affect the electrolyte viscosity and density can cause deviations from ideal conditions. Another possible explanation is that neither the CFD simulations nor the analytical model take the electrolyte outlet in the experimental flow cell design into account (see **Figure 19c**). In this study, only a radial outlet located far from the jet center was assumed. *Fadel et al.* [210] reported that two point-symmetrically placed cylindrical outlets do not interrupt an ideal radial channel-flow, when the electrode radius has at maximum the same dimension of the inlet diameter, e.g. $R \leq d$ and the distance

between the centers of the inlet and outlet is 1.8 mm. The latter is given in our experimental cell. Therefore, it is assumed that for an inlet diameter of $d = 0.5\ mm$ an electrode with a radius of $R = 0.5\ mm$ experience nearly ideal symmetrical flow, resulting in a negligible or very small impact of the outlet on the relative error of the total limiting current densities Δi_{lim}^{exp}. When the electrode radii tested here increases to $R = 1\ mm$ and 3.63 mm, the works by *Tschupp et al.* [189] indicate that the presence of outlets can affect the symmetry of the radial channel-flow region (region 3 in **Figure 18**). Although the symmetry of the wall-jet and wall-tube regions (1 and 2 in **Figure 18**) remains unaffected [179], the influence of the outlets using larger electrode (R > d) may be a significant reason for Δi_{lim}^{exp}. According to the theoretical assumption of a radial outlet located far from the center, it is suggested for future work to increase the distance of the centers of the inlet and outlet, resulting in minimizing Δi_{lim}^{exp}.

After the geometric arrangement of the outlet is excluded, a possible reason for the high relative errors of the smallest electrode $R = 0.5\ mm$ could be the accuracy of the hydrodynamic constant a^*. The CFD simulations appear to provide a more accurate prediction of this constant. An improvement could involve determining a^* using CFD simulations, as already reported by *Ahmed et al.* [209] , and incorporating this value into the universal analytical equation for instance.

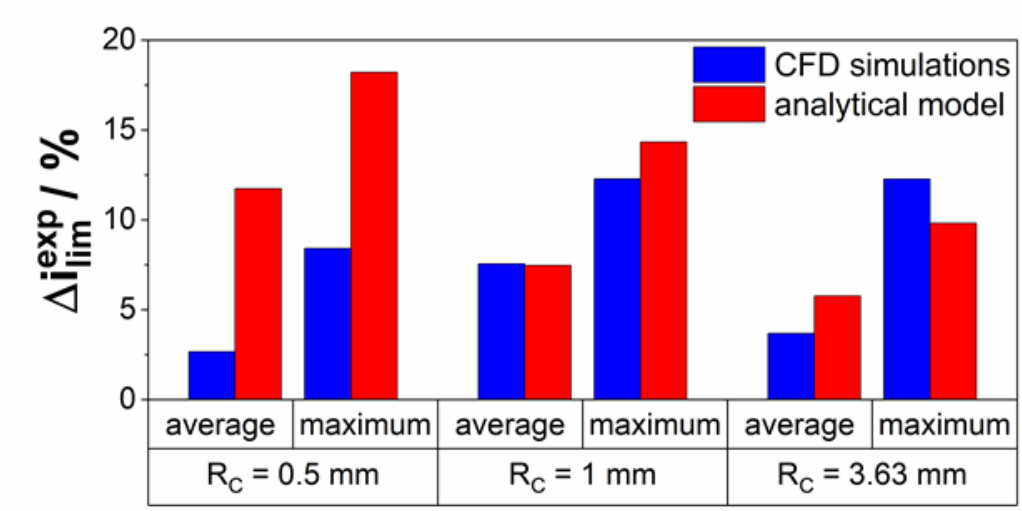

Figure 31: *Average and maximum relative error of the total limiting current density* Δi_{lim}^{exp} *established by the universal analytical model and CFD simulations in relation to the electrochemical experiment for all three electrode sizes* ($R_C = 0.5\,mm$; $R_C = 1\,mm$; $R_C = 3.63\,mm$). *Geometry parameters of the flow cell and calculations:* $d = 0.5\,mm$; $H = 0.7\,mm$.

Overall, only a slight deviation of the limiting current density calculated by our universal model for all three electrode radii compared to the values predicted by CFD simulations and particularly experimentally measured is revealed. Therefore, this model can be a suitable alternative to time-consuming numerical simulations. It is able to simply the design of such hydrodynamic electrodes, as it no longer requires in-deep knowledge of CFD simulations.

5.1.3 Conclusions to Chapter 5.1

In this chapter, a new universal analytical model for the limiting current characteristics in (confined) impinging jet electrodes was developed. The model is based on the superimposing established equations for the wall-tube, wall-jet and radial channel-flow electrode arrangements. It consists of four different logical cases depending on the volume flow rate and input parameters. A guideline has been compiled for the broad use of our model. To highlight the predictive power and accuracy of this model, the results with numerical CFD simulations and experimental data were systematically compared using the electrochemical oxidation of ferro(II)cyanide.

First, it could be demonstrated that our universal analytical model is able to predict the dynamic transition radii and their changes in relation to the volume flow for all different logical cases such as “Case Tube”, “Case Tube-Channel”, “Case Tube-Jet” and “Case-Tube Jet-Channel”. Very good agreements with results from the CFD simulations are obtained. Secondly, the local current density distributions and total limiting current densities derived from our model show very good approximation to the numerical calculations over all $N = 350$ CFD simulations. The statistical analysis for the total limiting current density predicted by this model shows an average relative error of 7.8 % compared with the CFD simulations and an average relative deviation of 8.3 % compared to the experiment. Only two main limitations have identified for this analytical model: (i) small local radii R_{loc} or small electrode sizes R_C likely due to the confinement of the jet and (ii) the prediction of complex flow patterns such as the laminar boundary layer separation.

Overall, the universal analytical model is a reliable alternative to time- and resource intensive CFD simulations for predicting (confined) impinging jet electrode experiments. It can contribute to further advancing the use of the impinging jet flow cell setup for electrochemical characterization of squared model electrodes prepared by e.g. molecular beam epitaxy (MBE), in the near future. This model could potentially be applied to other fields such as mass transfer processes or heat transport in impinging jets [211,212,230], by drawing an analogy between the Sherwood and Nusselt numbers. In the next chapter this model is used to simulate HER/HOR polarization curves inside the impinging jet flow cell and to compare the mass transport with the well-known RDE setup.

5.2 Comparison of Electrochemical Behavior and Mass Transport in Impinging Jet Flow Cell and RDE Setup

After successfully developing an analytical model describing mass transport in the impinging jet flow cell, the next step was to compare this setup with the well-established rotating disk electrode (RDE) method. The comparison focused on electrode surface area, mass transport characteristics, polarization curves and gas saturation levels. For this purpose, CV features as well as the HER/HOR reaction on polycrystalline platinum (Pt) surfaces were investigated.

5.2.1 Static Measurements – CV Features and Electrochemical Surface Area

Our first objective is to compare the electrochemical surface areas (A_{SA}) of different Pt electrodes. Cyclic voltammograms (CVs) were recorded in 0.5 M H_2SO_4 within each setup. Two electrodes with different geometric surface areas were examined in the flow cell: $R_C = 3.63\ mm$ (**Figure 32a**, red) and $R_C = 0.375\ mm$ (**Figure 32c**, black). For comparison, a CV of a polycrystalline Pt disk with $R_C = 2.5\ mm$ was recorded in the RDE setup (**Figure 32b**, blue). All CVs in **Figure 32** exhibit the typical pseudo capacitive features of a polycrystalline Pt electrode: the hydrogen adsorption and desorption region between 0.03 V and 0.4 V vs. RHE, the capacitive region between 0.4 V to 0.6 V vs. RHE, and the region for the region of formation and reduction of Pt-(hydr)oxide between 0.6 V and 1 V vs. RHE. Differences between the CVs are observed. In particular, the capacitive regions for both the large flow cell electrode (**Figure 32a**) and RDE disk (**Figure 32b**) exhibit identical absolute values for the oxidative and reductive currents, indicating good gas saturation with argon (Ar). If oxygen contamination is present, the oxygen reduction reaction (ORR) would appear as a shift towards reductive currents. This is visible for the smallest electrode size in the flow cell in **Figure 32c** suggesting partial oxygen presence and suboptimal Ar saturation. These issues will be discussed further in the polarization curves section.

The highest total currents in **Figure 32** are observed for the Pt foil in flow cell ($R_C = 3.63\ mm$). The Pt disk in RDE ($R_C = 2.5\ mm$) exhibits lower currents. Lastly the Pt microelectrode in flow cell ($R_C = 0.375\ mm$) has by far the lowest currents. The inset in **Figure 32c** shows the current in the same y-axis scale as in **Figure 32a** and **Figure**

32b to highlight this behavior. The hydrogen underpotential adsorption (H_{ads}) and hydrogen desorption areas H_{des} (hatched areas in **Figure 32**) are integrated with the capacitive currents as the base line. The electrochemical surface area (A_{SA}) is then given by:

$$A_{SA} = \frac{(H_{ads} + H_{des})}{2 \cdot s \cdot C_{pseudo}} \tag{63}$$

with the integral of the hydrogen underpotential adsorption H_{ads}, hydrogen underpotential desorption H_{des}, scan rate s and pseudo capacitance of Pt surface C_{pseudo}. Assuming a pseudo capacitance C_{pseudo} of $210\ \mu C\ cm^{-2}$ [231] an average over multiple measurements for the Pt foil in the flow cell of $A_{SA} = 1.07 \pm 0.06\ cm^2$, for the Pt disk in RDE $A_{SA} = 0.56 \pm 0.001\ cm^2$ and for the Pt microelectrode in the flow cell $A_{SA} = 0.0128 \pm 0.00085\ cm^2$ is obtained. These values indicate that the electrochemical SA of the Pt foil in the flow cell is approximately double that of Pt disk in the RDE. This agrees very well with the differences in the geometric surface area of $A_{geo} = 0.41396\ cm^2$ for the Pt foil in the flow cell and $A_{geo} = 0.196\ cm^2$ in the RDE. The microelectrode has significantly smaller A_{SA} because of the lower geometric surface area. If one considers the roughness factors according to:

$$rf = \frac{A_{SA}}{A_{geo}} \tag{64}$$

for the Pt foil in the flow cell $rf = 2.58 \pm 0.14$, for the Pt disk in the RDE $rf = 2.86 \pm 0.004$ and for the micro electrode $rf = 2.89 \pm 0.19$ are obtained. So overall, all electrodes in this setup exhibit similar surface roughness, also in agreement with the typical rf factors of polycrystalline Pt electrodes [232,233].

To sum up, similar Pt CV features are obtained between the different electrodes and hydrodynamical electrochemical setups. The main difference is found in the geometric and electrochemical SA. After establishing the comparable performance of the impinging jet flow cell in the static mode, the next step is investigating the dynamic mode, i.e. with gas-saturated electrolyte flow to investigate the HER/HOR reactions.

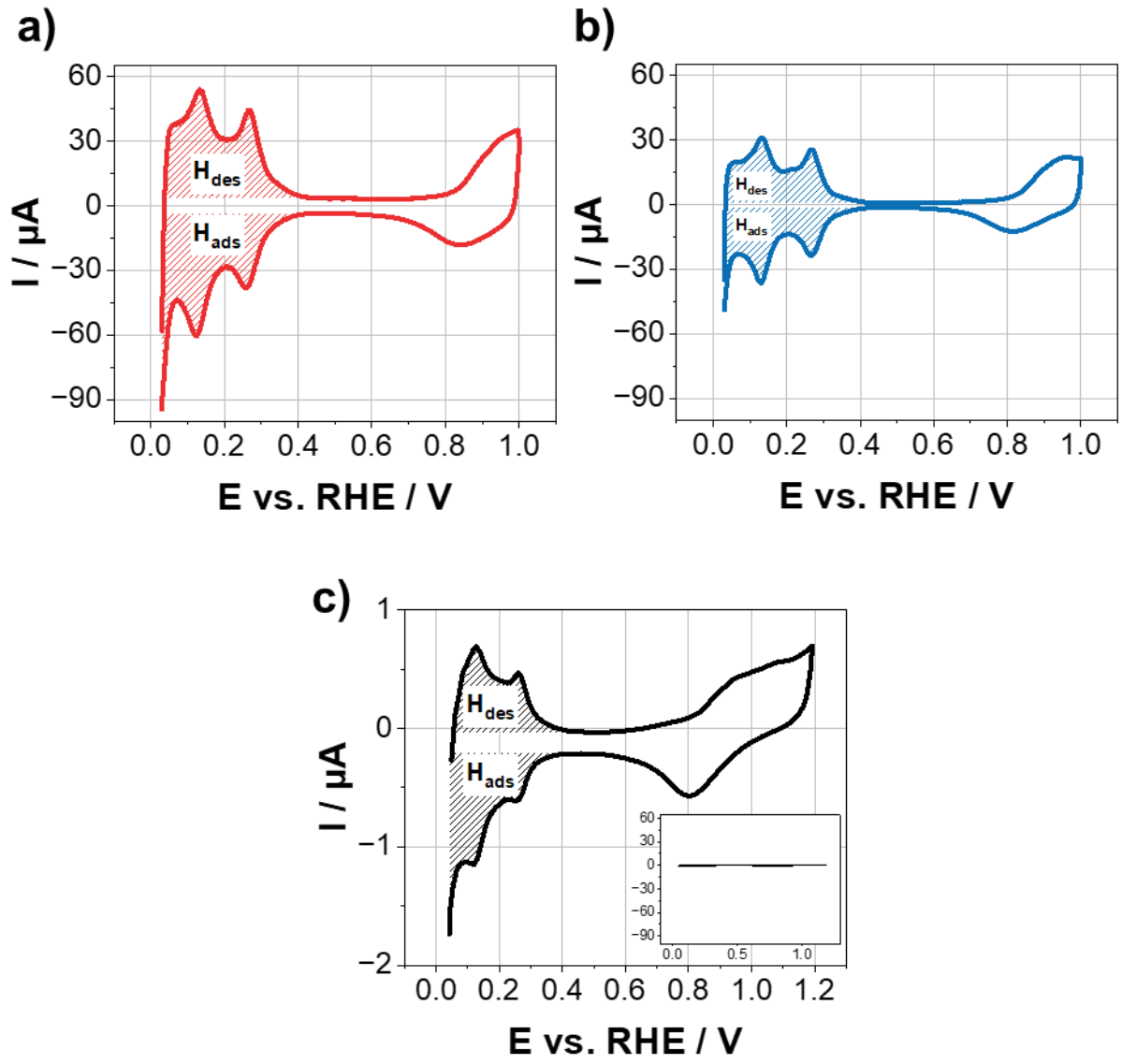

Figure 32: *Comparison of cyclic voltammograms and surface areas A_{SA} of polycrystalline Pt electrodes recorded with a scan rate of 50 mV s^{-1} in Ar-saturated 0.5 M H_2SO_4 in different setups:* ***a)*** *Impinging jet flow cell ($R_C = 3.63\ mm$).* ***b)*** *RDE ($R_C = 2.5\ mm$)* ***c)*** *Impinging jet flow cell ($R_C = 0.375\ mm$). The Inset in* ***c)*** *shows the CV with the same y-axis scaling as in* ***a)*** *and* ***b)****. The hatched areas in* ***a)****,* ***b)*** *and* ***c)*** *highlight the integrated H_{ads} and H_{des} areas used for integration and calculation of A_{SA} with equation (63).*

5.2.2 Comparison of HER/HOR Polarization Curves via Simulation

Before experimental HER/HOR curves were measured, theoretical curves were simulated. For this purpose the *Koutecký-Levich* equation (16) was used with parameters α, n and T given in **Table S2**. The total limiting current density i_{lim} was calculated using the universal analytical model from chapter 5.1 for the impinging jet flow cell and the *Levich* equation for the RDE (equation (37)), as well as the HER/HOR parameters given in **Table S2**. The experimental geometry parameters $d = 0.5\,mm$ and $H = 0.7\,mm$ for the impinging jet flow cell were used. Volume flow rate in case of the flow cell, rotation speed in the RDE and R_C was varied to simulate different mass transport conditions in all setups. **Figure 33** shows an overview of the simulated curves of the total current density i (solid lines) and the *Nernst* diffusion-controlled current i_{diff} (equation (15), dashed lines).

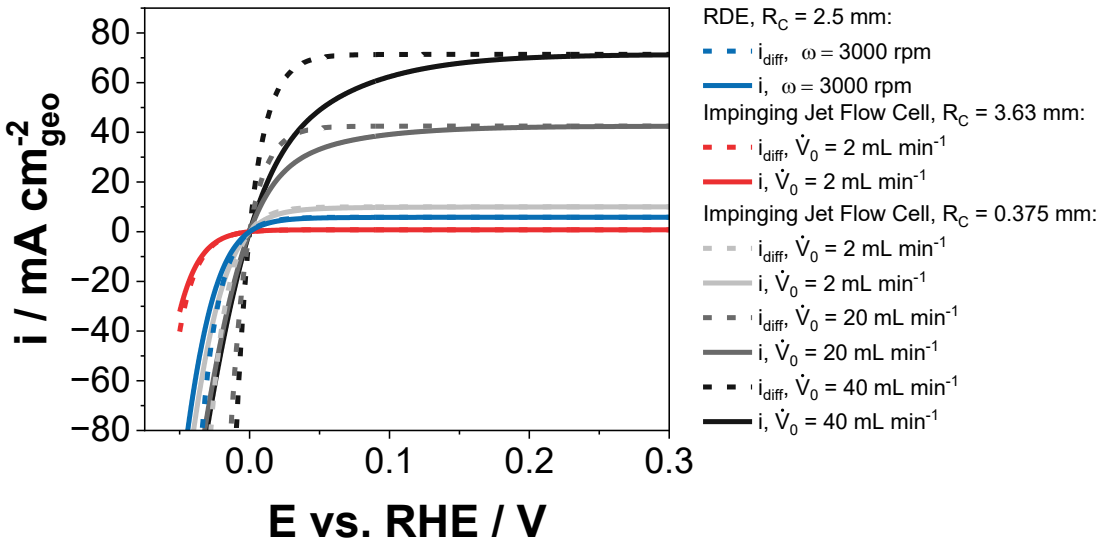

Figure 33: *Theoretical polarization curves of the HER/HOR reaction on Pt electrodes in the different setups and with different mass transport rates simulated in H_2-saturated 0.5 M H_2SO_4. Color code: blue: RDE; red: large Pt foil electrode in the impinging jet flow cell ($d = 0.5\,mm, H = 0.7\,mm, R_C = 3.63\,mm$); black: Pt micro electrode in the impinging jet flow cell ($d = 0.5\,mm, H = 0.7\,mm, R_C = 0.375\,mm$).*

The curves exhibit typical HER/HOR behavior: decreasing reduction current for HER below 0 V vs. RHE and increasing oxidation current for HOR above 0 V, reaching a plateau around 0.2–0.3 V vs. RHE. When comparing the total current densities i, it is evident that the large Pt electrode in the impinging jet flow cell (with a radius $R_C = 3.63\,mm$) at a volume flow rate of $\dot{V}_0 = 2\,mL\,min^{-1}$ (red solid curve in **Figure 33**) exhibits the lowest total current densities i. This includes the lowest limiting current

density plateau i_{lim}, observed between 0.05 and 0.3 V vs. RHE. This behavior indicates that the mass transport rate under these conditions is the lowest among the tested electrodes. Unsurprisingly, the *Nernst* diffusion-controlled current i_{diff} fully overlaps with the total current density across the entire potential range, suggesting that the observed polarization curve is dominated by mass transport limitations. Consequently, it is not possible to extract kinetic parameters of the Pt catalyst under these conditions. This aligns with the issue described in chapter 2.3.1 for RDE measurements, where the exchange current density of the HER on Pt surfaces is so high relative to the mass transport rate that kinetic parameters cannot be determined in this setup. A slightly higher limiting current plateau is observed for the RDE simulations ($R_C = 2.5\,mm$) at a rotation rate of $\omega = 3000\,rpm$ (blue solid curve in **Figure 33**). Nonetheless, in these cases i_{diff} is overlapping fully with i, indicating that the extraction of kinetic data remains unfeasible in this setup in agreement with chapter 2.3.1.

For the Pt micro electrode in the impinging jet flow cell ($R_C = 0.375\,mm$) three different volume flow rates $\dot{V}_0$ were simulated (grey curves in **Figure 33**). The limiting current plateau for $\dot{V}_0 = 2\,mL\,min^{-1}$ is slightly higher than that observed for the RDE and exceeds the plateau for the Pt foil electrode ($R_C = 3.63\,mm, \dot{V}_0 = 2\,mL\,min^{-1}$). However, comparing the total current density i with the *Nernst* diffusion overpotential again shows a complete overlap, implying that kinetic parameters cannot be determined in this mass transport regime.

Furthermore, very high mass transport rates were simulated using the Pt microelectrode with $\dot{V}_0 = 20\,mL\,min^{-1}$ and $\dot{V}_0 = 40\,mL\,min^{-1}$. The $\dot{V}_0 = 20\,mL\,min^{-1}$ case approaches practical limits in the impinging jet flow cell due to limitations of continuous fluid flow utilizing a syringe pump and the 60 mL syringe (see **Figure 20**). These conditions yielded orders of magnitude higher limiting current densities: $i_{lim} = 42\,mA\ cm_{geo}^{-2}$ and $i_{lim} = 71\,mA\ cm_{geo}^{-2}$ for $\dot{V}_0 = 20\,mL\,min^{-1}$ and $\dot{V}_0 = 40\,mL\,min^{-1}$, respectively. This is microelectrode is located at the center of the impinging jet, where local current densities are maximized, see chapter 5.1.2.2. Because these limiting current densities are on the same order of magnitude as the exchange current density i_0, the differences between i_{diff} and total i curves become apparent, making it possible to estimate i_0 in these cases. To sum up, the mass transport rates and HER/HOR polarization curves of the Pt foil in the impinging jet flow cell and the Pt disk in the RDE

are in theory quite comparable and similar. Overall the RDE would exhibit a higher mass transport rate under most conditions. In theory, with a microelectrode in an all-liquid electrolyte setup, it should be possible to determine realistic exchange current densities i_0 for the HER/HOR of noble metal catalysts. The next section will present the experimental results in that regards.

5.2.3 Dynamic Measurements – Experimental HER/HOR Polarization Curves

The next step involved an experimental comparison of HER/HOR polarization curves obtained in the impinging jet flow cell and the RDE. **Figure 34** presents these curves for different mass transport rates, achieved by varying either the rotation rate ω for the RDE setup or volume flow rate $\dot{V}_0$ for the impinging jet flow cell. **Figure 34a** shows the polarization curves for the Pt foil in the impinging jet flow cell, with volume flow rates ranging from $\dot{V}_0 = 0.5\,mL\,min^{-1}$ and $\dot{V}_0 = 2\,mL\,min^{-1}$ (color-coded from lighter to darker red with increasing flow). These curves exhibit the expected HER/HOR behavior: below 0 V vs. RHE, the cathodic HER current is visible; above 0 V, the HOR occurs, reaching a limiting current plateau around 0.075 V vs. RHE. As anticipated, this plateau increases with higher volume flow rates due to enhanced mass transport. The total current density i (solid lines) and the *Nernst* diffusion current i_{diff} (dashes lines) overlap across the entire potential range for all flow rates. This confirms that in this setup, mass transport is the limiting factor, consistent with the simulation results from **Figure 33** and the flow cell results shown in **Figure 5** for other flow cell setups from literature, which indicated that kinetic data cannot be reliably extracted under these conditions.

Next, HER/HOR curves were recorded in the well-known RDE setup, with rotation rates between 900 rpm and 2400 rpm (depicted with increasing blue tone in **Figure 34b**). The HER/HOR polarization curves show the same features as described in **Figure 34a**. However, the limiting current plateaus and HER currents are noticeably higher, signaling increased mass transport. This observation aligns with the simulation results from **Figure 33**. Again, the i (solid lines) and i_{diff} (dashed lines) overlap over most of the potential range, indicating that mass transport remains the limiting factor, thus preventing the extraction of kinetic current densities in this setup, consistent with previous simulation insights (**Figure 33**).

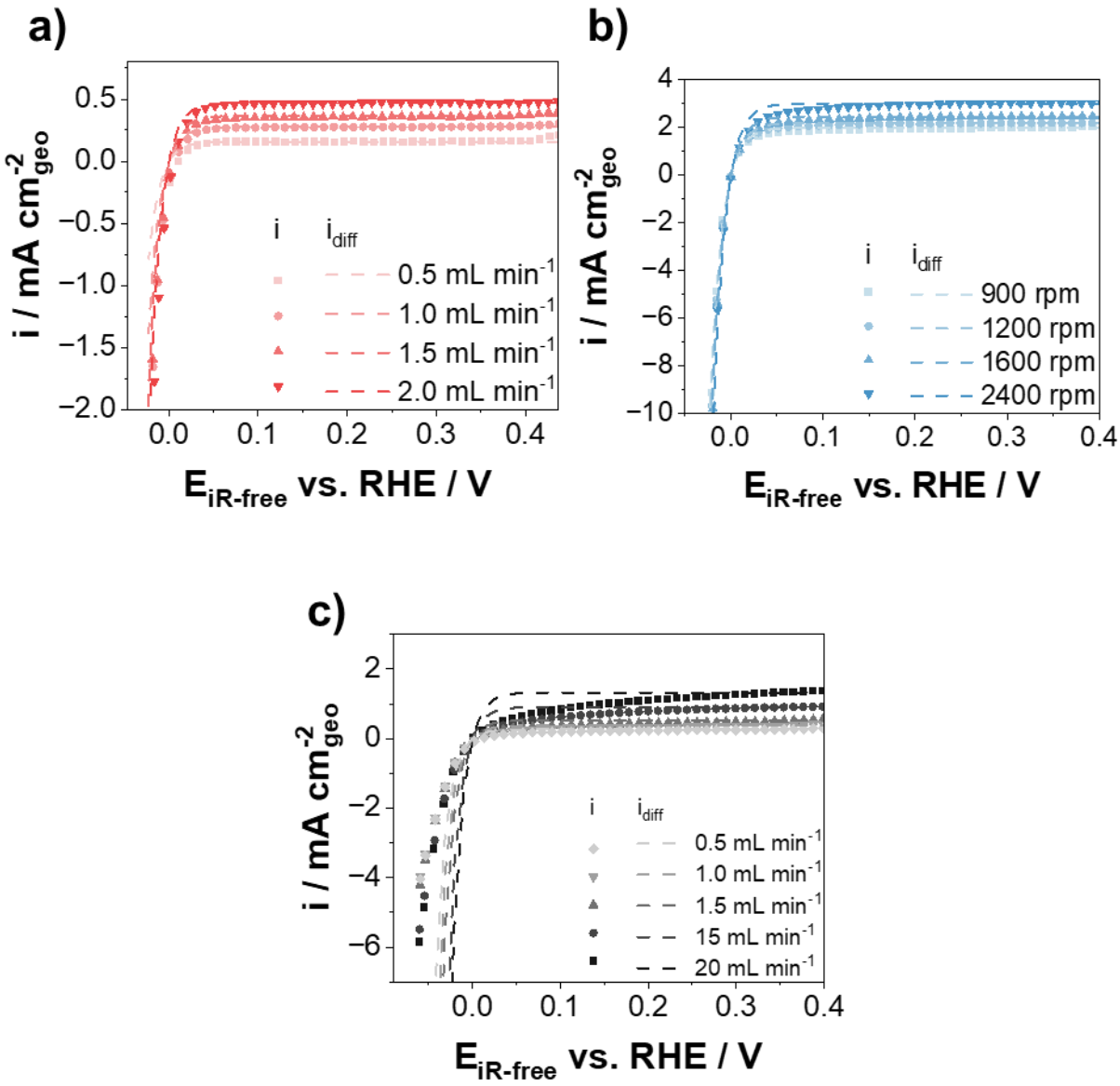

Figure 34: *HER/HOR polarization curves including the total current density i (solid lines) and the Nernst diffusion overpotential curve i_{diff} (dashed lines) recorded with a scan rate of 1 mV s^{-1} in Ar-saturated 0.5 M H_2SO_4 for* ***a)*** *Impinging jet flow cell ($R_C = 3.63\ mm$).* ***b)*** *RDE ($R_C = 2.5\ mm$)* ***c)*** *Impinging jet flow cell ($R_C = 0.375\ mm$) with different volume flow rates $\dot{V}_0$ in case of the impinging jet flow cell and different rotation speeds ω in case of the RDE.*

Lastly, **Figure 34c** shows the polarization curves for the Pt microelectrode ($R_C = 0.375\ mm$) in the impinging jet flow cell. Here, the overall currents i are higher than those for the larger Pt foil in the same flow cell ($R_C = 3.63\ mm$, **Figure 34a**) but lower than those for the Pt disk in the RDE setup (**Figure 34b**) for the whole volume flow range between $\dot{V}_0 = 0.5\ mL\ min^{-1}$ and $\dot{V}_0 = 20\ mL\ min^{-1}$. This suggests that the microelectrode experiences mass transport conditions that are superior to the large Pt foil in the impinging jet flow cell but inferior to the RDE. Interestingly, this contrasts with

the simulations in **Figure 34**, which predicted much higher mass transport rates, especially at high flow rates of $\dot{V}_0 = 20\ mL\ min^{-1}$ and $\dot{V}_0 = 40\ mL\ min^{-1}$. Notably, for all flow rates examined, the i and i_{diff} curves do not overlap, and no limiting current density plateau is reached over the entire potential range studied. While this might suggest that kinetic current densities could be derived from this setup, the limiting current densities and the resulting mass transport rates are in theory too low for reliable kinetic analysis. To summarize, the large Pt foil in the impinging jet flow cell and the RDE show comparable polarization curves with overlapping i and i_{diff}. The mass transport in the RDE is slightly higher compared to the Pt foil in the impinging jet flow cell. Both results and curves agree with the results from the theoretical simulations. For the Pt microelectrode a different behavior was obtained with non-overlapping i and i_{diff} curves. In theory the limiting current densities are much too low here especially at high volume flow rates (15 mL min^{-1} and 20 mL min^{-1}).

To better understand these trends, subsequent simulations of limiting currents were conducted, considering various mass transport conditions and different bulk H_2 concentrations c_∞. These simulations employed the universal analytical model from chapter 5.1 as well as the HER/HOR parameters η, ρ, D and n given in **Table S2**. The results are compared with experimental data in **Figure 35** for all tested electrodes. The green crosses denote the experimental points of i_{lim} from the measurements shown in **Figure 34**. **Figure 35a** compares the experimental limiting currents for the HOR on the Pt foil ($R_C = 3.63\ mm$) in the impinging jet flow cell with the simulated curves for different gas saturation concentrations (shown with increasing red tones). First of all, as seen in **Figure 35a** the theoretical limiting current increases with increasing volume flow rate and also with increasing gas concentration in the electrolyte c_∞. This result is expected based on the universal analytical model from chapter 5.1. The experimental data aligns well with the simulated curve at a gas concentration of $c_\infty = 0.5\ mmol\ L^{-1}$. This is slightly lower compared to the expected value of $c_\infty = 1\ mmol\ L^{-1}$, which is often found in literature both for simulations [179,228] and experimental data in impinging jet flow cells [189]. One way to improve this is to incorporate the proposed gas-in-gas saturation system by *Tschupp et al.* [189]. It allows the resaturation of the electrolyte directly before the entrance into the impinging jet flow cell via the inlet (so before entering (1) in **Figure 19**). However, this adds considerable setup complexity and was not pursued within this thesis.

In comparing the results for the Pt foil in the impinging jet flow cell (**Figure 35a**) with the data for the Pt disk in the RDE (**Figure 35b)** it is evident that the simulated limiting currents are generally higher within the typical rotation speed range of 0 to 6000 rpm. This agrees with the simulation outcomes (**Figure 33**) and also with experimental results from **Figure 34.** The experimental data (green crosses) again matches well with the simulated curve at $c_\infty = 0.5\ mmol/l$. So the gas saturation in the RDE and for the Pt foil in the impinging jet flow cell are very much comparable.

Finally, **Figure 35c** compares the data of the microelectrode in the impinging jet flow cell. The simulations predict the highest limiting current densities among all setups; however, the experimental data aligns only with the simulation curve corresponding to the lowest H_2 saturation $c_\infty = 0.05\ mmol\ L^{-1}$. This suggests that the actual gas saturation in this microelectrode system is approximately ten times lower than in the large Pt foil in the flow cell. A plausible explanation might be that the microelectrode, which is not glued into its Teflon holder (see **Figure 22b**), could allow air or oxygen ingress through gaps between the Teflon and the Pt wire, reducing the effective gas saturation in the working electrode chamber (**Figure 19b**). Another possible explanation could be the imperfect alignment of the Pt microelectrode, due to manufacturing tolerances. Even small misalignments of the micro electrode position in relation to the center of the impinging jet could drastically change the experimental limiting currents obtained, as described in previous literature [204,207]. However, as shown in chapter 5.1 a good agreement between theoretical and experimental limiting currents for oxidation of ferro(II)cyanide on glassy carbon electrodes were obtained with low relative errors Δi_{lim}^{exp}. The exact reason for the obtained polarization curves of the Pt microelectrode is not fully understood within the scope of this thesis but could be elaborated in future works.

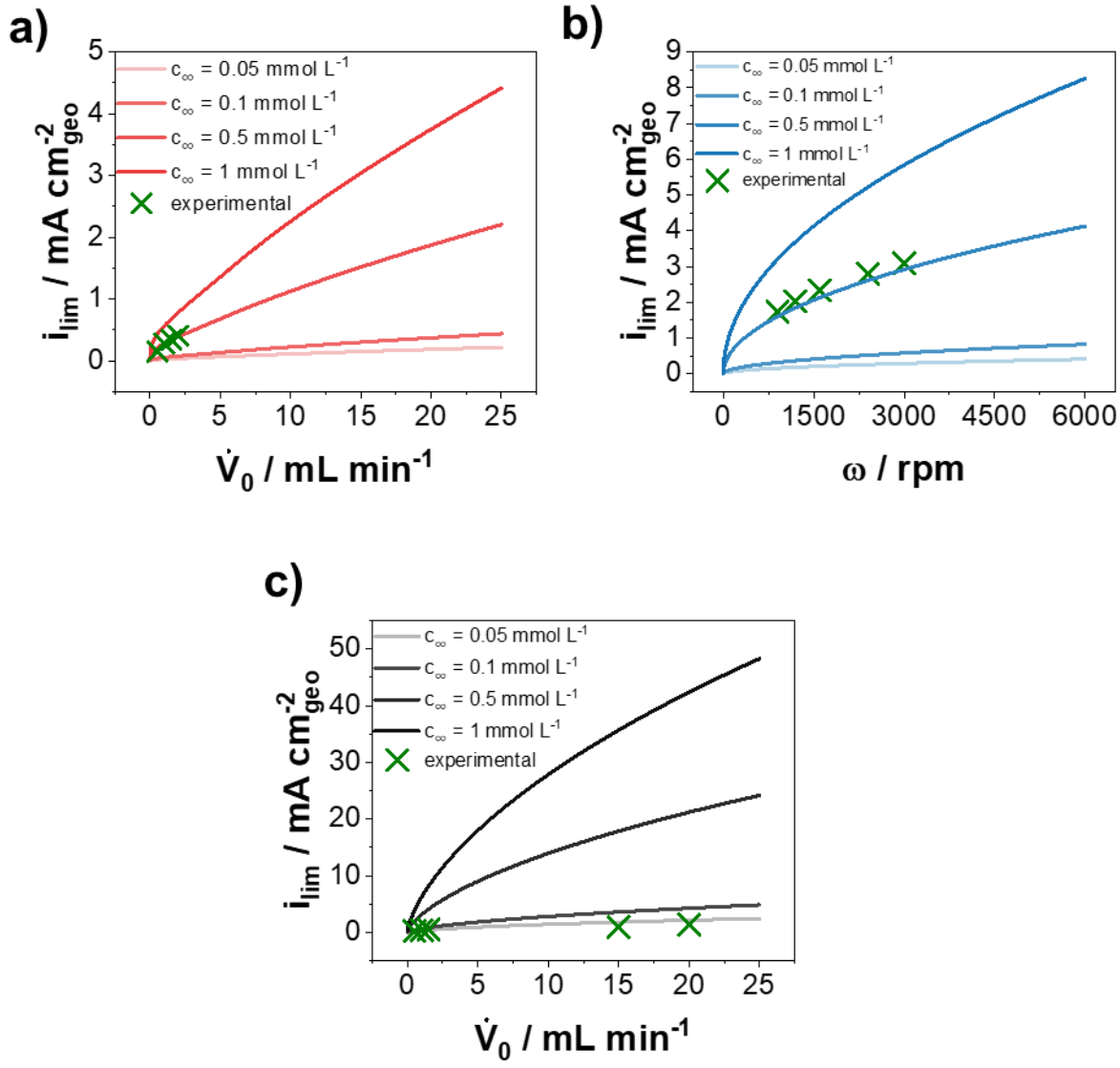

Figure 35: *Comparison of experimental (green crosses) and simulated limiting currents i_{lim} for different c_∞ concentrations of H_2 in the electrolyte for all electrodes tested herin. The color shade increases with increasing c_∞.* ***a)*** *Impinging jet flow cell ($R_C = 3.63\ mm$).* ***b)*** *RDE ($R_C = 2.5\ mm$)* ***c)*** *Impinging jet flow cell ($R_C = 0.375\ mm$) .*

5.2.5 Conclusions to Chapter 5.2

In this chapter, a comparative study is conducted between electrochemical measurements of Pt electrodes in the impinging jet flow cell and the RDE. The primary objective was to analyze and compare CV features, surface area, mass transport behavior, and gas saturation levels for different electrode sizes: $R_C = 0.375\,mm$ and $R_C = 3.63\,mm$ in the impinging jet flow cell and $R_C = 2.5\,mm$ in the well-known RDE setup.

Initially, the CVs of the Pt electrodes are examined. All electrodes in both setups exhibited the characteristic features of polycrystalline Pt. Using the HUPD method to determine the electrochemical surface area (SA), it is observed that the Pt foil in the impinging jet flow cell has approximately twice the electrochemical SA compared to the RDE, which aligns well with the doubling of the geometric SA and suggests similar surface roughening. Both electrodes displayed stable, parallel capacitive CV regions without signs of oxygen contamination. The microelectrode in the flow cell shows a significantly smaller electrochemical SA, consistent with its reduced geometric surface area. The capacitive CV region indicates minor oxygen species presence, pointing to insufficient gas saturation.

Subsequently, HER/HOR polarization curves are simulated using the universal analytical model from chapter 5.1 for the impinging jet flow cell and the *Levich* equation for the RDE. The simulations reveal notable differences in mass transport and potential behavior between the electrode setups. In the impinging jet flow cell setup, comparable mass transport conditions are achieved for the Pt foil compared to the RDE, with the total current i and the *Nernst* diffusion current i_{diff} overlapping over the entire potential range. For the micro electrode in the impinging jet flow cell it is theoretically demonstrated that extremely high mass-transport rates can be achieved at high volume flow rates ($\dot{V}_0 \geq 20\,mL\,min^{-1}$), leading to high limiting current densities, in the order of magnitude of commonly reported values for the exchange current density i_0 of Pt catalysts [18,44,56,59,60]. Under such conditions it should be feasible to extract realistic i_0 for HER on Pt surfaces from the polarization curves i in this all-liquid electrolyte setup.

The experimental polarization curves show that the Pt foil in the impinging jet flow cell and the Pt disk in the RDE exhibited similar features, aligning with the theoretical predictions. Furthermore, comparison with the simulation results indicated comparable

levels of gas saturation, with an approximate H_2 concentration of $c_\infty = 0.5\ mmol\ L^{-1}$. However, the microelectrode in the flow cell displayed greater deviations from the expected theoretical behavior, possibly due to very low gas saturation, probably stemming from the electrode's construction. Opportunities for improvement in future electrode designs are noted. Overall, it was demonstrated that both the RDE and the impinging jet flow cell, particularly with larger electrodes ($R_C = 3.63\ mm$) produce comparable mass transport rates and polarization behaviors for HER/HOR. Therefore, this setup can be confidently used for the investigation of HER/HOR model electrocatalysts. In the next section, studies will focus on the application of this system to model 2D Pt chalcogenides.

5.3 Activity and Stability of Novel 2D - Pt Chalcogenides for the HER in Acidic Media

Contributions:

- *C. Schneemann carried out the literature research, developed the impinging jet flow cell setup, carried out the electrochemical experiments and Raman spectroscopy experiments, curated the data, analyzed the data, visualized the data, discussed the data within the project team, wrote and edited the original draft.*
- *K. Lasek synthesized the 2D-PT_xTe_y materials on HOPG and discussed the data with other members in the project team.*
- *M. Ghorbani Asl carried out the DFT simulations and discussed data discussed the data with other members in the project team, reviewed and commented on the original draft.*
- *N. R. Rajapakse carried out XPS measurements and analyzed them*
- *S. Blaseio discussed Raman measurements within the project team, reviewed and commented on the original draft.*
- *M. Batzill, A. Krasheninnikov and M. Oezaslan had the original project idea, discussed the data with other members in the project team, supervised the work and reviewed and commented on the original draft*

Preface:

To reduce precious group metal (PGM) content in the hydrogen evolution reaction (HER), transition metal chalcogenides have emerged as promising alternatives. In this chapter, the experimental and theoretical HER activity of three two-dimensional (2D) platinum tellurides, prepared by molecular beam epitaxy (MBE), are correlated. Experimental HER activity is in the order 2D-$PtTe_2$ ($\left|E_{-0.1\ mA\ cm_{geo}^{-2}}\right| = 78 \pm 7\ mV\ vs.RHE$) ≈2D-$Pt_2Te_2$≪2D-$Pt_3Te_4$ ($\left|E_{-0.1\ mA\ cm_{geo}^{-2}}\right| = 115 \pm 11\ mV\ vs.RHE$). Density functional theory calculations relate these differences to the trend of hydrogen adsorption *Gibbs* free energies (ΔG_H) at tellurium vacancies V_{Te}: 2D-$PtTe_2$ (0.047 eV) ≈ 2D-Pt_2Te_2 ≪ 2D-Pt_3Te_4 (0.604 eV). *Tafel* slope analysis (68-71 mV dec^{-1} across all phases) confirms that all materials share the same rate determining step. Furthermore, the durability of these materials throughout the electrochemical protocol was monitored with Raman spectroscopy and XPS. Raman spectroscopy revealed that 2D-Pt_2Te_2 partially transformed into 2D-Pt_3Te_4 during electrochemical experiments, indicating its thermodynamic metastability. 2D-$PtTe_2$ degraded during electrochemical testing, likely by mechanical delamination. XPS analysis confirmed that none of these phases showed signs of degradation into metallic Pt. These insights into structure-activity relationships and durability will aid future development of Pt chalcogenide catalysts to reduce PGM usage in HER.

5.3.1 Structural Characterization

After validating the impinging jet flow cell setup in the previous chapter with the HER/HOR on Pt surfaces, this chapter will focus on the application of this setup to investigate model 2D Pt chalcogenides.

The three 2D-Pt_xTe_y phases were synthesized with molecular beam epitaxy, as previously described [100]. After the synthesis (see chapter 9.3.1) , the phase purity of the 2D-Pt_xTe_y compounds was verified by Raman spectroscopy and X-ray photoelectron spectroscopy (XPS) techniques. **Figure 36a** displays the characteristic ex-situ Raman spectra of three different compounds. All samples show Raman bands in the range of 92 to 200 cm^{-1} and in addition a Raman band with high intensity at 1583 cm^{-1}. The bands at 121 cm^{-1} and 158 cm^{-1} for 2D-$PtTe_2$ (green line) are assigned to the E_g and A_{1g} modes of lattice vibration, respectively [234]. For reference the lattice vibration modes are displayed for a monolayer of the material in **Figure 8a**. Similar for 2D-Pt_2Te_2 (red line) the E_g and A_{1g} modes can be found at 92 and 121 cm^{-1} in **Figure 36a** [234] (see **Figure 8b** for lattice vibration mode). The Raman band at high intensity is assigned to the graphite (G) band of the HOPG substrate [235]. The 2D-Pt_3Te_4 phase consists of alternating Pt_2Te_2 and $PtTe_2$ layers. The E_g and A_{1g} Raman bands of 2D-Pt_3Te_4 (blue line in **Figure 36a**) show a simple superposition of the Raman spectra from the $PtTe_2$ and Pt_2Te_2 phases, with all bands previously described visible. That is because Pt_3Te_4 consists of alternating layers of $PtTe_2$ and Pt_2Te_2.

The oxidation states of platinum (Pt) and tellurium (Te) in each sample were analyzed using XPS spectroscopy (**Figure 36b-c** and **Figure S5**). The raw data (black points) in **Figure 36b-d** display two distinct peaks corresponding to the spin-orbit split Pt 4f components: Pt $4f_5/_2$ at higher binding energy and Pt $4f_7/_2$ at lower binding energy. Deconvolution of the Pt $4f_7/_2$ spectra for 2D-$PtTe_2$ (**Figure 36b**) indicates a single species at 72.3 eV, assigned to Pt^{4+}.[100] The complementary Te 3d spectra revealed one component, with the Te $3d_5/_2$ and Te $3d_3/_2$ peaks located at 573.8 eV and 583.8 eV for 2D-$PtTe_2$ (**Figure S5a**), assigned to Te^{2-} in agreement with literature[100]. Both Pt 4f and Te 3d spectra are in agreement with the ideal chemical composition of $PtTe_2$ (Pt in oxidation state 4+, Te in the oxidation state -2). For 2D-Pt_2Te_2 the deconvolution of the Pt $4f_{7/2}$ spectra implies two species (**Figure 36c**) at 71.3 and 72.3 eV, assigned to Pt^{2+} and Pt^{4+}, respectively[100]. Comparing the peak area ratios of the Pt^{2+} and Pt^{4+} components yields a $PtTe_2$ to Pt_2Te_2 ratio of approximately 0.12, implying that around

10% of the initial material consists of $PtTe_2$. Here the Te $3d_{3/2}$ deconvolution reveals one component at 583.5 eV (**Figure S5b**), assigned to Te^{2-} in agreement with literature[100]. Finally, **Figure 36d** presents the XPS spectrum for the Pt_3Te_4 phase. The deconvolution of the Pt $4f_{7/2}$ spectra implies two species (**Figure 36d**) at 71.3 and 72.3 eV, assigned to Pt^{2+} and Pt^{4+}, respectively[100]. The ratio of the areas under these peaks (~0.45 for Pt^{4+} to Pt^{2+}) closely approximates an ideal 1:1 ratio. This is consistent with the ideal structure of Pt_3Te_4 consisting of alternating $PtTe_2$ (Pt^{4+}) and Pt_2Te_2 (Pt^{2+}) layers.

In summary, the structural characterization with Raman spectroscopy and XPS demonstrates the successful synthesis and phase purity of these three phases, which allows for a direct comparison of their intrinsic activity and durability.

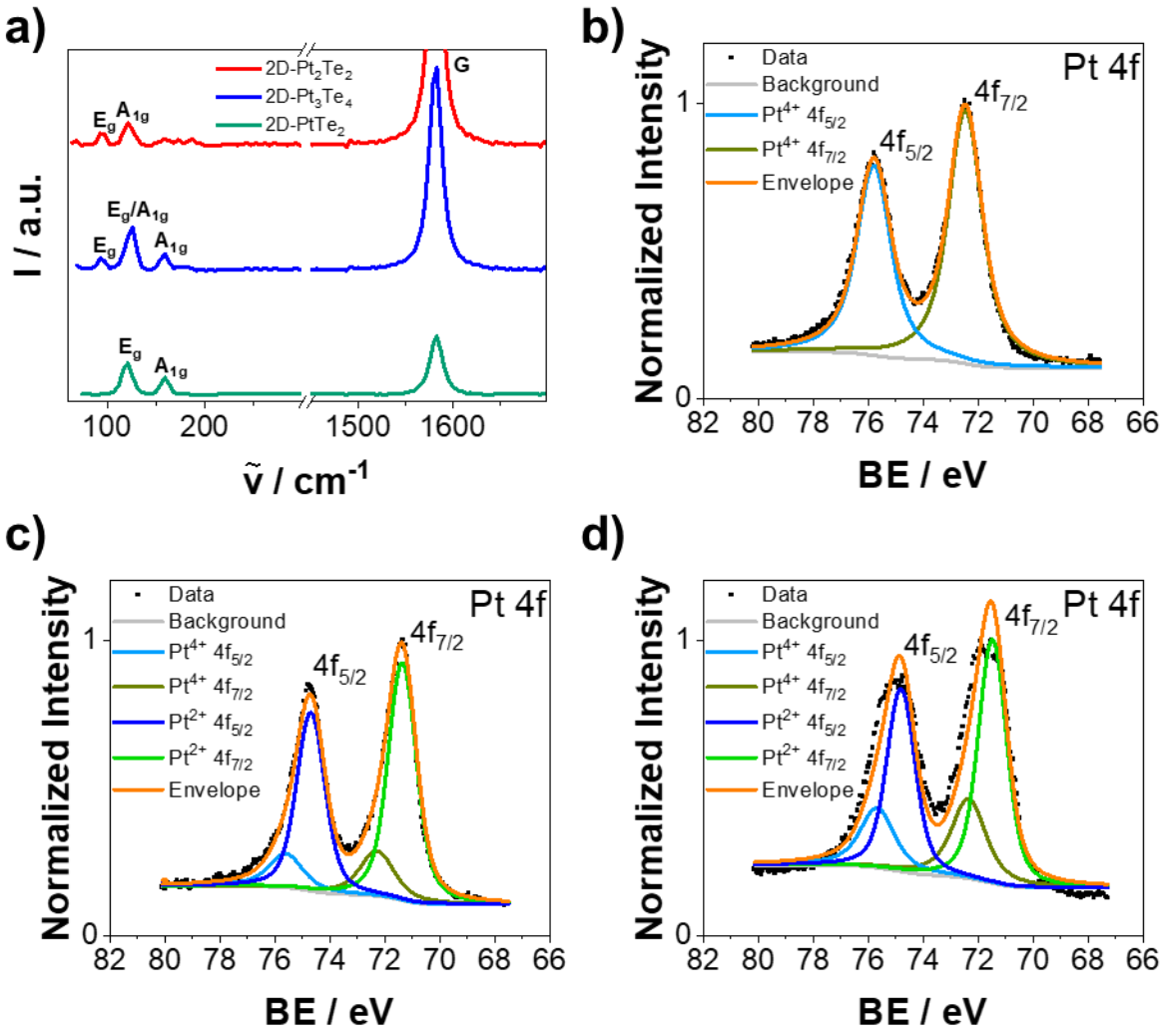

Figure 36: *Ex-situ initial structural characterization of 2D-Pt_xTe_y@HOPG materials.* ***a)*** *Raman spectra of three different Pt_xTe_y phases.* ***b)*** *Pt 4f XPS spectra of 2D-$PtTe_2$@HOPG.* ***c)*** *Pt 4f XPS spectra of 2D-Pt_2Te_2@HOPG.* ***d)*** *Pt 4f XPS spectra of 2D-Pt_3Te_4@HOPG.*

5.3.2 Electrochemical HER Activity

Open circuit potential (OCP) measurements were performed over a duration of 1 h in two different electrolytes: 0.1 M phosphate-buffered $NaClO_4$ (pH=7) and 0.5 M H_2SO_4 (pH=0) to test the chemical stability of Pt_xTe_y. The conditions were chosen based of the focus of recent literature investigations [76,77,107,109,110]. In both electrolytes (presented in **Figure S6a** for $NaClO_4$ and **Figure S6b** for H_2SO_4) all three 2D-Pt_xTe_y@HOPG materials exhibit stable OCP values over the one-hour measurement period. This indicates good chemical stability of the materials under the tested conditions. Notably, the open-circuit potential (OCP) values for the 2D Pt_xTe_y materials are closer to that of bulk platinum foil than to bare HOPG. The OCP is determined by the thermodynamic equilibrium potential of the relevant redox couples at the catalyst surface. Therefore, it is not surprising that the OCP values of Pt_xTe_y@HOPG are closer to those of platinum compared to HOPG. The OCP of Pt is also not reached because the OCP of Pt_xTe_y@HOPG is formed by a mixture of the equilibrium potentials of Pt and Te redox processes at the surface.

Afterwards linear sweep voltammograms of the HER and HOR were recorded in H_2-saturated 0.5 M H_2SO_4 (**Figure 37a)**. All polarization curves of 2D-Pt_xTe_y phases (green line: $PtTe_2$@HOPG; red line: 2D-Pt_2Te_2@HOPG; blue line: 2D-Pt_3Te_4@HOPG) and the bulk Pt foil (black line) show typical HER behavior below 0 V vs. RHE: with increasing cathodic potential, the HER current density remains low first and then exponentially increases. The 2D-$PtTe_2$@HOPG and 2D-Pt_2Te_2@HOPG phases show similar potentials necessary for a current density of $-0.1\ mA\ cm_{geo}^{-2}$: $|E_{-0.1\ mA\ cm_{geo}^{-2}}| = 78 \pm 7\ mV$ vs. RHE and $\left|E_{-0.1\ mA\ cm_{geo}^{-2}}\right| = 85 \pm 14\ mV$ vs. RHE, respectively. The 2D-Pt_3Te_4@HOPG phase shows a higher absolute potential necessary with $\left|E_{-0.1\ mA\ cm_{geo}^{-2}}\right| = 115 \pm 11\ mV$ vs. RHE, indicating significantly lower HER activity. The bare HOPG (grey line) reference remains inactive, showing no relevant current related to HER or HOR. The platinum foil, as a reference material for this study, exhibits the lowest HER potentials with $|E_{-0.1\ mA\ cm_{geo}^{-2}}| = 3 \pm 1\ mV$ vs. RHE, indicative of its high HER activity. Additionally, the bulk Pt foil shows oxidative currents in the region above 0 V vs. RHE. These currents are attributed to the hydrogen oxidation reaction (HOR) and not found for the 2D-Pt_xTe_y@HOPG materials.

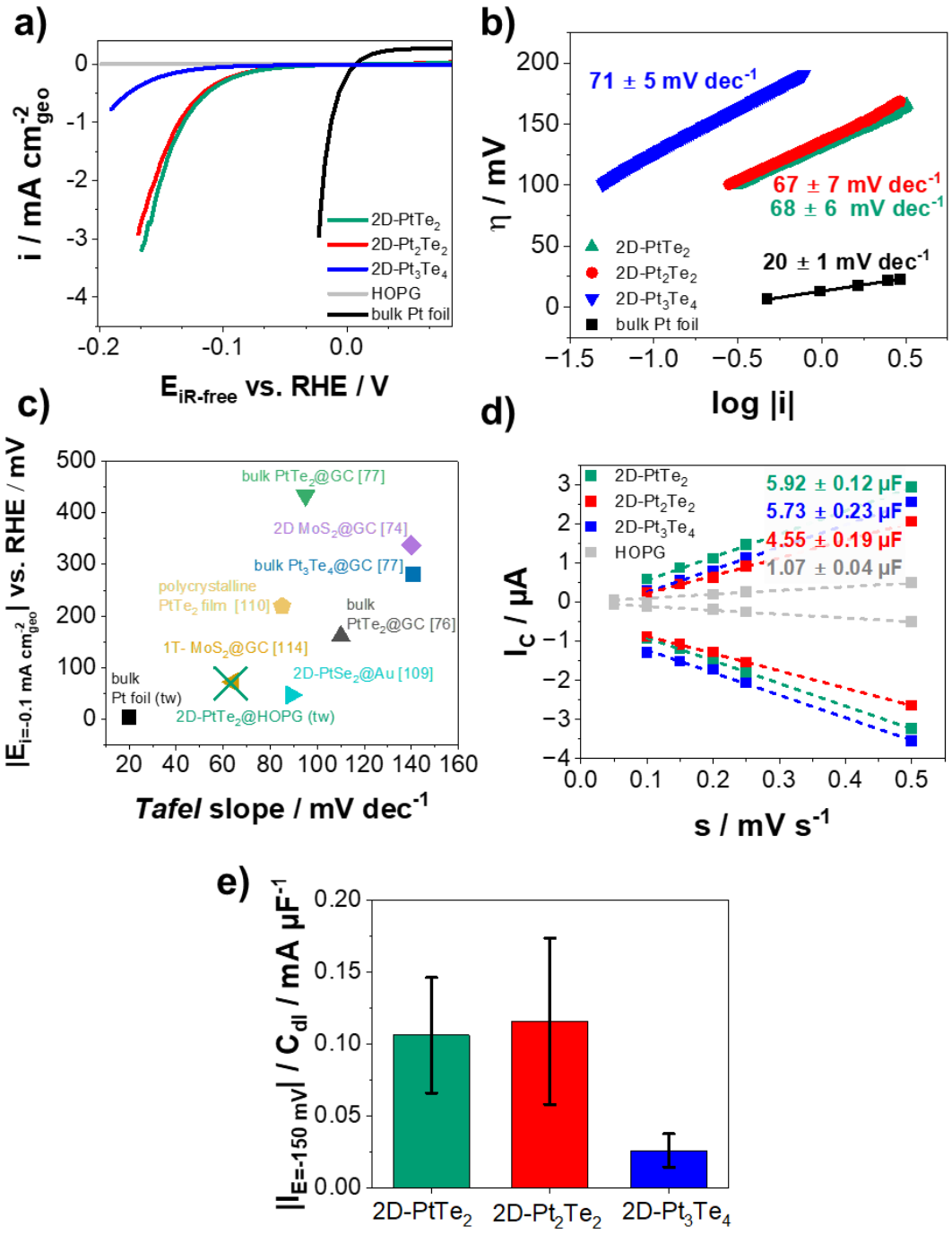

***Figure 37**: : Hydrogen evolution reaction (HER) activity of 2D-Pt_xTe_y@HOPG materials. **a)** Cathodic linear sweep voltammograms (LSV) recorded with a scanrate of s = 1 mV s^{-1} in H_2-saturated 0.5 M H_2SO_4 with a flow rate of $\dot{V}_0 = 1\ mL\ min^{-1}$. **b)** Tafel slope analysis of the different catalysts based on the LSVs in 0.5 M H_2SO_4. **c)** Comparison of the Tafel slope and potential for a current density of $-0.1\ mA\ cm_{geo}^{-2}$ $|E_{i=-0.1\ mA\ cm_{geo}^{-2}}|$ of 2D-PtTe2@HOPG from this work (tw- this work) with similar catalysts found in literature (see also **Table 3**). **d)** Determination of the double layer capacitance C_{dl}. The capacitive current I_C (as determined from **Figure S7**) is plotted versus the scanrate s for all tested materials and HOPG. **e)** Specific activity comparison of the 2D-Pt_xTe_y catalysts using the values of the double layer capacitance from **d)** and the current at a potential of $E = -150\ mV$ from **a)**.*

To further analyse the mechanism of HER, *Tafel* slopes for all samples in 0.5 M H_2SO_4 were determined and compared with the bulk Pt foil (**Figure 37b)**. The *Tafel* slope of the Pt_xTe_y phases increases in the order: 67±6 mV dec dec^{-1} for 2D-Pt_2Te_2 (red curve), 68±6 mV dec^{-1} for 2D-$PtTe_2$ (green curve), and 71±5 mV dec^{-1} for 2D-Pt_3Te_4 (blue curve) compared to Pt foil with approximately 20±1 mV dec^{-1}. In acidic media, it is well known that the kinetics of the HER/HOR on Pt surfaces are too fast to be accurately measured in a RDE or flow cell setup. The exchange current density is one to two orders of magnitude higher than the diffusion-limited currents measured in such setups [54]. Since the kinetics of the 2D-Pt_xTe_y catalysts are considerably slower, it is possible to derive a more detailed interpretation of the *Tafel* slopes for them. The HER in acidic media generally proceeds via either the *Volmer-Tafel* or *Volmer-Heyrovsky* mechanisms [34,236,237] (see chapter 2.2.1). Depending on the rate-determining step, different *Tafel* slopes are expected: approximately 120 mV dec^{-1} for the Volmer step, 40 mV dec^{-1} for the *Heyrovsky* step, and around 30 mV dec^{-1} for the *Tafel* step [238]. The observed values between 68 and 71 mV dec^{-1} for the 2D catalysts are closest to the ideal value if the *Heyrovsky* step would be rate determining. This possibly indicates a *Volmer-Heyrovsky* mechanism, as discussed in literature [239,240], for all Pt_xTe_y materials. However, the rate determining step cannot be unambiguously assigned from *Tafel* analysis alone.

To provide broader context, the activity during HER of the most active phase (2D-$PtTe_2$@HOPG, this work, abbreviated as "tw") is compared with data from other studies on bulk $PtTe_2$ and $PtTe_2$ films, as well as related 2D chalcogenide materials such as MoS_2. **Figure 37c** illustrates the comparison of the absolute value of the potential at a current density of $-0.1\ mA\ cm_{geo}^{-2}$ $\left|E_{-0.1\ mA\ cm_{geo}^{-2}}\right|$ and the *Tafel* slope for 2D-$PtTe_2$@HOPG with relevant literature. The details of all references and data from this figure are summarized in **Table 3**. Our 2D-$PtTe_2$@HOPG (depicted in turquoise) shows a higher $\left|E_{-0.1\ mA\ cm_{geo}^{-2}}\right|$ compared to the bulk Pt foil, which remains the most active material in this comparison. $\left|E_{-0.1\ mA\ cm_{geo}^{-2}}\right|$ as well as *Tafel* slope are comparable with those reported for 1T-MoS_2@GC[114]. Notably, our 2D material demonstrates significantly lower *Tafel* slopes and $\left|E_{-0.1\ mA\ cm_{geo}^{-2}}\right|$ than bulk $PtTe_2$, likely due to the exposure of the catalyst as an ideal 2D sheet. Among platinum

chalcogenide catalysts, 2D-$PtTe_2$@HOPG ranks among the most active reported to date.

To assess the specific activity based on the recorded LSVs, it is critical to determine the electrochemical surface areas (ECSA) of the synthesized 2D-Pt_xTe_y layers. Cyclic voltammetry (CV) was carried out in a non-faradaic potential window at various scan rates, as shown in **Figure S7a-d.** The capacitive currents observed increase linearly with scan rate according to

$$I_C = C_{dl} \cdot s \tag{65}$$

with the double layer capacitance C_{dl}, the scan rate s and the capacitive current I_C. Based on equation (65) the capacitive current I_C vs. the scanrate s is plotted in **Figure 37d** to obtain C_{dl} as an approximation for the surface area from the linear regression. All three 2D-Pt_xTe_y phases have double layer capacitances of 4.5-6 µF, indicating similar ECSA. These values are just 4.5 to 6 times higher than that of bare HOPG, which has a C_{dl} of about 1.07±0.04 µF.

The specific activities $\frac{|I_{E=-150\ mV}|}{C_{dl}}$ $[mA\ \mu F^{-}]$ of the materials can be directly compared based on extracting the HER current at $E = -150\ mV$ vs. RHE from the LSVs (**Figure 37a**) and normalizing to the obtained double layer capacitances from **Figure 37d**. This overpotential was selected based on the electrochemical flow cell's limitations regarding hydrogen bubble formation, specifically a range in which bubble interference does not significantly affect the current. As seen in **Figure 37e** the specific activities of 2D-$PtTe_2$ and 2D-Pt_2Te_2 are comparable and higher than the one from 2D-Pt_3Te_4. This finding is consistent with the trends observed in the LSVs (**Figure 37a**) and can be explained by the fact that the double layer capacitances of the materials are very similar (**Figure 37d**). Since the specific activities are normalized by these capacitances, the comparable double layer capacitances result in similar normalized current densities, thereby confirming the observed trend in specific activities.

To sum up the HER activity trends, considering the $\left|E_{-0.1\ mA\ cm_{geo}^{-2}}\right|$ and *Tafel* slope the activity is in the order 2D-$PtTe_2$≈2D-Pt_2Te_2>>2D-Pt_3Te_4. In literature, comparative studies directly evaluating different Pt_xTe_y phases are scarce. For instance, one study compared the HER activities of bulk $PtTe_2$ and bulk Pt_3Te_4 in 0.5 M H_2SO_4 using a

RDE setup[77]. They observed that $PtTe_2$ exhibited higher potentials near the HER onset, with $\left|E_{-0.1\ mA\ cm_{geo}^{-2}}\right| = 433$ mV vs. RHE for bulk $PtTe_2$ versus $\left|E_{-0.1\ mA\ cm_{geo}^{-2}}\right|$ = 280 mV vs. RHE for bulk Pt_3Te_4. Interestingly, this trend contrasts with our findings. A possible explanation is that our study employs well-defined 2D materials where the phase is exposed as a 2D sheet, whereas the bulk samples studied by *Supriya et al.* possess undefined morphology [77]. To the best of our knowledge, further studies directly comparing the different obtainable phases ($PtTe_2$, Pt_2Te_2, and Pt_3Te_4) are not found. The reason for the activity trend in this study will be further elucidated during the theoretical calculations using DFT. Having established these activity trends, the next step is to investigate the short-term atomic-level stability of the electrocatalyst to gain insights into its fundamental electrochemical durability.

5.3.3 Electrochemical Durability

The short term activity tests were carried out using cyclic voltammetry (CV, 0.03–0.9 V vs. RHE) in both electrolytes (phosphate buffered 0.1 M $NaClO_4$ and 0.5 M H_2SO_4) to investigate potential-induced degradation procedures as reported in similar literature studies [76].

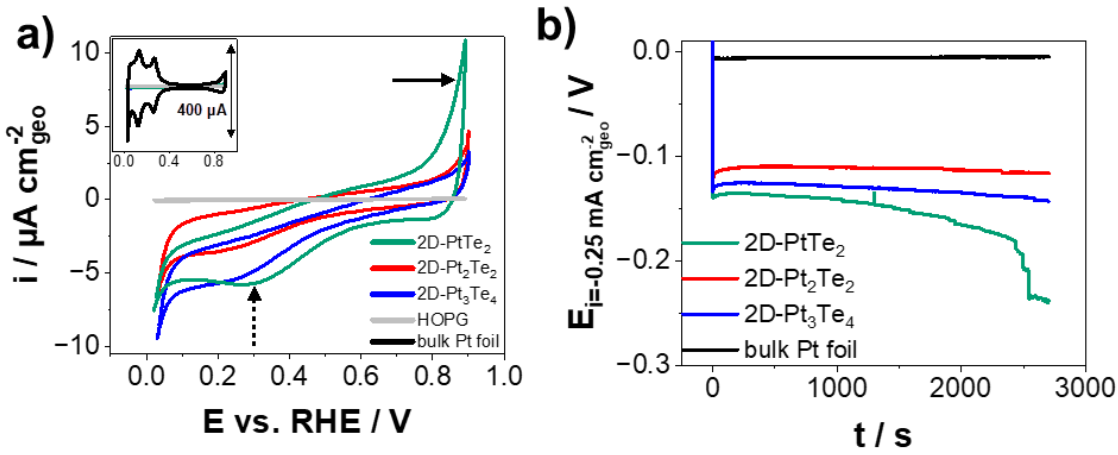

Figure 38: *Electrochemical stability of 2D-Pt_xTe_y@HOPG materials.* ***a)*** *Cyclic voltammograms recorded in Ar-saturated 0.5 M H_2SO_4 with a scanrate of 50 mV s^{-1}. The inset shows the CV of a Pt foil in comparison with the 2D Pt chalcogenides.* ***b)*** *Chronopotentiometry at $i = -0.25\ mA\ cm_{geo}^{-2}$ for t = 45 min. ($\dot{V}_0 = 1\ mL\ min^{-1}$). The chosen current density limited gas bubble formation, a critical factor in our flow cell setup (see* ***Figure 19b****) due to the height of the working electrode chamber ($H = 0.7\ mm$). The time period was chosen as $t = 45\ min$. The volume flow was set at $\dot{V}_0 = 1$ mL min^{-1} so that with a measurement duration of 45 min, the total pumped electrolyte volume was 45 mL. In this setup, the experiment duration was limited by the maximum volume of the syringe used in the syringe pump (50 mL).*

Figure 38a presents the CVs for all 2D-Pt_xTe_y phases, bulk Pt foil and the HOPG substrate in Ar-saturated 0.5 M H_2SO_4. All Pt_xTe_y phases exhibit similar CV profiles, each displaying a reduction peak between 0.1 and 0.5 V vs. RHE (see dashed arrow in **Figure 38a)**. The current densities of the reduction peaks are higher for 2D-$PtTe_2$ (green line) and 2D-Pt_3Te_4 (blue line) compared to 2D-Pt_2Te_2 (red line). Additionally, an oxidation current with an onset at approximately 0.7 V vs. RHE is observed for all phases, which is higher for 2D-$PtTe_2$ compared to the other phases (see solid arrow in **Figure 38a)**. Notably none of the Pt_xTe_y phases shows any Pt features, which confirms the absence of metallic Pt in these materials. The observed redox peaks for the 2D-Pt_xTe_y materials can be attributed to the oxidation and reduction of Te species, as reported in the literature.[76,241] The distinct, high oxidation current at around 0.7 V vs. RHE associated with the $PtTe_2$ phase suggests that it is particularly prone to chalcogenide oxidation and potential irreversible degradation under these conditions. The HOPG reference (grey curve) shows only capacitive currents, indicating the absence of active material. The inset in **Figure 38a** shows the characteristic CV profile of the bulk Pt foil as a reference with the typical pseudo capacitive features of a polycrystalline Pt electrode including hydrogen underpotential deposition and desorption and Pt(oxy)hydroxide formation. The CVs of the three 2D-Pt_xTe_y phases and HOPG are depicted in this inset with the same scaling. The obtained current densities for these materials are much lower compared to Pt. Because of the orders of magnitude larger double layer capacitance for the bulk Pt foil ($C_{dl} \approx 160\ \mu F$) the higher current densities for Pt can be explained by the higher surface area of the Pt foil as well as differences in the specific capacitance of metallic Pt vs. Pt_XTe_y materials. **Figure S8** shows the CVs recorded at pH = 7 in phosphate buffered and Ar-saturated 0.1 M $NaClO_4$. The same trends are seen as in 0.5 M H_2SO_4. All phases show the features for oxidation and reduction of Te species. The currents for oxidation (starting from 0.6 V vs. RHE) and reduction (around 0.5 V vs. RHE) for the $PtTe_2$ phase (green curve) are higher here as well compared to the Pt_2Te_2 (red curve) and Pt_3Te_4 (blue curve) phases.

Subsequent to the CV tests, galvanostatic durability measurements for all 2D-Pt_xTe_y@HOPG materials were perfromed at $i = -0.25\ mA\ cm_{geo}^{-2}$ for 45 min in 0.5 M H_2SO_4. The resulting chrono-potentiometric (CP) curves (**Figure 38b**) reveal the following: Comparing the 2D-Pt_xTe_y phases, Pt_2Te_2 (red) has the highest overall

highest potential, starting at $E_{i=-0.25\ mA\ cm_{geo}^{-2}}$=-0.126 V vs. RHE and rising slightly to -0.110 V vs. RHE, with minimal change over 45 min. The chronopotentiometry of Pt_3Te_4 (blue) begins at -0.133 V vs. RHE, rises to -0.126 V in 500 s, then drops by 17 mV over the course of 45 min. $PtTe_2$ (green) starts this test at the lowest potential with -0.140 V and decreases to -0.237 V within the whole time period. Bulk Pt foil (black) shows the highest, most stable potential at -0.006 V vs. RHE with no noticeable drift. Interpretation of these results shows that out of the 2D-Pt_xTe_y@HOPG samples, the Pt_2Te_2 phase demonstrates the best durability and best activity in this chronopotentiometry test, maintaining a high potential with minimal degradation.

In contrast, 2D-$PtTe_2$, which initially during the LSVs (**Figure 37a**) shows high activity, shows the lowest starting potential in the galvanostatic test. This is consistent with a degradation process, which will be further investigated in the following chapters. Furthermore, 2D-$PtTe_2$ also displays the steepest decrease in potentials, signalizing that this material is also the least durable under the galvanostatic HER conditions. The bulk Pt foil is the most active and stable under these conditions, due to its lowest overpotentials and negligible changes during the test.

To summarize these stability findings, during galvanostatic accelerated stress testing, the 2D-Pt_xTe_y phases rank in durability and activity as follows: 2D-Pt_2Te_2 > 2D-Pt_3Te_4 > 2D-$PtTe_2$. Given these clear indications of degradation, especially for 2D-$PtTe_2$, the next section will focus on monitoring relative material changes with Raman spectroscopy throughout the full electrochemical protocol.

5.3.4 Monitoring Stability During the Electrochemical Protocol with Raman Spectroscopy

To better understand the stability differences among the 2D-Pt_xTe_y phases during electrochemical treatment, Raman mapping was performed at various stages of the process. In the resulting Raman mappings, the peak areas of the highest 2D-Pt_xTe_y peak (compare with **Figure 36a**) for each phase were integrated and normalized with the peak area of the graphite band from the HOPG substrate as an internal standard. For 2D-$PtTe_2$ this corresponds to the normalized Raman peak area of the E_g band with respect to the G band , for 2D-Pt_2Te_2 it is the normalized Raman peak area of the A_{1g} band relative to the G band, and for 2D-Pt_3Te_4 it is the normalized Raman peak area of the E_g ($PtTe_2$) band with respect to the graphite G band. This gave normalized Raman peak area mappings after each electrochemical step (see protocol in **Figure 23**).

Figure 39 highlights these mappings at three key stages: the initial state (after step **(1)**), after the LSVs (after step **(4)**) and after the electrochemical protocol (after step **(8)**) for all materials. For comprehensive analysis, all normalized Raman peak area mappings corresponding to each electrochemical step (**(1)-(8)**, see measurement protocol in **Figure 23**) are displayed in **Figure S9** for 2D-$PtTe_2$, **Figure S10** for 2D-Pt_2Te_2 and **Figure S11** for 2D-Pt_3Te_4.

For 2D-$PtTe_2$, the normalized Raman peak area of the E_g band gradually decreases from the initial mapping ((**Figure 39a-(1)**) to the final mapping ((**Figure 39a-(8)**), as indicated by the color shift from initially predominantly red, over green ((**Figure 39a-(4)** towards blue.

For the 2D-Pt_2Te_2 phase, (**Figure 39b** shows that the mappings display consistently mixed high and low normalized A_{1g} peak areas at all stages (see also **Figure S10**), with no clear overall trend.

Figure 39c presents the normalized $A_{E_g(PtTe_2)/G}$ peak area mappings of the of the Pt_3Te_4 phase. Initially $A_{E_g(PtTe_2)/G}$ is high, as indicated by red colors (**Figure 39c-(1)**), but drops after the first electrochemical OCP measurement (color shift towards green **Figure S11-(2))** and is maintained throughout the electrochemical protocol then (**Figure 39c-(4)** and **Figure 39c-(8)**). Larger blue lines, indicative of material loss are

visible for all materials after different electrochemical steps, see for **Figure 39a-(4),** **Figure 39b-(4)** and **Figure 39c-(8).**

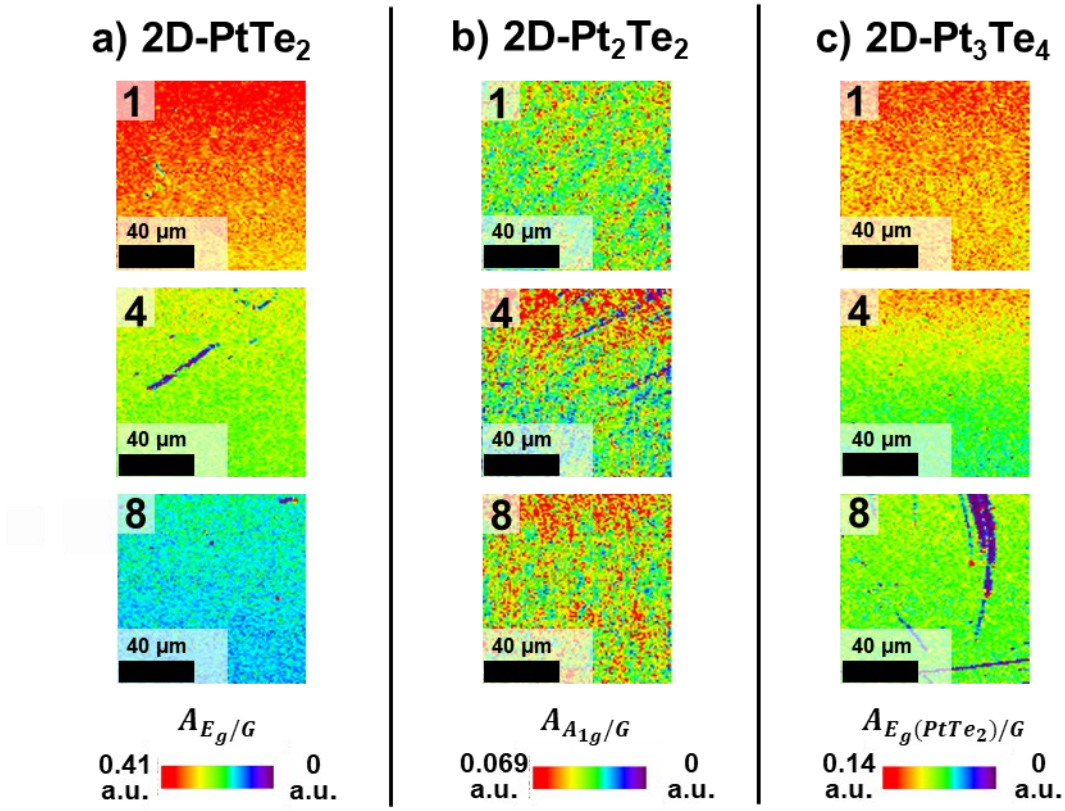

Figure 39: *Ex-situ Raman mappings of the normalized peak areas after the different electrochemical treatment steps: 1 – initial state, 4 – after linear sweep voltammetry in 0.5 M H_2SO_4, 8 – after capacitance measurement in 0.5 M H_2SO_4.* ***a)*** *Normalized Raman peak area mapping $A_{E_g/G}$ of 2D-$PtTe_2$.* ***b)*** *Normalized Raman peak area mapping $A_{A_{1g}/G}$ of 2D-Pt_2Te_2.* ***c)*** *Normalized Raman peak area mapping $A_{E_g(PtTe_2)/G}$ of 2D-Pt_3Te_4.*

To gain more statistical insight into these mappings, the average and standard deviation of the normalized peak areas within each mapping were calculated. These trends are summarized in **Figure 40**, where the average normalized peak area is plotted against the electrochemical step (from 1-initial state to 8- after the capacitance measurements). For 2D-$PtTe_2$@HOPG (**Figure 40a**) the average normalized peak area $\bar{A}_{E_g/G}$ declines from the initial value of 0.33±0.03 to 0.14±0.02 after the capacitance measurements (8 in **Figure 40a**), corresponding to a loss of approximately 60 %. In contrast, 2D-Pt_2Te_2 (**Figure 40b)** shows relatively constant average normalized peak area $\bar{A}_{A_{1g}/G}$ of 0.028 to 0.042 with standard deviations of

around 0.01. For the Pt_3Te_4 phase (**Figure 40c**) the average $\bar{A}_{E_g(PtTe_2)/G}$ decreases from the intial 0.10±0.01 (1 in **Figure 40c**) to 0.09±0.02 (2 in **Figure 40c**) after the first OCP measurement in phosphate buffered 0.1 M $NaClO_4$ and then drops only slightly till 0.07±0.01 after the full electrochemical sequence (8 in **Figure 40c**). This corresponds to a normalized peak area loss of around 30 %.

Interpreting these trends, the steady decline in the average normalized peak area $\bar{A}_{E_g/G}$ with the electrochemical steps (see **Figure 40a**) along with the corresponding color shift in the Raman mappings (**Figure S9** and **Figure 39a**), indicates significant degradation of 2D-$PtTe_2$ during the electrochemical treatments. This correlates with its poor durability in the chronopotentiometry test, which is the penultimate step in the protocol. For 2D-Pt_2Te_2 the average normalized peak areas change minimally, but the relatively high standard deviations compared to the averages, as well as the non-uniform color distributions, point to significant sample heterogeneity. Despite this, its presumed higher stability as indicated by Raman spectroscopy, is reflected by lower absolute potentials in the chronopotentiometry test (**Figure 38b**), surpassing 2D-$PtTe_2$. 2D-Pt_3Te_4 exhibits only a slight decrease in $\bar{A}_{E_g(PtTe_2)/G}$, indicating less degradation compared to 2D-Pt_2Te_2 and accordingly showing the second-best durability in the chronopotentiometry tests. In all phases, the dark blue lines observed after certain electrochemical steps likely indicate “cracks” within the 2D films of the Pt_XTe_Y phases. To sum up, a high degradation behavior for 2D-$PtTe_2$ and a smaller one for 2D-Pt_3Te_4 using Raman mapping is revealed. However, it remains unclear whether this degradation results solely from delamination of the van der Waals materials or if it involves chemical transformations, such as the reduction of Pt^{4+} to metallic Pt. The latter would also lead to decreased Raman intensity, since metallic Pt is not Raman active. To investigate this further, post-mortem XPS measurements were conducted, and compared with the initial XPS spectra in **Figure S12**. The upper row displays the Pt 4f XPS spectra before the electrochemical protocol and the lower row afterwards. Deconvolution of the Pt $4f_{7/2}$ peaks revealed the same components after the electrochemical protocol compared to the initial state. For neither of the phases additional Pt^0 species could be found. This confirms that metallic Pt is not formed during the electrochemical processes. It indicates that the main mechanism of degradation for 2D-$PtTe_2$ and also for 2D-Pt_3Te_4 is then likely a delamination of the layers who are only weakly held together by van der waals interactions[100]. What

remains unclear is the trend of the average normalized Raman peak area and the high relative standard deviations of the letter for the 2D-Pt_2Te_2 phase. For that a more detailed Raman analysis of this phase was performed in the following section.

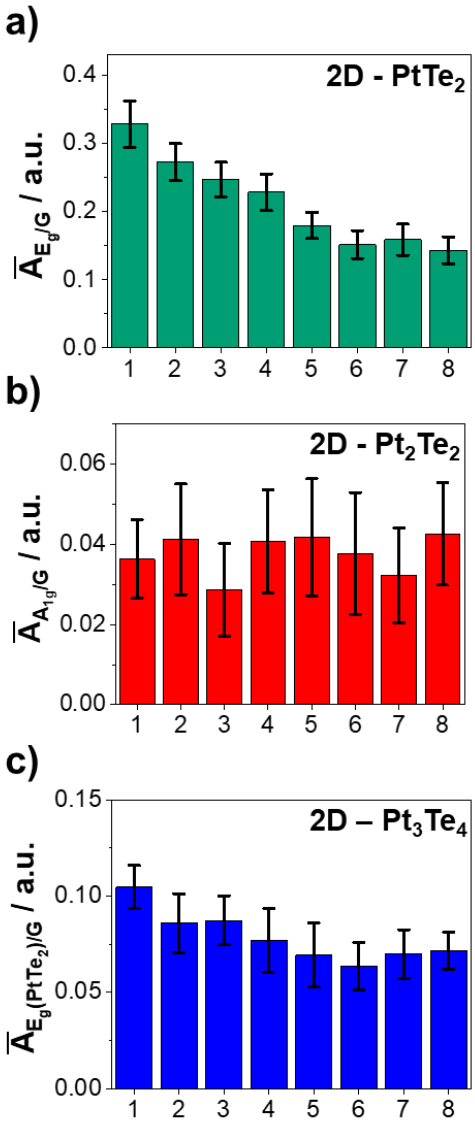

***Figure 40**: Raman investigation of the three different 2D-Pt_xTe_y materials after electrochemical treatment steps (see **Figure 23** for labelling as well): **1** – initial state, **2** – after OCP measurement in 0.5 M H_2SO_4, **3** – after OCP measurement in phosphate buffered 0.1 M $NaClO_4$, **4** – after linear sweep voltammetry in 0.5 M H_2SO_4, **5** – after CV in phosphate buffered 0.1 M $NaClO_4$, **6** – after CV in 0.5 M H_2SO_4, **7** – after CP, **8** – after capacitance measurement in 0.5 M H_2SO_4. **a)** Average normalized Raman peak area $\bar{A}_{E_g/G}$ of 2D-$PtTe_2$. **b)** Average normalized Raman peak area $\bar{A}_{A_{1g}/G}$ of 2D-Pt_2Te_2. **c)** Average normalized Raman peak area $\bar{A}_{E_g(PtTe_2)/G}$ of 2D-Pt_3Te_4. Error bars in **a)**, **b)** and **c)** show the standard deviation within the mappings. All mappings used for this analysis are displayed in **Figure S9**, **Figure S10** and **Figure S11**.*

5.3.5 Raman Principle Component Analysis of 2D-Pt_2Te_2

As shown previously, the averaged normalized peak area $\bar{A}_{A_{1g}/G}$ of 2D-Pt_2Te_2 remains relatively constant. However, the normalized peak area mappings **Figure 39b** and **Figure S10**) reveal significant heterogenity of the material throughout the electrochemical experiments. To further investigate this heterogeneity, additional single-spectrum Raman measurements at different locations on the sample were performed. These positions together with the position of the Raman mapping is indicated in the optical image of one Pt_2Te_2 sample in **Figure S13a**. All positions were chosen to be located inside the electrodes wetted area and inside the O-Ring (see **Figure 19**). The spectra from these four selected spots together with the average spectrum from the Raman mapping location are presented in **Figure S13b**. The spectra split into two different groups. The red and purple lines (spot 2 and spot 4) exhibit three peaks at 93 cm^{-1}, 121 cm^{-1} and 187 cm^{-1}, which can be assigned to the E_g, A_{1g} and further E_g modes of the 2D-Pt_2Te_2 phase[234]. The peak ratios agree with the initially recorded Raman spectra (compared with **Figure 36a**). However, the black and blue curves from spot 1 and spot 3 show a different behavior. The peaks at 93 cm^{-1} and 121 cm^{-1} are significantly enlarged compared to the Raman spectra from spots 2 and 4. Additionally, a new peak is found at 159 cm^{-1}. This peak can be assigned to the A_{1g} lattice vibration modes of the 2D-$PtTe_2$ or 2D-Pt_3Te_4 phase. This suggests that some regions of the whole 2D-Pt_3Te_4 surface experience transformation from 2D-Pt_2Te_2 into 2D-Pt_3Te_4. To confirm this hypothesis, a principal component analysis at a selected spot using the TrueComponent software feature of WITec Project SIX analysis package was performed. Two components were used: the initial spectra of the 2D-Pt_2Te_2 and 2D-Pt_3Te_4 phases as shown in **Figure S14a**. The results of the principal component analysis after selected electrochemical steps is shown in **Figure 41**. There the first row presents the Pt_2Te_2 phase component mapped as a percentage, and the second row shows the Pt_3Te_4 phase component similarly mapped. **Figure S14b** shows the statistical analysis of these component analysis after each step. The trend in both figures is clear: initially the Raman mapping indicates that the dominant component is Pt_2Te_2 (93 %), with a majority of the area in red, while the Pt_3Te_4 component is only found in some regions (7 %). This also agrees with the assessment of the sample composition from the initial XPS spectra (**Figure 36c)**, which indicated around 10 % of $PtTe_2$ in the material. As seen in **Figure 41**, the Pt_3Te_4 component continually decreases throughout the electrochemical protocol. **Figure S14b** confirms

statistically that the percentage of both components after the last step is 63 % for 2D-Pt_2Te_2 and 37 % for 2D-Pt_3Te_4. This partial phase transformation can explain why the interpretation of the average normalized Raman peak area $\bar{A}_{A_{1g}/G}$ is complicated. The partial phase transformation from 2D-Pt_2Te_2 to 2D-Pt_3Te_4 during the electrochemical protocol increases the peak intensity of the A_{1g} peak signifcantly (see **Figure S13b**), because the 2D-Pt_3Te_4 phase overall has bands with higher Raman intensity. This heavily influences the analysis of the normalized Raman peak area $\bar{A}_{A_{1g}/G}$ and explains the observed variations in **Figure 40b**. It should be noted that according to the Raman analysis at different spots (see **Figure S13**) and post-mortem XPS (see **Figure S12**) analysis, this transformations seems localized, indicating most of the sample remains in the 2D-Pt_2Te_2 phase state. In summary, the 2D-Pt_2Te_2 phase partially transforms into 2D-Pt_3Te_4 (at the location investigated herein 37 % of 2D-Pt_3Te_4 in the end) at certain sites during the electrochemical protocol, likely via a degradation mechanism. These results represent the first electrochemical and structural assessment of the 2D-Pt_2Te_2 phase. Importantly, this thermodynamic metastability during electrochemical testing does not appear to hinder its activity during the LSVs (**Figure 37a**) or galvanostatic experiments (**Figure 38b**).

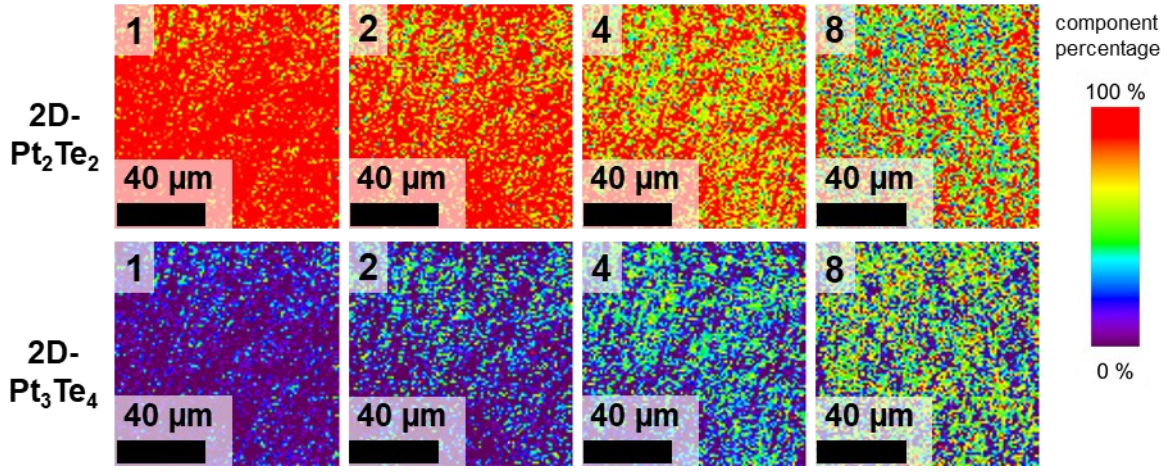

Figure 41: *Principal component analysis of the Raman mappings of 2D-Pt_2Te_2@HOPG after different electrochemical steps: 1 – initial, 2 – after OCP measurement in phosphate buffered 0.1 M $NaClO_4$, 4 - after linear sweep voltammetry in 0.5 M H_2SO_4, 8 - after capacitance measurement in 0.5 M H_2SO_4.*

5.3.6 Density Function Theory (DFT) – Theoretical Basis for the Activity Trends

To better understand the trends in catalytic activity observed in in **Figure 37**, we compared the *Gibb's* free energy diagrams of Pt_xTe_y compounds including both pristine and Te-vacancy surfaces. **Figure 42a**, shows the structures of the Pt_xTe_y compounds used for DFT calculations. The top half of the figure represents hydrogen adsorption on pristine materials, while the lower half focuses on hydrogen adsorption sites on Te vacancies with Pt atoms depicted in blue, Te atoms in orange, and adsorbed hydrogen atoms (H*) in green. Based on these structures **Figure 42b** shows the free energy profiles for the HER on pristine surfaces and **Figure 42c** of the HER on surfaces with Te-vacancy. For pristine systems, Pt_3Te_4-based structures (e.g., $PtTe_2/Pt_2Te_2$ and $Pt_2Te_2/PtTe_2$, in blue colors) exhibit lower HER barriers than $PtTe_2$ (green line in **Figure 42b**), with ΔG_H values of 1.059 eV and 0.791 eV, respectively, compared to 1.183 eV for $PtTe_2$ (**Table S3**). Among the pristine phases, Pt_2Te_2 (red line in **Figure 42b**) shows the most favorable catalytic activity (ΔG_H = 0.775 eV), although all pristine values remain considerably higher than that of Pt(111) (−0.222 eV [242]).

When Te vacancies (**Figure 42c**) are introduced, the catalytic performance improves dramatically. As summarized in **Table S4**, ΔG_H values decrease to nearly ideal thermoneutral levels, with $PtTe_2$ at 0.047 eV (green line in **Figure 42c**), Pt_2Te_2 at 0.116 eV (red line in **Figure 42c**), and $PtTe_2/PtTe_2$ at 0.007 eV(green dashed line in **Figure 42c**). Interestingly, the absolute values of ΔG_H of hydrogen on different Pt_xTe_y materials with Te vacancy are lower than that on pristine Pt (111) surfaces [242]. The dramatic lowering of the energy barrier highlights the critical role of Te vacancies in enhancing catalytic activity, pointing toward defect engineering as an effective strategy for optimizing Pt_xTe_y-based HER catalysts.

These computational insights are fully supported by the experimental data. The experimental specific activity for the 2D-Pt_xTe_y phases follows the order 2D-$PtTe_2$ ≈ 2D-Pt_2Te_2 >> 2D-Pt_3Te_4 (**Figure 37a,e**). and aligns well with the free energy profiles shown in **Figure 42b** for 2D-Pt_xTe_y surfaces with Te vacancies. Small differences between ΔG_H at V_{Te} of 2D-$PtTe_2$ and 2D-Pt_2Te_2 fall within margin of error of DFT calculations (typically 0.1 to 0.2 eV [243]) . While vacancies in the 2D-Pt_xTe_y phases reduce the Gibbs free energy of hydrogen adsorption, the HER activity of these transition metal chalcogenides (TMCs) remains lower than that of Pt, as shown in **Figure 37a**. The ΔG_H of hydrogen adsorption for Pt is lower (see black line in **Figure**

42b) on the pristine surface compared to any of the materials. Likely the 2D-Pt_xTe_y surfaces are not exclusively composed of vacancies but predominantly retain a pristine, less active structure, explaining the still strong gap in HER activity between Pt and these materials.

Overall, the DFT calculations align well with the experimental HER activity results. These results highlight the advantages of combining controlled single-crystal synthesis, electrochemical evaluation in a specialized flow cell and DFT calculations.

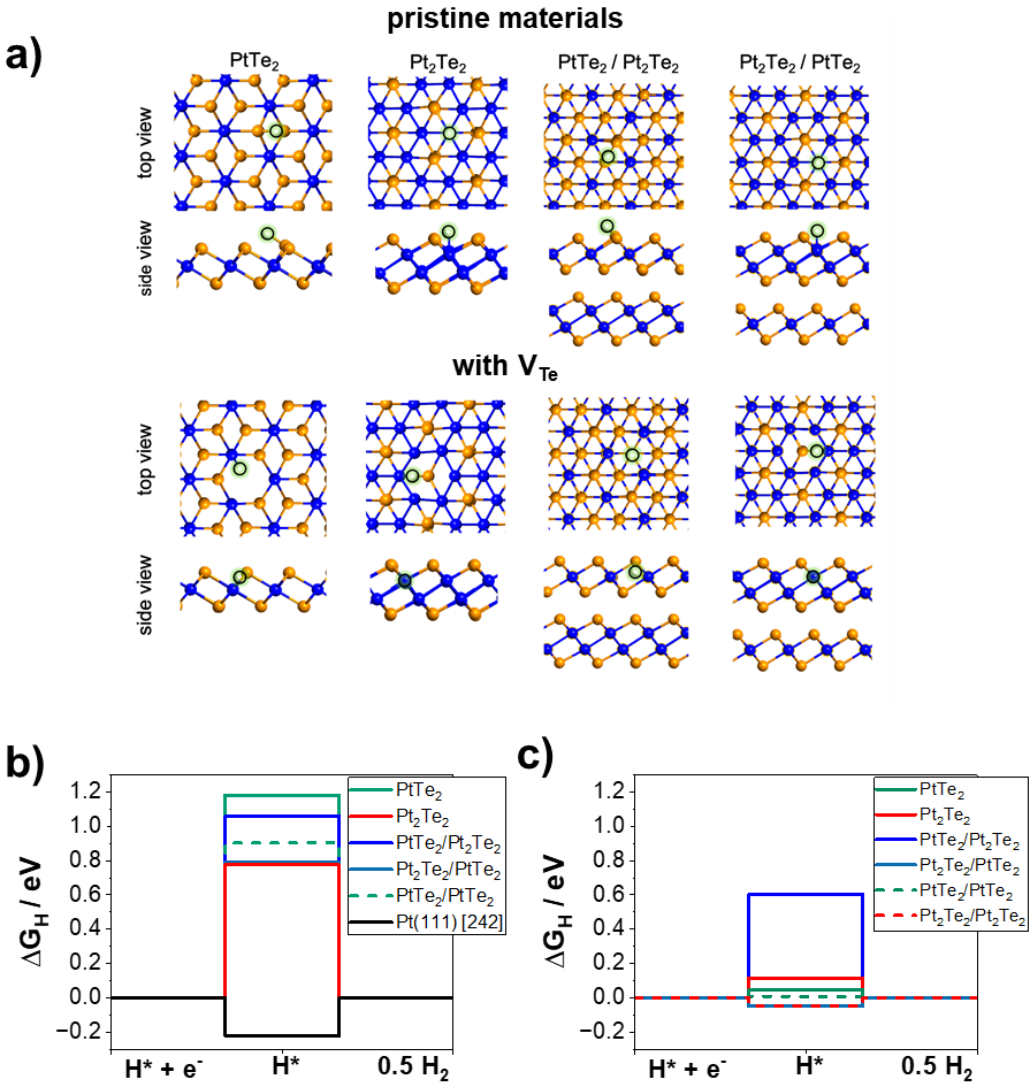

Figure 42: a) *Adsorption configurations of hydrogen on 2D-Pt_xTe_y materials with pristine and Te-vacancy surfaces. Blue, orange, and white spheres represent Pt, Te, and H atoms, respectively. Free energy profiles of the HER on 2D-Pt_xTe_y materials and Pt(111) at equilibrium:* ***b)*** *pristine surfaces and* ***c)*** *Te-vacancy surfaces.*

5.3.7 Conclusions to Chapter 5.3

In this study, the HER activity and durability of various 2D-Pt_xTe_y@HOPG materials was compared. After synthesizing three different phases (2D-$PtTe_2$, 2D-Pt_2Te_2 and 2D-Pt_3Te_4) with MBE, XPS and Raman spectroscopy confirmed the high phase purity of the 2D materials. Electrochemical testing in a custom-designed impinging jet flow cell revealed distinct activity and durability differences between the phases. HER activity was in the order: 2D-$PtTe_2$ ($\left|E_{-0.1\ mA\ cm_{geo}^{-2}}\right| = 78 \pm 7\ mV\ vs. RHE$) ≈ 2D-$Pt_2Te_2$ ≫ 2D-Pt_3Te_4 ($\left|E_{-0.1\ mA\ cm_{geo}^{-2}}\right| = 115 \pm 11\ mV\ vs. RHE$). DFT calculations demonstrated that the activity differences between the phases can be explained by differences in hydrogen adsorption *Gibbs* free energies (ΔG_H) at Te vacancies, which followed a parallel trend 2D-$PtTe_2$ (0.047 eV) ≈ 2D-Pt_2Te_2 ≪ 2D-Pt_3Te_4. *Tafel* slope analysis confirmed the same rate-determining step across all phases. The durability of all materials was investigated throughout the protocol with Raman spectroscopy. 2D-$PtTe_2$ showed degradation likely via delamination during electrochemical testing with a loss of normalized Raman material peak area $\bar{A}_{E_g/G}$ of around 60 %. Notably, 2D-Pt_2Te_2 underwent partial phase transformation into 2D-Pt_3Te_4 (up to 37 % transformation at certain locations), as revealed by Raman spectroscopy, yet maintained high catalytic activity throughout the durability protocol. Conversely, 2D-Pt_3Te_4 demonstrated the highest durability, showing only minor changes in Raman mappings ($\bar{A}_{E_g(PtTe_2)/G}$ drop of only 30 % throughout the electrochemical protocol) and exhibiting the second-best performance in galvanostatic durability tests. XPS analysis confirmed that none of these phases degraded into metallic Pt. Overall, by combining well-structured 2D material synthesis, electrochemical testing in a newly designed flow cell and DFT calculations, we directly correlate theoretical activity trends with experimental electrochemical activity. Furthermore, Raman spectroscopy revealed new insights into material stability during HER testing of this material class. These insights contribute to the rational design of noble metal chalcogenide catalysts with reduced Pt content for HER applications in the future.

5.4 The Influence of Iron Impurities on Ni HER Activity in Alkaline Media

This chapter 5.4 contains adapted parts from the submitted manuscript: *Khavala V.B.[=], Schneemann C.[=], Kallina V., Dosche C., Thomas T., Murty B.S., Oezaslan M., Concentration-Dependent Effects of Iron Impurities on Nickel Electrodes for Hydrogen Evolution Reaction in Alkaline Media, International Journal of Hydrogen Energy* ***2025****, submitted. The original manuscript has been adapted for this thesis and reflects equal contributions from both first authors, V. B. Khavala and C. Schneemann.*

Contributions:

- *C. Schneemann conducted the initial literature review, analyzed chronopotentiometric data, cyclic voltammetry (CV) and part of the impedance spectra, prepared the iron stock solutions, prepared XPS and µ-XRF reference samples, performed and analyzed ICP-OES measurements and tested the electrochemical protocol. Furthermore C. Schneemann adapted and added onto the submitted manuscript draft for this thesis.*
- *V. B. Khavala performed the majority of electrochemical measurements, prepared samples for XPS, µ-XRF, and SEM analyses, analyzed µ-XRF data, linear sweep voltammetry (LSV), Tafel slopes, and majority of the impedance spectra, and analyzed SEM data.*
- *Both C. Schneemann and V.B. Khavala developed and refined the measurement protocols, measured SEM samples, curated and discussed data within the project team, visualized data, developed the figure story for the manuscript, collaborated on manuscript drafting, and reviewed each other's contributions.*
- *V. Kallina assisted in developing the µ-XRF methodology, conducted µ-XRF measurements, discussed data within the team, and reviewed the manuscript.*
- *C. Dosche ran and analyzed the XPS data.*
- *C. Schneemann and M. Oezaslan developed the original project idea.*
- *M. Oezaslan supervised the work, discussed the data within the project team and reviewed and commented on the original submitted manuscript draft.*
- *B.S. Murty and T. Thomas discussed data within the project team and reviewed and commented on the original submitted manuscript draft.*

Preface:

Research on the HER in alkaline media is focused on investigation of long-term stability effects on the electrodes. Within this topic effects of iron impurities on the alkaline hydrogen evolution reaction (HER) for nickel-based electrodes remain insufficiently understood. Contrary to its low intrinsic activity, iron deposited from electrolyte on the Ni surface can either enhance HER kinetics due to the increased surface roughness or act as a protective layer against the NiH formation.

This chapter systematically evaluated how different iron concentrations affect the HER activity and durability of polycrystalline Ni (poly-Ni) as a model electrode system in 0.1 M KOH. Initially, marginal differences in HER activity are observed between 0 – 14 ppm Fe^{z+} species concentrations. However, 24 h chronopotentiometry tests at $i = -10\ mA\ cm_{geo}^{2}$ show as follows: Fe^{z+} species between 0 – 3 ppm leads to a pronounced deactivation, while higher concentrations (6 – 14 ppm) maintain relatively stable operation over time. The combined structural (SEM, XRF, XPS) and electrochemical analyses enables to correlate the changes in HER overpotential with the electrochemically accessible Ni sites instead of the surface roughness. The model proposed herein, establishes a clear link between protective iron-based particle deposition and Fe^{z+} concentration to prevent the NiH-induced deactivation. This study shows a critical impurity threshold ($\geq 6\ ppm$) Fe^{z+} in the electrolyte to exploit the beneficial effects of iron on HER durability of alkaline water electrolysis.

5.4.1 Effects of Iron Impurities on the Initial HER Activity for poly-Ni Electrodes

After investigating new catalysts and setups for the HER in acidic media, the focus in this chapter shifts to the HER in alkaline media. The main objective of this study is to uncover the effects of trace amounts of Fe^{z+} species on the HER activity for the polycrystalline nickel (poly-Ni) electrodes in 0.1 M KOH.

Based on the *Pourbaix* diagram for iron-water system in 0.1 M KOH (pH = 13), Fe^{z+} ions are not stable as "free" ions in solution [244]. Instead, they rapidly convert to insoluble iron hydroxides or oxides, such as $Fe(OH)_2$, Fe_3O_4, etc., which may coexist within the electrolyte solution. Due to the complex speciation, the exact oxidation state of Fe species cannot be definitively determined and is referred to as Fe^{z+} ions throughout this chapter. Advanced techniques like *Mössbauer* spectroscopy would be necessary for such species characterization.

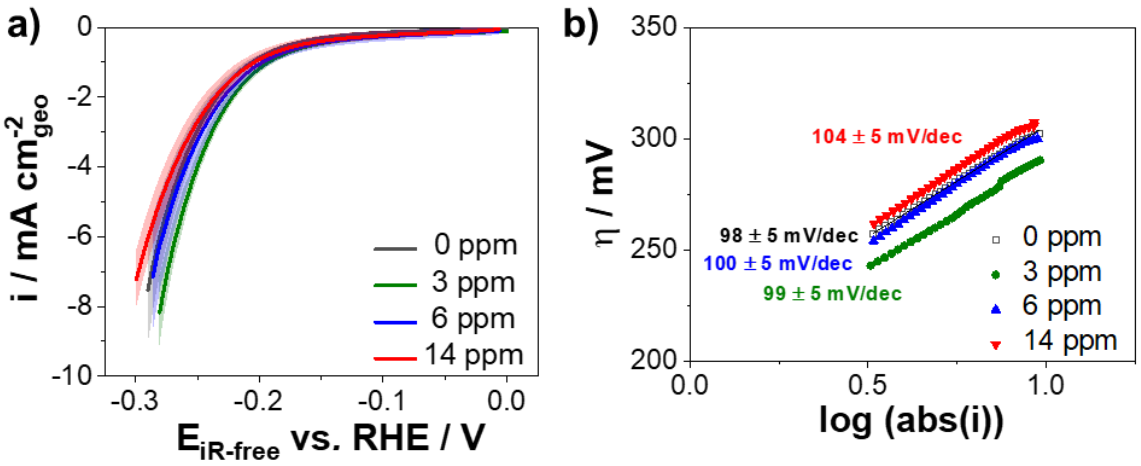

Figure 43: *Effects of iron impurities on the initial HER activity for a poly-Ni electrode. a) Average and standard deviations of polarization curves recorded from −0.4 to 0 V vs. RHE with a scan rate of 10 mV s^{-1} at 2400 rpm in Ar-saturated 0.1 M KOH spiked with different amounts of iron ions. Translucent areas represent the standard deviations within a sample number of N=7 independent measurements. b) Tafel plots based of representative examples of HER polarization curves for each Fe^{z+} concentration.*

The first step is to understand the effects of Fe^{z+} ions on the initial HER activity of poly-Ni electrodes via linear sweep voltammetry (LSV) method in 0.1 M KOH electrolyte solution. It is noted that 0.1 M KOH solution used in this chapter was utilized as received without any additional purification to remove trace metal impurities, e.g. iron. The ICP-OES analysis of the KOH pellets (**Table S5**) reveals trace amounts of Fe and

Zn at the ppb level; orders of magnitude lower than the ppm-range Fe concentrations examined in this chapter. Consequently, the presence of residual iron in the KOH pellets cannot be entirely excluded, but it is referred to as “0 ppm Fe^{z+}” for the electrolyte without addition of iron species.

Figure 43a displays the HER polarization curves of the poly-Ni electrodes exposed to 0.1 M KOH electrolyte solutions with 0 ppm (black), 3 ppm (green), 6 ppm (blue), and 14 ppm (red) Fe^{z+} species, respectively. These measurements are based on seven independent replicates. The mean curves are shown alongside semi-transparent shaded regions in corresponding colors which indicate the standard deviations. All curves show typical HER behavior: with increasing cathodic potential, the HER current density exponentially increases. Independent of Fe^{z+} concentration in the electrolyte, the polarization curves show comparable current density values at given iR-corrected potential. For example, the overpotential to achieve a current density of $-3\ mA$ cm^{-2}_{geo} ($\eta_{i=-3\ mA\ cm^{-2}_{geo}}$) for the poly-Ni electrodes exposed to 0, 3, 6, and 14 ppm Fe^{z+} species are $251 \pm 7\ mV$, $239 \pm 4\ mV$, $248 \pm 9\ mV$ and $255 \pm 8\ mV$ vs. RHE, respectively. The electrode exposed to 3 ppm Fe^{z+} appears marginally more active with a difference of 9 - 16 mV, compared to the other measurements. Several factors may contribute to this observation. Iron was reported to enhance HER activity by forming active Ni–Fe hydroxide [150], re-activating Ni via nanoparticle detachment, $HFeO_2^-$ oxidation or reduction of fresh highly active iron particles [172], respectively. Conversely, pure iron has lower intrinsic HER activity than nickel in alkaline media [53,152,171]. As structural analysis of the surface was not performed immediately after the initial LSV measurements, the interpretation is limited. However, these variations are negligible compared to the more significant effects observed during 24-h galvanostatic experiments, as shown in subsequent sections.

The *Tafel* plots, which relate the overpotential (η) to the logarithm of current density, are shown in **Figure 43b**. Obviously, the *Tafel* slopes were nearly identical, averaging approximately 100 ± 2 mV/decade for measurements with various concentrations of Fe^{z+} species, indicating a common rate-determining step (rds) on the poly-Ni surface, irrespective of Fe^{z+} content. The *Volmer–Heyrovsky* mechanism, with the *Heyrovsky* step as the rate-determining step on nickel-based surfaces, is often proposed [37,245,246]. However, some studies have reported *Tafel* slopes indicating both *Volmer–Heyrovsky* and *Volmer–Tafel* mechanisms depending on the specific

conditions [37,128]. Therefore, a detailed analysis of the rds based on the *Tafel* slope was not conducted in this chapter. Our *Tafel* slope values across all the measurements align with the range of 80 - 120 mV/decade reported in literature [36,153,159,171,247]. Variations in *Tafel* slopes might result from differences in surface morphology [126,248–251] (e.g., porosity, nanostructuring), oxidation of the Ni surfaces (e.g. NiOOH) [252], local trapping of the H_2 bubbles on the surface [253] and overpotential range analyzed [254]. These factors highlight the complexity and sensitivity of HER kinetics to the Ni surface structure.

Thus, it can be concluded that the variations in Fe^{z+} ion concentration from 0 up to 14 ppm in 0.1 M KOH have only marginal impact on the initial HER activity of the poly-Ni electrodes.

5.4.2 Long-term Effects of Traces of Iron Impurities on the HER Activity for poly-Ni Electrodes

After the initial HER activity assessment on poly-Ni showed that Fe^{z+} cation impurities had little effect, next their impact over an extended period of time was analyzed. Therefore, the next electrochemical step involved a galvanostatic accelerated stress test (AST) at $-10\ mA\ \mathrm{cm}_{\mathrm{geo}}^{-2}$ for 24 hours in 0.1 M KOH with different Fe^{z+} concentrations. This current density was chosen because it is commonly suggested for benchmarking HER catalyst stability in RDE setups [53] and is the approximate current density expected for an integrated solar water-splitting device under 1 sun illumination operating at 10% solar-to-fuels efficiency [255]. An example of the raw data after 24 h galvanostatic AST is shown in **Figure S15a**. The relatively high noise in the experimental data is because of the strong hydrogen gas evolution at this current density. To reduce the noise, the raw data was then averaged over the first 60 seconds at each hour, followed by an iR-drop correction using data from the galvanostatic impedance spectroscopy (GEIS) measured once every hour at the same current density ($-10\ mA\ \mathrm{cm}_{\mathrm{geo}}^{-2}$). As the interest lied mostly in how much the HER activity for the poly-Ni changes compared to the initial state, the relative change of the overpotential at t = n hours $\Delta\eta$ were calculated as follows:

$$\Delta\eta = (E_{initial} - E°) - (E_n - E°) \tag{66}$$

where $E_{initial}$ is the iR-corrected and averaged potential at t = 0 h, E_n is the iR-corrected and averaged potential at t = n hours, and $E°$ is the standard thermodynamic potential for HER (0 V vs. RHE). This results in 24 points for 24 hours as represented in **Figure S15b**. The $\Delta\eta$ values at each hour were then averaged over N = 7 individual measurements and represented in **Figure 44**.

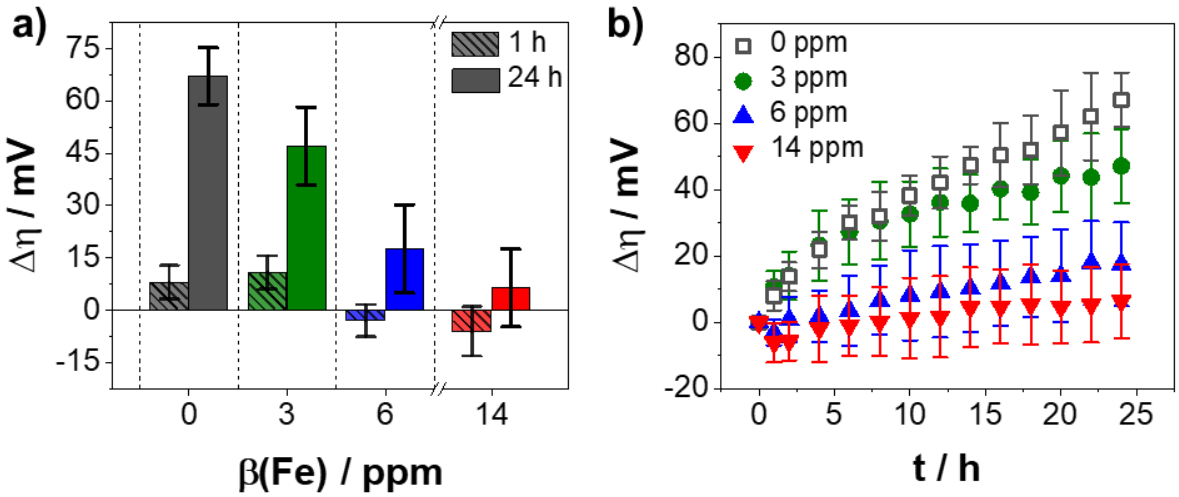

Figure 44: *Influence of Fe^{z+} cation impurities on a polycrystalline nickel electrode during galvanostatic experiment ($i = -10\ mA\ cm_{geo}^{-2}$).* ***a)*** *iR-corrected overpotential change $\Delta\eta$ within t =1 h and 24 h plotted against the Fe^{z+} cation concentration in 0.1 M KOH electrolyte.* ***b)*** *Time dependent $\Delta\eta$ for different Fe^{z+} cation concentrations in 0.1 M KOH. All error bars represent the standard deviations within a sample number of seven independent measurements.*

Figure 44a shows the overpotential change ($\Delta\eta$) within the first hour (translucent bar with diagonal hatching) and after 24 hours (solid color bar) for 0 (grey), 3 (green), 6 (blue) and 14 ppm (red) Fe^{z+} species, respectively. Noticeable differences are observed within the first hour despite of the relatively high error bars: the experiments with 0 and 3 ppm iron concentrations experience a significant increase in $\Delta\eta$ (~ 8 - 10 mV), whereas experiments with 6 and 14 ppm exhibits a small $\Delta\eta$ drop (~ $-3\ to\ -6$ mV). Over the full 24 hours these differences in HER activity became even more pronounced.

The poly-Ni electrode exposed to 0 ppm Fe^{z+} (grey squares) exhibits the greatest increase in overpotential (~67 ± 8 mV), followed by 3 ppm Fe^{z+} (green circles, ~47 ±

11 mV), 6 ppm Fe^{z+} (red triangles, ~17 ± 13 mV), with the smallest change observed in the poly-Ni electrode exposed to 14 ppm Fe^{z+} species (~6 ± 11 mV). **Figure 44b** shows the course of the iR-corrected overpotential change $\Delta\eta$ over time at $-10\ mA\ cm_{geo}^{-2}$. It is clearly visible that $\Delta\eta$ increases faster over time for the electrodes exposed to 0 ppm of Fe^{z+} (grey squares) and 3 ppm of Fe^{z+} (green squares) compared to 6 ppm of Fe^{z+} (blue squares) and 14 ppm of Fe^{z+} (red squares).

Based on these results, it can be pointed out that higher iron concentrations in 0.1 M KOH electrolyte maintain the HER activity for poly-Ni electrode during 24-h galvanostatic AST measurement ($-10\ mA\ \mathrm{cm}_{\mathrm{geo}}^{-2}$). The question arises whether the maintained HER activity is either due to an increase in surface area [157,171,173], or deposited iron layers, which reduce the hydrogen diffusion into the bulk nickel to prevent the formation of NiH [132,157,170,173].

5.4.3 Structural Characterization of Iron exposed poly-Ni Electrodes

To understand the mechanism of the HER durabilty on the poly-Ni electrode for 6 and 14 ppm Fe^{z+} cation concentrations during the 24 h galvanostatic AST measurement at $-10\ mA\ \mathrm{cm}_{\mathrm{geo}}^{-2}$, structural characterization was performed using SEM, μ−XRF, and XPS.

Figure 45a-d displays top-view SEM analysis of poly-Ni electrodes exposed to 0, 3, 6, and 14 ppm Fe^{z+} after 1 h and 24 h of galvanostatic measurement at $-10\ mA\ \mathrm{cm}_{\mathrm{geo}}^{-2}$, revealing notable differences in surface microstructures. The poly-Ni electrode exposed to 0 ppm Fe^{z+} species exhibits relatively low structural details after 1 hour, as seen in **Figure 45a**. After the AST measurement, island deposits are observed on the electrode surface. Similar island deposits have previously been attributed to the deposition of cationic impurities from the electrolyte solution during electrolysis [157,166,171,173]. The deposits observed in the 0 ppm spiked 0.1 M KOH solution point to the inherent iron and zinc impurities from the KOH pellets as verified by ICP-OES analysis (**Table S5**). In contrast, the electrodes exposed to higher concentrations of Fe^{z+} species show distinct variations in the microstructures compared to the deposition at 0 ppm Fe^{z+}. In **Figure 45b**, a higher amount of island deposits on the poly-Ni electrode surface exposed to 3 ppm Fe^{z+} could be seen after

just 1 h of galvanostatic experiment. These island deposits grow into larger deposits during the exposure time of 24 h.

Figure 45c-d show relatively dense films (but not completely closed) on the poly-Ni electrodes exposed to 6 and 14 ppm Fe^{z+} species in 0.1 M KOH after 1 h and 24 h of galvanostatic AST experiments. Notedly, the surface roughness of the poly-Ni electrode significantly increases higher Fe^{z+} ion concentration in 0.1 M KOH. To summarize, the top-view SEM images clearly show structural differences on the poly-Ni electrodes after 1 h and 24 h at $i = -10\ mA\ cm^{-2}_{geo}$ depending on the Fe^{z+} concentration in the electrolyte. While SEM analysis highlights variations in the microstructures of the deposits on poly-Ni electrodes after galvanostatic AST experiment at $i = -10\ mA\ cm^{-2}_{geo}$, it is essential to assess the chemical composition and mass loading of these deposits.

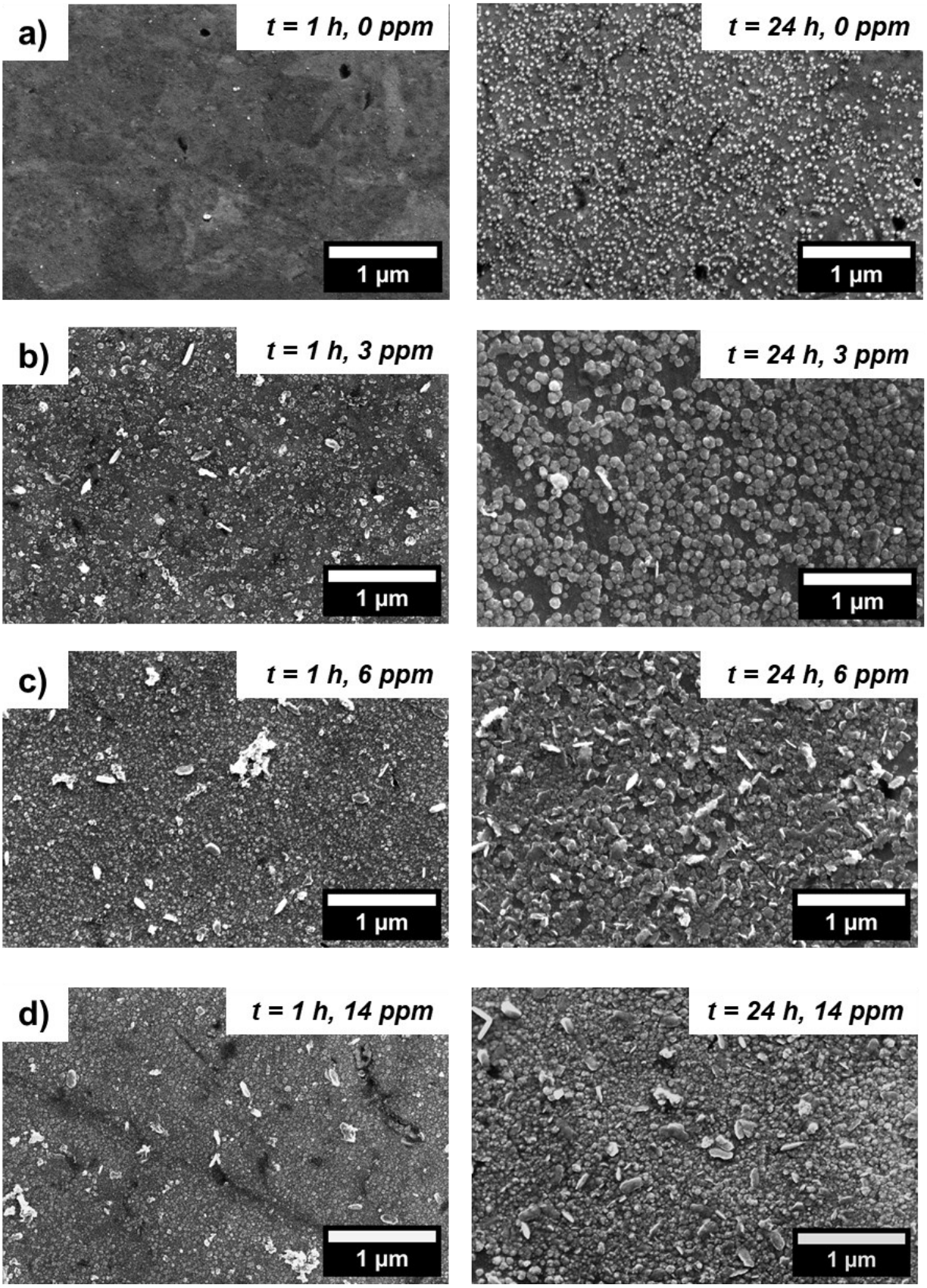

Figure 45: *Top-view SEM micrographs of polycrystalline nickel electrodes after galvanostatic experiment ($i = -10\ mA\ cm_{geo}^{-2}$) with exposure time of t = 1 h (left) and t = 24 h (right) and* ***a)*** *0 ppm,* ***b)*** *3 ppm,* ***c)*** *6 ppm and* ***d)*** *14 ppm Fe^{z+} species in 0.1 M KOH electrolyte solutions.*

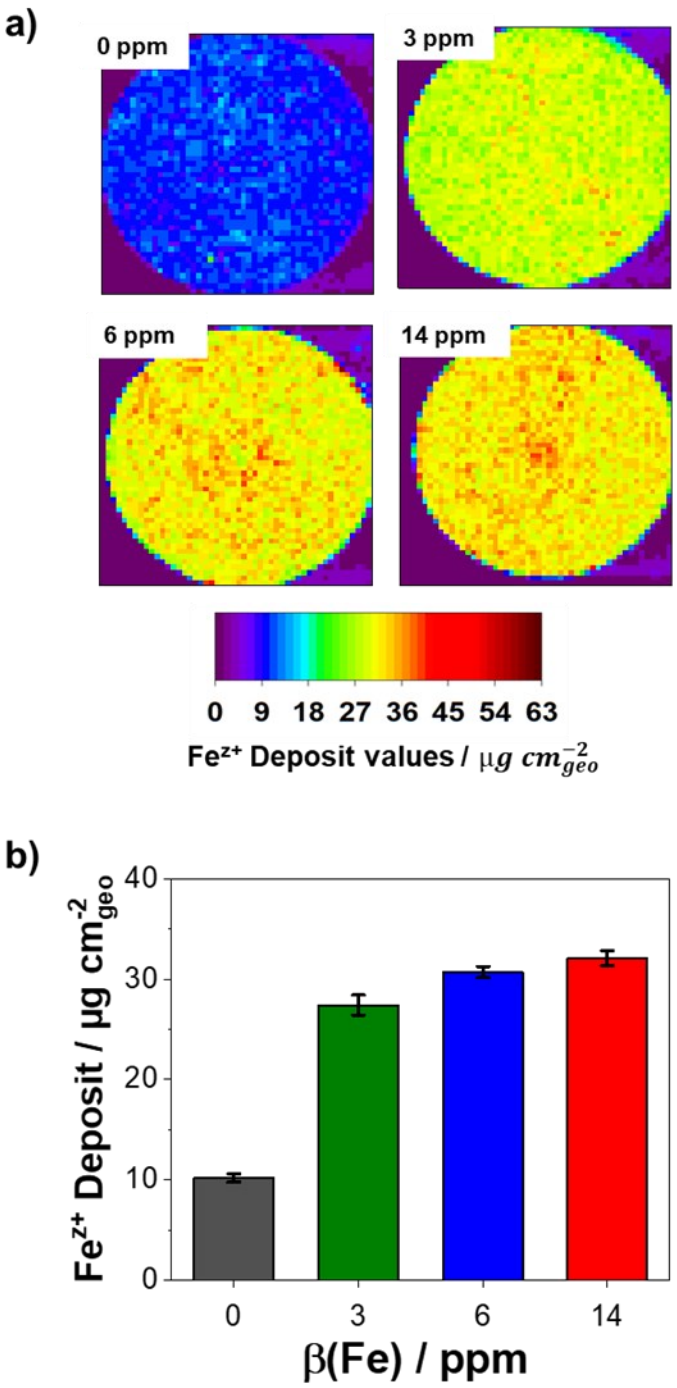

Figure 46: a) *μ−XRF mappings of the iron deposited on the poly-Ni electrode surface exposed to 0.1 M KOH solutions with different Fe^{z+} cation concentrations after 24-h galvanostatic experiments at $i = -10\ mA\ cm^{-2}_{geo}$. Thickness of the Fe deposits from 0 – 63 μg cm^{-2}_{geo} is represented with a rainbow colour scale.* ***b)*** *Plot of the average Fe deposits obtained from N = 4 samples after 24 h of galvanostatic measurement as a function of Fe^{z+} content added to the electrolyte. Data was acquired with a Rh source, spot size of 20 μm, acquisition time of 500 ms per pixel, pixel size of 0.01 mm^2 and <2 mbar vacuum level.*

To determine the elemental composition and spatial distribution of the deposits observed in the SEM micrographs (**Figure 45**), micro-X-ray fluorescence (μ−XRF) mapping was conducted on the poly-Ni electrodes directly after 24 h galvanostatic AST experiment. **Figure 46a** shows the μ−XRF mappings of the spatial distribution of iron deposits [in μg cm^{-2}] calculated based on the sum net counts of Fe Kα emission line. Data was acquired with a spot size of 20 μm and pixel size of 0.01 mm^2. The quantitative calibration of deposits was achieved by analyzing iron samples with known loadings ranging from 0 to 40 $\mu g\ cm_{geo}^{-2}$. The resulting linear standard curve (**Figure S16**) was used to estimate the iron loading onto the poly-Ni electrode surface. As Fe^{z+} concentration increases, the poly-Ni electrode mapping shifts from uniform bright blue at 0 ppm to light green with some yellow at 3 ppm, yellow with red spots at 6 ppm, and predominantly orangish red at 14 ppm. The heterogeneous pixel colors observed in the μ−XRF mappings as the Fe^{z+} concentration increases indicate a non-uniform spatial distribution of the iron deposits on the Ni surface. This heterogeneity suggests localized differences in the iron on the poly-Ni surface, which can arise from non-uniform deposition and growth mechanisms. The overall thickness of the iron layer on the poly-Ni electrode increases from 9 - 18 $\mu g\ cm_{geo}^{-2}$ (0 ppm Fe^{z+}) to 30 - 60 $\mu g\ cm_{geo}^{-2}$ (14 ppm Fe^{z+}). Therefore it is concluded, that the heterogeneity of deposited iron increases as the Fe^{z+} ion concentration in the electrolyte increases. To assess the presence of additional minor impurities deposited from the electrolyte onto the poly-Ni electrode during the galvanostatic AST, the average μ-XRF spectra from 0 and 14 ppm Fe^{z+} are plotted in **Figure S17**. Aside from Fe, only a silicon signal is observed, which is attributable to the silicon drift detector (SSD). No other impurities were detected within the acquisition time of the XRF data. The plot in **Figure 46b** shows the average iron deposit (N = 4 samples) on the 0.196 cm^2 poly-Ni electrodes after 24 h of galvanostatic AST experiment plotted against the Fe^{z+} cation concentration added into the electrolyte. The poly-Ni electrode exposed to 0 ppm Fe^{z+} exhibits “baseline” deposition of minimal average iron layer thickness of ~13 $\mu g\ cm_{geo}^{-2}$, attributed to the negligible Fe^{z+} concentration in 0.1 M KOH electrolyte. The most pronounced increase in the average thickness of the iron layer on the poly-Ni electrode occurs as it rises from ~10 ± 0.4 $\mu g\ cm_{geo}^{-2}$ (0 ppm Fe^{z+}) to ~ 27 ± 1 $\mu g\ cm_{geo}^{-2}$ (3 ppm Fe^{z+}). Beyond this point, the average layer thickness exhibits a gradual increase, reaching ~ 32 $\mu g\ cm_{geo}^{-2}$ at 14 ppm Fe^{z+}. When the Fe^{z+} concentration in the electrolyte increases, the average

iron mass deposited on the poly-Ni electrodes after 24 h galvanostatic AST experiment increases as well. Overall, the µ-XRF analysis verifies that the island and layer deposits on the poly-Ni electrode observed in the SEM images (**Figure 45**) mainly consist of iron.

While µ−XRF provides a clear picture of the amount of iron deposited, understanding their spatial distribution and thickness require more sophisticated techniques. To probe the layer thickness of the deposits in more detail, the XPS depth-profile analysis with Ar^+ sputtering was conducted, as illustrated in **Figure S18a-d**. This approach enables depth-resolved characterization, revealing gradients in elemental distribution across the deposit layers onto the poly-Ni surface. The raw Ni 2p and Fe 2p XPS data corresponding to the sputter profiles (**Figure S18a-d**) were analyzed with regard to the areas of the Ni $2p_{3/2}$ and Fe $2p_{3/2}$ XPS peaks to estimate the respective atomic ratios. It is important to note that the Ar^+ sputtering causes metal oxides to reduce to lower oxidation states or metallic forms, which makes it impossible to determine the initial oxidation states based of the XPS peaks. The analysis therefore just focused on the Fe and Ni atomic ratios as a function of sputter time, which is shown in the depth profiles in **Figure S20a-d.** The sputter time needed to remove a 50 nm thickness reference Ni film from a glass substrate is presented in **Figure S19**. The sigmoidal-shaped sputter profile (**Figure S20**) for all treated poly-Ni electrodes show a decrease of iron content (purple line), while the Ni content is increasing (orange line) with sputter time. This indicates the transition from an iron rich surface to a nickel rich one during the Ar^+ sputtering process. The initial rapid changes in composition during the first few seconds are very likely due to the loss of surface hydrocarbons, oxides and contaminants. In **Figure S20a**, the poly-Ni electrode exposed to 0 ppm Fe^{z+} exhibits a drastic loss in the Fe composition from 48 at.% to 9 at.% after 120 s. This “baseline” deposition has the thinnest iron deposits as there is minimal Fe^{z+} species in 0.1 M KOH. The depth profile for the poly-Ni electrode exposed to 3 ppm Fe^{z+} shows a gradual decrease in the Fe composition from 77 at.% to 23 at.% after approximately 1500 seconds of Ar^+ sputtering. In contrast, the sputter profiles for electrodes exposed to 6 ppm and 14 ppm Fe^{z+} species display more significant reductions, with Fe content dropping from about 81 at.% to 9 at.% and from approximately 79 at.% to 20 at.%, respectively, over a similar sputtering duration. Notably, the formed iron layer on the

poly-Ni electrode exposed to 6 ppm Fe^{z+} appears thinner than the iron layer on the poly-Ni exposed to 14 ppm Fe^{z+}. However, the slope of the sputter profile for the electrode exposed to 6 ppm Fe^{z+} closely resembles that of the 14 ppm Fe^{z+}, indicating similar layer architecture despite the variation in concentration. Interestingly, both the poly-Ni electrodes exposed to 3 ppm and 14 ppm Fe^{z+} species have comparable deposit thicknesses of around 30 nm, as shown in **Figure S20b&d**. But for these concentrations, the variations in the slopes of the sputter profiles suggest differences in the layer architecture.

These structural differences are consistent with SEM micrographs. The poly-Ni electrode exposed to 3 ppm Fe^{z+} form island-like iron deposits on the surface (**Figure 45b**), whereas the electrode exposed to 14 ppm Fe^{z+} develop a denser, although not fully continuous and close film (**Figure 45d**). Low Fe^{z+} concentrations lead to sparse nucleation and 3D island growth (*Volmer-Weber mechanism* [256,257]), as seen in **Figure 46a&b**. In contrast, higher Fe^{z+} concentrations promote rapid nucleation and layer-plus-island growth (*Stransky-Krastanov* mechanism [256,257]), as seen in **Figure 46c&d**. Additionally, hydrogen bubbles from the HER disrupt film continuity more at higher Fe^{z+} concentrations, increasing heterogeneity (see **Figure 46**).

Combining SEM micrographs (**Figure 45**), the μ−XRF mappings (**Figure 46**) and the XPS depth profiles (**Figure S20**), it is concluded that Fe^{z+} concentration influences growth modes and the resulting layer structures. However, the mechanistic basis for maintained HER durability of the poly-Ni in higher Fe^{z+}-containing electrolytes (e.g., 6 ppm Fe^{z+} and 14 ppm Fe^{z+}) remains unclear. The next sections will provide a more detailed electrochemical analysis to better understand the electrode surface processes.

5.4.4 Quantification of Surface Roughness via Galvanostatic Impedance Spectroscopy

To evaluate the surface roughness of the treated poly-Ni electrodes, the hourly galvanostatic electrochemical impedance spectroscopy (GEIS) measurements were analyzed. The double-layer capacitance (C_{dl}) was estimated using a simple Randles circuit fit, see **Figure S23**. Since Fe and Ni have comparable specific capacitances [117,258,259], changes in C_{dl} primarily indicate variations in electrochemical surface area rather than intrinsic elemental effects.

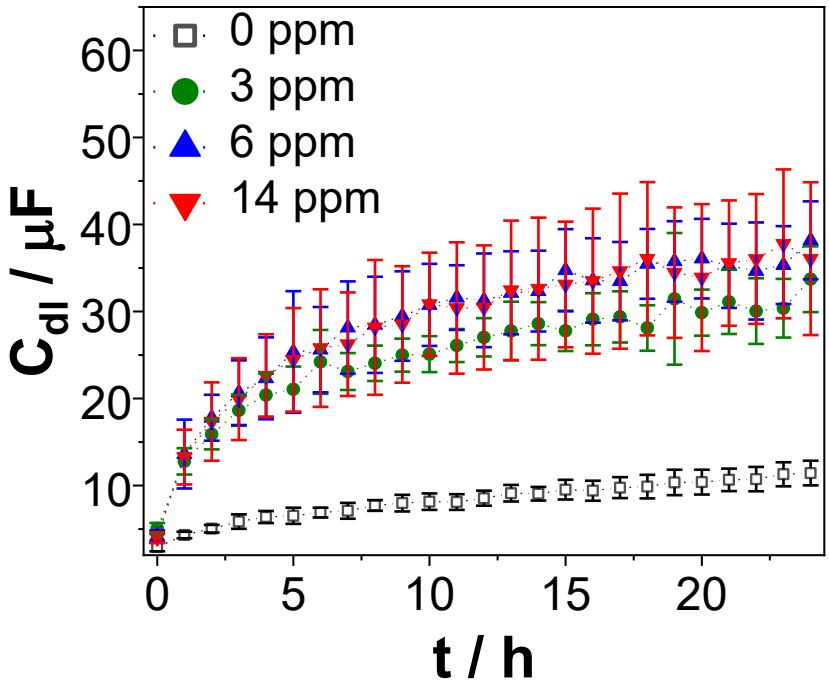

Figure 47: *Changes of the double layer capacitance C_{dl} for the treated poly-Ni electrodes during the galvanostatic experiments at $-10\ mA\ cm_{geo}^{-2}$ obtained from Randles circuit fit of the galvanostatic impedance spectroscopy (GEIS) data (see **Figure S23** as an example). Error bars represent the standard deviations within a sample number of $N = 7$ independent measurements. Color code: grey: 0 ppm, green: 3 ppm, blue: 6 ppm and red: 14 ppm Fe^{z+} species in 0.1 M KOH electrolyte solution.*

The evolution of the C_{dl} over 24 h galvanostatic AST experiment at $-10\ mA$ cm_{geo}^{-2} is shown in **Figure 47** for all iron concentrations and averaged across multiple experimental repetitions (N = 7). The electrodes exposed to 0 ppm Fe^{z+} species in the electrolyte (grey squares) show only a modest increase in C_{dl} from 3.0 ± 0.5 µF to

about 11.4 ± 1.4 µF after 24 hours, indicating minimal surface roughening. In contrast, the poly-Ni electrode exposed to 3 ppm (green circles), 6 ppm (blue triangles), and 14 ppm (red triangles) Fe^{z+} species concentration in the electrolyte show significantly larger increases in C_{dl}, reaching approximately 30 - 40 µF (with standard deviations up to 8.8 µF) after 24-h galvanostatic AST measurement at $-10\ mA\ cm_{geo}^{-2}$. However, the double-layer capacitance values for electrodes exposed to Fe^{z+}-spiked electrolytes remain very comparable throughout the galvanostatic measurements, indicating that similar extent of surface roughening of the poly-Ni electrode induced by Fe deposition. Since this similarity in surface roughness does not explain the observed trends in HER durability, it suggests that other factors play a more significant role in determining catalytic performance.

5.4.5 Quantification of Electrochemically Accessible Nickel Sites via Cyclic Voltammetry

To gain further insights into the effects of the iron deposits on the surface structure of the poly-Ni electrodes, cyclic voltammetry (CV) was measured after 24 hours of galvanostatic experiments at $-10\ mA\ cm_{geo}^{-2}$ in 0.1 M KOH. The CV profiles before (dashed lines) and after (solid lines) galvanostatic experiments are compared for the poly-Ni electrodes exposed to 0, 3, 6 and 14 ppm Fe^{z+} concentrations, as shown in **Figure S21a-d**. Initially, all CV profiles of the poly-Ni electrode (dashed lines) show the characteristic features of the formation and reduction of NiOOH at around 1.4 V vs. RHE [128] prior to the onset of the OER (see chapter 2.4.2.1):

$$Ni(OH)_2 + OH^- \rightleftharpoons NiOOH + e^- + H_2O \quad (23)$$

It is visible that all poly-Ni electrodes exposed to different Fe^{z+} concentrations exhibit new peaks at 0 - 0.16 V and 0.3 V vs. RHE after 24 h galvanostatic experiment. Based on the Pourbaix diagram for iron-water system in 0.1 M KOH (pH = 13), Fe ions are not stable as “free ions” in solution and rapidly convert to insoluble iron hydroxides or oxides, such as $Fe(OH)_2$, Fe_3O_4, etc.[244].

The oxidation peak between 0 and 0.16 V vs. RHE in 0.1 M KOH are assigned to the oxidation of metallic iron [155] (see also chapter 2.4.2.2):

$$Fe + 2\,OH^- \rightarrow Fe(OH)_2 + 2\,e^- \quad (25)$$

Furthermore, the anodic current at around 0.3 V vs. RHE is related to the oxidation of iron hydroxides to oxy-hydroxides and iron oxides [155]:

$$Fe(OH)_2 + OH^- \rightarrow \delta - FeOOH + H_2O + e^- \quad (26)$$

$$3\,Fe(OH)_2 + 2\,OH^- \rightarrow Fe_3O_4 + 4\,H_2O + 2e^- \quad (27)$$

The cathodic peak at ~ 0 V vs. RHE reflects the reduction of iron(hydr)oxide species. After 24-h galvanostatic AST at $-10\,mA\,cm^{-2}_{geo}$, all poly-Ni electrodes display pronounced iron redox features. The current density of Fe redox couples increases progressively from 0 ppm (**Figure S21a)** to 14 ppm (**Figure S21d**) Fe^{z+}, indicating more iron deposition at higher Fe^{z+} concentrations. This trend is consistent with results from structural characterization by top-view SEM, µ-XRF, and XPS.

After the 24-h galvanostatic experiments notable differences in the NiOOH reduction peak emerge among the treated poly-Ni electrodes. The electrodes exposed to 0 ppm Fe^{z+} in the electrolyte retain a pronounced NiOOH reduction peak (**Figure S21a)**, while electrodes exposed to 3 ppm Fe^{z+} show a diminished peak (**Figure S21b)** and those exposed to 6 ppm and 14 ppm Fe^{z+} in the electrolyte exhibit a drastically reduced peak (**Figure S21c-d**). As described by *Cossar et al.* [260], integration of this reduction peak has been a reliable method for quantifying the electrochemically accessible Ni surface area, based on the assumption that all $Ni(OH)_2$ can be reversibly oxidized to NiOOH during CV (see equation (23)). In this chapter, the charge associated with NiOOH reduction ($|Q_{NiOOH}|$) in the backward CV scan is used to estimate the electrochemically accessible nickel sites between different samples.

The NiOOH reduction peaks for all electrodes and cycles were integrated, as shown in **Figure 48a**. The $|Q_{NiOOH}|$ values averaged across $N = 7$ independent experiments are shown for all cycles in **Figure S22**. Averaged $|Q_{NiOOH}|$ values are shown for each cycle, with grey, green, blue, and red bars representing the poly-Ni electrode exposed to 0, 3, 6, and 14 ppm Fe^{z+} species concentration in 0.1 M KOH, respectively. The

$|Q_{NiOOH}|$ progressively increases with each CV cycle at the same Fe^{z+} concentration, indicating more electrochemically accessible nickel sites and irreversible oxidation of deposited iron on the poly-Ni electrode. As the trend across different Fe^{z+} concentrations is consistent and independent of the CV cycle, cycle 6 is chosen for further analysis. The averaged $|Q_{NiOOH}|$ from final cycle 6 of the CV after 24 h galvanostatic AST experiment is plotted as a function of Fe^{z+} concentration in **Figure 48b**. The highest value (112 ± 16 µC) is observed for the poly-Ni electrode exposed to 0 ppm of Fe^{z+} species (grey bar). Exposure to 3 ppm Fe^{z+} species (green bar) reduces $|Q_{NiOOH}|$ to 58 ± 10 µC, and further increase of Fe^{z+} species to 6 ppm (blue bar) and 14 ppm (red bar) decrease $|Q_{NiOOH}|$ to 34 ± 7 µC and 27 ± 6 µC, respectively. Exposure of poly-Ni electrodes to 3 ppm Fe^{z+} results in a significant (~50%) reduction in average $|Q_{NiOOH}|$ values compared to 0 ppm Fe^{z+}. Further increases in Fe^{z+} concentration to 6 and 14 ppm Fe^{z+} do not significantly alter the $|Q_{NiOOH}|$ values. This indicates a non-linear decrease in average $|Q_{NiOOH}|$ values that saturates at ≥ 6 ppm Fe^{z+} concentration in the electrolyte. Increasing Fe^{z+} concentration in the electrolyte results in similar surface roughening of poly-Ni electrodes (as analysed from the previous section), while inducing a non-linear decrease in average $|Q_{NiOOH}|$ values. The implications of these trends for HER activity and their interrelationship are addressed in the following section.

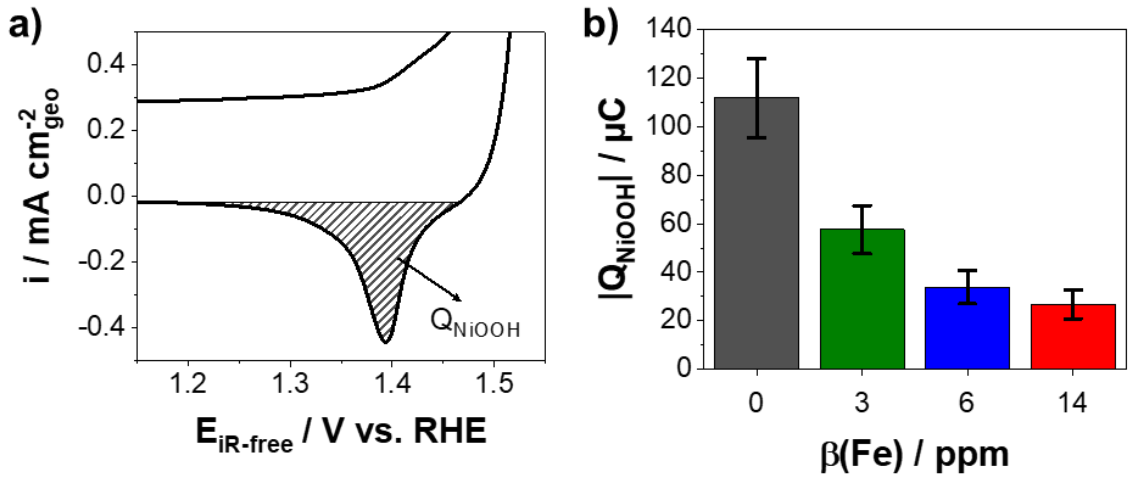

Figure 48: *Determination of the charge associated with the reduction of NiOOH* $|Q_{NiOOH}|$. ***a)*** *Exemplary integration of the NiOOH reduction peak from the CV profile.* ***b)*** *Charge associated with the reduction of NiOOH plotted against the iron concentration in the electrolyte. Error bars in* ***b)*** *represent the standard deviations within a sample number of* $N = 7$ *independent measurements. Color code: grey: 0 ppm, green: 3 ppm, blue: 6 ppm and red: 14 ppm* Fe^{z+} *species in 0.1 M KOH.*

5.4.6 Discussion

In this section, the influence of two electrochemical properties, surface roughness and electrochemically accessible nickel sites, on the change in overpotential ($\Delta\eta$) during galvanostatic AST experiments for HER is systematically analyzed. The first is the total surface roughness, which is reflected by the double layer capacitance (C_{dl}). The second is the electrochemically accessible nickel sites, quantified by the absolute charge associated with NiOOH reduction ($|Q_{NiOOH}|$). The objective is to assess whether the deactivation of the poly-Ni electrode during HER is more strongly affected by iron-induced roughening, indicated by the correlation between C_{dl} and $\Delta\eta$, or by the protection of Ni sites through iron deposits, based on the relationship between $|Q_{NiOOH}|$ and $\Delta\eta$.

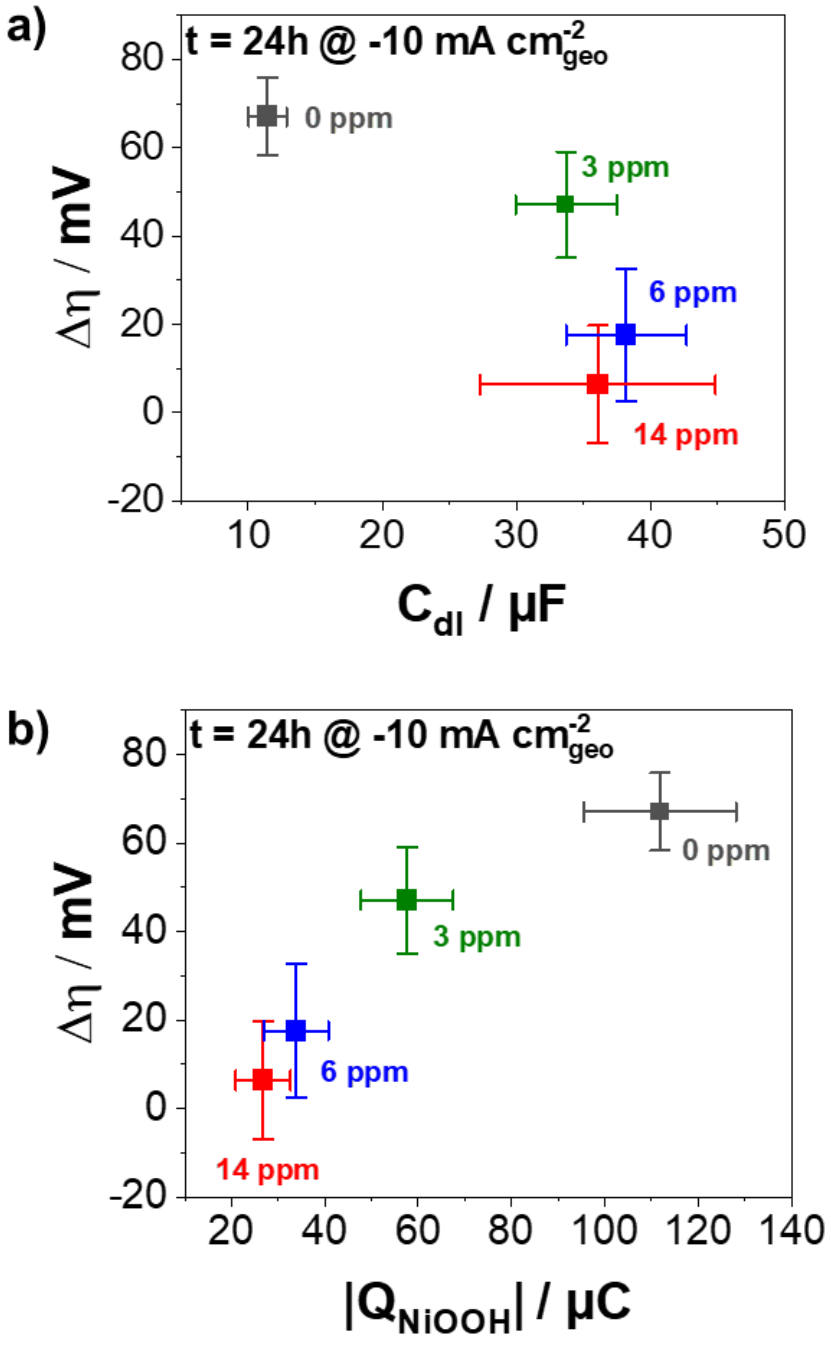

Figure 49: *Correlation diagrams between the changes in the overpotential $\Delta\eta$ during 24-h galvanostatic experiments at $i = -10\ mA\ cm_{geo}^{-2}$ and* ***a)*** *the double layer capacitance C_{dl} obtained from Randles circuit fit of the galvanostatic impedance spectroscopy (GEIS) data and,* ***b)*** *the charge associated with the reduction of NiOOH $|Q_{NiOOH}|$. Error bars represent the standard deviations within a sample size of N=7 independent measurements. Color code: grey: 0 ppm, green: 3 ppm, blue: 6 ppm and red: 14 ppm Fe^{z+} species in 0.1 M KOH.*

5.4.6.1 Correlation Between the Surface Roughness and HER Activity during Galvanostatic AST

First, the relationship between changes in the surface roughness, represented by C_{dl}, and changes in overpotential $\Delta\eta$ was evaluated. **Figure 49a** presents a correlation diagram plotting $\Delta\eta$ against C_{dl}. The poly-Ni electrodes exposed to 0 ppm Fe^{z+} (grey square) in the electrolyte exhibit the smallest C_{dl} with around 10 µF and the highest increase of the overpotential $\Delta\eta$. In contrast, the poly-Ni electrodes exposed to Fe^{z+} species (3, 6 and 14 ppm) in the electrolyte display higher, but similar C_{dl} values of around 30 to 40 µF, indicating increased surface roughness by a factor of 3 compared to that of 0 ppm. However, their overpotential changes differ substantially. Negligible changes in $\Delta\eta$ for 14 ppm (red square), a $\Delta\eta$ increase of ~ 20 mV for 6 ppm (blue square), and more pronounced $\Delta\eta$ increase of ~ 50 mV for 3 ppm (green square) are observed. There is thus no straightforward correlation between C_{dl} and overpotential changes, suggesting that surface roughness alone does not fully account for the HER durability of the poly-Ni electrodes among the different iron concentrations.

Previous studies indicate that iron-induced surface roughening can enhance the HER activity of poly-Ni electrodes. *Riley et al.* [157] observed a decrease of the overpotentials after 10,000 seconds of 3 ppm Fe^{z+} iron exposure for 1 cm² Ni plates in 30 wt.% KOH, attributed to iron deposit-induced roughening. Similarly, *Brossard et al.* [171] reported reduced charge transfer resistance and overpotentials on Ni wires at higher Fe^{z+} concentrations (14 ppm). In these experiments, during the first hour of galvanostatic AST at $-10\ mA\ cm_{geo}^{-2}$ in 0.1 M KOH, poly-Ni electrodes exposed to 6 and 14 ppm Fe^{z+} show a slight decrease in overpotential (**Figure 44a**), likely due to surface roughening effects discussed in previous literature [157,171]. However, after 24 hours, their overpotentials remain stable or increase slightly (**Figure 49a**, blue and red squares**)**, with no further activity improvement. In contrast, electrodes at lower Fe^{z+} concentrations exhibit higher overpotentials after both 1 h and 24-h galvanostatic AST measurement, indicating that degradation processes predominate any initial surface roughening benefits (**Figure 49a**, green and grey squares).

As monometallic iron has inherently lower HER activity compared to nickel, [53,152,171] it is essential to distinguish surface roughening effect from intrinsic activity effect. Thereby these results are compared to a purposely rough, laser-structured Ni

electrode (**Figure S24a**), fabricated by *Gabler et al.* [261]. PEIS measurements fit to a Randles circuit (**Figure S24b**) show C_{dl}, increasing from 3 µF for planar poly-Ni to 41 µF for laser-structured Ni, indicating enhanced electrochemical surface area. This level of roughness is comparable to that observed on the Ni electrodes exposed to 3, 6, and 14 ppm Fe^{z+} (**Figure 47**). The laser-structured Ni also exhibits significantly higher HER activity than the flat poly-Ni disk (**Figure S24c**), confirming that increased surface roughness enhances HER activity by providing more accessible active sites. During the 24-h galvanostatic AST at higher Fe^{z+} concentrations (6 and 14 ppm), dense and rough iron layers form on the electrode surface (**Figure 45c-d**). Although increasing the surface area typically enhances HER activity, no such effect is observed. It indicates that the positive effect of increased surface area is counteracted by the lower intrinsic activity of iron.

To sum up, dense (but not completely closed) iron films on nickel electrodes introduce increased surface roughness that temporarily, within the first hour of galvanostatic AST, boost the HER activity. However, under prolonged galvanostatic conditions, degradation processes offset these improvements and there is no direct correlation between C_{dl} and $\Delta\eta$.

5.4.6.2 Correlation Between the Electrochemically Accessible Ni Sites and HER Activity during Galvanostatic AST

Next, the effect of the electrochemically accessible Ni sites, represented by the $|Q_{NiOOH}|$ with the changes in HER overpotential $\Delta\eta$, is considered, see **Figure 49b**. The correlation plot reveals that the poly-Ni electrodes with higher $|Q_{NiOOH}|$ exposed to 0 (grey squares) and 3 ppm Fe^{z+} (green squares) species in the electrolyte exhibit larger overpotential changes ($\Delta\eta$ = ca. 40 – 70 mV). Conversely, electrodes with lower $|Q_{NiOOH}|$ exposed to 6 (blue squares) & 14 (red squares) ppm Fe^{z+} species, show smaller overpotential changes (ca. 6 – 17 mV increase). This direct correlation between $|Q_{NiOOH}|$ and $\Delta\eta$ highlights a clear link between electrochemically accessible Ni sites and HER durability. Next, these observations are related to the structural characterization results for two Fe^{z+} regimes - low and high iron concentrations.

Low Iron Concentrations in the Electrolyte (0 and 3 ppm Fe^{z+}): At low Fe^{z+} concentrations (0 and 3 ppm), SEM and XPS reveal that Fe deposits predominantly

form as discrete islands on the Ni surface (**Figure 45a&b** and **Figure S20a&b**). Based on SEM and μ−XRF (**Figure 45a&b** and **Figure 46a**), these deposits are larger and thicker for electrodes exposed to 3 ppm Fe^{z+} compared to 0 ppm Fe^{z+} species. The low Fe coverage leaves a significant amount of Ni surface sites exposed to the electrolyte, resulting in high $|Q_{NiOOH}|$ during the CV profiles after the 24-h galvanostatic AST. The correlation diagram (**Figure 49b**) indicates that the increased electrochemically accessible Ni sites accelerate electrode deactivation. Since Ni electrode degradation during 24 h galvanostatic AST is primarily linked to NiH formation due to atomic hydrogen absorption into the Ni lattice [130–132], electrodes with more electrochemically accessible Ni sites undergo are more susceptible to hydride-induced deterioration.

High Iron Concentrations in the Electrolyte (6 and 14 ppm Fe^{z+}): Increasing the Fe^{z+} concentration to 6 and 14 ppm rapidly forms dense but incomplete Fe layers, as confirmed by SEM and XPS (**Figure 45c&d** and **Figure S20c&d**). These layers are thicker at 14 ppm Fe^{z+} compared to 6 ppm Fe^{z+} species in the electrolyte, as seen from μ−XRF and XPS analysis (**Figure 46a&b** and **Figure S20c&d**). Near-complete Fe coverage on the nickel surface results in low $|Q_{NiOOH}|$ values during the CV profiles after 24-h galvanostatic AST experiment. The HER predominantly occurs on the dense iron layers instead of Ni surface, as indicated by pronounced iron-specific redox peaks in the CV profiles, see **Figure S21c-d**. It is consistent with previous studies by *Huot et al.* [166], who also reported the same characteristic iron features on a nickel electrode after holding multiple days at −100 mA cm^{-2}. Moreover, previous studies of magnetron sputtered Fe-coated Ni electrodes with controlled Fe coverages between 60 - 100 % have demonstrated that such layers act as physical barriers to hydrogen diffusion into Ni lattice [132,170]. This suppresses inactive NiH formation at high HER current densities. The observations from this study of low $|Q_{NiOOH}|$ and unchanged overpotentials after prolonged galvanostatic aging at high Fe^{z+} concentrations align with this protective mechanism model. Furthermore, literature indicates that a minimum Fe content is necessary to trigger the positive effects of electrode roughening on HER activity [153,157,171]. The combined analysis from this chapter shows that this "minimum Fe^{z+} concentration mainly governs Ni surface coverage by iron rather than

surface roughness. In the setup presented herein, Fe^{z+} concentrations above ~6 ppm are necessary to form protective Fe layers that prevent Ni degradation.

In summary, these findings demonstrate that insufficient Fe coverage produced by low electrolyte Fe^{z+} concentration results in island-like deposits that leave a large amount of Ni surface sites exposed and susceptible to hydride-induced deterioration. In contrast, dense, continuous but not completely closed Fe layers at higher Fe^{z+} concentrations effectively protect the nickel surface, reducing NiH formation and maintaining stable HER activity over time. The key to durable HER activity lies in controlling the extent of Fe surface coverage rather than surface roughening of the poly-Ni electrodes alone. These results and insights from literature are integrated into an iron-influenced HER mechanisms model, which is presented in the following section.

5.4.7 Proposed Model of the Influence of Iron Impurities for HER at Nickel Electrodes

A model for the influence of iron ions on HER durability on poly-Ni electrodes, based the experimental data of this chapter combined with insights from previous studies, is now presented. The results reveal two distinct regimes, dictated by the Fe^{z+} concentration in the electrolyte: low concentration (0 and 3 ppm Fe^{z+}) and high concentration (6 and 14 ppm Fe^{z+}), as illustrated in **Figure 50**.

Low iron concentrations (0 and 3 ppm Fe^{z+}): Fe^{z+} species from the electrolyte deposits as discontinuous islands on the poly-Ni surface after both 1 h and 24 h of galvanostatic AST. Both Fe^{z+} concentration and exposure time are critical factors influencing the morphological evolution of Fe deposits on polycrystalline nickel electrodes. While higher Fe^{z+} concentrations in the electrolyte promote greater iron accumulation, the duration of exposure also plays a significant role. Initially, Fe deposits are finer, but as the galvanostatic test progresses, these island deposits grow larger and thicker. Since even after 24 h, a significant portion of the Ni surface remains exposed to the electrolyte, the HER predominantly proceeds on the poly-Ni surface. At these low coverages, a continuous or protective iron layer is not formed. Instead, atomic hydrogen absorption into the nickel lattice is facilitated, which leads to pronounced deactivation during the galvanostatic AST, referred to as NiH formation [130–132]. This

observation aligns with existing literature, which indicates that low Fe concentrations have negligible impact on HER activity [159].

Higher iron concentrations (6 and 14 ppm Fe^{z+}): After just 1 hour of galvanostatic AST at $-10\ mA\ cm_{geo}^{-2}$, dense, continuous iron layers are already visible. The layer thickness is greater at 14 ppm Fe^{z+} compared to 6 ppm Fe^{z+}, indicating substantial iron deposition at higher concentrations. During this initial hour, the overpotentials decrease slightly (see **Figure 44a**). This decrease in overpotential may result from iron deposition-induced surface roughening, which increases the electrochemically active surface area.

After 24 hours of AST, however, the overpotentials either remain stable or increase slightly (see **Figure 44**). Notably, electrode degradation for HER at high Fe^{z+} concentrations is less severe than degradation at lower Fe^{z+} concentrations. The dense iron layer acts as a protective barrier, limiting hydrogen diffusion into the nickel lattice and reducing NiH-related degradation. Furthermore, the HER predominantly occurs at the dense iron layer making surface roughening through iron deposits crucial. Increased roughness enlarges the active surface area, compensating for the lower intrinsic activity of iron compared to nickel and helping maintain stable HER overpotential during prolonged operation.

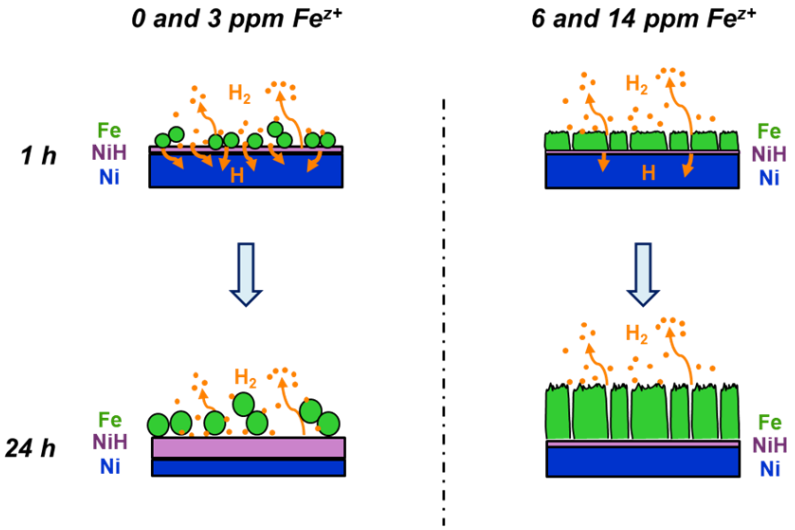

Figure 50: *Proposed model for the influence of iron impurities on a polycrystalline nickel electrode during 24 h galvanostatic experiment (i = −10 $mA\ cm_{geo}^{-2}$) being exposed to low iron concentrations (0 and 3 ppm Fe^{z+}) or high iron concentrations (6 and 14 ppm Fe^{z+}) in the 0.1 M KOH electrolyte solutions for t = 1 h (top) and t = 24 h (bottom).*

In summary, iron impurities protect the poly-Ni surface from degradation mechanisms during galvanostatic AST experiments, primarily by inhibiting NiH formation. The detrimental effects of electrode degradation outweigh any potential benefits of surface roughening induced by iron deposits. At higher Fe^{z+} concentrations, increased surface roughness via iron deposition helps compensate for the lower intrinsic activity of iron and ensuring electrochemical durability of Ni electrodes.

5.4.8 Conclusions to Chapter 5.4

In this chapter, it was investigated how iron impurities in different concentrations (0, 3, 6 and 14 ppm Fe^{z+}) affect the HER durability of poly-Ni electrodes in 0.1 M KOH. By integrating the experimental findings with literature insights, a model was developed highlighting the concentration-dependent influence of iron on HER durability of poly-Ni electrodes. At low Fe^{z+} concentrations (0 and 3 ppm) in the electrolyte, SEM and XPS analyses show that discontinuous, island-like iron deposits form during 24-h galvanostatic AST experiment at $i = -10\ mA\ cm_{geo}^{-2}$. These islands increase in thickness from 1 to 24 h but do not develop into a continuous layer. This partial iron coverage of the poly-Ni electrodes leaves significant nickel surface exposed, as indicated by high $|Q_{NiOOH}|$ values in CV measurements post-AST. The resulting abundance of electrochemically accessible Ni sites results in increased $\Delta\eta$ (~ 40 – 70 mV) during AST, with the primary degradation pathway being hydrogen adsorption into the Ni lattice and subsequent NiH formation.

In contrast, at elevated Fe^{z+} concentrations (6 and 14 ppm), SEM and XPS reveal the formation of dense, continuous but incomplete iron films that cover the Ni electrode surface. These layers develop within the first hour and grow thicker throughout the 24-h galvanostatic AST. Low $|Q_{NiOOH}|$ values from post-AST CV measurements reflect a significant reduction in electrochemically accessible Ni sites, attributed to the near-complete coverage of the surface by the deposited Fe layer. This correlated with only minor overpotential increases during HER, suggesting that the HER shifts to the roughened Fe layer, which effectively compensates for Fe's lower intrinsic activity relative to Ni. Additionally, the Fe film serves as a barrier, limiting hydrogen diffusion into Ni and preventing further degradation.

In summary, these findings illustrate a direct correlation: as the Ni surface becomes increasingly covered by dense Fe films at higher Fe^{z+} concentrations, the effective exposed Ni surface sites diminish, resulting in stabilized overpotentials. Controlling Ni surface sites through Fe deposition strategies is highly critical to maintain the alkaline HER activity. Although direct translation to ALWEs is limited by temperature and electrolyte concentration differences, analogous Fe-driven mechanisms are expected. A better understanding of the iron-influenced HER degradation processes enables the design of more robust cathode catalyst materials for alkaline water electrolysis in the near future.

6 Overall Conclusions

This thesis investigates fundamental topics of the hydrogen evolution reaction (HER) on model-based electrocatalysts through the application of two hydrodynamic electrochemical techniques: the well-established rotating disk electrode (RDE) and a novel impinging jet flow cell.

First, a specialized impinging jet flow cell is designed for studying atomically thin model electrocatalysts. In the absence of an existing analytical framework for the mass transport description for this setup, analogous to the *Levich* equation, a universal analytical model describing mass transport and limiting current characteristics is developed in **chapter 5.1**. This model unifies established theories for wall-tube, wall-jet, and radial channel-flow electrode configurations. The validation includes systematic comparison to numerical CFD simulations and experiments using the oxidation of ferro(II)cyanide. The model accurately predicts transition radii between the flow regimes, local current density distributions, and total limiting current densities across 350 CFD simulations, with average relative errors of 7.8% compared to CFD simulations and average relative errors of 8.3% versus experimental results. Overall, the universal analytical model is a reliable alternative to time- and resource intensive CFD simulations for predicting (confined) impinging jet electrode experiments. It also offers potential application in broader mass and heat transfer contexts, by analogy between *Sherwood* and *Nusselt* numbers.

After establishing a theoretical foundation for mass transport in this flow cell setup, the next **chapter 5.2** compares this newly developed setup with the well-known RDE using Pt model electrodes. Key aspects analyzed include cyclic voltammetry (CV) features, electrochemical surface area, mass transport, and gas saturation for electrode radii of $R_C = 3.63\ mm$ (impinging jet flow cell) and $R_C = 2.5\ mm$ (RDE). Pt electrodes in both setups display typical polycrystalline Pt features. The Pt foil in the flow cell ($R_C = 3.63\ mm$) exhibits twice the ECSA compared to the RDE, consistent with its geometric surface area. Comparison of the experimental HER/HOR polarization curves with simulations using the model developed in chapter 5.1 indicates similar gas saturation levels (c_∞~ 0.5 mmol L^{-1} H_2) in the impinging jet flow cell and RDE. These findings confirm that, particularly for larger electrodes, both systems provide comparable electrochemical conditions for HER/HOR studies, validating the impinging jet flow cell as an alternative to the RDE for the investigation of squared model electrodes.

Building upon this validation, the impinging jet system is employed to investigate phase-pure 2D platinum chalcogenides as model catalysts for the HER in acidic media. **Chapter 5.3** compares HER activity and durability among several 2D-Pt_xTe_y@HOPG materials. Following synthesis of 2D-$PtTe_2$, 2D-Pt_2Te_2, and 2D-Pt_3Te_4 by MBE, their high phase purity is verified using XPS and Raman spectroscopy. Electrochemical testing in the custom impinging jet flow cell reveals pronounced differences in HER activity: 2D-$PtTe_2$ and 2D-Pt_2Te_2 show significantly higher activity ($\left|E_{-0.1\ mA\ cm_{geo}^{-2}}\right| = 78 \pm 7\ mV\ vs.RHE$) than 2D-$Pt_3Te_4$ ($\left|E_{-0.1\ mA\ cm_{geo}^{-2}}\right| = 115 \pm 11\ mV\ vs.RHE$). DFT calculations demonstrate that the activity differences between the phases can be explained by differences in hydrogen adsorption Gibbs free energies (ΔG_H) at Te vacancies, following a parallel trend (2D-$PtTe_2$ ≈ 2D-Pt_2Te_2 ≪ 2D-Pt_3Te_4). *Tafel* slopes suggest a consistent rate-determining step for all materials. Durability studies with Raman indicate that 2D-$PtTe_2$ degrades, likely through delamination (≈ 60% decrease in normalized Raman peak area $\bar{A}_{E_g/G}$ throughout the electrochemical protocol), while 2D-Pt_2Te_2 partially transforms (up to 37%) into 2D-Pt_3Te_4 but retains good HER activity. 2D-Pt_3Te_4 is the most durable (only 30% decrease of normalized Raman peak areas $\bar{A}_{E_g(PtTe_2)/G}$ during electrochemical testing) and has the second-best durability in galvanostatic tests. XPS analysis shows no conversion to metallic Pt for any of the phases. This integrated study, combining 2D material synthesis, DFT modeling, and measurements in a specialized electrochemical flow cell, establishes a direct link between theoretical and experimental HER activity trends, while additionally providing important insights into phase stability. These findings are valuable for designing future Pt chalcogenide HER catalysts in efforts to reduce PGM usage for PEMWE.

In the last part of this thesis, **chapter 5.4** investigates how iron impurities (0, 3, 6, and 14 ppm Fe^{z+}) in 0.1 M KOH influence the HER durability of polycrystalline Ni electrodes. Integrating experiments and literature, a model is formulated to explain concentration-dependent effects of iron ions on alkaline HER. At low Fe^{z+} concentrations in the electrolyte (0, 3 ppm), SEM and XPS show the formation of discontinuous island-like iron deposits during 24-h galvanostatic AST on the Ni electrode surface. A substantial amount of Ni surface sites remains exposed, as confirmed by higher $|Q_{NiOOH}|$ in post-galvanostatic CVs. The exposed Ni surface results in larger changes of overpotential $\Delta\eta$ (~ 40 – 70 mV) during AST, likely due to

hydrogen absorption into the Ni lattice and degradation via NiH formation. In contrast, higher Fe^{z+} concentrations in the electrolyte (6, 14 ppm) lead to rapid formation of denser, nearly continuous iron films, verified by SEM and lower $|Q_{NiOOH}|$, indicating most of the Ni surface is covered. Overpotentials under galvanostatic load increase only minimally since HER activity shifts onto the rough Fe film, reducing hydrogen diffusion into the nickel lattice and Ni degradation. Additionally, the rough surface formed during deposition compensates for Fe's lower intrinsic activity. These findings underscore the critical role of surface site control via Fe deposition for alkaline HER activity. Even though conditions differ in real alkaline water electrolyzers (e.g., temperature, electrolyte concentration), similar Fe-related deposition and degradation mechanisms are expected. The deeper understanding of the role of iron impurities for HER durability supports the future design of more durable nickel cathode materials for alkaline water electrolysis.

Overall, the present research advances the mechanistic understanding of activity and stability determinants of HER catalysts in acidic and alkaline media utilizing well-defined model electrode systems. The insights gained contribute to the development of more durable and efficient HER catalysts, supporting ongoing efforts toward sustainable hydrogen production.

7 Outlook

Fundamental insights into the mechanisms and structure–property relationships of model electrocatalysts were gained in this thesis. However, there is still room for improvement.

The impinging jet flow cell was validated as a suitable platform for investigating model HER electrocatalysts. However, enhancements in the fluidic design within the cell are possible. At present, the outlets of the fluid system are located within the wetted area of the electrodes, particularly for larger electrodes ($R_C = 3.63\ mm$). This configuration introduces uncertainties in the universal analytical model, as detailed in **chapter 5.1**. To address this, an embedded working electrode system for the larger electrodes, analogous to the Teflon-embedment (see **Figure 21b)** used for smaller electrodes ($R_C = 0.5\ mm$ and $R_C = 1\ mm$), could be developed. With this improvement, the outlets could be positioned further from the electrode, thereby enhancing the accuracy of the simplified universal analytical model.

Additionally, as detailed in **chapter 5.2**, the developed setup could benefit from improved gas saturation, especially for small electrode sizes. One potential strategy is to construct the entire setup described in chapter 4.1 within a custom-made gas atmosphere chamber. Alternatively, implementing a gas-in-gas saturation system at the inlet of the impinging jet flow cell, similar to systems employed in related setups [189], could significantly increase hydrogen saturation. Notably, such systems have achieved hydrogen concentrations up to $c_\infty = 1$ mmol L^{-1} [189]. These modifications would enable further investigations of the HER/HOR under higher mass-transport conditions, as predicted by the theoretical simulations in **chapter 5.2**.

Beyond HER studies, the impinging jet flow cell offers potential for investigating other electrochemical reactions. For example, this setup has been utilized to study laser-structured gold electrodes produced via laser-induced forward transfer (LIFT) for the methanol oxidation reaction in alkaline media [188] (not included in this thesis). Preliminary tests also showed promising results for the investigation of sputtered Pt-Ir films for the oxygen reduction reaction (ORR). By employing mass transport–dependent reactions such as the ORR, the universal analytical model developed herein could be further validated with a broader set of experimental limiting current density data.

Initial investigations into 2D transition metal chalcogenides (TMCs) as HER catalysts in acidic media were reported in **chapter 5.3**. The impinging jet flow cell presented herein can now be established as a versatile screening platform for HER activity in a wider array of these materials. Future work could include investigating other 2D materials such as PdX_2 (X=S, Se, Te), PtX_2 (X=S, Se), or bimetallic $Pt_xIr_{1-x}Te_2$ phase mixtures synthesized via MBE [262–264], providing a comprehensive overview of HER activity trends among TMCs. The development of standardized measurement protocols and the direct comparison of activities within a single setup will accelerate the advancement of these materials as alternative HER catalysts, thereby minimizing current variability due to differences in synthesis methods and testing conditions (chapter 2.3.2.3).

As demonstrated in **chapter 5.3**, the HER activity of the investigated materials correlates directly with hydrogen adsorption energies at Te vacancies. It is established that such vacancies can be induced by doping with other metals during synthesis. For instance, STM studies confirm that doping 2D-$MoTe_2$ with vanadium creates Te vacancies [265]. Comparable synthesis strategies could be explored for 2D Pt chalcogenides to further enhance their HER activity, as suggested by the results presented here. Building on mechanistic insights and observed activity trends from these fundamental studies, the materials tested should also be synthesized and evaluated at larger scales for deployment in full-cell PEM water electrolysis (PEMWE) setups. As discussed previously, significant performance gaps exist between RDE and full-cell operation (see chapter 2.5.1), and these warrant comprehensive investigation.

Chapter 5.4 provided insights into the influence of iron impurities on model nickel electrodes, but additional studies are warranted to deepen understanding of these effects and to bridge the gap to practical applications. The current study focused on disk-shaped Ni model electrodes in 0.1 M KOH at room temperature, whereas industrial electrolyzers typically utilize nickel foam or mesh electrodes operating in 30 wt% KOH at elevated temperatures (see chapter 2.1.2). Thus, a systematic investigation of iron-spiked electrolyte solutions in full-cell alkaline electrolysis setups is a logical next step. Here, further variables such as higher current densities, ranging from $i = 10\ mA\ cm_{geo}^{-2}$ up to $i = 800\ mA\ cm_{geo}^{-2}$, should be explored to simulate practical operation. To differentiate the roles of iron at the cathode and anode, incorporation of

reference electrodes within the full-cell configuration, as demonstrated in recent literature [266], would provide valuable mechanistic insights.

Methodologically, there are several targeted experiments that could address key open questions. To conclusively demonstrate the formation of NiH during accelerated stress testing (AST), advanced characterization techniques such as grazing incidence X-ray diffraction could be applied [128]. In addition, conducting comparative studies using permeation-type cells with iron-spiked solutions [132] would enable direct assessment of hydrogen uptake into the Ni lattice for different electrolyte compositions, thereby further validating and refining the model proposed herein. Varying the electrolyte concentration (e.g., testing with 1 M or 5 M KOH) and investigating a broader range of current densities (such as $i = 1\ mA\ cm_{geo}^{-2}$ or $i = 5\ mA\ cm_{geo}^{-2}$) in the RDE setup could elucidate the influence of these operational parameters. Moreover, while the present work concentrated on the effect of iron impurities, it would also be instructive to study how other metal contaminants, such as aluminum, impact nickel electrode behavior.

Finally, bridging the gap to industrial relevance calls for long-term studies. The holding times explored in this model electrode study (24 hours) are much shorter than the operational lifetimes typical of industrial alkaline electrolysis stacks (60,000 to 90,000 hours) [7,8]. Therefore, future investigations should monitor iron deposition and its effects on overall cell performance over significantly extended durations to gain insights applicable to commercial-scale systems

8 References

[1] Schleussner C-F, Rogelj J, Schaeffer M, Lissner T, Licker R, Fischer EM et al. Science and policy characteristics of the Paris Agreement temperature goal. Nat. Clim. Chang. 2016;6(9):827–35. https://doi.org/10.1038/nclimate3096.

[2] Nnabuife SG, Oko E, Kuang B, Bello A, Onwualu AP, Oyagha S et al. The prospects of hydrogen in achieving net zero emissions by 2050: A critical review. Sustain. Chem. Clim. Action 2023;2:100024. https://doi.org/10.1016/j.scca.2023.100024.

[3] Chatenet M, Pollet BG, Dekel DR, Dionigi F, Deseure J, Millet P et al. Water electrolysis: from textbook knowledge to the latest scientific strategies and industrial developments. Chem. Soc. Rev. 2022;51(11):4583–762. https://doi.org/10.1039/D0CS01079K.

[4] Colbertaldo P, Agustin SB, Campanari S, Brouwer J. Impact of hydrogen energy storage on California electric power system: Towards 100% renewable electricity. Int. J. Hydrogen Energy 2019;44(19):9558–76. https://doi.org/10.1016/j.ijhydene.2018.11.062.

[5] Wappler M, Unguder D, Lu X, Ohlmeyer H, Teschke H, Lueke W. Building the green hydrogen market – Current state and outlook on green hydrogen demand and electrolyzer manufacturing. Int. J. Hydrogen Energy 2022;47(79):33551–70. https://doi.org/10.1016/j.ijhydene.2022.07.253.

[6] Sebbahi S, Assila A, Alaoui Belghiti A, Laasri S, Kaya S, Hlil EK et al. A comprehensive review of recent advances in alkaline water electrolysis for hydrogen production. International Journal of Hydrogen Energy 2024;82:583–99. https://doi.org/10.1016/j.ijhydene.2024.07.428.

[7] Carmo M, Fritz DL, Mergel J, Stolten D. A comprehensive review on PEM water electrolysis. International Journal of Hydrogen Energy 2013;38(12):4901–34. https://doi.org/10.1016/j.ijhydene.2013.01.151.

[8] Shiva Kumar S, Himabindu V. Hydrogen production by PEM water electrolysis – A review. Materials Science for Energy Technologies 2019;2(3):442–54. https://doi.org/10.1016/j.mset.2019.03.002.

[9] Santos DMF, Sequeira CAC, Figueiredo JL. Hydrogen production by alkaline water electrolysis. Quím. Nova 2013;36(8):1176–93. https://doi.org/10.1590/S0100-40422013000800017.

[10] Zeng K, Zhang D. Recent progress in alkaline water electrolysis for hydrogen production and applications. Progress in Energy and Combustion Science 2010;36(3):307–26. https://doi.org/10.1016/j.pecs.2009.11.002.

[11] Xu Y, Cai S, Chi B, Tu Z. Technological limitations and recent developments in a solid oxide electrolyzer cell: A review. International Journal of Hydrogen Energy 2024;50:548–91. https://doi.org/10.1016/j.ijhydene.2023.08.314.

[12] Wolf SE, Winterhalder FE, Vibhu V, Haart LGJ de, Guillon O, Eichel R-A et al. Solid oxide electrolysis cells – current material development and industrial application. J. Mater. Chem. A 2023;11(34):17977–8028. https://doi.org/10.1039/D3TA02161K.

[13] Du N, Roy C, Peach R, Turnbull M, Thiele S, Bock C. Anion-Exchange Membrane Water Electrolyzers. Chem Rev 2022;122(13):11830–95. https://doi.org/10.1021/acs.chemrev.1c00854.

[14] Bühler L, Möst D. Projecting technological advancement of electrolyzers and the impact on the competitiveness of hydrogen. International Journal of Hydrogen Energy 2025;98:1174–84. https://doi.org/10.1016/j.ijhydene.2024.12.078.

[15] Lee JK, Lau GY, Sabharwal M, Weber AZ, Peng X, Tucker MC. Titanium porous-transport layers for PEM water electrolysis prepared by tape casting. Journal of Power Sources 2023;559:232606. https://doi.org/10.1016/j.jpowsour.2022.232606.

[16] Xu W, Scott K. The effects of ionomer content on PEM water electrolyser membrane electrode assembly performance. International Journal of Hydrogen Energy 2010;35(21):12029–37. https://doi.org/10.1016/j.ijhydene.2010.08.055.

[17] Benmehel A, Chabab S, Do Nascimento Rocha AL, Chepy M, Kousksou T. PEM water electrolyzer modeling: Issues and reflections. Energy Conversion and Management: X 2024;24:100738. https://doi.org/10.1016/j.ecmx.2024.100738.

[18] Hansen JN, Prats H, Toudahl KK, Mørch Secher N, Chan K, Kibsgaard J et al. Is There Anything Better than Pt for HER? ACS Energy Lett. 2021;6(4):1175–80. https://doi.org/10.1021/acsenergylett.1c00246.

[19] Siracusano S, Baglio V, Lufrano F, Staiti P, Aricò AS. Electrochemical characterization of a PEM water electrolyzer based on a sulfonated polysulfone membrane. Journal of Membrane Science 2013;448:209–14. https://doi.org/10.1016/j.memsci.2013.07.058.

[20] Zhang Z, Baudy A, Testino A, Gubler L. Cathode Catalyst Layer Design in PEM Water Electrolysis toward Reduced Pt Loading and Hydrogen Crossover. ACS Appl. Mater. Interfaces 2024;16(18):23265–77. https://doi.org/10.1021/acsami.4c01827.

[21] Wang CR, Stansberry JM, Mukundan R, Chang H-MJ, Kulkarni D, Park AM et al. Proton Exchange Membrane (PEM) Water Electrolysis: Cell-Level Considerations for Gigawatt-Scale Deployment. Chem Rev 2025;125(3):1257–302. https://doi.org/10.1021/acs.chemrev.3c00904.

[22] Slade S, Campbell SA, Ralph TR, Walsh FC. Ionic Conductivity of an Extruded Nafion 1100 EW Series of Membranes. J. Electrochem. Soc. 2002;149(12):A1556. https://doi.org/10.1149/1.1517281.

[23] Barbir F. PEM electrolysis for production of hydrogen from renewable energy sources. Solar Energy 2005;78(5):661–9. https://doi.org/10.1016/j.solener.2004.09.003.

[24] Sezer N, Bayhan S, Fesli U, Sanfilippo A. A comprehensive review of the state-of-the-art of proton exchange membrane water electrolysis. Materials Science for Energy Technologies 2025;8:44–65. https://doi.org/10.1016/j.mset.2024.07.006.

[25] Schmidt O, Gambhir A, Staffell I, Hawkes A, Nelson J, Few S. Future cost and performance of water electrolysis: An expert elicitation study. International Journal of Hydrogen Energy 2017;42(52):30470–92. https://doi.org/10.1016/j.ijhydene.2017.10.045.

[26] Shiva Kumar S, Lim H. An overview of water electrolysis technologies for green hydrogen production. Energy Reports 2022;8:13793–813. https://doi.org/10.1016/j.egyr.2022.10.127.

[27] Hall DE. Electrodes for Alkaline Water Electrolysis. J. Electrochem. Soc. 1981;128(4):740–6. https://doi.org/10.1149/1.2127498.

[28] Hall DE. Ni (OH) 2 - Impregnated Anodes for Alkaline Water Electrolysis. J. Electrochem. Soc. 1983;130(2):317–21. https://doi.org/10.1149/1.2119702.

[29] Hall DE. Porous Nickel-Coated Steel Anodes for Alkaline Water Electrolysis: Corrosion Resistance. J. Electrochem. Soc. 1982;129(2):310–5. https://doi.org/10.1149/1.2123817.

[30] El-Shafie M. Hydrogen production by water electrolysis technologies: A review. Results in Engineering 2023;20:101426. https://doi.org/10.1016/j.rineng.2023.101426.

[31] Kuleshov VN, Kurochkin SV, Kuleshov NV, Gavrilyuk AA, Klimova MA, Grigorieva OY. Diaphragm and Membrane for Alkaline Water Electrolysis with Zirconium Hydroxide Hydrogel as Hydrophilic Filler. Inorg. Mater. Appl. Res. 2024;15(5):1360–6. https://doi.org/10.1134/S2075113324701004.

[32] Chialvo M de, Chialvo AC. Hydrogen evolution reaction: Analysis of the Volmer-Heyrovsky-Tafel mechanism with a generalized adsorption model. Journal of Electroanalytical Chemistry 1994;372(1-2):209–23. https://doi.org/10.1016/0022-0728(93)03043-O.

[33] Skúlason E, Karlberg GS, Rossmeisl J, Bligaard T, Greeley J, Jónsson H et al. Density functional theory calculations for the hydrogen evolution reaction in an electrochemical double layer on the Pt(111) electrode. Phys. Chem. Chem. Phys. 2007;9(25):3241–50. https://doi.org/10.1039/B700099E.

[34] Watzele S, Fichtner J, Garlyyev B, Schwämmlein JN, Bandarenka AS. On the Dominating Mechanism of the Hydrogen Evolution Reaction at Polycrystalline Pt Electrodes in Acidic Media. ACS Catal. 2018;8(10):9456–62. https://doi.org/10.1021/acscatal.8b03365.

[35] Prats H, Chan K. The determination of the HOR/HER reaction mechanism from experimental kinetic data. Phys Chem Chem Phys 2021;23(48):27150–8. https://doi.org/10.1039/d1cp04134g.

[36] Bao F, Kemppainen E, Dorbandt I, Bors R, Xi F, Schlatmann R et al. Understanding the Hydrogen Evolution Reaction Kinetics of Electrodeposited Nickel-Molybdenum in Acidic, Near-Neutral, and Alkaline Conditions. ChemElectroChem 2021;8(1):195–208. https://doi.org/10.1002/celc.202001436.

[37] Krstajić N, Popović M, Grgur B, Vojnović M, Šepa D. On the kinetics of the hydrogen evolution reaction on nickel in alkaline solution. J. Electroanal. Chem. 2001;512(1-2):16–26. https://doi.org/10.1016/S0022-0728(01)00590-3.

[38] Alobaid A, Wang C, Adomaitis RA. Mechanism and Kinetics of HER and OER on NiFe LDH Films in an Alkaline Electrolyte. Journal of The Electrochemical Society 2018;165(15):J3395-J3404. https://doi.org/10.1149/2.0481815jes.

[39] Nørskov JK, Bligaard T, Logadottir A, Kitchin JR, Chen JG, Pandelov S et al. Trends in the Exchange Current for Hydrogen Evolution. J. Electrochem. Soc. 2005;152(3):J23. https://doi.org/10.1149/1.1856988兴.

[40] Skúlason E, Tripkovic V, Björketun ME, Gudmundsdóttir S, Karlberg G, Rossmeisl J et al. Modeling the Electrochemical Hydrogen Oxidation and

Evolution Reactions on the Basis of Density Functional Theory Calculations. J. Phys. Chem. C 2010;114(42):18182–97. https://doi.org/10.1021/jp1048887.

[41] Nørskov JK, Bligaard T, Logadottir A, Kitchin JR, Chen JG, Pandelov S et al. Trends in the Exchange Current for Hydrogen Evolution. J. Electrochem. Soc. 2005;152(3):J23. https://doi.org/10.1149/1.1856988.

[42] Morales-Guio CG, Stern L-A, Hu X. Nanostructured hydrotreating catalysts for electrochemical hydrogen evolution. Chem Soc Rev 2014;43(18):6555–69. https://doi.org/10.1039/c3cs60468c.

[43] Durst J, Simon C, Siebel A, Rheinlander PJ, Schuler T, Hanzlik M et al. (Invited) Hydrogen Oxidation and Evolution Reaction (HOR/HER) on Pt Electrodes in Acid vs. Alkaline Electrolytes: Mechanism, Activity and Particle Size Effects. ECS Transactions 2014;64(3):1069–80. https://doi.org/10.1149/06403.1069ecst.

[44] Durst J, Simon C, Hasché F, Gasteiger HA. Hydrogen Oxidation and Evolution Reaction Kinetics on Carbon Supported Pt, Ir, Rh, and Pd Electrocatalysts in Acidic Media. J. Electrochem. Soc. 2015;162(1):F190-F203. https://doi.org/10.1149/2.0981501jes.

[45] Nørskov JK, Abild-Pedersen F, Studt F, Bligaard T. Density functional theory in surface chemistry and catalysis. Proceedings of the National Academy of Sciences 2011;108(3):937–43. https://doi.org/10.1073/pnas.1006652108.

[46] Chen H, Wu Q, Wang Y, Zhao Q, Ai X, Shen Y et al. d-sp orbital hybridization: a strategy for activity improvement of transition metal catalysts. Chem Commun (Camb) 2022;58(56):7730–40. https://doi.org/10.1039/D2CC02299K.

[47] Hammer B, Nørskov JK. Theoretical surface science and catalysis—calculations and concepts. In: Impact of Surface Science on Catalysis. Elsevier; 2000, p. 71–129.

[48] Greeley J, Nørskov JK. Large-scale, density functional theory-based screening of alloys for hydrogen evolution. Surface Science 2007;601(6):1590–8. https://doi.org/10.1016/j.susc.2007.01.037.

[49] Lei B, Zhang Y-Y, Du S-X. Prediction of structured void-containing 1T-PtTe 2 monolayer with potential catalytic activity for hydrogen evolution reaction. Chinese Phys. B 2020;29(5):58104. https://doi.org/10.1088/1674-1056/ab8203.

[50] Lin J-W, Liao C-A, Chen B-H, Cai X, Chen P-T. Understanding mechanism conversion in hydrogen evolution reaction on PtSe2: Role of layer number

explored by density functional theory. International Journal of Hydrogen Energy 2024;69:1129–36. https://doi.org/10.1016/j.ijhydene.2024.05.172.

[51] Wang Z, Xiao B, Lin Z, Xu Y, Lin Y, Meng F et al. PtSe2 /Pt Heterointerface with Reduced Coordination for Boosted Hydrogen Evolution Reaction. Angew Chem Int Ed Engl 2021;60(43):23388–93. https://doi.org/10.1002/anie.202110335.

[52] Strmcnik D, Uchimura M, Wang C, Subbaraman R, Danilovic N, van der Vliet D et al. Improving the hydrogen oxidation reaction rate by promotion of hydroxyl adsorption. Nat Chem 2013;5(4):300–6. https://doi.org/10.1038/NCHEM.1574.

[53] McCrory CCL, Jung S, Ferrer IM, Chatman SM, Peters JC, Jaramillo TF. Benchmarking hydrogen evolving reaction and oxygen evolving reaction electrocatalysts for solar water splitting devices. J Am Chem Soc 2015;137(13):4347–57. https://doi.org/10.1021/ja510442p.

[54] Sheng W, Gasteiger HA, Shao-Horn Y. Hydrogen Oxidation and Evolution Reaction Kinetics on Platinum: Acid vs Alkaline Electrolytes. J. Electrochem. Soc. 2010;157(11):B1529. https://doi.org/10.1149/1.3483106兴.

[55] Pomerantseva E, Resini C, Kovnir K, Kolen'ko YV. Emerging nanostructured electrode materials for water electrolysis and rechargeable beyond Li-ion batteries. Advances in Physics: X 2017;2(2):211–53. https://doi.org/10.1080/23746149.2016.1273796.

[56] Zalitis CM, Kramer D, Kucernak AR. Electrocatalytic performance of fuel cell reactions at low catalyst loading and high mass transport. Phys Chem Chem Phys 2013;15(12):4329–40. https://doi.org/10.1039/c3cp44431g.

[57] Bagotzky VS, Osetrova NV. Investigations of hydrogen ionization on platinum with the help of micro-electrodes. Journal of Electroanalytical Chemistry and Interfacial Electrochemistry 1973;43(2):233–49. https://doi.org/10.1016/S0022-0728(73)80494-2.

[58] Rheinländer PJ, Herranz J, Durst J, Gasteiger HA. Kinetics of the Hydrogen Oxidation/Evolution Reaction on Polycrystalline Platinum in Alkaline Electrolyte Reaction Order with Respect to Hydrogen Pressure. J. Electrochem. Soc. 2014;161(14):F1448-F1457. https://doi.org/10.1149/2.0501414jes.

[59] Zhou J, Zu Y, Bard AJ. Scanning electrochemical microscopy. Journal of Electroanalytical Chemistry 2000;491(1-2):22–9. https://doi.org/10.1016/S0022-0728(00)00100-5.

[60] Zoski CG. Scanning Electrochemical Microscopy: Investigation of Hydrogen Oxidation at Polycrystalline Noble Metal Electrodes. J. Phys. Chem. B 2003;107(26):6401–5. https://doi.org/10.1021/jp027436g.

[61] Uchida H, Izumi K, Aoki K, Watanabe M. Temperature-dependence of hydrogen oxidation reaction rates and CO-tolerance at carbon-supported Pt, Pt-Co, and Pt-Ru catalysts. Phys. Chem. Chem. Phys. 2009;11(11):1771–9. https://doi.org/10.1039/B811516H.

[62] Chen S, Kucernak A. Electrocatalysis under Conditions of High Mass Transport: Investigation of Hydrogen Oxidation on Single Submicron Pt Particles Supported on Carbon. J. Phys. Chem. B 2004;108(37):13984–94. https://doi.org/10.1021/jp048641u.

[63] Kucernak AR, Toyoda E. Studying the oxygen reduction and hydrogen oxidation reactions under realistic fuel cell conditions. Electrochemistry Communications 2008;10(11):1728–31. https://doi.org/10.1016/j.elecom.2008.09.001.

[64] Zalitis CM, Sharman J, Wright E, Kucernak AR. Properties of the hydrogen oxidation reaction on Pt/C catalysts at optimised high mass transport conditions and its relevance to the anode reaction in PEFCs and cathode reactions in electrolysers. Electrochimica Acta 2015;176:763–76. https://doi.org/10.1016/j.electacta.2015.06.146.

[65] Neyerlin KC, Gu W, Jorne J, Gasteiger HA. Study of the Exchange Current Density for the Hydrogen Oxidation and Evolution Reactions. J. Electrochem. Soc. 2007;154(7):B631. https://doi.org/10.1149/1.2733987.

[66] Durst J, Siebel A, Simon C, Hasché F, Herranz J, Gasteiger HA. New insights into the electrochemical hydrogen oxidation and evolution reaction mechanism. Energy Environ. Sci. 2014;7(7):2255–60. https://doi.org/10.1039/c4ee00440j.

[67] Sun Y, Lu J, Zhuang L. Rational determination of exchange current density for hydrogen electrode reactions at carbon-supported Pt catalysts. Electrochimica Acta 2010;55(3):844–50. https://doi.org/10.1016/j.electacta.2009.09.047.

[68] Park J-W, Hu Z, Gao S, Campbell IH, Gong H. Platinum group element abundances in the upper continental crust revisited – New constraints from analyses of Chinese loess. Geochimica et Cosmochimica Acta 2012;93:63–76. https://doi.org/10.1016/j.gca.2012.06.026.

[69] Kim H, Choe S, Park H, Jang JH, Ahn SH, Kim S-K. An extremely low Pt loading cathode for a highly efficient proton exchange membrane water electrolyzer. Nanoscale 2017;9(48):19045–9. https://doi.org/10.1039/C7NR07224D.

[70] Gupta A, Chellehbari YM, Shahgaldi S. Achieving high performance and durability with ultra-low precious metal nanolayer on porous transport layer for PEMWE application. Journal of Power Sources 2025;630:236088. https://doi.org/10.1016/j.jpowsour.2024.236088.

[71] Choi KJ, Kim S-K. A Pt cathode with high mass activity for proton exchange membrane water electrolysis. International Journal of Hydrogen Energy 2023;48(3):849–63. https://doi.org/10.1016/j.ijhydene.2022.09.308.

[72] Duan X, Zhang H. Introduction: Two-Dimensional Layered Transition Metal Dichalcogenides. Chem Rev 2024;124(19):10619–22. https://doi.org/10.1021/acs.chemrev.4c00586.

[73] van Nguyen T, Tekalgne M, Nguyen TP, van Le Q, Ahn SH, Kim SY. Electrocatalysts based on MoS 2 and WS 2 for hydrogen evolution reaction: An overview. Battery Energy 2023;2(3). https://doi.org/10.1002/bte2.20220057.

[74] Yu Y, Huang S-Y, Li Y, Steinmann SN, Yang W, Cao L. Layer-dependent electrocatalysis of MoS2 for hydrogen evolution. Nano Lett 2014;14(2):553–8. https://doi.org/10.1021/nl403620g.

[75] Yu Y, Nam G-H, He Q, Wu X-J, Zhang K, Yang Z et al. High phase-purity 1T'-MoS2- and 1T'-MoSe2-layered crystals. Nat Chem 2018;10(6):638–43. https://doi.org/10.1038/s41557-018-0035-6.

[76] Chia X, Adriano A, Lazar P, Sofer Z, Luxa J, Pumera M. Layered Platinum Dichalcogenides (PtS 2 PtSe 2 and PtTe 2) Electrocatalysis: Monotonic Dependence on the Chalcogen Size. Adv. Funct. Mater. 2016;26(24):4306–18. https://doi.org/10.1002/adfm.201505402.

[77] Supriya S, Antonatos N, Luxa J, Gusmão R, Sofer Z. Comparison between layered Pt3Te4 and PtTe2 for electrocatalytic reduction reactions. FlatChem 2021;29:100280. https://doi.org/10.1016/j.flatc.2021.100280.

[78] Lin Z, Xiao B, Wang Z, Tao W, Shen S, Huang L et al. Planar-Coordination PdSe 2 Nanosheets as Highly Active Electrocatalyst for Hydrogen Evolution Reaction. Advanced Functional Materials 2021;31(32):2102321. https://doi.org/10.1002/adfm.202102321.

[79] Mxakaza LF, Mashindi V, Linganiso CE, Moloto N, Tetana ZN. Evaluating the Hydrogen Evolution Reaction Activity of Colloidally Prepared PtSe2 and PtTe2 Catalysts in an Alkaline Medium. ChemistryOpen 2024;13(10):e202400146. https://doi.org/10.1002/open.202400146.

[80] Niu S, Cai J, Wang G. Two-dimensional MOS2 for hydrogen evolution reaction catalysis: The electronic structure regulation. Nano Res. 2021;14(6):1985–2002. https://doi.org/10.1007/s12274-020-3249-z.

[81] Ye G, Gong Y, Lin J, Li B, He Y, Pantelides ST et al. Defects Engineered Monolayer MoS2 for Improved Hydrogen Evolution Reaction. Nano Lett 2016;16(2):1097–103. https://doi.org/10.1021/acs.nanolett.5b04331.

[82] Liu L, Wu J, Wu L, Ye M, Liu X, Wang Q et al. Phase-selective synthesis of 1T' MoS2 monolayers and heterophase bilayers. Nat Mater 2018;17(12):1108–14. https://doi.org/10.1038/s41563-018-0187-1.

[83] Chen Y-C, Lu A-Y, Lu P, Yang X, Jiang C-M, Mariano M et al. Structurally Deformed MoS2 for Electrochemically Stable, Thermally Resistant, and Highly Efficient Hydrogen Evolution Reaction. Adv Mater 2017;29(44). https://doi.org/10.1002/adma.201703863.

[84] Xu Y, Ge R, Yang J, Li J, Li S, Li Y et al. Molybdenum disulfide (MoS2)-based electrocatalysts for hydrogen evolution reaction: From mechanism to manipulation. Journal of Energy Chemistry 2022;74:45–71. https://doi.org/10.1016/j.jechem.2022.06.031.

[85] Zhu J, Wang Z-C, Dai H, Wang Q, Yang R, Yu H et al. Boundary activated hydrogen evolution reaction on monolayer MoS2. Nat Commun 2019;10(1):1348. https://doi.org/10.1038/s41467-019-09269-9.

[86] Solati N, Karakaya C, Kaya S. Advancing the Understanding of the Structure–Activity–Durability Relation of 2D MoS 2 for the Hydrogen Evolution Reaction. ACS Catal. 2023;13(1):342–54. https://doi.org/10.1021/acscatal.2c03719.

[87] Lukowski MA, Daniel AS, Meng F, Forticaux A, Li L, Jin S. Enhanced hydrogen evolution catalysis from chemically exfoliated metallic MoS2 nanosheets. J Am Chem Soc 2013;135(28):10274–7. https://doi.org/10.1021/ja404523s.

[88] Zhang J, Wu J, Guo H, Chen W, Yuan J, Martinez U et al. Unveiling Active Sites for the Hydrogen Evolution Reaction on Monolayer MoS2. Adv Mater 2017;29(42). https://doi.org/10.1002/adma.201701955.

[89] Li G, Du Zhang, Qiao Q, Yu Y, Peterson D, Zafar A et al. All The Catalytic Active Sites of MoS2 for Hydrogen Evolution. J Am Chem Soc 2016;138(51):16632–8. https://doi.org/10.1021/jacs.6b05940.

[90] Zalitis CM, Kramer D, Sharman J, Wright E, Kucernak AR. Pt Nano-Particle Performance for PEFC Reactions at Low Catalyst Loading and High Reactant Mass Transport. ECS Transactions 2013;58(1):39–47. https://doi.org/10.1149/05801.0039ecst.

[91] Jaramillo TF, Jørgensen KP, Bonde J, Nielsen JH, Horch S, Chorkendorff I. Identification of active edge sites for electrochemical H2 evolution from MoS2 nanocatalysts. Science 2007;317(5834):100–2. https://doi.org/10.1126/science.1141483.

[92] Kibsgaard J, Jaramillo TF. Molybdenum phosphosulfide: an active, acid-stable, earth-abundant catalyst for the hydrogen evolution reaction. Angew. Chem. Int. Ed. 2014;53(52):14433–7. https://doi.org/10.1002/anie.201408222.

[93] Hellstern TR, Benck JD, Kibsgaard J, Hahn C, Jaramillo TF. Engineering Cobalt Phosphide (CoP) Thin Film Catalysts for Enhanced Hydrogen Evolution Activity on Silicon Photocathodes. Adv. Energy Mater. 2016;6(4). https://doi.org/10.1002/aenm.201501758.

[94] Anantharaj S, Noda S. Layered 2D PtX 2 (X = S, Se, Te) for the electrocatalytic HER in comparison with Mo/WX 2 and Pt/C: are we missing the bigger picture? Energy & Environmental Science 2022;15(4):1461–78. https://doi.org/10.1039/D1EE03516A.

[95] Cao Y. Roadmap and Direction toward High-Performance MoS2 Hydrogen Evolution Catalysts. ACS Nano 2021;15(7):11014–39. https://doi.org/10.1021/acsnano.1c01879.

[96] Shi Y, Zhou Y, Yang D-R, Xu W-X, Wang C, Wang F-B et al. Energy Level Engineering of MoS2 by Transition-Metal Doping for Accelerating Hydrogen Evolution Reaction. J Am Chem Soc 2017;139(43):15479–85. https://doi.org/10.1021/jacs.7b08881.

[97] Lai B, Singh SC, Bindra JK, Saraj CS, Shukla A, Yadav TP et al. Hydrogen evolution reaction from bare and surface-functionalized few-layered MoS2 nanosheets in acidic and alkaline electrolytes. Materials Today Chemistry 2019;14:100207. https://doi.org/10.1016/j.mtchem.2019.100207.

[98] Deng S, Luo M, Ai C, Zhang Y, Liu B, Huang L et al. Synergistic Doping and Intercalation: Realizing Deep Phase Modulation on MoS2 Arrays for High-Efficiency Hydrogen Evolution Reaction. Angew. Chem. Int. Ed. 2019;58(45):16289–96. https://doi.org/10.1002/anie.201909698.

[99] Li J, Kolekar S, Xin Y, Coelho PM, Lasek K, Nugera FA et al. Thermal Phase Control of Two-Dimensional Pt-Chalcogenide (Se and Te) Ultrathin Epitaxial Films and Nanocrystals. Chem. Mater. 2021;33(20):8018–27. https://doi.org/10.1021/acs.chemmater.1c02163.

[100] Lasek K, Ghorbani-Asl M, Pathirage V, Krasheninnikov AV, Batzill M. Controlling Stoichiometry in Ultrathin van der Waals Films: PtTe2, Pt2Te3, Pt3Te4, and Pt2Te2. ACS Nano 2022;16(6):9908–19. https://doi.org/10.1021/acsnano.2c04303.

[101] Furuseth S, Selte K, Kjekshus A, Gronowitz S, Hoffman RA, Westerdahl A. Redetermined Crystal Structures of NiTe2, PdTe2, PtS2, PtSe2, and PtTe2. Acta Chem. Scand. 1965;19:257–8. https://doi.org/10.3891/ACTA.CHEM.SCAND.19-0257.

[102] Bhan S, Gödecke T, Schubert K. Konstitution einiger mischungen des platins mit b-elementen (B = Sn, Sb, Te). Journal of the Less Common Metals 1969;19(2):121–40. https://doi.org/10.1016/0022-5088(69)90027-7.

[103] Cenzual K, Gelato LM, Penzo M, Parthé E. Overlooked trigonal symmetry in structures reported with monoclinic centred Bravais lattices; trigonal description of Li 8 Pb 3 PtTe, Pt 3 Te 4 Pt 2 Te 3 LiFe 6 Ge 4 LiFe 6 Ge 5 CaGa 6 Te 10 and La 3.266 Mn 1.1 S 6. Zeitschrift für Kristallographie - Crystalline Materials 1990;193(1-4):217–42. https://doi.org/10.1524/zkri.1990.193.14.217.

[104] Bredig G, Allolio R. Röntgenuntersuchungen an katalytisch wirkenden Metallen. Zeitschrift für Physikalische Chemie 1927;126U(1):41–71. https://doi.org/10.1515/zpch-1927-12604.

[105] Yuan J-H, Li L-H, Zhang W, Xue K-H, Wang C, Wang J et al. Pt5Se4 Monolayer: A Highly Efficient Electrocatalyst toward Hydrogen and Oxygen Electrode Reactions. ACS Appl Mater Interfaces 2020;12(12):13896–903. https://doi.org/10.1021/acsami.9b22674.

[106] Huang H, Fan X, Singh DJ, Zheng W. Modulation of Hydrogen Evolution Catalytic Activity of Basal Plane in Monolayer Platinum and Palladium

Dichalcogenides. ACS Omega 2018;3(8):10058–65. https://doi.org/10.1021/acsomega.8b01414.

[107] Hussain S, Akbar K, Vikraman D, Rabani I, Song W, An K-S et al. Experimental and theoretical insights to demonstrate the hydrogen evolution activity of layered platinum dichalcogenides electrocatalysts. Journal of Materials Research and Technology 2021;12:385–98. https://doi.org/10.1016/j.jmrt.2021.02.097.

[108] Lin S, Liu Y, Hu Z, Lu W, Mak CH, Zeng L et al. Tunable active edge sites in PtSe2 films towards hydrogen evolution reaction. Nano Energy 2017;42:26–33. https://doi.org/10.1016/j.nanoen.2017.10.038.

[109] Hu D, Zhao T, Ping X, Zheng H, Xing L, Liu X et al. Unveiling the Layer-Dependent Catalytic Activity of PtSe 2 Atomic Crystals for the Hydrogen Evolution Reaction. Angew. Chem. 2019;131(21):7051–5. https://doi.org/10.1002/ange.201901612.

[110] Mc Manus JB, Horvath DV, Browne MP, Cullen CP, Cunningham G, Hallam T et al. Low-temperature synthesis and electrocatalytic application of large-area PtTe2 thin films. Nanotechnology 2020;31(37):375601. https://doi.org/10.1088/1361-6528/ab9973.

[111] Boukhvalov DW, Cheng J, D'Olimpio G, Bocquet FC, Kuo C-N, Sarkar AB et al. Unveiling the Mechanisms Ruling the Efficient Hydrogen Evolution Reaction with Mitrofanovite Pt3Te4. J Phys Chem Lett 2021;12(35):8627–36. https://doi.org/10.1021/acs.jpclett.1c01261.

[112] Ping X, Liang D, Wu Y, Yan X, Zhou S, Hu D et al. Activating a Two-Dimensional PtSe2 Basal Plane for the Hydrogen Evolution Reaction through the Simultaneous Generation of Atomic Vacancies and Pt Clusters. Nano Lett 2021;21(9):3857–63. https://doi.org/10.1021/acs.nanolett.1c00380.

[113] Liu G, Li J, Dong C, Wu L, Liang D, Cao H et al. Hydrogen evolution reaction on in-plane platinum and palladium dichalcogenides via single-atom doping. International Journal of Hydrogen Energy 2021;46(35):18294–304. https://doi.org/10.1016/j.ijhydene.2021.02.206.

[114] Qiao W, Xu W, Xu X, Wu L, Yan S, Wang D. Construction of Active Orbital via Single-Atom Cobalt Anchoring on the Surface of 1T-MoS 2 Basal Plane toward Efficient Hydrogen Evolution. ACS Appl. Energy Mater. 2020;3(3):2315–22. https://doi.org/10.1021/acsaem.0c00163.

[115] Diaz HC, Chaghi R, Ma Y, Batzill M. Molecular beam epitaxy of the van der Waals heterostructure MoTe 2 on MoS 2 phase, thermal, and chemical stability. 2D Mater. 2015;2(4):44010. https://doi.org/10.1088/2053-1583/2/4/044010.

[116] Diaz HC, Ma Y, Chaghi R, Batzill M. High density of (pseudo) periodic twin-grain boundaries in molecular beam epitaxy-grown van der Waals heterostructure: MoTe2/MoS2. Appl. Phys. Lett. 2016;108(19). https://doi.org/10.1063/1.4949559.

[117] McCrory CCL, Jung S, Peters JC, Jaramillo TF. Benchmarking heterogeneous electrocatalysts for the oxygen evolution reaction. J Am Chem Soc 2013;135(45):16977–87. https://doi.org/10.1021/ja407115p.

[118] Gong M, Wang D-Y, Chen C-C, Hwang B-J, Dai H. A mini review on nickel-based electrocatalysts for alkaline hydrogen evolution reaction. Nano Res. 2016;9(1):28–46. https://doi.org/10.1007/s12274-015-0965-x.

[119] Phillips R, Dunnill CW. Zero gap alkaline electrolysis cell design for renewable energy storage as hydrogen gas. RSC Adv. 2016;6(102):100643–51. https://doi.org/10.1039/c6ra22242k.

[120] Schalenbach M, Speck FD, Ledendecker M, Kasian O, Goehl D, Mingers AM et al. Nickel-molybdenum alloy catalysts for the hydrogen evolution reaction: Activity and stability revised. Electrochimica Acta 2018;259:1154–61. https://doi.org/10.1016/j.electacta.2017.11.069.

[121] Lasia A, Rami A. Kinetics of hydrogen evolution on nickel electrodes. Journal of Electroanalytical Chemistry and Interfacial Electrochemistry 1990;294(1-2):123–41. https://doi.org/10.1016/0022-0728(90)87140-F.

[122] Raj IA, Vasu KI. Transition metal-based hydrogen electrodes in alkaline solution ? electrocatalysis on nickel based binary alloy coatings. J Appl Electrochem 1990;20(1):32–8. https://doi.org/10.1007/BF01012468.

[123] Birry L, Lasia A. Studies of the Hydrogen Evolution Reaction on Raney Nickel–Molybdenum Electrodes. J Appl Electrochem 2004;34(7):735–49. https://doi.org/10.1023/B:JACH.0000031161.26544.6a.

[124] Li X-P, Han W-K, Xiao K, Ouyang T, Li N, Peng F et al. Enhancing hydrogen evolution reaction through modulating electronic structure of self-supported NiFe LDH. Catal. Sci. Technol. 2020;10(13):4184–90. https://doi.org/10.1039/d0cy00315h.

[125] Franceschini EA, Lacconi GI, Corti HR. Kinetics of the hydrogen evolution on nickel in alkaline solution: new insight from rotating disk electrode and impedance spectroscopy analysis. Electrochimica Acta 2015;159:210–8. https://doi.org/10.1016/j.electacta.2015.01.110.

[126] I.J. BROWN and S. SOTIROPOULOS. Preparation and characterization of microporous Ni coatings as hydrogen evolving cathodes. J. Appl. Electrochem. 2000;30:107–11. https://doi.org/10.1023/A:1003888402752.

[127] Huang L-F, Hutchison MJ, Santucci RJ, Scully JR, Rondinelli JM. Improved Electrochemical Phase Diagrams from Theory and Experiment: The Ni–Water System and Its Complex Compounds. J. Phys. Chem. C 2017;121(18):9782–9. https://doi.org/10.1021/acs.jpcc.7b02771.

[128] Hall DS, Bock C, MacDougall BR. The Electrochemistry of Metallic Nickel: Oxides, Hydroxides, Hydrides and Alkaline Hydrogen Evolution. J. Electrochem. Soc. 2013;160(3):F235-F243. https://doi.org/10.1149/2.026303jes.

[129] Szklarska-Smialowska Z, Smialowski M. Electrochemical Study of the Nickel-Hydrogen System. J. Electrochem. Soc. 1963;110(5):444. https://doi.org/10.1149/1.2425783.

[130] Soares DM, Teschke O, Torriani I. Hydride Effect on the Kinetics of the Hydrogen Evolution Reaction on Nickel Cathodes in Alkaline Media. J. Electrochem. Soc. 1992;139(1):98–105. https://doi.org/10.1149/1.2069207.

[131] Rommal HEG, Moran PJ. Time-Dependent Energy Efficiency Losses at Nickel Cathodes in Alkaline Water Electrolysis Systems. J. Electrochem. Soc. 1985;132(2):325–9. https://doi.org/10.1149/1.2113831.

[132] Mauer AE, Kirk DW, Thorpe SJ. The role of iron in the prevention of nickel electrode deactivation in alkaline electrolysis. Electrochim. Acta 2007;52(11):3505–9. https://doi.org/10.1016/j.electacta.2006.10.037.

[133] M. A. V. Devanathan, Z. Stachurski. The adsorption and diffusion of electrolytic hydrogen in palladium. Proc. R. Soc. Lond. A 1962;270(1340):90–102. https://doi.org/10.1098/rspa.1962.0205.

[134] David R. Lide. CRC Handbook of Chemistry and Physics, Internet Version 2005. Boca Raton, FL: CRC Press; 2005.

[135] Hall DS, Lockwood DJ, Poirier S, Bock C, MacDougall BR. Raman and infrared spectroscopy of α and β phases of thin nickel hydroxide films

electrochemically formed on nickel. J Phys Chem A 2012;116(25):6771–84. https://doi.org/10.1021/jp303546r.

[136] Delahaye-Vidal A. Structural and textural investigations of the nickel hydroxide electrode. Solid State Ionics 1996;84(3-4):239–48. https://doi.org/10.1016/0167-2738(96)00030-6.

[137] Lee JW, Ko JM, Kim J-D. Hierarchical Microspheres Based on α-Ni(OH) 2 Nanosheets Intercalated with Different Anions: Synthesis, Anion Exchange, and Effect of Intercalated Anions on Electrochemical Capacitance. J. Phys. Chem. C 2011;115(39):19445–54. https://doi.org/10.1021/jp206379h.

[138] Taibi M, Ammar S, Jouini N, Fiévet F, Molinié P, Drillon M. Layered nickel hydroxide salts: synthesis, characterization and magnetic behaviour in relation to the basal spacing. J. Mater. Chem. 2002;12(11):3238–44. https://doi.org/10.1039/B204087E.

[139] Faure C, Delmas C, Fouassier M. Characterization of a turbostratic α-nickel hydroxide quantitatively obtained from an NiSO4 solution. Journal of Power Sources 1991;35(3):279–90. https://doi.org/10.1016/0378-7753(91)80112-B.

[140] Tkalych AJ, Yu K, Carter EA. Structural and Electronic Features of β-Ni(OH) 2 and β-NiOOH from First Principles. J. Phys. Chem. C 2015;119(43):24315–22. https://doi.org/10.1021/acs.jpcc.5b08481.

[141] Bode H, Dehmelt K, Witte J. Zur kenntnis der nickelhydroxidelektrode—I.Über das nickel (II)-hydroxidhydrat. Electrochimica Acta 1966;11(8):1079–87. https://doi.org/10.1016/0013-4686(66)80045-2.

[142] Oliva P, Leonardi J, Laurent JF, Delmas C, Braconnier JJ, Figlarz M et al. Review of the structure and the electrochemistry of nickel hydroxides and oxy-hydroxides. Journal of Power Sources 1982;8(2):229–55. https://doi.org/10.1016/0378-7753(82)80057-8.

[143] Klaus S, Louie MW, Trotochaud L, Bell AT. Role of Catalyst Preparation on the Electrocatalytic Activity of Ni 1– x Fe x OOH for the Oxygen Evolution Reaction. J. Phys. Chem. C 2015;119(32):18303–16. https://doi.org/10.1021/acs.jpcc.5b04776.

[144] Wehrens-Dijksma M, Notten P. Electrochemical Quartz Microbalance characterization of Ni(OH)2-based thin film electrodes. Electrochimica Acta 2006;51(18):3609–21. https://doi.org/10.1016/j.electacta.2005.10.022.

[145] Ji L, Lv C, Chen Z, Huang Z, Zhang C. Nickel-Based (Photo)Electrocatalysts for Hydrogen Production. Advanced Materials 2018;30(17):e1705653. https://doi.org/10.1002/adma.201705653.

[146] Ge Z, Fu B, Zhao J, Li X, Ma B, Chen Y. A review of the electrocatalysts on hydrogen evolution reaction with an emphasis on Fe, Co and Ni-based phosphides. J Mater Sci 2020;55(29):14081–104. https://doi.org/10.1007/s10853-020-05010-w.

[147] Griffin PW, Hammond GP. Industrial energy use and carbon emissions reduction in the iron and steel sector: A UK perspective. Applied Energy 2019;249:109–25. https://doi.org/10.1016/j.apenergy.2019.04.148.

[148] He K, Wang L. A review of energy use and energy-efficient technologies for the iron and steel industry. Renewable and Sustainable Energy Reviews 2017;70:1022–39. https://doi.org/10.1016/j.rser.2016.12.007.

[149] Pentland N, Bockris JO, Sheldon E. Hydrogen Evolution Reaction on Copper, Gold, Molybdenum, Palladium, Rhodium, and Iron. J. Electrochem. Soc. 1957;104(3):182. https://doi.org/10.1149/1.2428530.

[150] Flis-Kabulska I, Flis J. Electroactivity of Ni–Fe cathodes in alkaline water electrolysis and effect of corrosion. Corros. Sci. 2016;112:255–63. https://doi.org/10.1016/j.corsci.2016.07.017.

[151] Armbruster MH. The Solubility of Hydrogen at Low Pressure in Iron, Nickel and Certain Steels at 400 to 600°. J Am Chem Soc 1943;65(6):1043–54. https://doi.org/10.1021/ja01246a012.

[152] Suryanto BHR, Wang Y, Hocking RK, Adamson W, Zhao C. Overall electrochemical splitting of water at the heterogeneous interface of nickel and iron oxide. Nat. Commun. 2019;10(1):5599. https://doi.org/10.1038/s41467-019-13415-8.

[153] Brossard L, Huot J-Y. In situ activation of cathodes during alkaline water electrolysis by dissolved iron and molybdenum species. J. Appl. Electrochem. 1991;21(6):508–15. https://doi.org/10.1007/BF01018603.

[154] Townsend HE. Potential-pH diagrams at elevatedtemperature for the system Fe-H2O. Corrosion Science 1970;10(5):343–58. https://doi.org/10.1016/S0010-938X(70)80025-7.

[155] Posada JOG, Hall PJ. Controlling hydrogen evolution on iron electrodes. Int. J. Hydrogen Energy 2016;41(45):20807–17. https://doi.org/10.1016/j.ijhydene.2016.04.123.

[156] Mahmoudi L, Kissner R. Electrode reactions of iron oxide-hydroxide colloids. Dalton Trans 2014;43(41):15407–13. https://doi.org/10.1039/C4DT02040E.

[157] Riley MA, Moran PJ. The Influence of Iron Deposition on the Voltage-Time Behavior of Nickel Cathodes in Alkaline Water Electrolysis. J. Electrochem. Soc. 1986;133(4):760–1. https://doi.org/10.1149/1.2108670.

[158] Corrigan DA. The Catalysis of the Oxygen Evolution Reaction by Iron Impurities in Thin Film Nickel Oxide Electrodes. J. Electrochem. Soc. 1987;134(2):377. https://doi.org/10.1149/1.2100463.

[159] HUOT J, Brossard L. Time dependence of the hydrogen discharge at 70°C on nickel cathodes. Int. J. Hydrogen Energy 1987;12(12):821–30. https://doi.org/10.1016/0360-3199(87)90103-0.

[160] Becker H, Murawski J, Shinde DV, Stephens IEL, Hinds G, Smith G. Impact of impurities on water electrolysis: a review. Sustain. Energy Fuels 2023;7(7):1565–603. https://doi.org/10.1039/D2SE01517J.

[161] Klaus S, Cai Y, Louie MW, Trotochaud L, Bell AT. Effects of Fe Electrolyte Impurities on Ni(OH) 2 /NiOOH Structure and Oxygen Evolution Activity. J. Phys. Chem. C 2015;119(13):7243–54. https://doi.org/10.1021/acs.jpcc.5b00105.

[162] Salmanion M, Najafpour MM. Oxygen-Evolution Reaction Performance of Nickel (Hydr)Oxide in Alkaline Media: Iron and Nickel Impurities. J. Phys. Chem. C 2023;127(37):18340–9. https://doi.org/10.1021/acs.jpcc.3c05164.

[163] Spanos I, Masa J, Zeradjanin A, Schlögl R. The Effect of Iron Impurities on Transition Metal Catalysts for the Oxygen Evolution Reaction in Alkaline Environment: Activity Mediators or Active Sites? Catal. Letters 2021;151(7):1843–56. https://doi.org/10.1007/s10562-020-03478-4.

[164] Trotochaud L, Young SL, Ranney JK, Boettcher SW. Nickel-iron oxyhydroxide oxygen-evolution electrocatalysts: the role of intentional and incidental iron incorporation. J Am Chem Soc 2014;136(18):6744–53. https://doi.org/10.1021/ja502379c.

[165] Swierk JR, Klaus S, Trotochaud L, Bell AT, Tilley TD. Electrochemical Study of the Energetics of the Oxygen Evolution Reaction at Nickel Iron (Oxy)Hydroxide

Catalysts. J. Phys. Chem. C 2015;119(33):19022–9. https://doi.org/10.1021/acs.jpcc.5b05861.

[166] Brossard L, Huot J-Y. Influence of iron impurities on the time dependence of the hydrogen evolution reaction on platinum cathodes during electrolysis of 30 w/o KOH. J. Appl. Electrochem. 1989;19(6):882–8. https://doi.org/10.1007/BF01007936.

[167] Conway BE, Angerstein-Kozlowska H. The electrochemical study of multiple-state adsorption in monolayers. Acc. Chem. Res. 1981;14(2):49–56. https://doi.org/10.1021/ar00062a004.

[168] Weber DJ, Dosche C, Oezaslan M. Fundamental Aspects of Contamination during the Hydrogen Evolution/Oxidation Reaction in Alkaline Media. J. Electrochem. Soc. 2020;167(2):24506. https://doi.org/10.1149/1945-7111/ab681f.

[169] Huot J-Y. Hydrogen Evolution and Interface Phenomena on a Nickel Cathode in 30 w/o KOH I Kinetics Parameters and Electrode Impedance Between 303 and 363 K. J. Electrochem. Soc. 1989;136(7):1933–9. https://doi.org/10.1149/1.2097088.

[170] Kirk DW, Thorpe S. Nickel Cathode Passivation in Alkaline Water Electrolysis. ECS Trans. 2007;2(14):71–6. https://doi.org/10.1149/1.2408970.

[171] Brossard L. Electrocatalytic performance for alkaline water electrolysis of Ni electrodes electrocoated with Fe or Fe/Mo. Int. J. Hydrogen Energy 1991;16(1):13–21. https://doi.org/10.1016/0360-3199(91)90056-O.

[172] Flis-Kabulska I, Flis J. Hydrogen evolution and corrosion products on iron cathodes in hot alkaline solution. Int. J. Hydrogen Energy 2014;39(8):3597–605. https://doi.org/10.1016/j.ijhydene.2013.12.158.

[173] Demnitz M, Lamas YM, Garcia Barros RL, Leeuw den Bouter A de, van der Schaaf J, Theodorus de Groot M. Effect of iron addition to the electrolyte on alkaline water electrolysis performance. iScience 2024;27(1):108695. https://doi.org/10.1016/j.isci.2023.108695.

[174] Du C, Tan Q, Yin G, Zhang J. Rotating Disk Electrode Method. In: Rotating Electrode Methods and Oxygen Reduction Electrocatalysts. Elsevier; 2014, p. 171–198.

[175] Kármán TV. Über laminare und turbulente Reibung. Z. angew. Math. Mech. 1921;1(4):233–52. https://doi.org/10.1002/zamm.19210010401.

[176] Wissler EH. Physicochemical hydrodynamics (Levich, Veniamin G.). J. Chem. Educ. 1963;40(10):112-116. https://doi.org/10.1021/ed040pA827.2.

[177] Lazaridis T, Stühmeier BM, Gasteiger HA, El-Sayed HA. Capabilities and limitations of rotating disk electrodes versus membrane electrode assemblies in the investigation of electrocatalysts. Nat Catal 2022;5(5):363–73. https://doi.org/10.1038/s41929-022-00776-5.

[178] Kulyk N, Cherevko S, Auinger M, Laska C, Mayrhofer KJJ. Numerical Simulation of an Electrochemical Flow Cell with V-Shape Channel Geometry. J. Electrochem. Soc. 2015;162(12):H860-H866. https://doi.org/10.1149/2.0261512jes.

[179] Tschupp SA, Temmel SE, Salguero NP, Herranz J, Schmidt TJ. Numerical Partitioning Model for the Koutecký-Levich Analysis of Electrochemical Flow Cells with a Combined Channel/Wall-Jet Geometry. J. Electrochem. Soc. 2017;164(11):E3448-E3456. https://doi.org/10.1149/2.0441711jes.

[180] Ehelebe K, Schmitt N, Sievers G, Jensen AW, Hrnjić A, Collantes Jiménez P et al. Benchmarking Fuel Cell Electrocatalysts Using Gas Diffusion Electrodes: Inter-lab Comparison and Best Practices. ACS Energy Lett. 2022;7(2):816–26. https://doi.org/10.1021/acsenergylett.1c02659.

[181] Nösberger S, Du J, Quinson J, Berner E, Zana A, Wiberg GK et al. The gas diffusion electrode setup as a testing platform for evaluating fuel cell catalysts: A comparative RDE-GDE study. Electrochemical Science Adv 2023;3(1). https://doi.org/10.1002/elsa.202100190.

[182] Fathi Tovini M, Hartig-Weiß A, Gasteiger HA, El-Sayed HA. The Discrepancy in Oxygen Evolution Reaction Catalyst Lifetime Explained: RDE vs MEA - Dynamicity within the Catalyst Layer Matters. Journal of The Electrochemical Society 2021;168(1):14512. https://doi.org/10.1149/1945-7111/abdcc9.

[183] Inaba M, Jensen AW, Sievers GW, Escudero-Escribano M, Zana A, Arenz M. Benchmarking high surface area electrocatalysts in a gas diffusion electrode: measurement of oxygen reduction activities under realistic conditions. Energy & Environmental Science 2018;11(4):988–94. https://doi.org/10.1039/C8EE00019K.

[184] Ehelebe K, Seeberger D, Paul MTY, Thiele S, Mayrhofer KJJ, Cherevko S. Evaluating Electrocatalysts at Relevant Currents in a Half-Cell: The Impact of Pt

Loading on Oxygen Reduction Reaction. Journal of The Electrochemical Society 2019;166(16):F1259-F1268. https://doi.org/10.1149/2.0911915jes.

[185] Riasse R, Lafforgue C, Vandenberghe F, Micoud F, Morin A, Arenz M et al. Benchmarking proton exchange membrane fuel cell cathode catalyst at high current density: A comparison between the rotating disk electrode, the gas diffusion electrode and differential cell. Journal of Power Sources 2023;556:232491. https://doi.org/10.1016/j.jpowsour.2022.232491.

[186] Kim H-E, Kwon J, Lee H. Catalytic approaches towards highly durable proton exchange membrane fuel cells with minimized Pt use. Chem Sci 2022;13(23):6782–95. https://doi.org/10.1039/D2SC00541G.

[187] Gasteiger HA, Kocha SS, Sompalli B, Wagner FT. Activity benchmarks and requirements for Pt, Pt-alloy, and non-Pt oxygen reduction catalysts for PEMFCs. Applied Catalysis B: Environmental 2005;56(1-2):9–35. https://doi.org/10.1016/j.apcatb.2004.06.021.

[188] Rager K, Tang B, Schneemann C, Dworzak A, Oezaslan M, Dietzel A. Ordered Porous Electrodes Obtained Using LIFT for Electrochemical Applications. Materials (Basel) 2023;16(2):596. https://doi.org/10.3390/ma16020596.

[189] Tschupp SA. Model Catalysts Fabricated via Interference Lithography and their Electrochemical Characterization: ETH Zurich; 2017.

[190] Zhou Y, Silva JL, Woods JM, Pondick JV, Feng Q, Liang Z et al. Revealing the Contribution of Individual Factors to Hydrogen Evolution Reaction Catalytic Activity. Adv Mater 2018;30(18):e1706076. https://doi.org/10.1002/adma.201706076.

[191] Bruce JP, Nguyen K-LC, Scholten F, Arán-Ais RM, Navarro JJ, Hartmann J et al. Development of a single crystal sample holder for interfacing ultrahigh vacuum and electrochemical experimentation. Review of Scientific Instruments 2021;92(7):74104. https://doi.org/10.1063/5.0057822.

[192] Sun Z, Lauritsen JV. A versatile electrochemical cell for hanging meniscus or flow cell measurement of planar model electrodes characterized with scanning tunneling microscopy and x-ray photoelectron spectroscopy. Rev Sci Instrum 2021;92(9):94101. https://doi.org/10.1063/5.0060643.

[193] Schneemann C, Traegner J, Mindermann L, Friedrichs-Schucht M, Tang B, Dietzel A et al. A Universal Analytical Model for the Limiting Current

Characteristics in Impinging Jet Electrodes. Journal of The Electrochemical Society 2025;172(6):66503. https://doi.org/10.1149/1945-7111/add840.

[194] Soucaze-Guillous B, Kutner W. Flow characteristics of a versatile wall-jet or radial-flow thin-layer large-volume cell for electrochemical detection in flow-through analytical systems. Electroanalysis 1997;9(1):32–9. https://doi.org/10.1002/elan.1140090109.

[195] Jusys Z, Massong H, Baltruschat H. A New Approach for Simultaneous DEMS and EQCM: Electro-oxidation of Adsorbed CO on Pt and Pt-Ru. J. Electrochem. Soc. 1999;146(3):1093–8. https://doi.org/10.1149/1.1391726.

[196] Temmel SE, Tschupp SA, Schmidt TJ. A highly flexible electrochemical flow cell designed for the use of model electrode materials on non-conventional substrates. Rev Sci Instrum 2016;87(4):45115. https://doi.org/10.1063/1.4947459.

[197] Scherson DA, Tolmachev YV, Wang Z, Wang J, Palencsar A. Extensions of the Koutecky–Levich Equation to Channel Electrodes. Electrochem. Solid-State Lett. 2008;11(2):F1. https://doi.org/10.1149/1.2818649.

[198] Wakabayashi N, Takeichi M, Itagaki M, Uchida H, Watanabe M. Temperature-dependence of oxygen reduction activity at a platinum electrode in an acidic electrolyte solution investigated with a channel flow double electrode. Journal of Electroanalytical Chemistry 2005;574(2):339–46. https://doi.org/10.1016/j.jelechem.2004.08.013.

[199] Snowden ME, King PH, Covington JA, Macpherson JV, Unwin PR. Fabrication of versatile channel flow cells for quantitative electroanalysis using prototyping. Anal Chem 2010;82(8):3124–31. https://doi.org/10.1021/ac100345v.

[200] Blaedel WJ, Olson CL, Sharma LR. The Tubular Platinum Electrode. Anal. Chem. 1963;35(13):2100–3. https://doi.org/10.1021/ac60206a034.

[201] Chin D-T, Tsang C-H. Mass Transfer to an Impinging Jet Electrode. J. Electrochem. Soc. 1978;125(9):1461–70. https://doi.org/10.1149/1.2131697.

[202] Homann F. Der Einfluß großer Zähigkeit bei der Strömung um den Zylinder und um die Kugel. Z. angew. Math. Mech. 1936;16(3):153–64. https://doi.org/10.1002/zamm.19360160304.

[203] Albery WJ, Bruckenstein S. Uniformly accessible electrodes. Journal of Electroanalytical Chemistry and Interfacial Electrochemistry 1983;144(1-2):105–12. https://doi.org/10.1016/S0022-0728(83)80148-X.

[204] Melville JL, Coles BA, Compton RG, Simjee N, Macpherson JV, Unwin PR. Hydrodynamics and Mass Transport in Wall Tube and Microjet Electrodes. Simulation and Experiment for Micrometer-Scale Electrodes. J. Phys. Chem. B 2003;107(1):379–86. https://doi.org/10.1021/jp021361z.

[205] Melville J, Simjee N, Unwin PR, Coles BA, Compton RG. Hydrodynamics and Mass Transport in Wall Tube and Microjet Electrodes. 1. Finite Element Simulations. J. Phys. Chem. B 2002;106(10):2690–8. https://doi.org/10.1021/jp013897a.

[206] Melville JL, Simjee N, Unwin PR, Coles BA, Compton RG. Hydrodynamics and Mass Transport in Wall Tube and Microjet Electrodes: Effect of Vortex Formation and Cell Geometry on Limiting Currents. J. Phys. Chem. B 2002;106(40):10424–31. https://doi.org/10.1021/jp021358f.

[207] Rees NV, Klymenko OV, Coles BA, Compton RG. Hydrodynamics and Mass Transport in Wall-Tube and Microjet Electrodes: An Experimental Evaluation of Current Theory. J. Phys. Chem. B 2003;107(49):13649–60. https://doi.org/10.1021/jp030883r.

[208] Rees NV, Klymenko OV, Coles BA, Compton RG. Fast scan linear sweep voltammetry at a high-speed wall-tube electrode. Journal of Electroanalytical Chemistry 2003;557:99–107. https://doi.org/10.1016/S0022-0728(03)00352-8.

[209] Hadj Ahmed A, Daurelle J-V, Fourmond V. Optimizing the mass transport of wall-tube electrodes for protein film electrochemistry. Electrochimica Acta 2022;403:139521. https://doi.org/10.1016/j.electacta.2021.139521.

[210] Fadel M, Daurelle J-V, Fourmond V, Vicente J. A new electrochemical cell with a uniformly accessible electrode to study fast catalytic reactions. Phys Chem Chem Phys 2019;21(23):12360–71. https://doi.org/10.1039/c9cp01487j.

[211] Martin H. Heat and Mass Transfer between Impinging Gas Jets and Solid Surfaces. In: Advances in Heat Transfer Volume 13. Elsevier; 1977, p. 1–60.

[212] Schwarz WH, Caswell B. Some heat transfer characteristics of the two-dimensional laminar incompressible wall jet. Chemical Engineering Science 1961;16(3-4):338–51. https://doi.org/10.1016/0009-2509(61)80041-9.

[213] Sparrow EM, Lee L. Analysis of Flow Field and Impingement Heat/Mass Transfer Due to a Nonuniform Slot Jet. Journal of Heat Transfer 1975;97(2):191–7. https://doi.org/10.1115/1.3450340.

[214] Macpherson JV, Marcar S, Unwin PR. Microjet Electrode: A Hydrodynamic Ultramicroelectrode with High Mass-Transfer Rates. Anal. Chem. 1994;66(13):2175–9. https://doi.org/10.1021/ac00085a037.

[215] Yamada J, Matsuda H. Limiting diffusion currents in hydrodynamic voltammetry. Journal of Electroanalytical Chemistry and Interfacial Electrochemistry 1973;44(2):189–98. https://doi.org/10.1016/S0022-0728(73)80245-1.

[216] Albery WJ. The current distribution on a wall-jet electrode. Journal of Electroanalytical Chemistry and Interfacial Electrochemistry 1985;191(1):1–13. https://doi.org/10.1016/S0022-0728(85)80002-4.

[217] Compton RG, Fisher AC, Tyley GP. Non-uniform accessibility and the use of hydrodynamic electrodes for mechanistic studies: A comparison of wall-jet and rotating disc electrodes. J Appl Electrochem 1991;21(4):295–300. https://doi.org/10.1007/BF01020211.

[218] Compton RG, Greaves CR, Waller AM. A general computational method for mass-transport problems involving wall-jet electrodes and its application to simple electron-transfer, ECE and DISP1 reactions. J Appl Electrochem 1990;20(4):575–85. https://doi.org/10.1007/BF01008866.

[219] Laevers P, Hubin A, Terryn H, Vereecken J. A wall-jet electrode reactor and its application to the study of electrode reaction mechanisms Part I: Design and construction. J Appl Electrochem 1995;25(11). https://doi.org/10.1007/BF00241950.

[220] Glauert MB. The wall jet. J. Fluid Mech. 1956;1(06):625. https://doi.org/10.1017/S002211205600041X.

[221] Laevers P, Hubin A, Terryn H, Vereecken J. A wall jet electrode reactor and its application to the study of electrode reaction mechanisms Part II: A general computational method for the mass transport problems involved. J Appl Electrochem 1995;25(11). https://doi.org/10.1007/BF00241951.

[222] Laevers P, Hubin A, Terryn H, Vereecken J. A wall-jet electrode reactor and its application to the study of electrode reaction mechanisms Part III: Study of the mechanism of the a.c. electrolytic graining of aluminium in hydrochloric acid. J Appl Electrochem 1998;28(4):387–96. https://doi.org/10.1023/A:1003288305367.

[223] Dalhuijsen AJ, van der Meer T, Hoogendoorn CJ, Hoogvliet JC, van Bennekom WP. Hydrodynamic properties and mass transfer characteristics of

electrochemical flow-through cells of the confined wall—jet type. Journal of Electroanalytical Chemistry and Interfacial Electrochemistry 1985;182(2):295–313. https://doi.org/10.1016/0368-1874(85)87007-6.

[224] Fitzgerald JA, Garimella SV. A study of the flow field of a confined and submerged impinging jet. International Journal of Heat and Mass Transfer 1998;41(8-9):1025–34. https://doi.org/10.1016/S0017-9310(97)00205-6.

[225] Law H-S, Masliyah JH. Mass transfer due to a confined laminar impinging two-dimensional jet. International Journal of Heat and Mass Transfer 1984;27(4):529–39. https://doi.org/10.1016/0017-9310(84)90026-7.

[226] Bart M, van Os P, Kamp B, Bult A, van Bennekom WP. Development of a confined wall-jet flow-through cell for simultaneous electrochemical and surface plasmon resonance applications. Sensors and Actuators B: Chemical 2002;84(2-3):129–35. https://doi.org/10.1016/S0925-4005(02)00013-8.

[227] Fuhrmann J, Linke A, Langmach H, Baltruschat H. Numerical calculation of the limiting current for a cylindrical thin layer flow cell. Electrochimica Acta 2009;55(2):430–8. https://doi.org/10.1016/j.electacta.2009.03.065.

[228] Fuhrmann J, Zhao H, Holzbecher E, Langmach H, Chojak M, Halseid R et al. Experimental and numerical model study of the limiting current in a channel flow cell with a circular electrode. Phys Chem Chem Phys 2008;10(25):3784–95. https://doi.org/10.1039/b802812p.

[229] VDI Heat Atlas. Berlin, Heidelberg: Springer Berlin Heidelberg; 2010.

[230] Polat S, Huang B, Mujumdar AS, Douglas WJM. NUMERICAL FLOW AND HEAT TRANSFER UNDER IMPINGING JETS: A REVIEW. Annual Rev Heat Transfer 1989;2(2):157–97. https://doi.org/10.1615/AnnualRevHeatTransfer.v2.60.

[231] Shinozaki K, Zack JW, Richards RM, Pivovar BS, Kocha SS. Oxygen Reduction Reaction Measurements on Platinum Electrocatalysts Utilizing Rotating Disk Electrode Technique. Journal of The Electrochemical Society 2015;162(10):F1144-F1158. https://doi.org/10.1149/2.1071509jes.

[232] Chen D, Tao Q, Liao LW, Liu SX, Chen YX, Ye S. Determining the Active Surface Area for Various Platinum Electrodes. Electrocatalysis 2011;2(3):207–19. https://doi.org/10.1007/s12678-011-0054-1.

[233] Wei X, Reiner A, Müller E, Wokaun A, Scherer GG, Zhang L et al. Electrochemical surface reshaping of polycrystalline platinum: Morphology and

crystallography. Electrochimica Acta 2008;53(11):4051–8. https://doi.org/10.1016/j.electacta.2007.08.071.

[234] Li J, Kolekar S, Xin Y, Coelho PM, Lasek K, Nugera FA et al. Thermal Phase Control of Two-Dimensional Pt-Chalcogenide (Se and Te) Ultrathin Epitaxial Films and Nanocrystals. Chem. Mater. 2021;33(20):8018–27. https://doi.org/10.1021/acs.chemmater.1c02163.

[235] Jorio A, Saito R, Dresselhaus G, Dresselhaus MS. Determination of nanotubes properties by Raman spectroscopy. Philos Trans A Math Phys Eng Sci 2004;362(1824):2311–36. https://doi.org/10.1098/rsta.2004.1443.

[236] Tavares M, Machado S, Mazo L. Study of hydrogen evolution reaction in acid medium on Pt microelectrodes. Electrochimica Acta 2001;46(28):4359–69. https://doi.org/10.1016/S0013-4686(01)00726-5.

[237] Wang JX, Springer TE, Liu P, Shao M, Adzic RR. Hydrogen Oxidation Reaction on Pt in Acidic Media: Adsorption Isotherm and Activation Free Energies. J. Phys. Chem. C 2007;111(33):12425–33. https://doi.org/10.1021/jp073400i.

[238] Shinagawa T, Garcia-Esparza AT, Takanabe K. Insight on Tafel slopes from a microkinetic analysis of aqueous electrocatalysis for energy conversion. Sci Rep 2015;5:13801. https://doi.org/10.1038/srep13801.

[239] Wang J, Zang W, Liu X, Sun J, Xi S, Liu W et al. Switch Volmer-Heyrovsky to Volmer-Tafel Pathway for Efficient Acidic Electrocatalytic Hydrogen Evolution by Correlating Pt Single Atoms with Clusters. Small 2024;20(25):e2309427. https://doi.org/10.1002/smll.202309427.

[240] Santana JA, Saavedra-Arias JJ, Ishikawa Y. Electrochemical Hydrogen Oxidation on Pt(100): a Combined Direct Molecular Dynamics/Density Functional Theory Study. Electrocatalysis 2015;6(6):534–43. https://doi.org/10.1007/s12678-015-0272-z.

[241] Guascito MR, Chirizzi D, Malitesta C, Siciliano M, Siciliano T, Tepore A. Amperometric non-enzymatic bimetallic glucose sensor based on platinum tellurium microtubes modified electrode. Electrochemistry Communications 2012;22:45–8. https://doi.org/10.1016/j.elecom.2012.05.024.

[242] Cui J, Liu X, Wang Y, Song D, Ren Y, Shen X. Hydrogen evolution reaction on transition metal nanoparticles from first-principles. Applied Surface Science 2021;570:151211. https://doi.org/10.1016/j.apsusc.2021.151211.

[243] Araujo RB, Rodrigues GLS, Dos Santos EC, Pettersson LGM. Adsorption energies on transition metal surfaces: towards an accurate and balanced description. Nat Commun 2022;13(1):6853. https://doi.org/10.1038/s41467-022-34507-y.

[244] Pourbaix, M.Atlas of Electrochemical Equilibria in Aqueous Solution;Pergamon Press:Oxford, 1966, p307–321; 1966.

[245] Conway BE, Bai L. Determination of the adsorption behaviour of 'overpotential-deposited' hydrogen-atom species in the cathodic hydrogen-evolution reaction by analysis of potential-relaxation transients. J. Chem. Soc., Faraday Trans. 1 1985;81(8):1841. https://doi.org/10.1039/F19858101841.

[246] Machado S, Avaca LA. The hydrogen evolution reaction on nickel surfaces stabilized by H-absorption. Electrochim. Acta 1994;39(10):1385–91. https://doi.org/10.1016/0013-4686(94)E0003-I.

[247] Kibria M. Electrochemical studies of a nickel electrode for the hydrogen evolution reaction. Int. J. Hydrogen Energy 1995;20(6):435–40. https://doi.org/10.1016/0360-3199(94)00073-9.

[248] McArthur MA, Jorge L, Coulombe S, Omanovic S. Synthesis and characterization of 3D Ni nanoparticle/carbon nanotube cathodes for hydrogen evolution in alkaline electrolyte. J. Power Sources 2014;266:365–73. https://doi.org/10.1016/j.jpowsour.2014.05.036.

[249] Ouyang C, Wang X, Wang C, Zhang X, Wu J, Ma Z et al. Hierarchically Porous Ni3S2 Nanorod Array Foam as Highly Efficient Electrocatalyst for Hydrogen Evolution Reaction and Oxygen Evolution Reaction. Electrochim. Acta 2015;174:297–301. https://doi.org/10.1016/j.electacta.2015.05.186.

[250] M.F. Kibria, M.Sh. Mridha, A.H. Khan. Electrochemical studies of a nickel electrode for the hydrogen evolution reaction. Int. J. Hydrogen Energy 1995;20(6):435–40. https://doi.org/10.1016/0360-3199(94)00073-9.

[251] Zhang K, Li J, Liu W, Liu J, Yan C. Electrocatalytic activity and electrochemical stability of Ni–S/CeO2 composite electrode for hydrogen evolution in alkaline water electrolysis. Int. J. Hydrogen Energy 2016;41(48):22643–51. https://doi.org/10.1016/j.ijhydene.2016.08.229.

[252] Foroughi F, Tintor M, Faid AY, Sunde S, Jerkiewicz G, Coutanceau C et al. In Situ Sonoactivation of Polycrystalline Ni for the Hydrogen Evolution Reaction in

Alkaline Media. ACS Appl. Energy Mater. 2023;6(9):4520–9. https://doi.org/10.1021/acsaem.2c02443.

[253] Wan C, Ling Y, Wang S, Pu H, Huang Y, Duan X. Unraveling and Resolving the Inconsistencies in Tafel Analysis for Hydrogen Evolution Reactions. ACS Cent. Sci. 2024;10(3):658–65. https://doi.org/10.1021/acscentsci.3c01439.

[254] van der Heijden O, Park S, Vos RE, Eggebeen JJJ, Koper MTM. Tafel Slope Plot as a Tool to Analyze Electrocatalytic Reactions. ACS Energy Lett. 2024;9(4):1871–9. https://doi.org/10.1021/acsenergylett.4c00266.

[255] Walter MG, Warren EL, McKone JR, Boettcher SW, Mi Q, Santori EA et al. Solar water splitting cells. Chem. Rev. 2010;110(11):6446–73. https://doi.org/10.1021/cr1002326.

[256] Cao C, An Q. Elucidating thin film growth mechanisms for high-performance II–VI photovoltaic semiconductors: simulation-driven insights and challenges. CrystEngComm 2025;27(21):3404–15. https://doi.org/10.1039/D5CE00244C.

[257] Johansson J. Heteroepitaxial growth modes revisited. CrystEngComm 2023;25(48):6671–6. https://doi.org/10.1039/D3CE00664F.

[258] Weininger JL, Breiter MW. Hydrogen Evolution and Surface Oxidation of Nickel Electrodes in Alkaline Solution. J. Electrochem. Soc. 1964;111(6):707. https://doi.org/10.1149/1.2426216.

[259] O'Brien RN, Seto P. Time domain reflectometry, a new method of finding electrical double-layer capacities. Journal of Electroanalytical Chemistry and Interfacial Electrochemistry 1968;18(3):219–30. https://doi.org/10.1016/S0022-0728(68)80253-0.

[260] Cossar E, Houache MS, Zhang Z, Baranova EA. Comparison of electrochemical active surface area methods for various nickel nanostructures. J. Electroanal. Chem. 2020;870:114246. https://doi.org/10.1016/j.jelechem.2020.114246.

[261] Gabler A, Müller CI, Rauscher T, Köhring M, Kieback B, Röntzsch L et al. Ultrashort pulse laser-structured nickel surfaces as hydrogen evolution electrodes for alkaline water electrolysis. Int. J. Hydrogen Energy 2017;42(16):10826–33. https://doi.org/10.1016/j.ijhydene.2017.02.006.

[262] Tai K-L, Chen J, Wen Y, Park H, Zhang Q, Lu Y et al. Phase Variations and Layer Epitaxy of 2D PdSe2 Grown on 2D Monolayers by Direct Selenization of

Molecular Pd Precursors. ACS Nano 2020;14(9):11677–90. https://doi.org/10.1021/acsnano.0c04230.

[263] Li E, Wang D, Fan P, Zhang R, Zhang Y-Y, Li G et al. Construction of bilayer PdSe2 on epitaxial graphene. Nano Res. 2018;11(11):5858–65. https://doi.org/10.1007/s12274-018-2090-0.

[264] Yan M, Wang E, Zhou X, Zhang G, Zhang H, Zhang K et al. High quality atomically thin PtSe 2 films grown by molecular beam epitaxy. 2D Mater. 2017;4(4):45015. https://doi.org/10.1088/2053-1583/aa8919.

[265] Coelho PM, Komsa H-P, Lasek K, Kalappattil V, Karthikeyan J, Phan M-H et al. Room-Temperature Ferromagnetism in MoTe 2 by Post-Growth Incorporation of Vanadium Impurities. Adv Elect Materials 2019;5(5). https://doi.org/10.1002/aelm.201900044.

[266] Leuaa P, Kraglund MR, Chatzichristodoulou C. Decoupling of Reaction Overpotentials and Ionic Transport Losses within 3D Porous Electrodes in Zero-Gap Alkaline Electrolysis Cells. Electrochimica Acta 2023;470:143306. https://doi.org/10.1016/j.electacta.2023.143306.

[267] Levich B. The theory of concentration polarisation. Discuss. Faraday Soc. 1947;1:37. https://doi.org/10.1039/df9470100037.

[268] Pathirage V, Ravinath Rajapakse N, Lasek K, Píš I, Bondino F, Batzill M. Thermal- and air- stability of the compositional variants of van der Waals Pt-Telluride thin films probed by high resolution photoemission spectroscopy. Applied Surface Science 2024;644:158785. https://doi.org/10.1016/j.apsusc.2023.158785.

[269] Dieing T, Ibach W. Software Requirements and Data Analysis in Confocal Raman Microscopy. In: Dieing T, Hollricher O, Toporski J, editors. Confocal Raman Microscopy. Berlin, Heidelberg: Springer Berlin Heidelberg; 2011, p. 61–89.

9 Supplementary Information

9.1 Supplementary Information for Chapter 5.1

9.1.1 Determination of the Diffusion Constant D

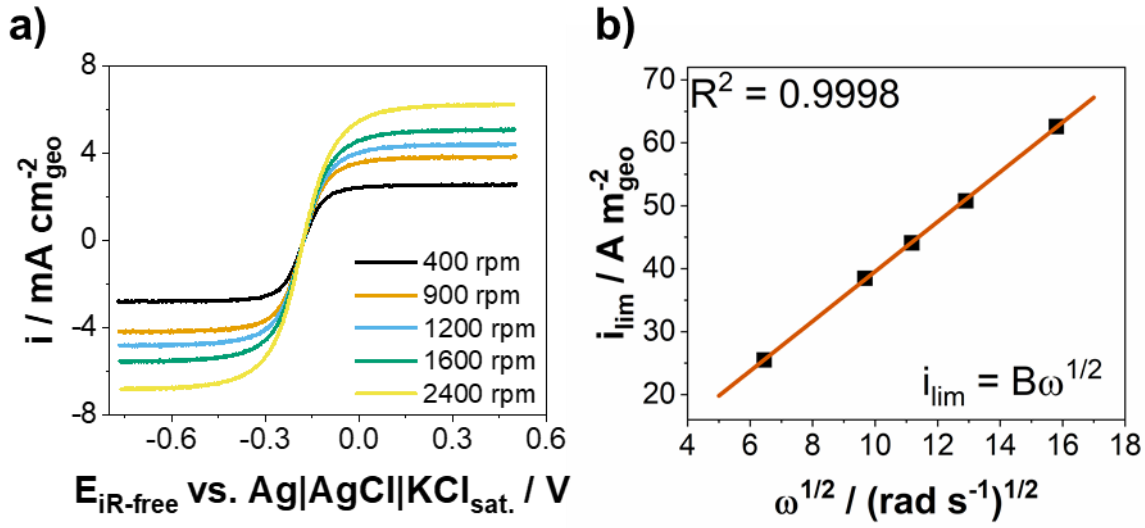

Figure S1: *Determination of the diffusion constant D.* ***a)*** *Linear sweep voltammograms for 10 mM $[Fe(CN)_6]^{4-}$/ 10 mM $[Fe(CN)_6]^{3-}$ in Ar-saturated 0.5 M K_2SO_4 at $T = 20\,°C$. Experimental data: glassy carbon working electrode, scan rate of 5 mV s^{-1}, rotation speed from 400 to 2400 rounds per minute (rpm).* ***b)*** *Levich plot of the limiting current density of the oxidation of ferrocyanide(II) as a function of the square root of the rotational speed.*

Rotating disk electrode (RDE) experiments were conducted in a self-designed electrochemical three-compartment glass cell using a rotator (Pine Research Instrumentation, USA) and a potentiostat (VSP300, Bio-Logic, France). The three-electrode arrangement consisted of a glassy carbon electrode ($d = 5\,mm$) as a working electrode, Au mesh as a counter electrode and silver/silver chloride electrode as a reference electrode, respectively. The electrolyte solution contained 10 mM potassium hexacyanidoferrate(II) trihydrate (VWR Chemicals, ≥99.0%) and 10 mM potassium hexacyanoferrate(III) (VWR Chemicals, ≥99.0%) in 0.5 M potassium sulfate (Carl Roth, ≥99.0%).

Linear sweep voltammograms were cathodically recorded at various rotation speeds and 5 mV s^{-1} between 0.5 and -0.8 V vs. Ag|AgCl|KCl(sat.), as illustrated in **Figure S1a**. The limiting current for the oxidation of ferrocyanide(II) was extracted from these voltammograms at a potential of 0.4 V vs. Ag/AgCl/KCl(sat.), and the data were plotted against the square root of the rotation speed (**Figure S1b)**. The diffusion constant (D)

was determined from the slope (B) of the resulting plot using linear regression, according to the rearranged *Levich* equation [267]:

$$D = \left(\frac{B}{0.62\, n\, FA\, \nu^{-\frac{1}{6}}\, c_{\infty}} \right)^{\frac{3}{2}} \tag{67}$$

where n is the number of electrons involved in the reaction, F is the Faraday constant, A is the electrode area, ν is the kinematic viscosity of the electrolyte, and c_{∞} is the bulk concentration of the analyte.

These experiments were repeated six times ($N = 6$), and the diffusion constant was averaged across all measurements to yield an average D value of $(5.56 \pm 0.14) \cdot 10^{-10}\ m^2 s^{-1}$.

9.1.2 Additional Model Parameters for the CFD Simulations

Table S1: Model parameters for the oxidation of $[Fe(CN)_6]^{4-}$ in 0.5 M K_2SO_4.

Parameter	Value	Source
T	293.15 K	-
ρ	1065.22 kg m^{-3}	[134](a)
η	0.00110455 Pa· s	[134](a)
$c_{K_2SO_4}$	500 mol m^{-3}	Experimental
c_∞	10 mol m^{-3}	Experimental
D	$5.56 \cdot 10^{-10}$ m^2 s^{-1}	Experimental(b)

(a)interpolated for 0.5 M K_2SO_4 from “concentrative properties of aqueous solutions: density, refractive index, freezing point depression, and viscosity”, **8**-75 in [134]

(b)average experimentally determined value as described in **Figure S1**

9.1.3 Comparison of the Transition Radius R_A with Critical Maximum Radii of Wall-Tube Electrodes Discussed in Literature

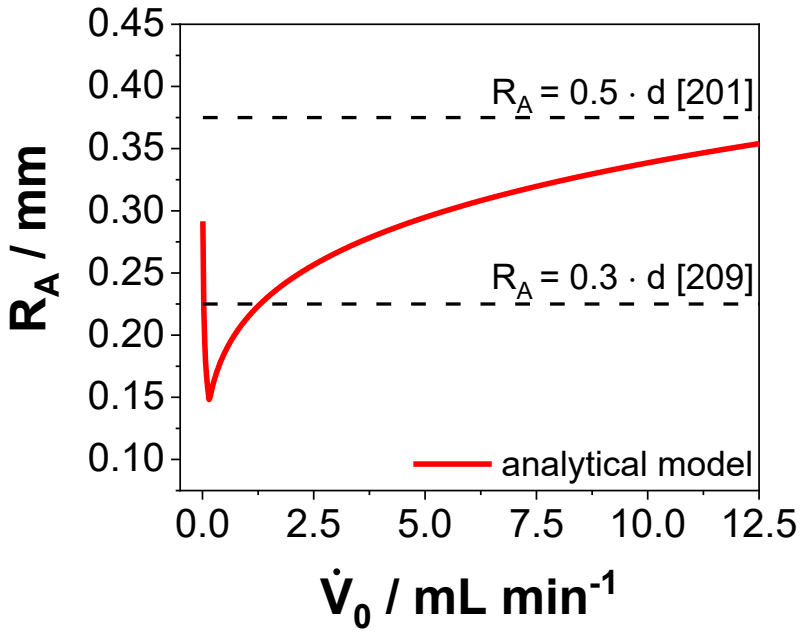

Figure S2: *Transition radius R_A calculated by our analytical model (red solid line) plotted against the volume flow $\dot{V}_0$. Common critical maximum radii for wall-tube electrodes from literature [201,209] are denoted with black dashed lines. Parameter: $d = 0.75\,mm$; $H = 0.7\,mm$; $R_C = 2.81\,mm$.*

9.1.4 Local Current Density Functions of the other Theoretical Cases based on the Universal Analytical Model

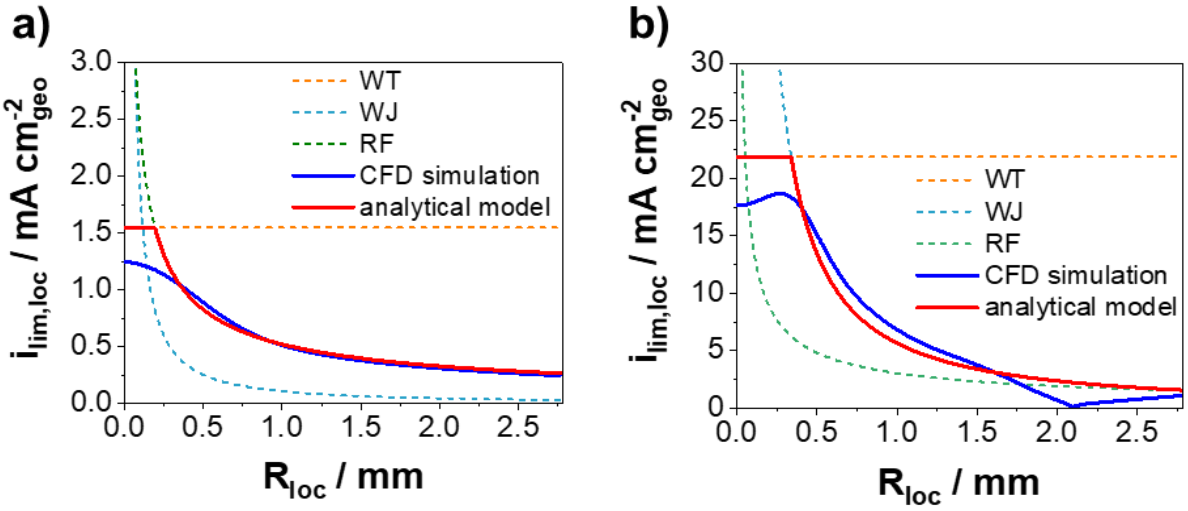

Figure S3: *Examples of the local current density functions based on the equations from the literature (equations (3),(4) and (5)) (orange, light blue and green dashed lines), CFD simulations (solid blue line) and analytical model (solid red line) plotted against the local radius* R_{loc} *for different cases.* ***a)*** *"Case Tube-Channel":* $R_A = R_B = R_{WT-RF}$ *with parameters:* $d = 0.75\ mm$; $H = 0.7\ mm$; $\dot{V}_0 = 0.05\ mL\ min^{-1}$; $R_C = 2.81\ mm$ *and* ***b)*** *"Case Tube-Jet":* $R_A = R_{WT-WJ}$ *and* $R_B = R_C$ *with parameters:* $d = 0.75\ mm$; $H = 0.7\ mm$; $\dot{V}_0 = 10\ mL\ min^{-1}$; $R_C = 2.81\ mm$.

9.1.5 Effect of the Hydrodynamic Constant a^*

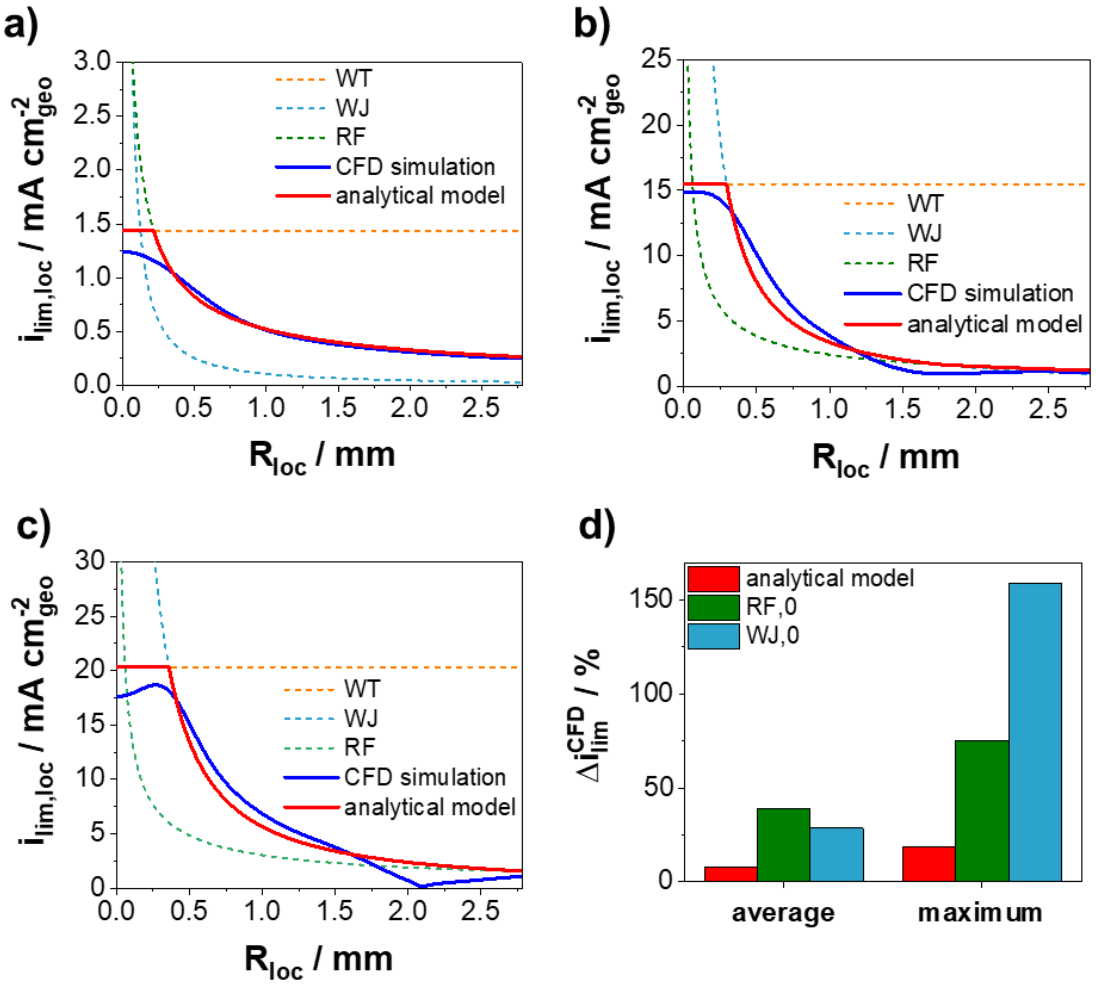

Figure S4: *Effect of the hydrodynamic constant a* on the local current densities* $i_{lim,loc}$ *and relative error* Δi_{lim}^{CFD} *compared to the results from the CFD simulations.* $\sqrt{a^*} = 1.648$ *and* $f\left(\frac{H}{d}\right) = 1$ *were used [213]. Local current density functions based on the equations from the literature (equations (3),(4) and (5)), CFD simulations and analytical model are plotted against the local radius* R_{loc} *for different theoretical cases:* ***a)*** *"Case Tube-Channel":* $R_A = R_B = R_{WT-RF}$ *with parameters:* $d = 0.75\ mm;\ H = 0.7\ mm;\ \dot{V}_0 = 0.05\ mL\ min^{-1};\ R_C = 2.81\ mm;$ ***b)*** *"Case Tube-Jet-Channel":* $R_A = R_{WT-WJ}$ *and* $R_B = R_{WJ-RF}$ *with parameters:* $d = 0.75\ mm;\ H = 0.7\ mm;\ \dot{V}_0 = 5\ mL\ min^{-1};\ R_C = 2.81\ mm;$ ***c)*** *"Case Tube-Jet":* $R_A = R_{WT-WJ}$ *and* $R_B = R_C$ *with parameters:* $d = 0.75\ mm;\ H = 0.7\ mm;\ \dot{V}_0 = 10\ mL\ min^{-1};\ R_C = 2.81\ mm.$ ***Figure S4d)*** *shows a statistical comparison of the relative error of the total limiting current density (*$\sqrt{a^*} = 1.648$*) towards CFD data* Δi_{lim}^{CFD} *for all* $N = 350$ *CFD simulations. Red, light blue and green bars are denoted for the analytical model, the established equation for the wall-jet electrode (WJ,0) and the established equation for the radial channel-flow electrode (RF,0), see* ***Table 1****, respectively.*

9.2 Supplementary Information for Chapter 5.2

9.2.1 Model Parameters for the Simulation of HER/HOR Polarization Curves

Table S2: Model parameters for the HER/HOR in 0.5 M H_2SO_4.

Parameter	Value	Source
T	293.15 K	-
ρ	1001.6 kg m^3	(**8**-82) in [134]
η	0.00101 Pa· s	(**8**-82) in [134]
c_∞	1 mol m^{-3}	[179]
n	2	-
α	0.5	[179]
i_0	70 mA cm^{-2}	[179]
D	$4.58 \cdot 10^{-9}$ m^2 s^{-1}	(**6**-180) in [134]

9.3 Supplementary Information for Chapter 5.3

9.3.1 Synthesis

The highly ordered pyrolyzed graphite (HOPG) substrates used for synthesis were freshly cleaved in air and degassed in vacuum at 450°C for 4 hours. 2D-$PtTe_2$ was prepared by co-deposition of Pt and Te at 200 °C in an ultrahigh vacuum (UHV) molecular beam epitaxy chamber on these substrates. Pt was evaporated from an e-beam evaporator. Te was supplied from a *Knudsen* cell at 260 °C. Pt:Te flux ratio was 1:10 with a growth rate of 1 mono layer (ML) per 1 hour. Post growth annealing of 2D-$PtTe_2$ samples was performed in vacuum at 390°C or 410°C to form 2D-Pt_3Te_4 or 2D-Pt_2Te_2 respectively, as described in previous literature [100].

9.3.2 XPS Settings

XPS studies of the initial materials were performed using a PREVAC RS 40B1 X-ray source with Al Kα radiation with 1486.6 eV photon energy and a Scienta R3000 hemispherical analyzer. The as-grown samples were transferred in-situ to an UHV analysis chamber for XPS studies ($p = 2.5 - 4.0 \cdot 10^{-9}\, Torr$). A total number of 5 sweeps were performed for each sample with a dwell time per sweep of 0.043 s.

After electrochemical experiments, 2D-PtTe2 and 2D-Pt3Te4 samples were annealed at 280°C and 2D-Pt2Te2 samples were annealed at 190°C [268] respectively in UHV to desorb surface oxygen. Afterwards, XPS studies were performed using a seven-channel Omicron-Sphera hemispherical analyzer and using a non-monochromatized dual anode X-ray source (Omicron DAR 400) with Al Kα radiation of 1486.6 eV photon energy. Again, a total number of 5 sweeps were performed with a dwell time per sweep of 0.1 s.

The energy step size in all studies was 0.05 eV. All XPS data were analysed using the KolXPD software by substracting a Shirley background and peaks were fitted using Voigt function.

9.3.3 Te – XPS Spectra

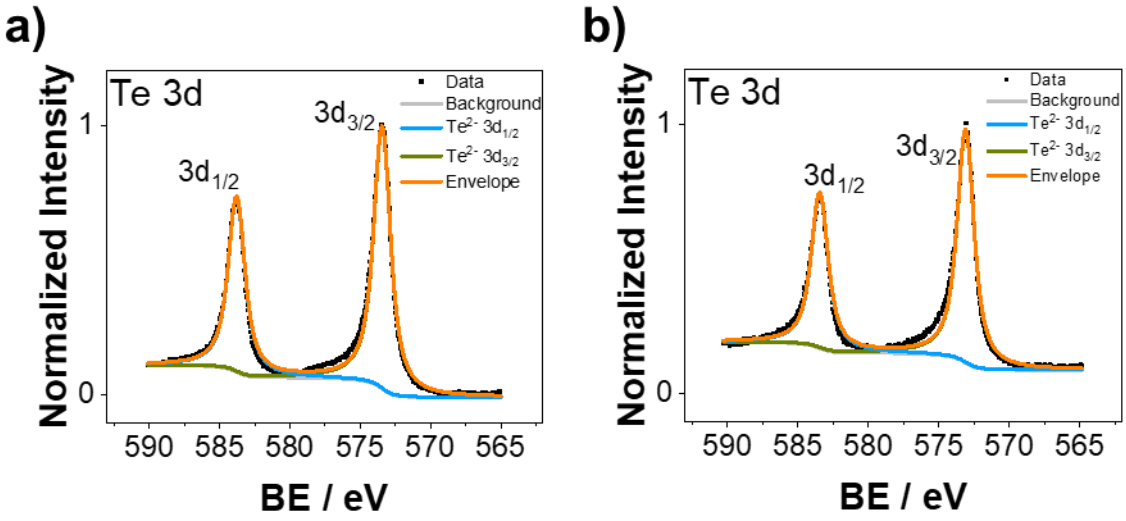

***Figure S5**: Initial Structural Characterization of the 2D-Pt_xTe_y@HOPG materials. a) Te 3d XPS spectra of 2D-$PtTe_2$@HOPG. c) Te 3d XPS spectra of 2D-Pt_2Te_2@HOPG. Te 3d spectra from the 2D-Pt_3Te_4 can be found in literature [100].*

9.3.4 Open Circuit Potential Measurements

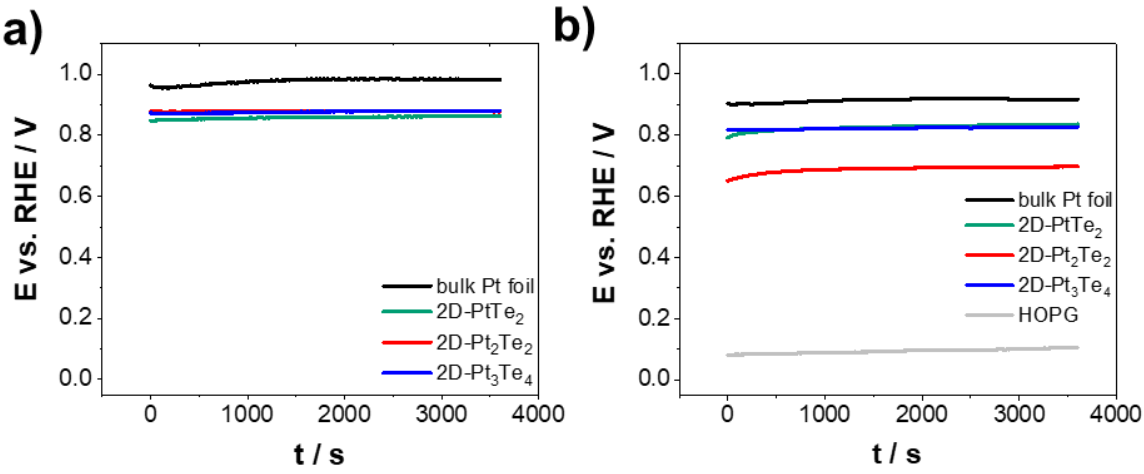

***Figure S6**: Open circuit potential measurements of the different 2D-Pt_xTe_y phases, Pt and HOPG in **a)** phosphate buffered 0.1 M $NaClO_4$ and **b)** 0.5 M H_2SO_4.*

9.3.5 Measurements to Establish the Double Layer Capacitance C_{dl}

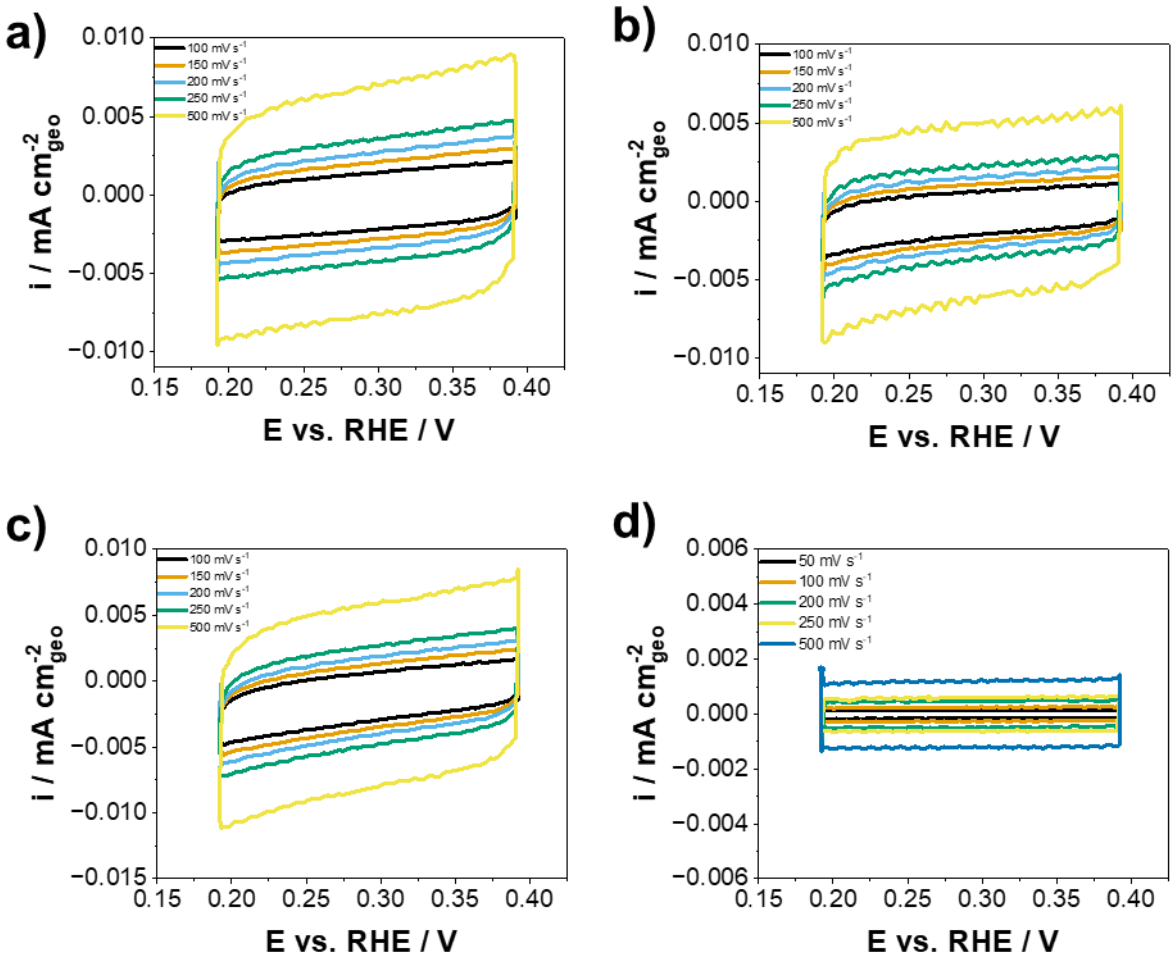

***Figure S7**: Cyclic voltammetry with different scan rates in Ar-saturated 0.5 M H_2SO_4 to establish the double layer capacitance C_{dl} of **a)** 2D-$PtTe_2$@HOPG, **b)** 2D-Pt_2Te_2@HOPG, **c)** 2D-Pt_3Te_4, **d)** HOPG.*

9.3.6 Cyclic Voltammetry in Phosphate Buffered 0.1 M $NaClO_4$

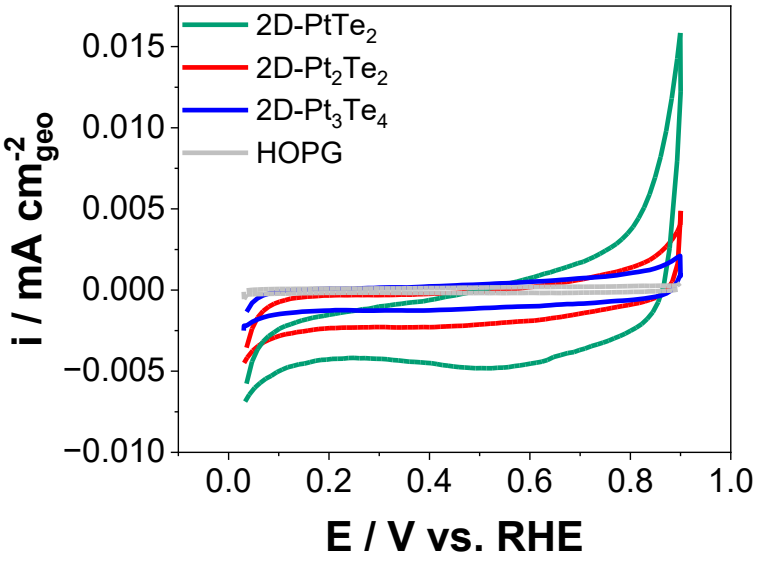

***Figure S8**: Cyclic voltammograms of the 2D-Pt_xTe_y@HOPG materials and HOPG recorded in Ar-satured phosphate buffered 0.1 M $NaClO_4$ with a scanrate of 50 mV s^{-1}.*

9.3.7 Raman Peak Area Ratio Mappings

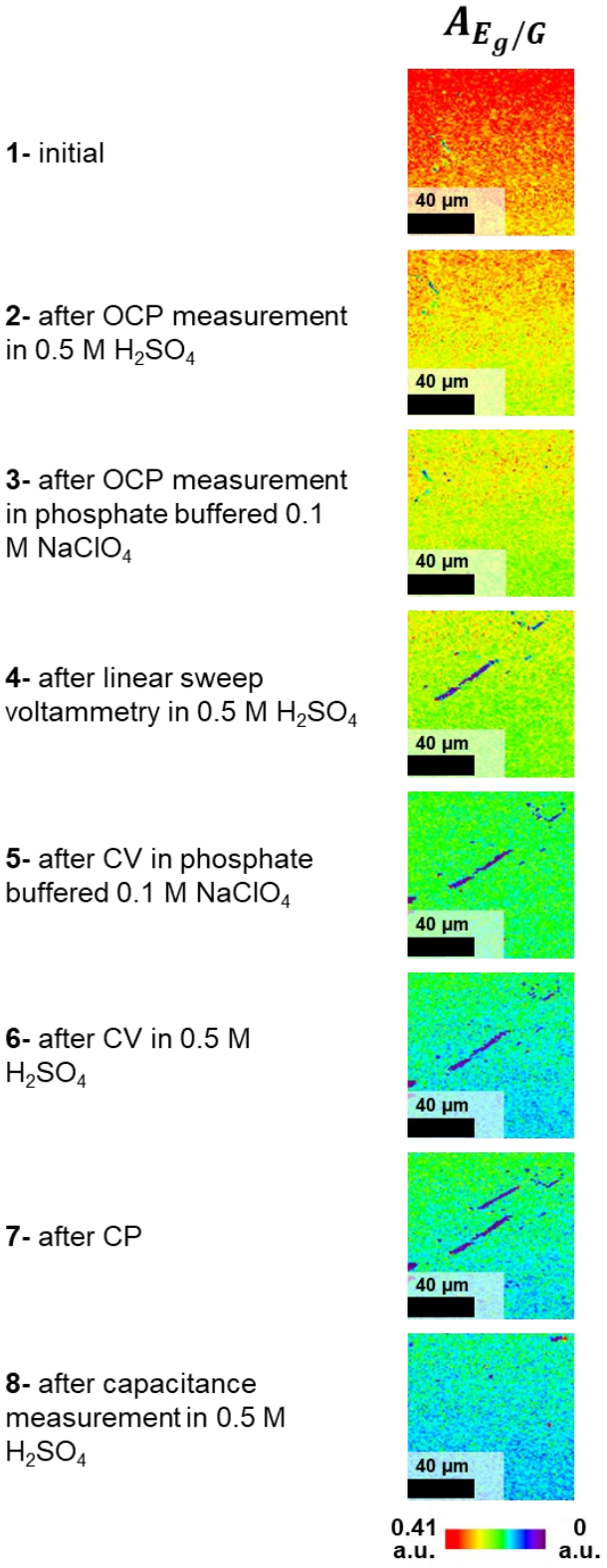

***Figure S9**: Normalized Raman peak area mappings $A_{E_g/G}$ of 2D-$PtTe_2$ after the different electrochemical treatment steps (see also **Figure 23** for number references (**1-8**)).*

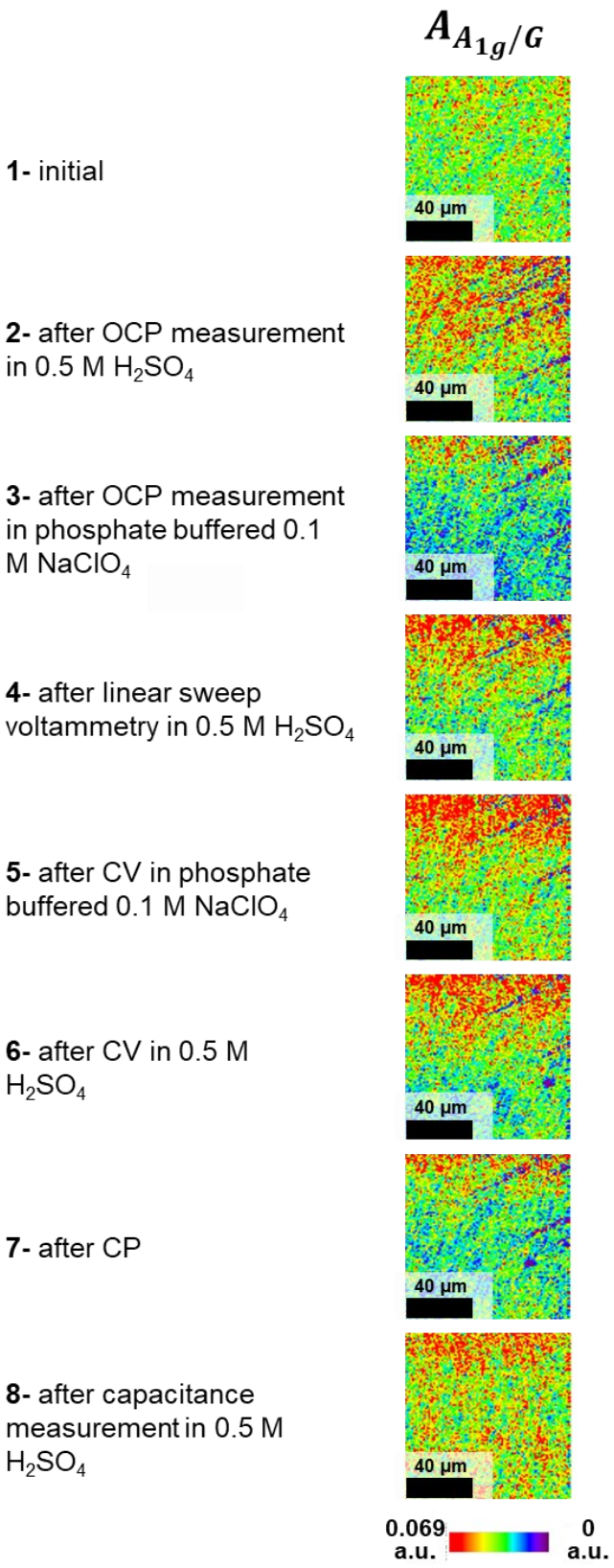

***Figure S10**: Normalized Raman peak area mappings $A_{A_{1g}/G}$ of 2D-Pt_2Te_2 after the different electrochemical treatment steps (see also **Figure 23** for number references (**1-8**)).*

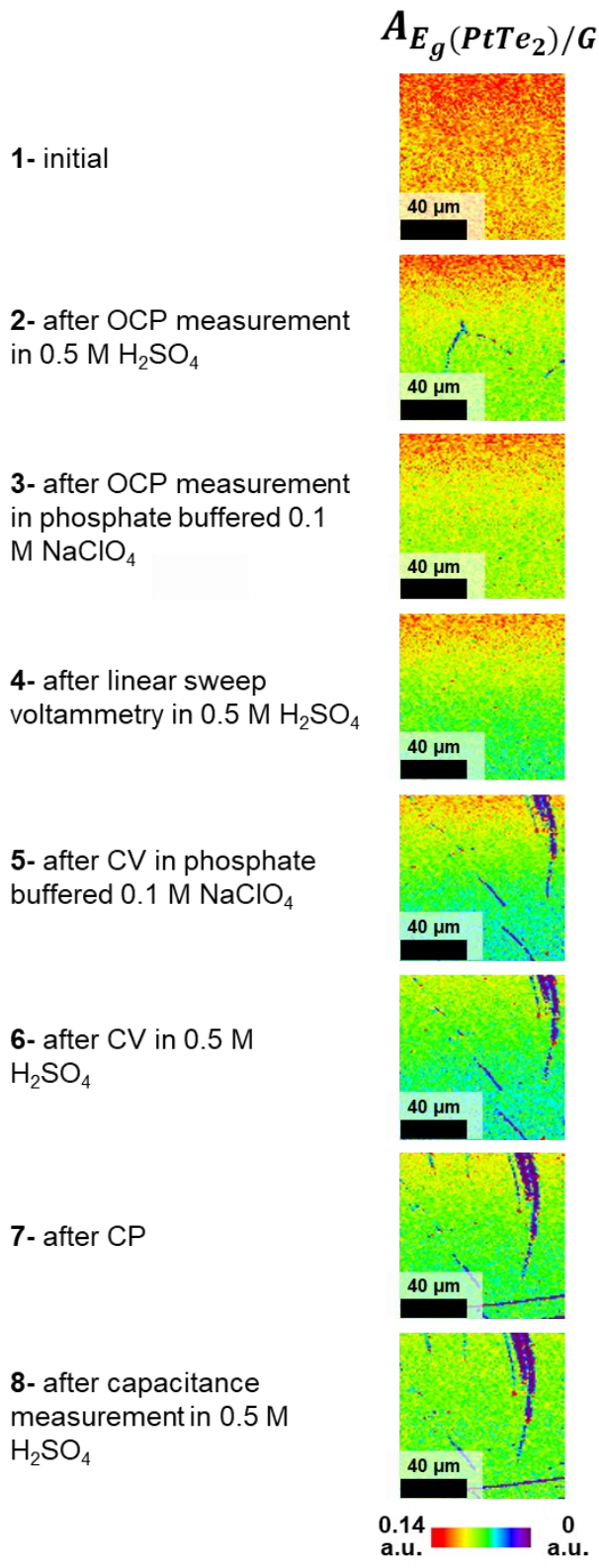

***Figure S11**: Normalized Raman peak area mappings $A_{E_g(PtTe_2)/G}$ of 2D-Pt_3Te_4 after the different electrochemical treatment steps (see also **Figure 23** for number references (**1-8**)).*

9.3.8 XPS Analysis Before and After the Electrochemical Treatment

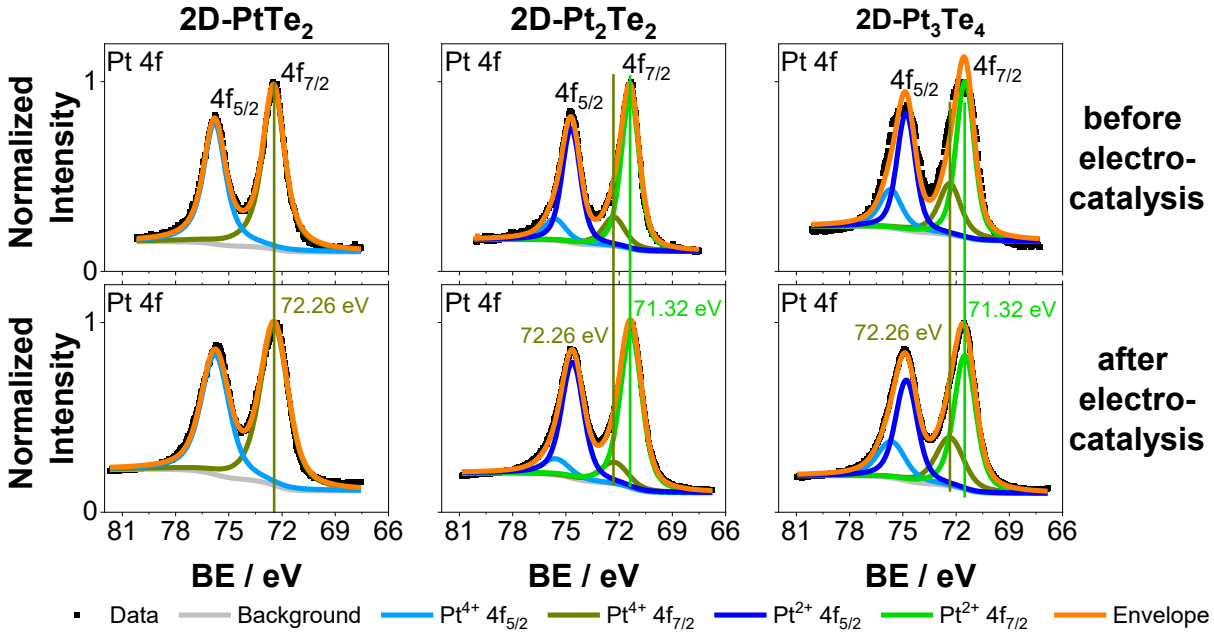

***Figure S12**: Pt 4f XPS spectra and fits of the Pt-Chalcogenides before (upper row) and after (lower row) electrocatalysis. The peak positions of Pt^{2+} and Pt^{4+} $4f_{7/2}$ are indicated as an oliv and light green line, respectively.*

9.3.9 Raman Analysis of 2D-Pt_2Te_2

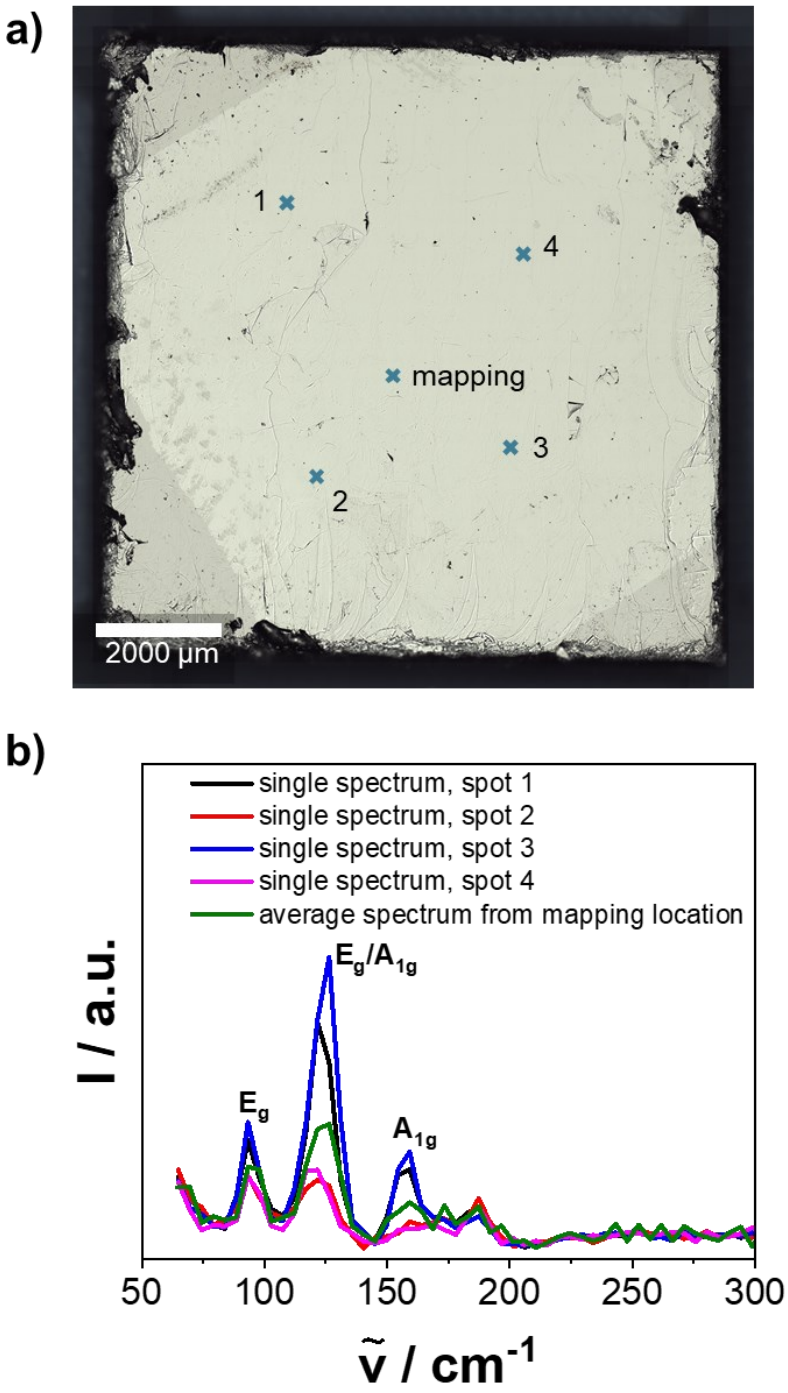

***Figure S13**: **a)** Optical image stitching of one 2D-Pt_2Te_2@HOPG sample. magnification: 20x. The spots of the Raman mappings from **Figure S10** and spots from additional single Raman spectra are marked blue. **b)** Additional single Raman spectra recorded on 2D-Pt_2Te_2@HOPG at different locations (spots 1-4) after the electrochemical capacitance measurements (settings: wavelength: 532 nm, integration time: 5 s, grating: 600 g mm-1, accumulations: 10, objective: 100x). The average Raman spectrum from the mappings in **Figure S10** is displayed for comparison (settings: wavelength: 532 nm, integration time: 5 s, grating: 600 g mm^{-1}, objective: 100x, mapping size: 100x100 µm, resolution: 1 µm).*

9.3.10 Principal Component Analysis of 2D-Pt_2Te_2

To assess material changes and evaluate relative sample concentrations, the characteristic peaks of the 2D-Pt_xTe_y@HOPG materials were integrated and normalized to the area of the graphite band ($\tilde{\nu}$ = 1580 cm^{-1}), which served as an internal standard. Furthermore, to gain insights into the compositional changes in 2D-Pt_2Te_2, a principal component analysis was performed. This was based on a linear combination of the most different spectra of the Pt_2Te_2 and Pt_3Te_4 phases, utilizing the "True Component Analysis" algorithm within Project SIX Plus (WITec, Germany) [269].

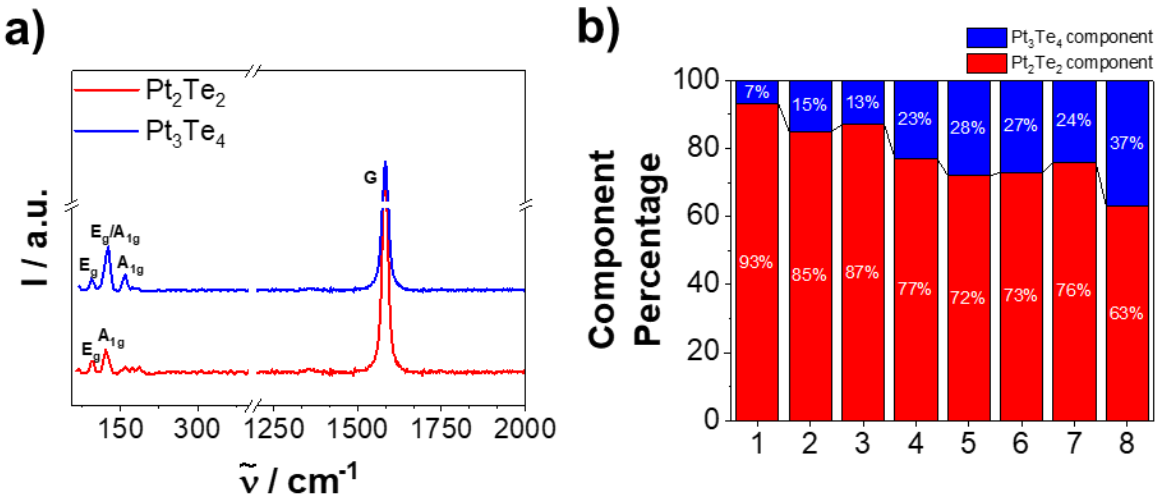

***Figure S14**: Principal component analysis of the Raman mappings of 2D-Pt_2Te_2@HOPG. **a)** Spectra of Pt_2Te_2 and Pt_3Te_4 which were used for the principal component analysis. **b)** Percentage of the Pt_2Te_2 and the Pt_3Te_4 component in 2D-Pt_2Te_2 @HOPG after the electrochemical steps: 1 – initial state, 2 – after OCP measurement in 0.5 M H_2SO_4, 3 – after OCP measurement in phosphate buffered 0.1 M $NaClO_4$, 4 – after linear sweep voltammetry in 0.5 M H_2SO_4, 5 – after CV in phosphate buffered 0.1 M $NaClO_4$, 6 – after CV in 0.5 M H_2SO_4, 7 – after CP, 8 – after capacitance measurement in 0.5 M H_2SO_4.*

9.3.11 Density Functional Theory Calculations

The thermodynamics of hydrogen adsorption can be characterized by the *Gibbs* free energy ΔG_H according to the following equation:

$$\Delta G_H = \Delta E_H + \Delta E_{ZPE} - T\Delta S_H \quad (68)$$

ΔE_H indicates the change in the internal energy, ΔE_{ZPE} denotes the change in the vibrational zero-point energy, and ΔS_H stands for the difference in entropy due to hydrogen adsorption. The term $\Delta E_{ZPE} - T\Delta S_H$ can be estimated to be +0.24 eV at room temperature, as shown previously. [40,41] As a result, equation (68) can be simplified to:

$$\Delta G_H = \Delta E_H + 0.24\ eV \quad (69)$$

The **Table S3** and **Table S4** show the results from these calculations of ΔG_H for the pristine 2D-Pt_xTe_y materials and the materials with Te vacancy, respectively.

Table S3: ΔG_H values of HER on pristine 2D-Pt_xTe_y materials.

	$PtTe_2$	Pt_2Te_2	$PtTe_2/PtTe_2$	$PtTe_2/Pt2Te_2$	$Pt_2Te_2/PtTe_2$	Pt (111)
ΔG_H (eV)	1.183	0.775	0.904	1.059	0.791	-0.222 *

*Source:[242]

Table S4: ΔG_H values of HER on 2D-Pt_xTe_y materials with Te vacancy.

	$PtTe_2$	Pt_2Te_2	$PtTe_2/PtTe_2$	$PtTe_2/Pt2Te_2$	$Pt_2Te_2/PtTe_2$	Pt_2Te_2/Pt_2Te_2
ΔG_H (eV)	0.047	0.116	0.007	0.604	-0.051	-0.048

9.4 Supplementary Information for Chapter 5.4

9.4.1 Processing of Chronopotentiometry Data

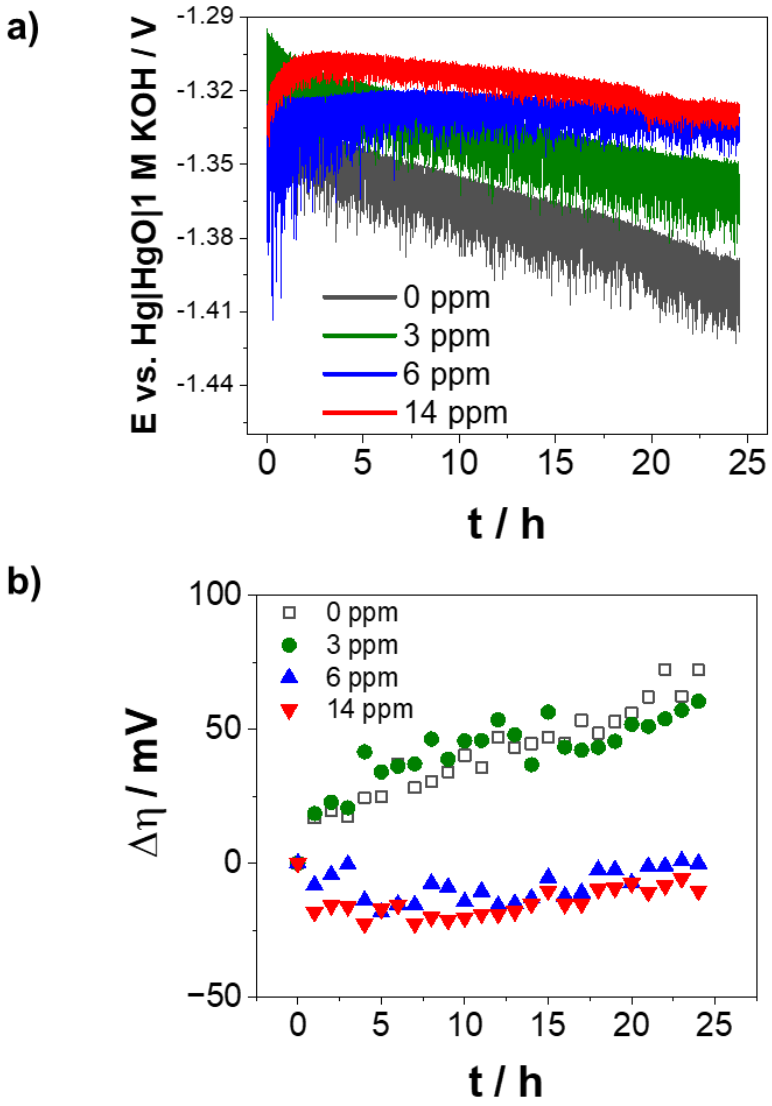

Figure S15: *Processing the chronopotentiometry data from the galvanostatic experiments ($i = -10\ mA\ cm_{geo}^{-2}$).* ***a)*** *Examples of the raw data for all tested Fe^{z+} species concentrations in 0.1 M KOH.* ***b)*** *Changes of the averaged and iR-corrected overpotential changes $\Delta\eta$ based on the chronopotentiometric data from* ***a)*** *for each hour.*

$\Delta\eta$ was calculated according to equation (66):

$$\Delta\eta = (E_{initial} - E°) - (E_n - E°) \tag{66}$$

where $E_{initial}$ is the iR-corrected and averaged potential at t = 0 h, E_n is the iR-corrected and averaged potential at t = n hours, and $E°$ is the standard thermodynamic potential for HER (0 V vs. RHE)

9.4.2 ICP-OES Measurements

To assess trace metal impurities in the electrolyte solution, 185 mL of freshly prepared 0.1 M KOH was neutralized with 2 mL of concentrated HNO_3 (Carl Roth, ROTIPURAN® Supra 69%). A standard addition method was used by adding a certain amount (5, 10, 15, 20, 25, and 50 ppb) of a commercially available multi-element standard solution to 5 mL of the neutralized KOH aliquot. Each sample was then diluted to 10 mL with highly purified water (18 MΩ·cm at 25 °C). The standard used was Roti®Star Multi-Element ICP Standard Solution (Carl Roth), containing 28 elements at 1 ppm each. Measurements were performed using an Agilent 5100 ICP-OES instrument. The detected impurities are shown in **Table S5**. Other impurities' peaks were below the signal-to-noise ratio.

Table S5: Quantification of key impurities in 0.1 M KOH via ICP-OES including the quantification and detection limits.

Element	Measured Amount / ppb	Quantification Limit (QL) / ppb	Detection Limit (DL) / ppb
Fe	< QL	7.4 ± 0.4	2.2 ± 0.1
Ni	--	35 ± 1.7	10.5 ± 0.5
Zn	5.8 ± 0.2	1.5 ± 0.1	0.4 ± 0.1

9.4.3 µ−XRF Calibration

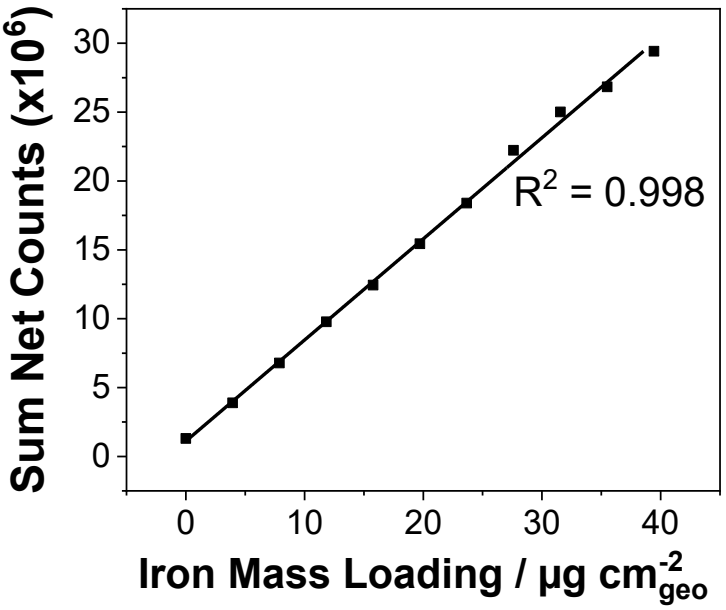

Figure S16: *Calibration plot of the sum net counts obtained from µ−XRF data versus the iron mass loading* $[\mu g\ cm_{geo}^{-2}]$. *Calibration samples with a defined iron amount from 0 to 40* $\mu g\ cm_{geo}^{-2}$ *were used.*

For calibration, filter papers with iron amounts of 0 to 8 µg were prepared. Depending on the desired loading different volumes of 1 or 2 mg mL^{-1} (depending on the desired loading) $FeCl_2 \cdot 4\ H_2O$ (Merck, 99.99 % trace metals basis) solution were drop-casted onto filter paper disks (diameter = 5 mm). Afterwards, they were measured with the same setting parameters as the measurements for treated poly-Ni electrodes. M4 Tornado plus micro-X-ray fluorescence (µ−XRF) spectrometer (Bruker) equipped with a rhodium X-ray source operated at 50 kV and 300 µA and two silico drift detectors (SDD type: 660 PAR-LE) was employed. Measurements were performed with a spot size of 20 µm, pixel size of 0.01 mm^2, acquisition time of 500 ms per pixel and in vacuum of <2 mbar. Analysis was performed using Bruker Software M4 TORNADO (version 1.6.621.0). The sum net counts of the Fe Kα line were correlated with the amount of iron to get a calibration curve for the iron deposits on the treated poly-Ni electrodes, as shown in **Figure S16**.

9.4.4 Examples of the Mean μ−XRF Spectra Across a Single Electrode

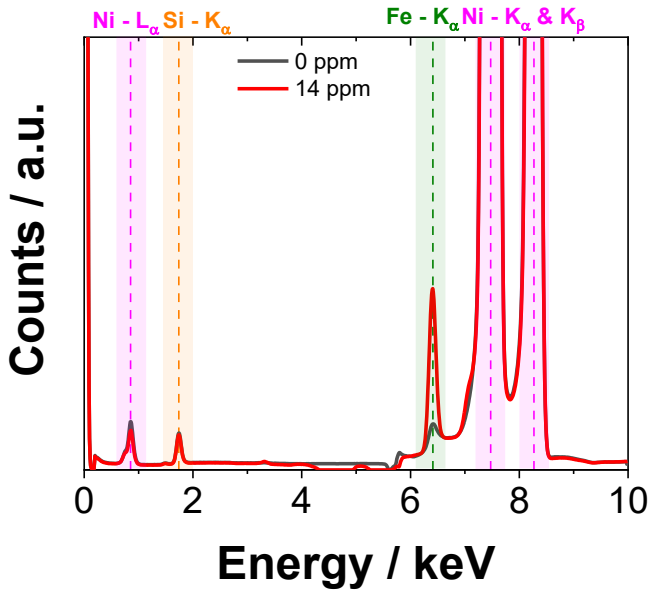

Figure S17: *Mean μ-XRF spectra of Fe deposits on polycrystalline Ni electrodes after 24-h galvanostatic AST experiment at* $i = -10\ mA\ cm_{geo}^{-2}$ *in 0.1 M KOH containing either 0 or 14 ppm* Fe^{z+} *cation concentrations. Each spectrum is the average signal from μ-XRF mapping covering the entire surface of a single electrode specimen as an example. The relevant elemental emission lines, which can be assigned are marked in orange (Si), pink (Ni) and green (Fe),respectively.*

9.4.5 X-ray photoelectron spectroscopy (XPS)

X-ray photoelectron spectroscopy (XPS) was conducted using an Escalab 250 Xi instrument (ThermoFisher) with an Avantage software (version 5.982). The radiation source employed was Mg Kα with an energy of 1253.6 eV instead of the default Al Kα for avoiding overlap of XP and Auger signals. The power was set to 400 W. For spectral acquisition, a pass energy of 100 eV was applied for survey scans and 20 eV for detailed scans. Each spectrum was averaged over five scans. The dwell time was set to 10 milliseconds for survey scans and 50 milliseconds for detailed scans. The energy step size was 1 eV for the survey scan and 0.05 eV for the detailed scan. Surface cleaning was performed using a MAGCIS Ar ion source (ThermoFisher) in Ar-cluster mode at an energy of 6 keV for 120 seconds. The XPS analysis focused on the Ni 2p and Fe 2p core-level lines for argon sputtering layer by layer with the Ar ion source in Ar-ion mode at 3 keV. The calibration for this process was performed using a 50 nm Ni film on a glass substrate as a reference. The reference supplied by the company LiMedion GmbH was prepared by magnetron sputtering and evaluated using using profilometry to be 50 ± 2 nm.

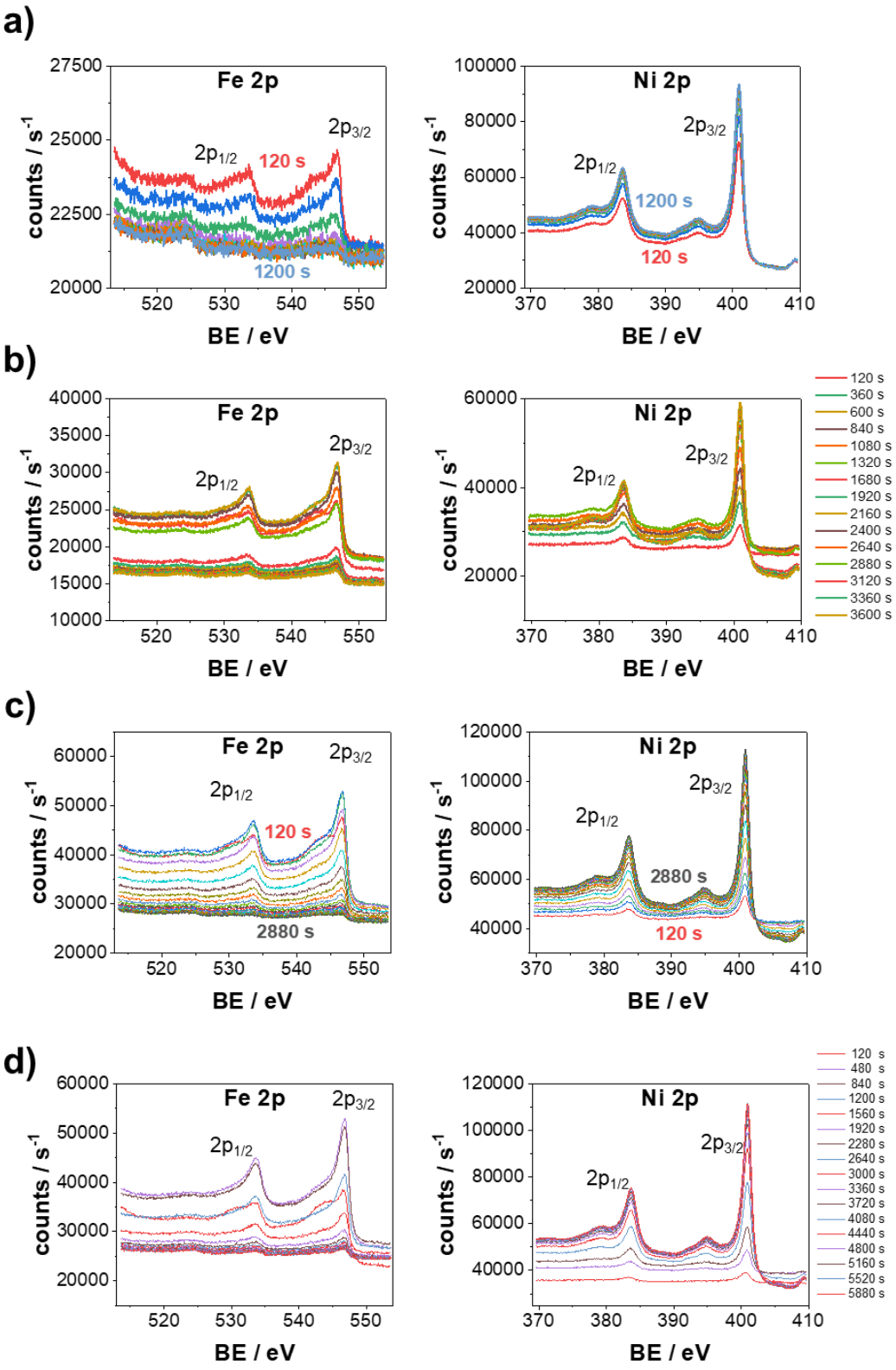

Figure S18: *Sputter time resolved high resolution Fe 2p and Ni 2p XPS spectra for poly-Ni electrodes exposed to a) 0 ppm, b) 3 ppm, c) 6 ppm, d) 14 ppm Fe $^{z+}$ ions in 0.1 M KOH electrolyte. Sputter process was performed with Ar^+ beam energy of 6 keV and t = 120 s per cycle.*

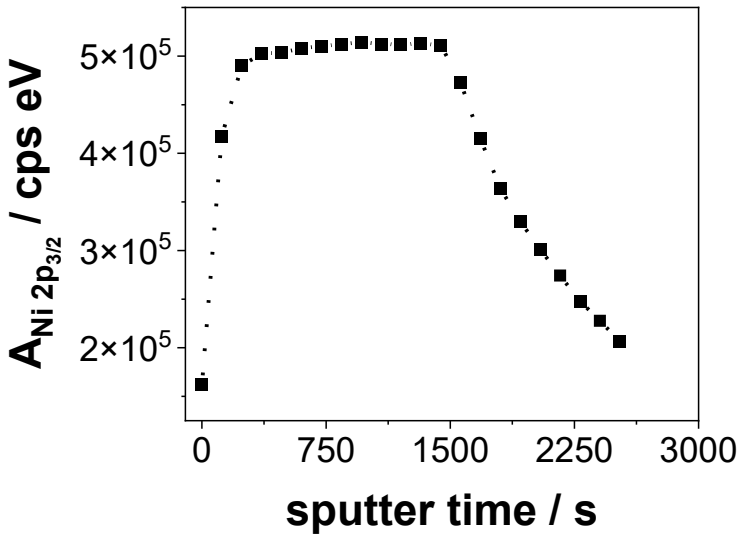

Figure S19: *Depth profile of a 50 nm thick Ni film on a glass substrate obtained by sputtering process. The area of the Ni $2p_{3/2}$ XPS peak is plotted against the sputter time.*

Figure S19 presents the XPS depth profile of a 50 nm thick Ni film deposited on a glass substrate obtained by Ar^+ sputtering. The sample, prepared by LiMedion GmbH, was measured using profilometry to be 50 ± 2 nm thick. The area of the Ni $2p_3/_2$ XPS peak is plotted against the sputtering time, providing insights into the sputter rate of the nickel layer as it is progressively etched. This was used as a thickness reference for the sputter profiles of the electrochemically treated poly-Ni electrodes.

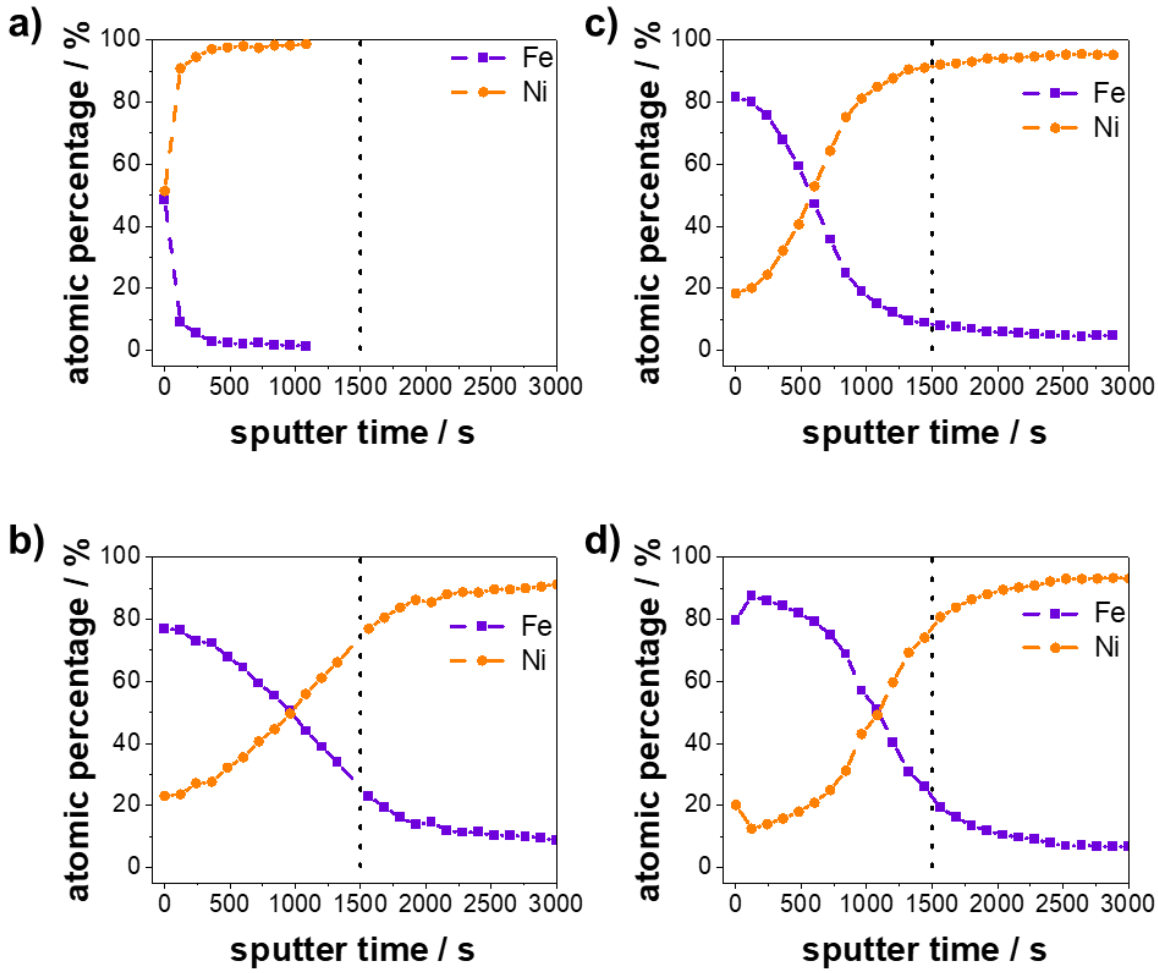

Figure S20: *XPS Depth profiles obtained by Ar^+ sputtering for the electrochemically treated poly-Ni disks exposed to a) 0 ppm, b) 3 ppm, c) 6 ppm and d) 14 ppm Fe^{z+} species after 24 h galvanostatic AST measurement at $i = -10\ mA\ cm_{geo}^{-2}$. The atomic percentage of nickel and iron based on the area ratio of the $2p_{3/2}$ XPS peaks is plotted against the Ar^+ sputter time. The total sputter time needed to remove a 50 nm thick Ni layer from a glass substrate is denoted with a dashed line. The sputter profile of the 50 nm reference is shown in* ***Figure S19****.*

9.4.6 Cyclic Voltammetry (CV) Analysis

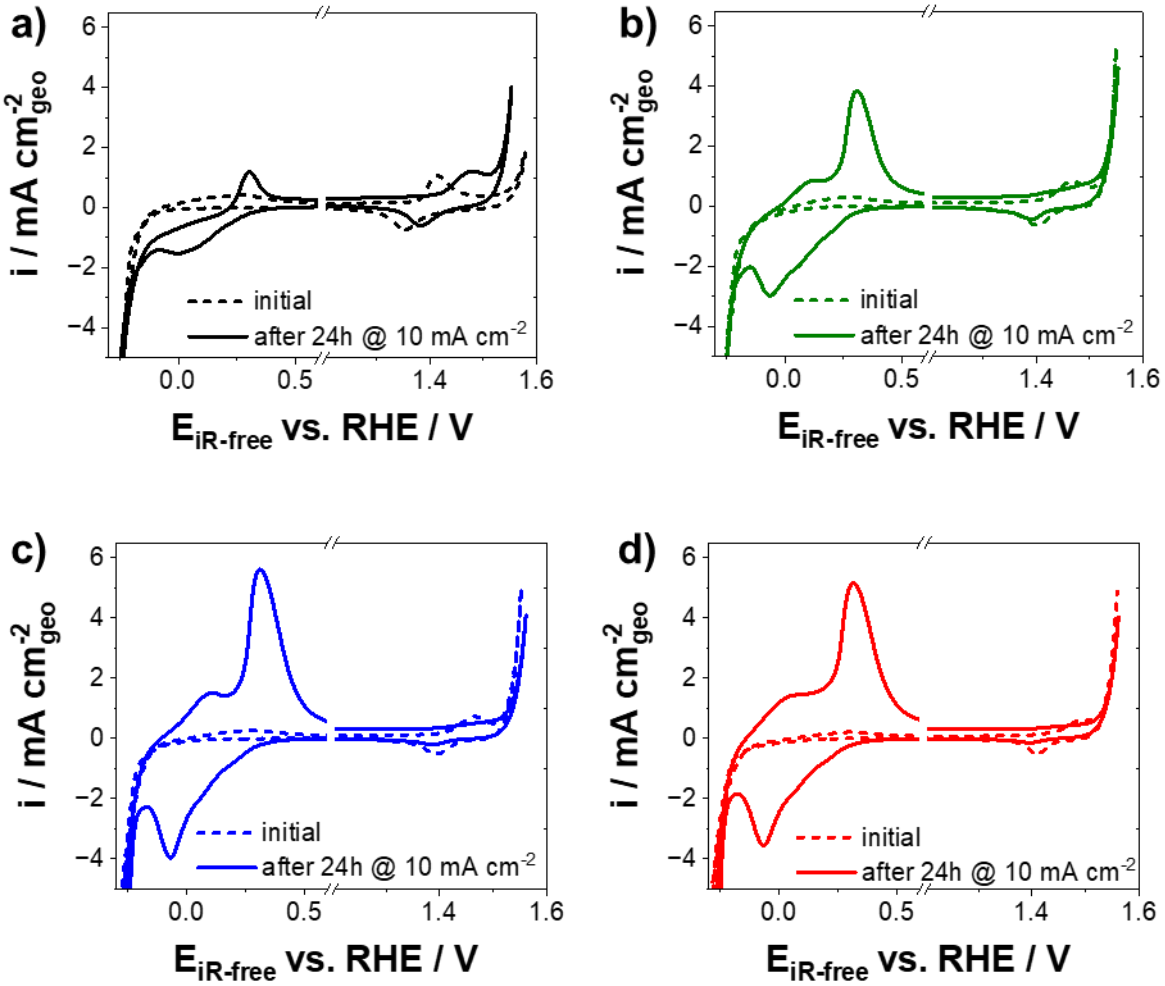

Figure S21: *Examples of cycle 6 of the CV profiles for poly-Ni electrode exposed to a) 0 ppm, b) 3 ppm, c) 6 ppm and d) 14 ppm* Fe^{z+} *species in 0.1 M KOH before (dashed line) and after the 24-h galvanostatic AST experiment at* $-10\ mA\ cm_{geo}^{-2}$ *(solid line). The CV profiles were recorded with a scan rate of 100 mV* s^{-1}*.*

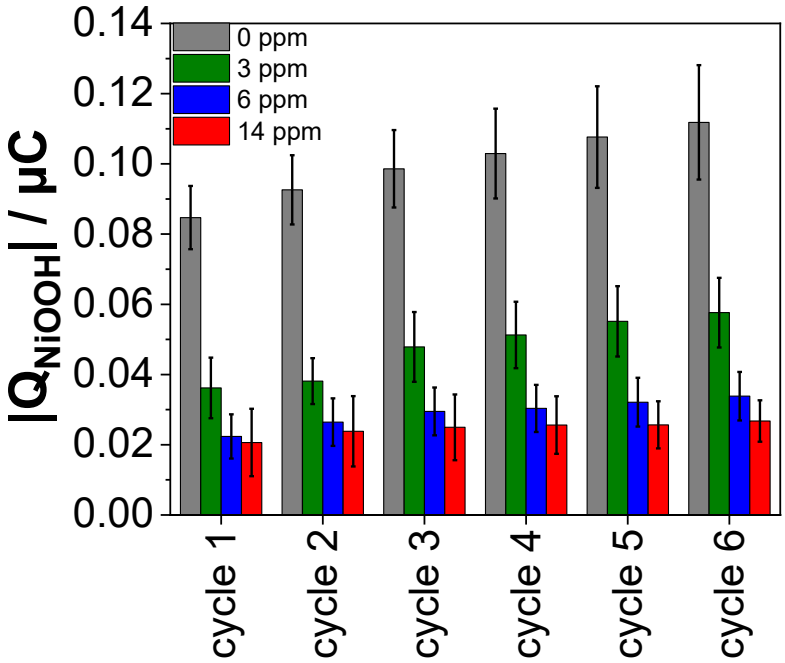

Figure S22: *Charge associated with the reduction of NiOOH peak for all cycles of the final CV profiles and all tested Fe^{z+} concentrations between 0 and 14 ppm. Error bars represent the standard deviations within a sample number of $N = 7$ independent measurements. Bar diagrams display the $|Q_{NiOOH}|$ for each cycle at different Fe^{z+} concentrations and are shown in grey (0 ppm), green (3 ppm), blue (6 ppm), and red (14 ppm), respectively.*

9.4.7 Example of Galvanostatic Impedance Fitting

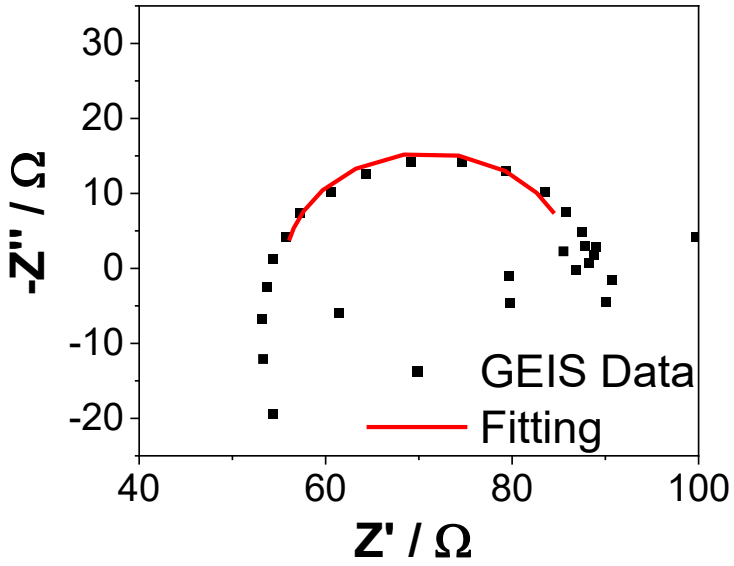

Figure S23: *Example of the galvanostatic impedance spectroscopy (GEIS) data recorded each hour at* $-10\ mA\ cm_{geo}^{-2}$ *and the corresponding fit using the Randles circuit method.*

9.4.8 Investigation on a High Surface Area Nickel Electrode

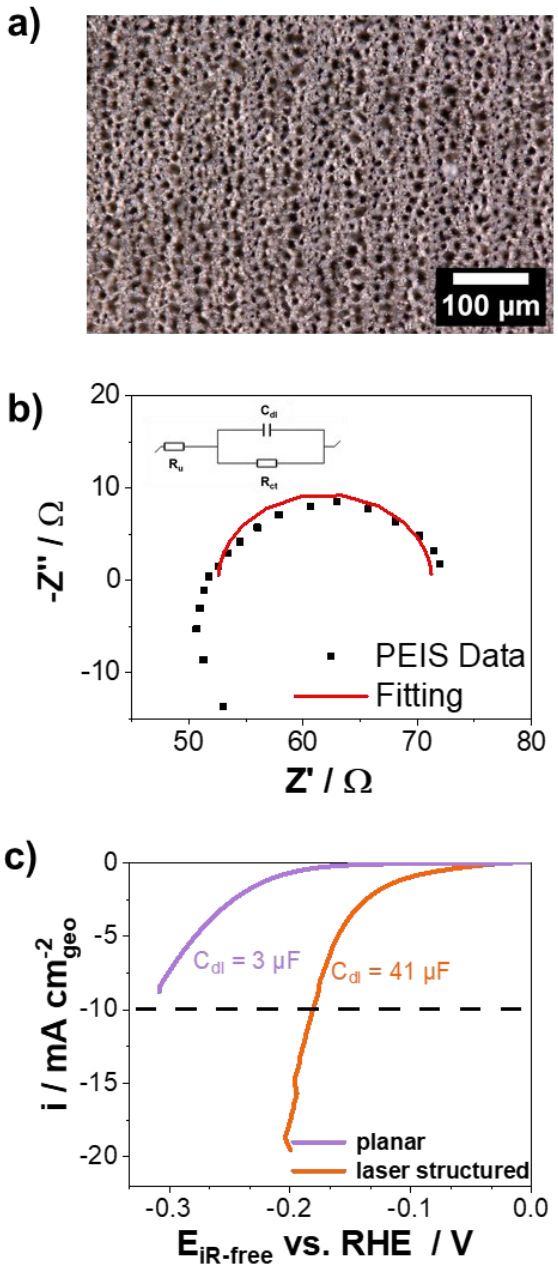

Figure S24: *Electrochemical investigation on a high surface area nickel electrode.* ***a)*** *Optical image of laser-structured Ni disk (diameter = 5 mm) at 500x magnification as prepared according to the procedure in literature [261].* ***b)*** *Representative potentiostatic impedance spectroscopy (PEIS) data and the respective fit based on the Randles circuit method to obtain the double layer capacitance.* ***c)*** *HER polarization curves (i vs. $E_{iR\text{-}free}$) for a flat polycrystalline and a laser structured nickel disk recorded from −0.4 to 0 V vs. RHE with a scan rate of 10 mV s^{-1} at 2400 rpm in Ar-saturated 0.1 M KOH.*

10 List of Hazardous Substances

Chemical	CAS-No.	Pictograms	H statements	P statements
2-propanol	67-63-0		H: 225-319-336	P: 210-240-305+351+338-403+233
argon	7440-37-1		H: 280	P: 403
hydrochloric acid	7647-01-0		H: 290-314-335	P: 280-303+361+353-305+351+338+310
hydrogen	1333-74-0		H: 220-280	P: 210-377-381-403
iron(II) chloride tetra hydrate	13478-10-9		H: 302-314	P: 280-305+351+338-310
iron(II) sulfate hydrate	13463-43-9		H: 302-315-319	P: 301+312+330-302+352-305+351+338
nickel rod	7440-02-0		H: 317-351 - 372	P: 202-260-264-280-302+352-308 + 313

nitric acid	7697-37-2		H: 272-290-330-314	P: 210-220-280-303+361+353-304+340+310-305+351+338
platinum powder	7440-06-4		H: 228	P: 210-240-241-280-370+378
potassium ferricyanide	13746-66-2		H: 319-411 EUH: 032	P: 264-273-280-305+351+338-337+313-391
potassium ferrocyanide	14459-95-1	--	H: 412 EUH: 032	P: 273
potassium hydroxide	1310-58-3		H: 290-302-314	P: 234-260-280-301+312-303+361+353-305+351+338
ROTI®Star 28 elements in 5 % HNO_3	Mixture		H: 290-314-317-H350-412 EUH: 071	P: 280
sodium per chlorate	7601-89-0		H: 271-302-319-373	P: 210-220-301+312-305+351+338-314

		 		
sulfuric acid	7664-93-9		H: 290-H314	P: 280-301+330+331-303+361+353-305+351+338+310
tellurium powder	13494-80-9	 	H: 317-332-360Df-362-413	P: 260-263-273-280-304+340+312-308+313

H Sentences:

H220	Extrem entzündbares Gas.
H225	Flüssigkeit und Dampf leicht entzündbar.
H228	Entzündbarer Feststoff.
H272	Kann Brand oder Explosion verursachen; oxidierend.
H280	Enthält Gas unter Druck; kann bei Erwärmung explodieren.
H290	Kann ätzend auf Metalle wirken.
H302	Gesundheitsschädlich bei Verschlucken.
H314	Verursacht schwere Verätzungen der Haut und schwere Augenschäden.
H315	Verursacht Hautreizungen.
H317	Kann allergische Hautreaktionen verursachen.
H319	Verursacht schwere Augenreizung.
H330	Lebensgefahr bei Einatmen.
H332	Gesundheitsschädlich bei Einatmen.
H336	Kann Schläfrigkeit und Benommenheit verursachen.
H351	Verdächtigt krebserzeugend zu sein.
H350	Kann Krebs erzeugen.
H360Df	Kann die Fruchtbarkeit beeinträchtigen. Kann das Kind im Mutterleib schädigen.

H372	Schädigt Organe bei längerer oder wiederholter Exposition.
H373	Kann die Organe schädigen bei längerer oder wiederholter Exposition.
H411	Giftig für Wasserorganismen, mit langfristiger Wirkung.
H412	Schädlich für Wasserorganismen, mit langfristiger Wirkung.
EUH032	Entwickelt bei Berührung mit Säure sehr giftige Gase.
EUH071	Wirkt ätzend auf die Atemwege.

P Sentences:

P202	Vor der Handhabung alle Sicherheitsvorkehrungen lesen.
P210	Von Hitze, heißen Oberflächen, Funken, offenen Flammen und anderen Zündquellen fernhalten. – Nicht rauchen.
P220	Von Kleidung und anderen brennbaren Materialien fernhalten.
P234	Nur im Originalbehälter aufbewahren.
P240	Behälter und zugehörige Ausrüstung erden.
P260	Dampf/Aerosol nicht einatmen.
P264	Nach Gebrauch gründlich waschen.
P273	Freisetzung in die Umwelt vermeiden.
P280	Schutzhandschuhe/Schutzkleidung/Augenschutz/Gesichtsschutz tragen.
P301+312	BEI VERSCHLUCKEN: Bei Unwohlsein GIFTINFORMATIONSZENTRUM/Arzt anrufen.
P301+330+331	BEI VERSCHLUCKEN: Mund ausspülen. KEIN Erbrechen herbeiführen.
P302+352	BEI BERÜHRUNG MIT DER HAUT: Mit viel Wasser und Seife waschen.
P303+361+353	BEI KONTAKT MIT DER HAUT (oder dem Haar): Alle kontaminierten Kleidungsstücke sofort ausziehen. Haut mit Wasser abspülen/duschen.
P304+340	BEI EINATMEN: An die frische Luft bringen und in einer Position ruhigstellen, die das Atmen erleichtert.
P305+351+338	BEI KONTAKT MIT DEN AUGEN: Einige Minuten lang behutsam mit Wasser spülen. Vorhandene Kontaktlinsen nach Möglichkeit entfernen. Weiter spülen.
P308+313	BEI Exposition oder falls betroffen: Ärztlichen Rat einholen/ärztliche Hilfe hinzuziehen.
P310	Sofort GIFTINFORMATIONSZENTRUM/Arzt anrufen.

P314	Bei Unwohlsein ärztliche Hilfe hinzuziehen.
P337+313	Bei anhaltender Augenreizung: Ärztlichen Rat einholen/ärztliche Hilfe hinzuziehen.
P370+378	Bei Brand: Geeignetes Löschmittel verwenden.
P377	Bei Leckage: Kein offenes Feuer oder Funken erzeugen.
P381	Alle Zündquellen entfernen, falls gefahrlos möglich.
P403	An einem gut belüfteten Ort aufbewahren.
P403+233	An einem gut belüfteten Ort aufbewahren. Behälter dicht verschlossen halten.
P202	Vor der Handhabung alle Sicherheitsvorkehrungen lesen.

11 Acknowledgements

First of all, I'd like to thank Prof. Dr. Mehtap Oezaslan for giving me the opportunity to pursue my PhD thesis within her group and for evaluating this work. Your continued support and insightful discussions have been invaluable to me. I am deeply grateful for the freedom you allowed me to explore, develop, and execute my own research ideas.

I'd also like to express my gratitude to Prof. Dr. Matthias Arenz for evaluating my thesis. Special thanks to Prof. Dr.-Ing. Jakob Albert and Prof. Dr. Alf Mews for agreeing to evaluate my disputation.

A heartfelt thank you to all members of the DFG-NSF project for your unwavering dedication throughout this journey, even during challenging moments. Many collaborators contributed in different ways to this thesis, and while there's not enough space to mention everyone individually, I truly appreciate all your efforts.

I'd like to specifically thank Jakob Traegner for developing the theory for the impinging jet electrodes with me, for investing countless hours in executing CFD simulations, and for discussing the research data so thoroughly. Your encouragement to automate my data analysis was also a huge help.

I'm also deeply grateful to the entire Technical Electrocatalysis Laboratory working group for being such supportive colleagues and for inspiring me to develop my fitness and engage in sports. There are a few individuals I'd like to highlight. My deepest thanks go to Vedasri Bai Khavala. Without your hard work, the study on iron impurities would never have been possible. Thank you for being an amazing lab partner and an even better friend. Thanks for all the time and your trust in me guiding through this project, even when things were difficult. You really helped me to learn to manage myself and others and also to grow personally in my life.

I also want to thank Marek Janssen for being an outstanding office mate and discussion partner on all things electrochemistry. Your mentorship, especially when I was struggling with the PhD process, was invaluable. I'm also incredibly grateful to you for helping me land my first job post-PhD and even assisting with my room search.

A big thank you to Maurice Friedrichs-Schucht for our many discussions on water electrolysis and engineering topics related to my projects. I believe our conversations

were key in helping us both reach the finish line with our PhDs. Your lessons on full-cell testing and test stations will be incredibly useful in my next job.

Special thanks to Sonja Blaseio for guiding me through the complexities of Raman spectroscopy and for answering all my questions. I also want to thank Jan-Steffen Haverkamp for teaching me how to manage myself and how to meal-prep, and Luana Schwendler for inspiring me to prioritize fitness no matter how demanding work becomes. A special mention goes to Stefan Panic, who helped me become more open and confident in interacting with others, especially during conferences.

I'd like to thank my family for their continued support over many years of study. You've never let me down and have always believed in me. You picked me up when I most needed it and greatly helped me during the writing process of this thesis by just being there whenever I needed it. A special thanks to my grandpa, Hubert Schneemann, for sparking my curiosity about nature, which eventually led me to pursue a career as a natural scientist. I'm also thankful to Dominik Schönleiter for his help ship to ship samples around the world when it seemed impossible.

I owe a huge thank you to a very special person in this workgroup, who has always understood me. You cheered me up when I was down and catalyzed my journey toward discovering my true self. Your enthusiasm and energy made every outing something I looked forward to, and your reminder that research can be exciting and fun has stayed with me throughout. Without you I would've not made such a strong final push for my thesis. Thank you so much for everything Helena, you helped me more than you know.

Lastly, I want to express my gratitude to my ex-girlfriend for her unwavering support during the most difficult times of my thesis. You pulled me out of the stress and struggle when everything seemed dark and I almost wanted to give up. You made me stay strong last year no matter what happened and reminded me what really matters in life when I needed it. I'm thankful for all the time we spent together, and you taught me to remember that there's life outside of research. I'm rooting for your future as you do for mine, and I'll always be grateful for this chapter of my life. I think we both grew in ways that will stay with us, and I'll always be thankful for the time we shared and the lessons we learned together.

12 Declaration of Oath / Eidesstaatliche Erklärung

I hereby declare and affirm that this doctoral dissertation is my own work and that I have not used any aids and sources other than those indicated. If electronic resources based on generative artificial intelligence (gAI) were used in the course of writing this dissertation, I confirm that my own work was the main and value-adding contribution and that complete documentation of all resources used is available in accordance with good scientific practice. I am responsible for any erroneous or distorted content, incorrect references, violations of data protection and copyright law or plagiarism that may have been generated by the gAI.

Hiermit versichere ich an Eides statt, die vorliegende Dissertationsschrift selbst verfasst und keine anderen als die angegebenen Quellen und Hilfsmittel benutzt zu haben. Sofern im Zuge der Erstellung der vorliegenden Dissertationsschrift generative Künstliche Intelligenz (gKI) basierte elektronische Hilfsmittel verwendet wurden, versichere ich, dass meine eigene Leistung im Vordergrund stand und dass eine vollständige Dokumentation aller verwendeten Hilfsmittel gemäß der Guten wissenschaftlichen Praxis vorliegt. Ich trage die Verantwortung für eventuell durch die gKI generierte fehlerhafte oder verzerrte Inhalte, fehlerhafte Referenzen, Verstöße gegen das Datenschutz- und Urheberrecht oder Plagiate.

27.11.2025 

(Date, Signature)